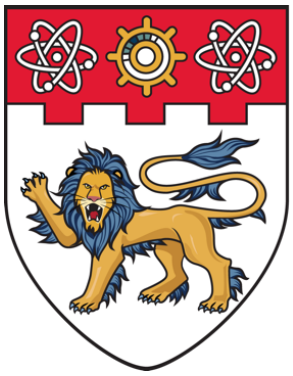

NANYANG TECHNOLOGICAL UNIVERSITY
SINGAPORE

Stabilization of Superoxocopper(II) and Oxoiron(IV) Complexes using Bulky Bis- and Tris(2-pyridylmethyl)amine Ligand

Sebastian Quek Yongsen

SCHOOL OF PHYSICAL AND MATHEMATICAL SCIENCES

2019

Stabilization of Superoxocopper(II) and Oxoiron(IV) Complexes using Bulky Bis- and Tris(2-pyridylmethyl)amine Ligand

Sebastian Quek Yongsen

SCHOOL OF PHYSICAL AND MATHEMATICAL SCIENCES

A thesis submitted to the Nanyang Technological University in partial fulfilment of the requirement for the degree of Doctor of Philosophy

2019

Statement of Originality

I hereby certify that the work embodied in this thesis is the result of original research done by me except where otherwise stated in this thesis. The thesis work has not been submitted for a degree or professional qualification to any other university or institution. I declare that this thesis is written by myself and is free of plagiarism and of sufficient grammatical clarity to be examined. I confirm that the investigations were conducted in accord with the ethics policies and integrity standards of Nanyang Technological University and that the research data are presented honestly and without prejudice.

13/05/2019
Date

Sebastian Quek Yongsen

Supervisor Declaration Statement

I have reviewed the content and presentation style of this thesis and declare it of sufficient grammatical clarity to be examined. To the best of my knowledge, the thesis is free of plagiarism and the research and writing are those of the candidate's except as acknowledged in the Author Attribution Statement. I confirm that the investigations were conducted in accord with the ethics policies and integrity standards of Nanyang Technological University and that the research data are presented honestly and without prejudice.

14/05/2019
.....
Date

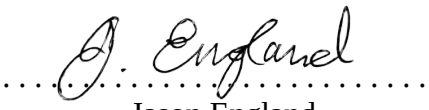
.....
Jason England

Authorship Attribution Statement

Please select one of the following; *delete as appropriate:

*(A) This thesis **does not** contain any materials from papers published in peer-reviewed journals or from papers accepted at conferences in which I am listed as an author.

~~*(B) This thesis contains material from [x number] paper(s) published in the following peer-reviewed journal(s) / from papers accepted at conferences in which I am listed as an author.~~

. . . . 13/05/2019 . . .
Date

. . . . . .
Sebastian Quek Yongsen

Abstract

Highly reactive ‘end-on’ superoxocopper(II) and oxoiron(IV) intermediates are recognized as active oxidants responsible for substrate C-H bond hydroxylation in a wide range of non-heme metalloenzymes. Mimicking such reactivity in synthetic systems would provide a major improvement over the current de-facto methods used in oxidation chemistry, where direct C-H remains inefficient and a niche concern. This goal requires a greater understanding of the properties of the aforementioned oxidants and how they can be tailored. As part of a greater effort to achieve these ends, mononuclear ‘end-on’ superoxocopper(II) and intermediate-spin (S = 1) oxoiron(IV) supported by new ligands, ^{Ar3}TPA and ^{Ar2}RBPA (Me or Bn), have been prepared and their reactivity characterized (**Figure 1**).

Figure 1: Ligands used herein to support superoxocopper(II) and oxoiron(IV) complexes.

From a survey of the literature, it can be inferred that the ligands bearing significant steric bulk are able to stabilize mononuclear ‘end-on’ superoxocopper(II) complexes *and* provide high-spin oxoiron(IV) species by enforcing a trigonal bipyramidal geometry at the iron centre. Unfortunately, the use of bulky ligands was accompanied, in both cases, by poor intermolecular reactivity toward substrates. It is tempting to assign such observation to steric effects, but the influence of the different donor properties of ligands used has not been accounted for. In an effort to address this glaring omission and obtain sterically stabilized superoxocopper(II) and oxoiron(IV) that retain the reactivity properties of non-bulky systems, we developed tris- and bis(2-pyridylmethyl)amine ligands that incorporate bulky aryl substituents at the 5th position of the pyridyl donors.

Coordination of ^{Ar3}TPA to first-row transition M^{2+} ions revealed that with weak field co-ligands, in the solution state, five coordinate geometries are preferred (**Chapter 2**). In contrast, X-ray crystallographic studies show that these complexes display either octahedral (Fe and Mn) or trigonal bipyramidal (Fe, Co and Cu) geometries, depending on the metal and the co-ligand involved. Moreover, comparison of the electrochemical properties of these complexes with the unsubstituted parent TPA complexes indicate that the bulky aryl substituents do not weaken the donor strength of the ligand, which suggests that their complexes should display similar inherent reactivity. Similar conclusions were reached from electrochemical studies of an analogous series of ^{Ar2}RBPA complexes (**Chapter 3**). In the case of the ^{Ar2}RBPA ligands, only 6-coordinate geometries, in which the ligand coordinated in a 'mer' fashion, were observed. Crucially, unlike the parent BPA ligand, no evidence was found for formation of bischelate metal(II) complexes, $[M^{II}(^{Ar2}RBPA)_2]^{2+}$.

Reaction of $[Cu^{I}(^{Ar3}TPA)(NCMe)]^{+}$ with O_2 yielded mononuclear 'end-on' superoxocopper(II) complexes (**Chapter 4**). Remarkably, this reaction was found to be reversible, there was no 'dimerization' to yield a peroxo-bridged dicopper(II) complex at any temperature, and evidence for formation of the superoxocopper(II) moiety could be observed even at room temperature. Furthermore, the superoxocopper(II) complexes possess good reactivity with a range of 2,6-di-*tert*-buyl-*para*-subsituted-phenols, despite it being slower than observed for less hindered TPA systems. In-depth mechanistic studies were performed and, the activation parameters and relationship with oxidation potential of the phenols, suggest the possibility that their comparatively poor reactivity may be contributed, in part, by the difference in donor properties of the ligand, rather than steric factors alone. Regardless, this is the first example of a stable mononuclear 'end-on' superoxocoppr(II) complex that displays significant substrate reactivity.

In contrast, whereas oxygenation of $[Cu^{I}(^{tpb2}MeBPA)(NCMe)]^{+}$ still yielded only superoxocopper(II) complexes (i.e., no dimerization was observed), they were only stable at temperatures below -85°C. Furthermore, the UV-vis spectra of these superoxocopper(II) complexes displayed smaller extinctions coefficients compared with published systems. This, combined with the high sensitivity of oxygenation to the solvent medium and issues regarding reproducibility, raises the possibility of incomplete reaction.

Oxidation of the $[Fe^{II}(^{tpb3}TPA)]^{2+}$ starting complex yielded $[Fe^{IV}(O)(^{tpb3}TPA)]^{2+}$ (**Chapter 5**) that, on the basis of Mössbauer and UV-vis spectroscopic studies, is assigned to be of intermediate-spin (S = 1). This spin-state is indicative of an octahedral geometry and, thus, there is insufficient inter-pyridine repulsion in the ^{tpb3}TPA ligand to enforce trigonal bipyramidial geometry. Various anions were coordinated in the *cis*-labile site of the oxoiron(IV) complex and their stability is discussed. Unfortunately, these weak field anions did not elicit a change in spin-state. Although the targeted high-spin state was not achieved, the complex $[Fe^{IV}(O)(^{tpb3}TPA)(NCMe)]^{2+}$ showed good stability at room temperature and reactivity towards a wide range of substrates, including those with strong C-H bonds (e.g., cyclohexane). The linear correlation of the logarithm of experimentally determined second order rate constants versus C-H bond dissociation energy, and the large KIEs observed are all consistent with H-atom transfer reactivity involving tunneling.

Acknowledgements

I would like to express my sincere gratitude to the following people who supported, guided and helped me in these important four years journey in my PhD studies.

First of all, I would like to thank my supervisor, Dr Jason England for giving me an opportunity for working in his lab and guidance on how to solve research problems when arised. A special thank must be mentioned to the senior members of the lab group, which includes Dr Chan Siu Chung, Dr Kumaran, Dr Liu Zhao and Dr Suman, for their guidance and help. A special thank must be mention to Dr Suman for his help in Chapter 5 for generate some of the important results in my studies. I would like to show my appreciation to the junior members and my students in the lab group, such as Mr Benny, Mr Ang Zhi Zhong, Mr Lim Ming Hui, Mr Tan Xian Yi, Ms Ang Yu Ting, Ms Amanda Sng, Ms Loh Hui Xin, Ms Fiona Jamieson, Ms Tam Siman, Mr Ryan Ong Yan Xun, Mr Rahmat and Ms Nicole Lu Ci'En for their help in my project and lessen my workload especially in my final year of my PhD.

Secondly, I would like to show my appreciate to the X-ray Crystallographer, Dr Rakesh Ganguly and Dr Li Yongxin for running and solving my X-ray structure especially when some of the crystals can be quite difficulty to run. Thanks will also go to the NMR staff, Ms Goh Ee Ling, Mr Derek Ong and Mr Keith Leung for my NMR studies, especially some of the compounds require paramagnetic parameters as well as Ms Pui Pang Yi and Ms Zhu Wen Wei for their assistance on elemental analysis and mass spectrometry.

I would also like to thank my same batch of NTU friends via course mate, namely Mr Luthfi, Dr Sim Ying, Dr Sabrina Khoo, Mr Choo Xing Yao, Ms Gan Sherli, Ms Ng Shue Mei, Ms Ng Yik Yek, Dr Jonathan Wong and Dr Ivan Solics for their upmost support during the course of my PhD by listening to my problems faced and providing a helping hand in my research studies.

I would like to thank Mr Anders See Yang Feng, Ms Ko Wei Ting and Dr Wang Yang for their knowledge of organic chemistry during the stage of my ligand synthesis.

Next up, I would also like to show my appreciation to my group of army friends, namely Mr Yap Wei Chong, Mr Maurice Ng, Mr Ng Chok Kee, Mr Tan Wei Jie, Mr Tan Ji Xiang, Mr Lew Xu Dong, Mr Ng Keng Siang, Mr Lee Zhi Xuan and Mr Daniel Goh for their support during my PhD time as well as my wedding during the course of my PhD.

Furthermore, I would also like to show my appreciation to my group of friends, namely Mr Chow Wei Guang, Mr Lim Zhi Xuan, Mr Ong Guang Shen, Mr Pang Wei Sheng, Mr Alvin, Ms Candy Soh, Mr Tee Hongda and Mr Tay Meng How for their support and understanding during my journey of PhD.

Most importantly, I would like to thank my family, especially my wife, Ms Tay Yu Shan, for their upmost support, constant love and concern during the course of my PhD timeline.

I am grateful to Nanyang Technological University for providing me the opportunity and funding for my research studies.

Table of Contents

Abbreviations

BDE	Bond dissociation energies
BDPP	2,6- Bis((2-(S)-diphenylhydroxylmethyl-1-pyrrolidinyl)methyl)pyridine
Bis-Pi1	2,4-(2-pyridyl)-3-methyl-7-(2-pyridylmethyl)-3,7-diazabicyclo[3.3.1]nonanone
Bn	Benzyl
BNAH	1-Benzyl-1,4-dihydronicotinamide
BPA	Bis(2-pyridylmethyl)amine
BzImH	1,3-Dimethyl-2,3-dihydrobenzimidazole
CHD	1,4-Cyclohexadiene
CV	Cyclic Voltammetry
Cyclam	1,4,8,12-tetraazacyclopentadecane
DβM	Dopamine β monooxygenase
DCM	Dichloromethane
DFT	Density functional theory
DHA	9,10-dihydroanthracene
dtbt	[2,6-(*para*-di-*tert*-butyl)-diphenyl]benzene
EPR	Electron paramagnetic resonance
ESI-MS	Electrospray Ionization Mass Spectrometry
HIPT	Hexaisopropylterphenyl
HPCD	Homoprotocatechuate-2,3-dioxygenase
H_3buea	1,1,1-tris[(*N'*-tert-butylureaylato)-*N*-ethyl]aminato
IPNS	Isopenicilin N Synthase
KIE	Kinetic Isotope Effects
α-KG	α-Ketogulatrarate

Me	Methyl
MeCN	Acetonitrile
Mes	Mesityl
Me_3NTB	Tris((N-methylbenzimidazol-2-yl)methyl)amine
MIOX	*Myo*-inosoitol oxygenase
NADH	Nicotinamide adenine dinucleotide
N4Py	*N*,*N*-bis(2-pyridylmethyl)-*N*-bis(2-pyridyl)methylamine
NMR	Nuclear Magnetic Resonance
*n*Bu-P2DA	*N*-(1'1'-bis(2-pyridyl)pentyl)iminodiacetate
PDP	2-({(S)-2-[(S)-1-(pyridin-2-ylmethyl)pyrrolidin-2-yl]pyrrolidin-1-yl}methyl)pyridine
PHM	Peptidylglycine α-hydroxylating monooxygenase
py	pyridine
Py-tacn	1,4-dimethyl-7-(2'-pyridy*N*'ylmethyl)-1,4,7-triazonane
OTf	trifluoromethanesulfonate
τ	tau (geometry index of the complex)
TAML	Tetra-amido macrocyclic ligands
TA-tren	Triaryl-tris(2-ethylamino)amine
*t*Bu	*tert*-butyl
THF	Tetrahydrofuran
Tips	Tri-*iso*-propyl-silyl
TIB	2,4,6-tri-*iso*-propylbenzene
TMC	1,4,8,12-Tetramethyl-1,4,8,12-tetraazacyclopentadecane
TMCO	4,8,12-trimethyl-1-oxa-4,8,12-triazacyclotetradecane

TMG_2dien	2',2'-(2,2'-(methylazanediyl)bis(ethane-1,2-diyl))bis(1,1,3,3-tetramethylguanidine
TMG_3tren	1,1,1-tris(2-[*N2*-(1,1,3,3-tetramethylguanidino)]ethyl)amine
TPA	Tris(2-pyridylmethyl)amine
tpa^{Ph}	Tris(5-phenylpyrrol-2-ylmethyl)amine)
tpb	Triphenylbenzene
TPEN	Tris(2-pyridylmethyl)-1,2-diaminoethane
tpy	2,6-diphenylbenzene
TQA	Tris(2-quinolylmethyl)amine

List of Schemes

List of Figures

List of Table

Chapter 1
Introduction

1.1 Traditional Oxidation Chemistry

Traditional powerful oxidants, such as inorganic permanganate and dichromate, are only able to oxidize substrates with activated C-H bonds. For instance, the oxidation of toluene to benzoic acid by stoichiometric $KMnO_4$ (**Figure 1.1**). Such reagents are problematic because they are toxic, generate large amounts of waste and are potentially explosive.

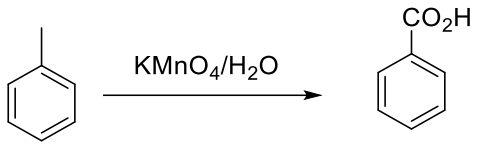

Figure 1.1: Oxidation of toluene to benzoic acid using $KMnO_4$.

In addition, many traditional oxidants used in synthetic chemistry are based upon expensive noble metals and utilize costly oxidants. For example, the widely employed Sharpless asymmetric dihydroxylation of alkenes utilizes a combination of catalytic amounts of highly toxic osmium(VIII) oxide and, usually, either potassium ferricyanide or *N*-methylmorphiline *N*-oxide as terminal oxidants (**Figure 1.2)**, neither of which can be described as cheap or non-toxic.[1,2] In response, efforts are being made to develop first-row transition metal complexes that are able to catalyze these reactions using cheap oxidants. Much of this work is bioinspired.

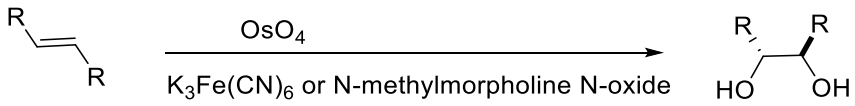

Figure 1.2: Hydroxylation of alkene to diols acid using osmium(VIII) oxide.

1.2 Biological Systems

Potential solutions for the above problems can be seen in biological systems, where highly selective oxidation of organic molecules is prominent. These processes are, usually, catalyzed by metalloenzymes that contain highly abundant iron and copper ions, which are able to access a variety of oxidations states. The organic products are obtained in high chemo- and stereoselectivity, and non-toxic dioxygen (O_2) is predomiantly used as the terminal oxidant. Furthermore, these metalloenzymes operate under ambient conditions and are able to efficiently catalyze oxidation of highly inert C-H bonds. Such biological systems have inspired intense efforts among chemists and biochemists to understand their active sites and mechanisms of action. It should be highlighted that without the use of transition metals, harnessing the oxidative potential of O_2 for synthetic reactions is challenging. This is due to significant kinetic barriers to reaction stemming from its strong O=O bond and its triplet ground state, which inhibits reaction with closed-shell ($S = 0$) substrates. Transition metals, which are often open-shell and possess low-lying excited states, are able to circumvent these problems and activate O_2 for further reaction.[3] Metalloenzymes that are able to facilitate C-H bond oxidation can be crudely separated into 3 different classes,[4] namely heme iron, non-heme iron and copper-containing.

1.3 Heme Systems

The cytochrome P450 enzymes are the paradigm example of enzymatic O_2 activation for C-H bond oxidation, and their spectroscopic and reactivity properties are well understood. They are involved in the metabolism of a wide variety of drugs, as well as the biosynthesis of steroids.[5,6] More fundamentally, they perform a wide range of oxidation chemistry, including hydroxylation of aliphatic C-H bonds and epoxidation of C-C double bonds, all with excellent regioselectivity and stereoselectivity.

The activity of Cytochrome P450 is dependent upon an iron porphyrin co-factor that is anchored to active site by the axial coordination of a cysteine residue (**Figure 1.3**).[7] Dioxygen coordinates and is activated at the remaining vacant site. It is worth noting that the strongly electron donating cysteine residue is believed to be key for generation of the active oxidant, by promoting O-O bond cleavage and delocalization of charge in the resulting high oxidation state species.[8] Furthermore, a recent study suggests that the thiolate ligand is also key in promoting C-H bond abstraction from substrates over the alternative oxidation of the heme functionality.[9]

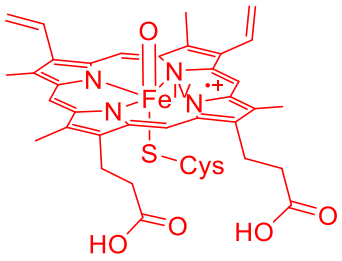

Figure 1.3: Structure of the active oxidant for Cyctrochrome P450.

The general mechanism of Cyctochrome P450 involves reaction of O_2 with a reduced iron(II)-containing active state to yield a superoxoiron(III) complex. Subsequent electron and proton transfer from co-factors (**Figure 1.4**) gives an Fe^{III}-OOH intermediate. Upon further protonation, heterolytic O-O bond cleavage affords the active oxidant, which is an oxoiron(IV) centred ligated by a porphyrin radical cation[7]. This species is able to oxidize substrates by two electrons (**Figure 1.4**), so gives an iron(III) state that must be reduced by 1 e^- to close the catalaytic cycle. Thus, the substrate provides only 2 of the 4 e^- required for reduction of O_2, and the other 2 originate from co-factors.

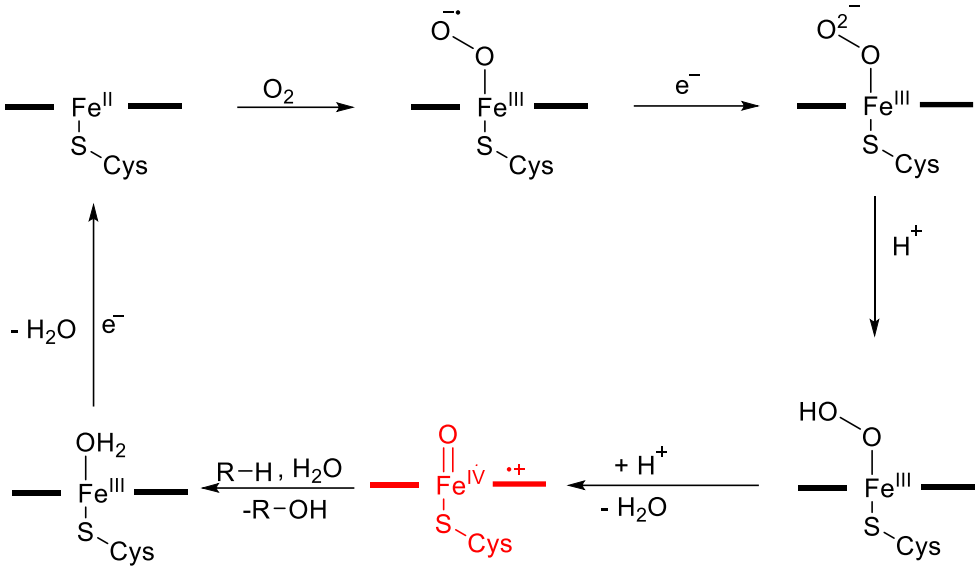

Figure 1.4: General reaction mechanism for Cytochrome P450

1.4 Non-heme Iron Enzymes

The rigidity of heme systems and the synthetic difficulties associated with modifing them limits their future development as synthetic catalysts. Thus, the emergence of non-heme iron oxygenases has garnered significant interest.[4]

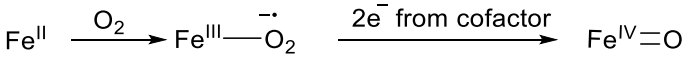

Figure 1.5: General mechanism for the formation of oxoiron(IV) intermediate

In most O_2 activating mononuclear non-heme iron enzymes, organic co-factors, such as the reductant NADH, α-ketoglutarate (α-KG), tetrahydrobiopterin or ascorbate, function as $2e^-$ sacrificial electron donors. They provide 2 of the 4 e^- required for O-O bond cleavage and formation of oxoiron(IV) intermediates (**Figure 1.5)**, which are responsible for substrate oxidation. These co-factor dependent oxygenases catalyze a broad range of oxidation reactivity, including many C-H bond oxidation processes. As such, they are commonly involved in the biosynthesis of antibiotics (**Figure 1.6**) and plant products, including Flavonol (**Figure 1.7**) ,and repair of alkylated DNA via demethylation(**Figure 1.8**).[10]

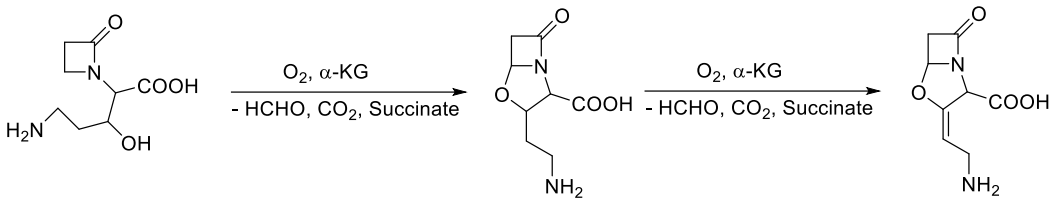

Figure 1.6: Biosynthesis of antibiotics, clavaminic acid catalyzed by α-KG dependent enzyme, clavaminate synthase.

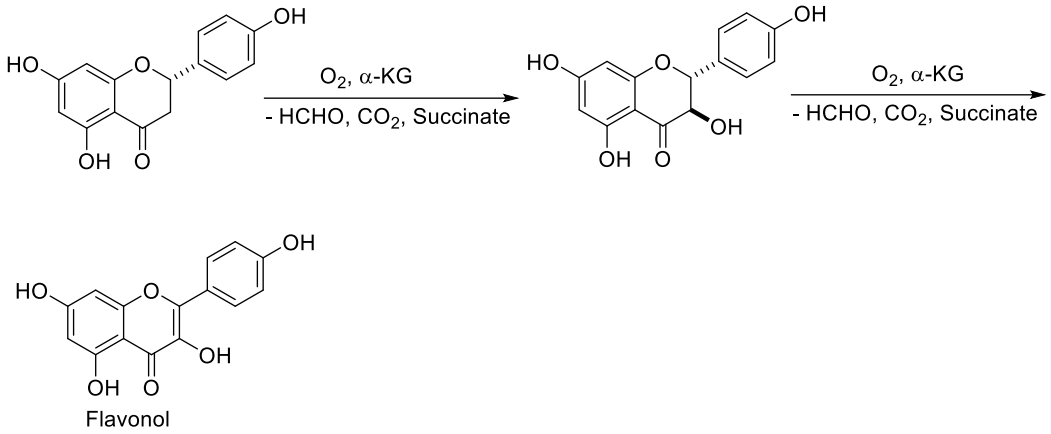

Figure 1.7: Biosynthesis of Flavonol catalyzed by α-KG dependent enzyme, flavanone 3β-hydroxylase.

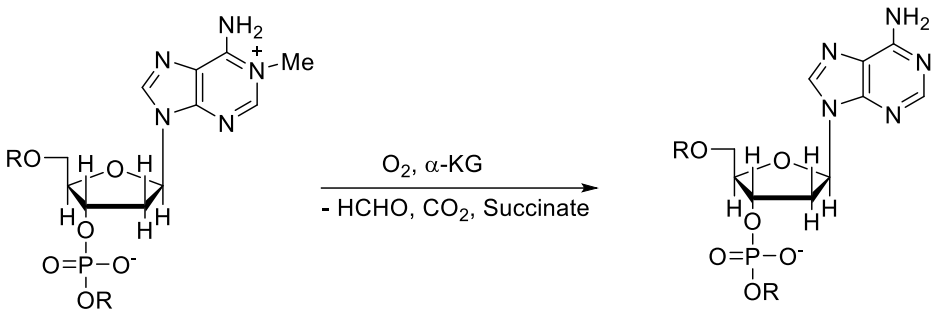

Figure 1.8: Reparing of alkylated DNA via demethylation catalyzed by α-KG dependent enzyme, AlkB protein.

1.4.1 Mechanistic Analysis of Non-heme Iron Enzymes

Nearly all members of this class of oxygenase exhibit similar general mechanisms, and are characterized by a coordination by a 2-histidine-1-carboxylate facial traid of amino acid residues. The remaining coordination sites are available for coordination of O_2, co-factor and (sometimes) substrate. The general mode of action displayed by oxygenases is exemplified by the catalytic cycle of the α-KG dependent enzyme taurine dioxygenase, TauD (**Figure 1.9**). [4,10–14] In this system, reaction with O_2 requires initial binding of α-KG co-factor and substrate to the reduced iron(II) state of the enzyme, and yields a superoxoiron(III) intermediate. This species reacts with the keto group of α-KG to yield a putative alkylperoxoiron(IV) intermediate. Heterolytic O-O bond cleavage is accompanied by release of CO_2 gas and affords a high-spin (S = 2) oxoiron(IV) intermediate and succinate ligand. It has been shown that the oxoiron(IV) species is the oxidant responsible for hydrogen atom abstraction from the substrate. Subsequent oxygen rebound between the substrate-centred radical and the hydroxoiron(III) species, thereby formed, yields the hydroxylated substrate product. Such oxoiron(IV) intermediates have been spectroscopically characterized in several enzymes (**Table 1.1**) and found to possess high-spin iron(IV) centres in all cases. Studies suggest that the high spin-state is the key for their high reactivity.

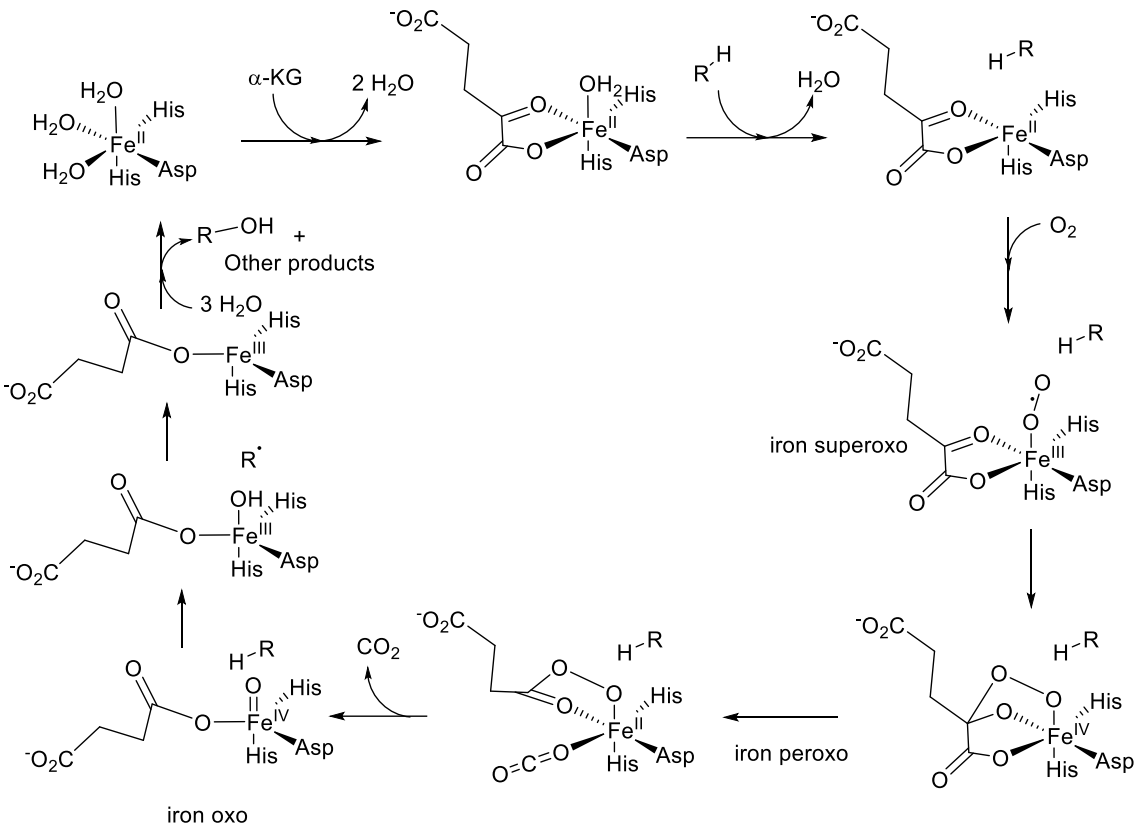

Figure 1.9: Enzymatic catalytic cycle for TauD.

1.4.2 Synthetic Intermediate-Spin (*S* = 1) Oxoiron(IV) Complexes

Inspired by the aforementioned enzymatic systems, numerous non-heme oxoiron(IV) complexes have now been synthesized and their reactivity towards substrates studied. The first example of successful generation of a synthetic non-heme *S* = 1 oxoiron(IV) complex was reported by Wieghardt and co-workers in 2000. The species in question, $[Fe^{IV}(O)(cyclam\text{-}CH_2CO_2)]$, was obtained by reaction of $[Fe^{III}(cyclam\text{-}CH_2CO_2)(OTf)](PF_6)$ with O_3 at -80°C (**Figure 1.10**) and, based upon frozen solution Mössbauer measurements, it was concluded that it possessed an *S* = 1 spin-state.[15] However, this complex proved to be highly unstable and no further evidence of the proposed formulation was obtained.

The most significant development in synthetic non-heme oxoiron(IV) chemistry was, arguably, successful isolation of $[Fe^{IV}(O)(TMC)(NCMe)]^{2+}$ from the reaction of $[Fe^{II}(TMC)(OTf)_2]$ with iodosylbenzene (PhIO) in acetonitrile solution by Que and co-workers in 2003.[16] It's high

stablilty ($t_{1/2}$ = 10 h) at room temperature and high reported yield allowed for the X-ray crystallographic analysis, conclusive spectroscopic studies and extensive substrate reactivity studies. Since then, a wide array of octahedral S = 1 oxoiron(IV) complexes with cyclic and acyclic ligands (**Figure 1.10**) have been reported, all of which have similar UV-vis spectroscopic features (**Table 1.1**).[11,17] More specifically, near-infrared-centred ligand field transitions of moderate intensity and intense oxo-to-metal charge transfers in the UV region. Most of these complexes possess a low-lying high-spin excited state and it is generally accepted that reactions proceed via spin-crossover from the S = 1 ground state to the S = 2 reaction surface. This is referred to as two-state reactivity, and calculations suggest that there is a lower energy barrier to the rate determining hydrogen atom abstraction reaction for the high-spin species. This phenomenon of higher reactivity for higher spin-states in hydrogen atom abstraction has been generalized and is referred to as Exchange Enhanced Reactivity.[18,19] Such studies rationalized the high reactivity of the enzymatic oxoiron(IV) intermediates and focus shifted to studying high-spin (S = 2) oxoiron(IV) complexes.

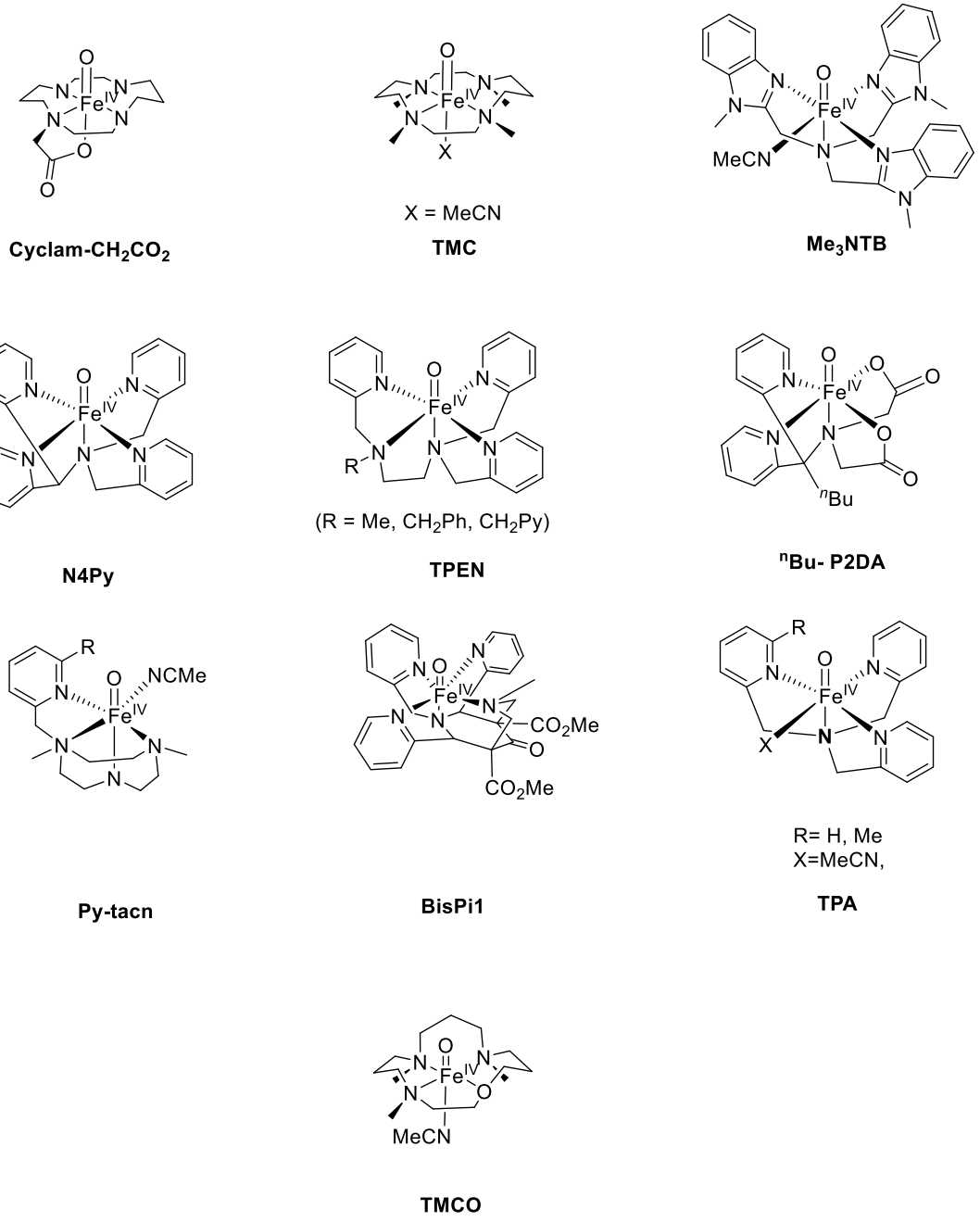

Figure 1.10: A selection of the *S* = 1 oxoiron(IV) complexes report thus far.

Table 1.1: Spectroscopic properties for selected octahedral intermediate-spin oxoiron(IV) complexes and TauD, which contains a high-spin Fe^{IV} ion.

Fe^{IV}(O)(L) where L =	λ_{max}/nm (ε/M^{-1} cm^{-1})	δ (mm s^{-1})	ΔE_Q (mm s^{-1})	Fe-O (Å)	$\upsilon_{Fe=O}$ (cm^{-1})	Ref.
TauD	318 nm (15000)	0.33	-0.88 mm/s	1.62	821	[20]
Cyclam-CH_2CO_2	676 (−)	0.01	1.37	-	-	[15]
TMC(MeCN)	824 (400)	0.17	1.24	1.646	839	[16]
Me_3NTB	770 (200)	0.02	1.53	-	-	[21]
N4Py	695 (400)	−0.04	0.93	1.639	824	[22]
TPEN-Bn	740 (400)	0.01	0.87	1.67	-	[23]
nBu-P2DA	770 (220)	0.04	1.13	1.66	-	[24]
Py-tacn	750 (200)	0.05	0.73	-	-	[25]
BisPi1	728 (400)	0.02	0.69	-	-	[26]
TPA-MeCN	724 (300)	0.01	0.92	1.67	-	[27]
6-Me-TPA-MeCN	770 (300)	-	-	-	-	[28]
TMCO	390 (>3000), 585 (200), 848 (130), 992 (125)	0.21	1.58	1.64	850	[17]

1.4.3 Synthetic High-Spin (*S* = 2) Oxoiron(IV) Complexes

One approach to obtaining high-spin oxoiron(IV) complexes is to employ weak field ligands in the equatorial plane of an octahedral oxoiron(IV) complex. This reduces the energy gap between the associated $d_{x^2-y^2}$ anti-bonding combination and the non-bonding d_{xy} orbital, thereby causing spin-pairing to be energetically more costly than promotion of an electron from the former orbital to the latter. The first example of this approach being used was in the report

of the high-spin octahedral oxoiron(IV) complex $[Fe^{IV}(O)(H_2O)_5]^{2+}$ (**Figure 1.11**), by Bakac and co-workers.[29] It was obtained by oxidation of an aqueous solution of $[Fe^{II}(H_2O)_6]^{2+}$ using ozone. However, spectroscopic and reactivity analyses were rather limited due to the short lifetime of 20 s at room temperature and poor yield.

In 2015, Que and co-workers reported generation of the oxoiron(IV) complex $[Fe^{IV}(O)(TQA)(NCMe)]^{2+}$ (**Figure 1.11**), which had a half-life of 15 min at room temperature. This relatively high stability allowed more extensive spectroscopic and reactivity characteristics to be probed, with a maximum absorbance of 400 nm, 650 nm (300 M^{-1} cm^{-1}) and 900 nm (75 M^{-1} cm^{-1}).[30,31] In addition, substitution of the MeCN ligand by chloride and bromide ions yielded further high-spin oxoiron(IV) complexes. It should be noted that these high-spin oxoiron(IV) complexes, with an isomer shift of more than 0.20 mm/s in Mössbauer spectroscopy, have spectroscopic features that differ significantly from their intermediate-spin counterparts, with an isomer shift of less than 0.22 mm/s and UV-Vis absorbance of near IR region (**Table 1.2**). Also, consistent with expectations, these high-spin complexes displayed some of the fastest rates of reaction with C-H bond susbtrates ever recorded.

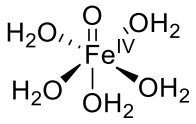

H_2O
Bakac 2005

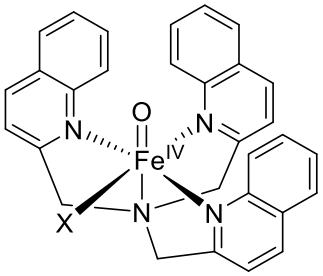

X = MeCN, Cl, Br

TQA
Que 2015

Figure 1.11: Synthetic octahedral high-spin (S = 2) oxoiron(IV) complexes.

Table 1.2: Spectroscopic properties for synthetic high-spin (S = 2) octahedral oxoiron(IV) complexes.[29–31]

entry	$Fe^{IV}(O)(L)$ where L =	λ_{max}/nm (ε/M^{-1} cm^{-1})	δ (mm/s)	(ΔE_Q/mm s^{-1})	Fe-O (Å)	$\upsilon_{Fe=O}$ (cm^{-1})	ref
1	$(H_2O)_5$	-	0.38 (2)	0.33 (3)	1.62	-	[29]
2	TQA (MeCN)	400 (sh), 650 (300), 900 (75)	0.24 (2)	-1.05 (2)	1.64	838 (−35)	[30]
3	TQA (Cl)	370 (br), 625, 875	0.22	0.96	1.64	827 (−35)	[31]
4	TQA (Br)	370 (br), 625, 875	0.21	0.96	1.64	828 (−35)	[31]

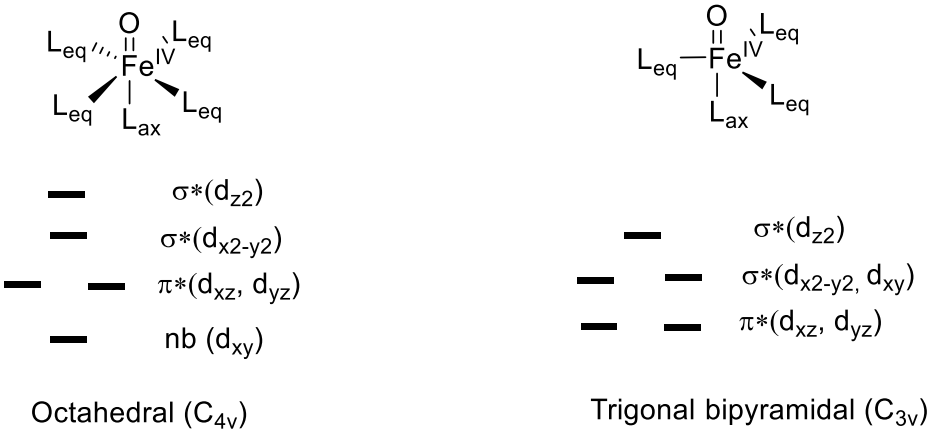

Figure 1.12: Qualitative ligand-field splitting diagrams for oxoiron(IV) complexes with tetragonal and trigonal bipyramidal geometries

Weak field donors tend to result in very reactive/unstable species, which makes isolation of high-spin oxoiron(IV) complexes of tetragonal symmetry highly challenging. An alternative, more successfully used approach is to synthesize oxoiron(IV) complexes possessing a trigonal bipyramidal geometry, which leads to degeneracy of the d_{xy} and $d_{x^2-y^2}$ orbitals (**Figure 1.12**).

This will, in turn, favour the $S = 2$ ground state.[11] To obtain such an outcome, the ligands must possess sufficient steric bulk to impose local C_{3v} symmetry at the metal centre, with the oxo donor located at the axial position.

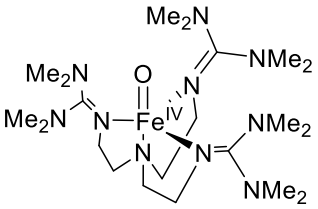

TMG_3tren
Que 2009

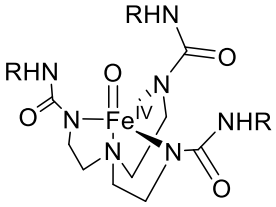

H_3buea
Borovik 2010

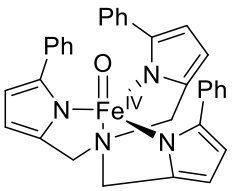

tpa^{Ph}
Chang 2010

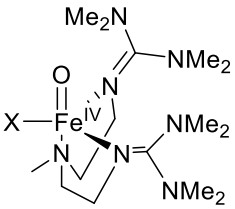

TMG_2dien
$X=NCCH_3, N_3, Cl$
Que 2010

Figure 1.13: Synthetic high-spin ($S = 2$) trigonal bipyramidal oxoiron(IV) complexes.

Que and co-workers reported the first high-yield synthesis and comprehensive characterization of a high-spin oxoiron(IV) complex in 2009,[32] earlier than which is earlier than the aforementioned octahedral species $[Fe^{IV}(O)(TQA)(NCMe)]^{2+}$. They employed the sterically encumbered ligand TMG_3tren and the resultant complex $[Fe^{IV}(O)(TMG_3tren)]^{2+}$ displayed a trigonal bipyramidal geometry. Subsequently, several examples of high-spin oxoiron(IV) complexes possessing a trigonal bipyramidal geometry were reported (**Figure 1.13** and **Table 1.3**).[11] They displayed spectroscopic features of similar to those of $[Fe^{IV}(O)(TQA)(NCMe)]^{2+}$ and TauD, with a two distinct UV-Vis features near 400 and 900 nm.

Table 1.3: Selected Spectroscopic properties for trigonal bipyramidal oxoiron(IV) complexes.

$Fe^{IV}(O)(L)$ where L =	λ_{max}/nm (ε/M^{-1} cm^{-1})	δ (mm/s)	(ΔE_Q/mm s^{-1})	Fe-O (Å)	$\upsilon_{Fe=O}$ (cm^{-1})	Ref.
TMG_3tren	400 (9800), 825 (260)	0.09	−0.29	1.661	843	[32]
H_3buea	440 (3100), 550 (1900), 808 (280)	0.02	0.43	1.680	799	[33]
tpa^{Ph}	400 (−), ∼900 (−)	0.09	0.51	1.62	850	[34]
TMG_2dien (MeCN)	380 (8200), 805 (270)	0.08	0.58	1.65	807	[35]
TMG_2dien (N_3)	412 (9700), 827 (290)	0.12	−0.30	-	833	[35]
TMG_2dien (Cl)	385 (7800), 803 (290)	0.08	0.41	1.65	810	[35]

1.4.4 The Influence of Spin-State Over Reactivity of Oxoiron(IV) Complexes

Theoretical calculations suggest that high-spin (S = 2) oxoiron(IV) complexes have higher reactivity in hydrogen atom abstraction than their intermediate spin (S = 1) analogues. Of all the published S = 2 complexes, only octahedral $[Fe^{IV}(O)(TQA)(NCMe)]^{2+}$ has exhibited higher reactivity than existing S = 1 complexes (**Entry 3** of **Table 1.4**). Moreover, several S = 1 oxoiron(IV) complexes (**Entry 6** to **8** of **Table 1.4**) have high reactivity towards substrates with inert C-H bonds, such as cyclohexane. Notable examples are $[Fe^{IV}(O)(Me_3NTB)(NCMe)]^{2+}$ and $[Fe^{IV}(O)(TMCO)(NCMe)]^{2+}$, with the former possessing reactivity comparable to the S = 2 system $[Fe^{IV}(O)(TQA)(NCMe)]^{2+}$. It has been postulated that the high reactivity of the former is due either to a very small energy gap between the ground S = 1 and excited S = 2 potential energy surfaces or a possible change of geometry to trigonal bipyramidal at the transition state. [21]

On the other hand, most of the trigonal bipyramidal oxoiron(IV) complexes, which are high-spin, have displayed reactivity that is, at best, comparable to their S = 1 counterparts (**Entry 1** and **2** of **Table 1.4**).[11] In fact, thus far, reactivity with substrates possessing only weak C-H bonds (e.g., CHD and DHA) has been reported. This comparatively low reactivity has been attributed to the bulky nature of the ligands used to obtain the trigonal bipyramidal geometry, which sterically inhibits the approach of substrate to the oxoiron(IV) centre.[32,33,35–37] Consistent with this notion, commensurate with the decrease in steric congestion around the metal centre accompanying moving from $[Fe^{IV}(O)(TMG_3tren)]^{2+}$ to $[Fe^{IV}(O)(TMG_2dien)(NCMe)]^{2+}$ (**Entry 1** and **2** of **Table 1.4)** a significant increase in the rate of reaction with the C-H bonds of substrates was seen. However, this reduction in steric bulk did not allow reactivion with substrates possesing strong C-H bonds, unlike some of it intermediate-spin counterparts.

This low reactivity of the trigonal bipyramidal S = 2 oxoiron(IV) complexes may, in part, derive from the donor properties of the ligands that support them. They are all very basic and in some cases are even trianionic. In contrast, the S = 1 complexes are predominantly ligated by neutral amine and pyridine donors. The high basicity of the ligands used to produce the trigonal bipyramidal geometries would be expected to suppress the reduction potential of the oxoiron(IV) centre, thereby limiting their oxidative capabilities. To investigate this possibility, there is a need to obtain trigonal bipyramidal oxoiron(IV) complexes employing the same types of donor atom types used to support their S = 1 congeners (i.e., pyridines and amines).

Table 1.4: Comparison of the second order rate constants, k_2 ,for reaction of selected oxoiron(IV) complexes with substrate.[16,17,21,30,32,35,38]

entry	$Fe^{IV}(O)(L)$, where L =	Geometry	Spin State	k_2/ M^{-1} s^{-1} (Temp / °C)				Ref.
				CHD	DHA	Cyclohexane	Toluene	
1	TMG_3tren	Trigonal Bipyramidal	2	1.2 (-30)	0.090 (-30)	NR	NR	[32]
2	TMG_2dien (MeCN)	Trigonal Bipyramidal	2	18 (-30)	57 (-30)	NR	NR	[35]
3	TQA	Octahedral	2	Not reported	Not reported	0.37 (-40)	0.64 (-40)	[30]
4	TPA	Octahedral	1	1.9 (-40)	Not reported	NR (-40)	Not reported	[30]
5	TMC(MeCN)	Octahedral	1	0.018 (-30)	0.016 (-30)	NR	NR	[16]
6	Me_3NTB	Octahedral	1	94 (-40)	310 (-40)	0.25 (-40)	0.47 (-40)	[21]
7	N4Py	Octahedral	1	1.3 (-30)	2.0 (-30)	0.000055 (25)	Not reported	[22]
8	TMCO	Octahdral	1	Not reported	Not reported	0.01 (-40)	0.013 (-60)	[17]

1.5 Non-heme Copper Enzymes

1.5.1 Biological Systems

Enzymatic dioxygen activation for substrate oxidation is not restricted to iron centres. Oxygenases containing copper active sites are plentiful, with a notable sub-section being responsible for hydroxylation of intermediate strength C-H bonds. Examples include dopamine β monooxygenase (DβM) and peptidylglycine α-hydroxylating monooxogyenase (PHM) (**Figure 1.14**)

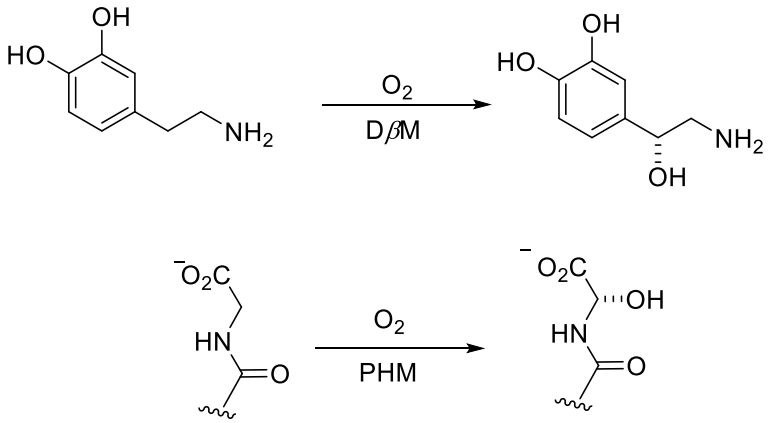

Figure 1.14: C-H bond oxidation reactions catalyzed by DβM (top) and PHM (bottom)

It is believed that these copper metalloenzymes react via analogous mechanisms, with the mononuclear superoxocopper(II) intermediate formed after the initial binding of O_2 being responsible for initial hydrogen atom abstraction (**Figure 1.15**).[4] In some cases, the resulting hydroperoxocopper(II) complex is believed to undergo heterolytic O-O scission to yield a water molecule and a oxylcopper(II) species, which acts as a secondary oxidant in the catalytic cycle. It is worth noting that theoretical calculations predict that oxylcopper(III) species are very potent oxidants that are much more reactive than mononuclear superoxocopper(II) intermediates.[39,40] Perhaps reflecting this high reactivity, oxylcopper(III) species have yet to be detected in either biological or synthetic systems.

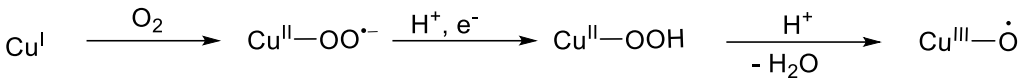

Figure 1.15: General mechanism for the dioxygen activation by non-heme copper hydroxylases[4]

Significant evidence has been reported supporting mononuclear superoxocopper(II) species as reactive intermediates responsible for hydrogen atom abstraction in enzymatic systems. X-ray crystallographic studies for PHM have shown that there are two non-interacting Cu(I) centres in its active site, which are separated by 11 Å.[13] Furthermore, a structure was obtained showing O_2 binding to one of these copper centres in an end-on fashion. Although there was clear evidence of photoreduction, this supports the intermediacy of a superoxocopper(II) species and is consistent with kinetic data gathered.[41]

Mechanistic studies for PHM and DβM suggest that their mechanisms are analogous and that the 2 copper centres each provide a single electron during catalysis, with the first being oxidation of Cu(I) to Cu(II) upon binding of dioxygen (**Figure 1.16**).[42] It is, broadly, agreed that this step yields an end-on superoxocopper(II) complex that is responsible for initial abstraction of a hydrogen atom from the substrate, which yields a hydroperoxcopper(II) complex and a carbon-centred radical. However, the timing of electron transfer step from the second non-interacting copper centre is debatable. On possibility is that it preceeded by rebound of carbon-based radical with the hydroperoxocopper(II) intermediate, which results in O-O bond cleavage and formation of the hydroxylated substrate and oxylcopper(II) intermediate. The alternative is that electron transfer promotes O-O bond cleavage to obtain oxylcopper(II) intermediate, which then reacts with the carbon-based radical to give the hydroxylated product. These observations have attracted significant interest and synthetic chemists have synthesized mononuclear end-on superoxocopper(II) complexes with various ligand systems in the hope of gaining further insight into such species, including their potential reactivity.

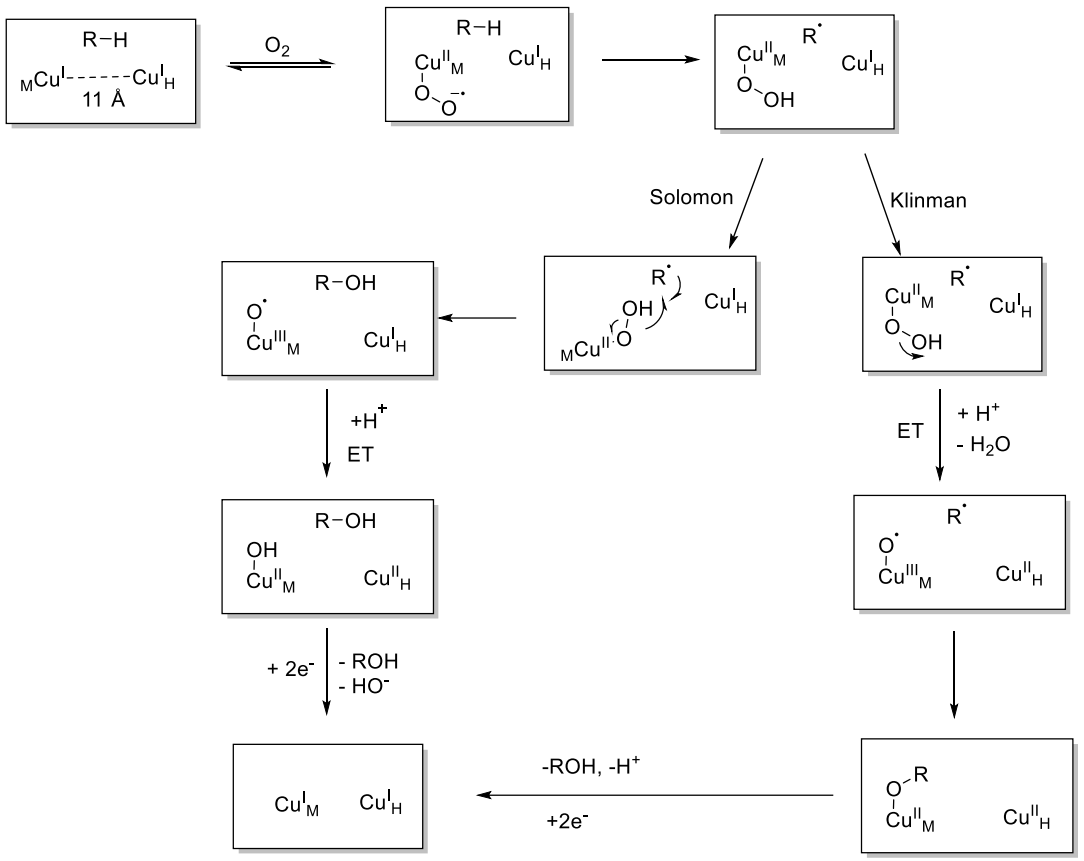

Figure 1.16: The two mechanistic pathways proposed for DβM and PHM by Klinder and Solomon, respectively.[41]

1.5.2 Synthetic Mononuclear End-on Superoxocopper(II) Complexes

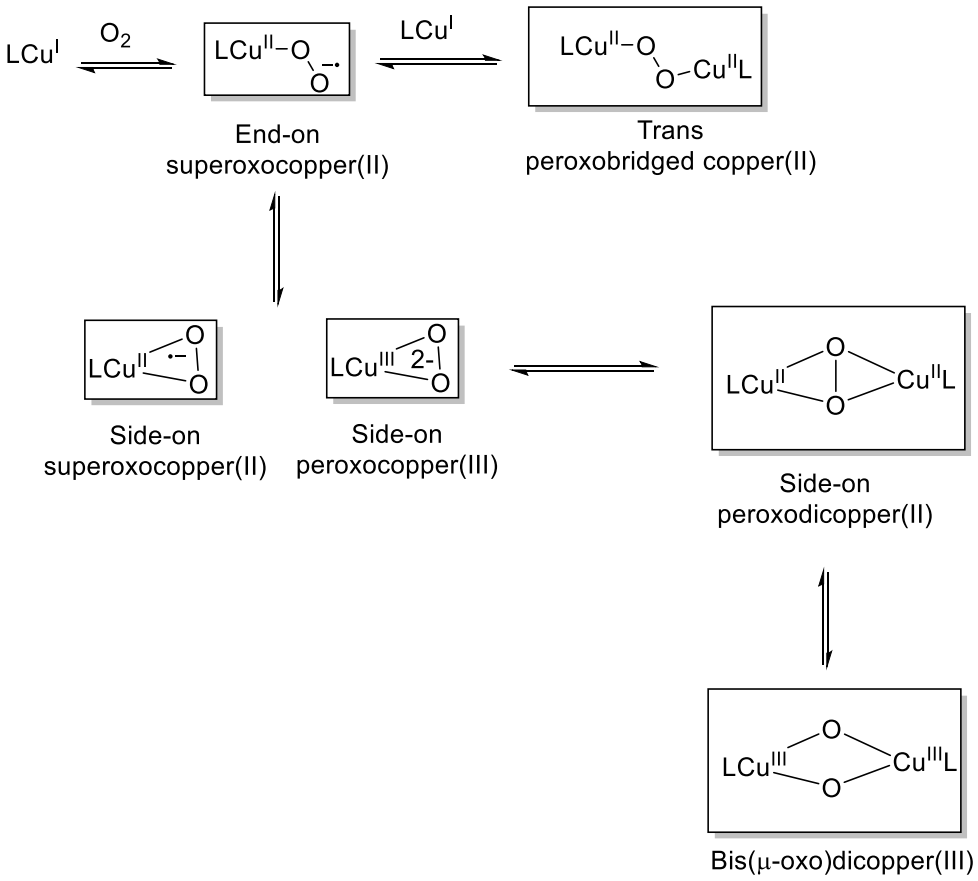

Figure 1.17: Some of the species observed upon binding O_2 to copper(I) complexes.

Synthetic end-on (η^1) superoxocopper(II) complexes are usually detected as short-lived intermediates. This is, primarily, because subsequent 'dimerization' to form peroxo-bridged dicopper(II) complexes is thermodynamically favoured (**Figure 1.17**). Alternatively, irreversible oxidation of ligand occurs or dioxygen binds in a more stable side-on (η^2) fashion. Prior to 2006, only two 'side-on' superoxocopper(II) complexes, [$Cu^{II}(\eta^2\text{-}O_2^{\bullet-})(^{iPr}Tp^{R}$)], and two 'side-on' peroxocopper(III) complexes, [$Cu(\eta^2\text{-}O_2^{2-}$)(DKR)] and [$Cu(\eta^2\text{-}O_2^{2-}$)(AI)], with sterically bulky ligands had been isolated and characterized crystallographically (**Figure 1.18**).[43–45]

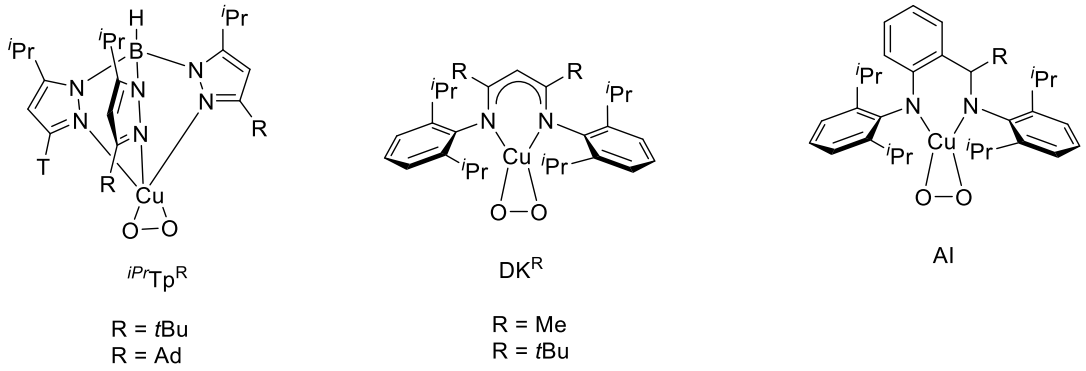

Figure 1.18: Side on (η^2) binding 1:1 Cu:O_2 complexes that have been characterized crystallographically.

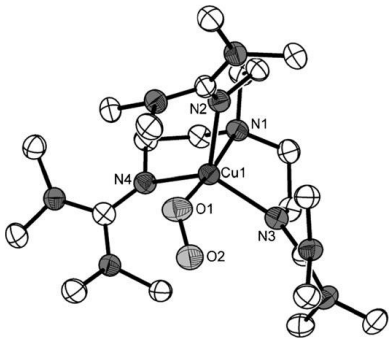

Figure 1.19: X-ray crystal structure of $[Cu^{II}(\eta^1\text{-}O_2^{\bullet-})(TMG_3tren)]^+$. [46]

However, in 2006, Schindler and co-workers reported that through the use of the sterically bulky TMG_3tren ligand, they could isolate and crystallographically characterize a η^1-superoxocopper(II) complex (**Figure 1.19**).[46] This allowed for extensive characterization of its reactivity and electronic properties.[47,48] Spectroscopic studies, supported by DFT calculations, revealed the presence of a S = 1 ground state, from which ferromagnetic coupling of the oxygen- and copper-centred spins can be inferred.

Since then, various research group have reported superoxocopper(II) intermediates stabilized (though not stable) through various ligand modifications The use of strictly control of reaction conditions, combined sterically demanding ligands (**Figure 1.20)**[46,47,49–51] and ligands with electron and intramolecular hydrogen bond donor functional groups (**Figure 1.21**), [52–56] have allowed a relatively broad range of 5-coordinate and some 4-coordinate [51,57] end-on

superoxocopper(II) complexes to be obtained. All examples display exhibit remarkably similar spectroscopic features (**Table 1.5**). Furthermore, it is worth noting that all were obtained by reaction of Cu^{I} precursors with O_2, except for the Tolman's system supported by N,N'-bis(2,6-diisopropylphenyl)-2,6-pyridinedicarboxamide, which was synthesized by reaction of $[Cu^{II}$(N,N'-bis(2,6-diisopropylphenyl)-2,6-pyridinedicarboxamide)(NCMe)$]^{2+}$ with potassium superoxide.

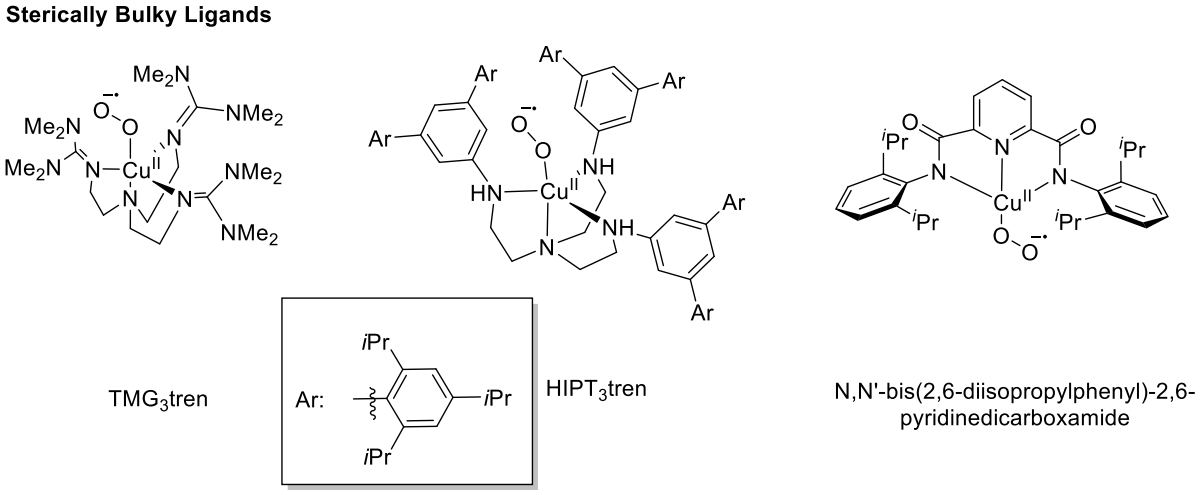

Figure 1.20: Previously reported end-on superoxocopper(II) complexes that incorporated sterically bulky ligand

Increased electron donating ability

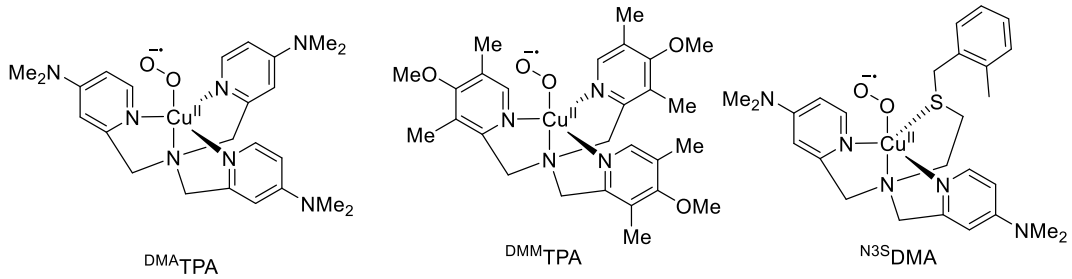

Hydrogen Bonding

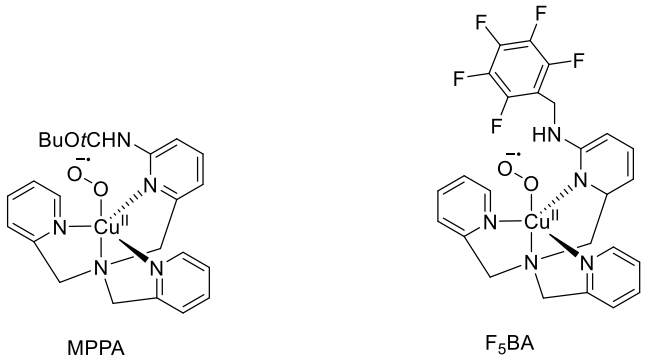

Change of reaction geometry

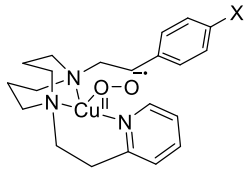

Figure 1.21: Previously reported end-on superoxocopper(II) complexes that does not have sterically bulky ligand.

Table 1.5: Spectroscopic properties of selected mononuclear end-on and side-on superoxocopper(II) complexes

$[Cu^{II}(O_2^{\bullet-})(L)]^+$ where L =	λmax/nm (ε/M^{-1} cm^{-1})	υ_{O-O} ($\Delta^{18}O$) /cm^{-1}	υ_{Cu-O} ($\Delta^{18}O$) /cm^{-1}	O_2^{n-} hapticitiy	ref
TMG_3tren	444 (3500) 680 780	1122 (28)	435 (20)	η_1	[46]
$HIPT_3$tren	434 (3850) 549 (1350) 675 (1910) 790 (3520)	1096 (67)	459 (17)	η_1	[50]
^{DMA}TPA	418 (4300) 615 (1100) 767 (840)	1121 (63)	472 (20)	η_1	[54]
^{DMM}TPA	409 (4250) 587 (1100) 743 (1030)	1121 (63)	474 (20)	η_1	[47]
MMPA	410 (3700) 585 (900) 741 (1150)	1130 (63)	482 (20)	η_1	[55]
F_5BA	414 (4000) 605 748	1126 (64)	465 (20)	η_1	[55]
^{N3S}DMA	418 605 743	1117 (61)	460 (20)	η_1	[53]
Cyclic	397 (4200) 570 (850) 705 (1150)	1033 (65)	457 (15)	η_1	[57]
N,N'-bis(2,6-diisopropylphenyl)-2,6-pyridinedicarboxamide	627 (1700)	1104 (60)	Not reported	η_1	[51]
$^{i\text{Pr}}$Tp$^{t\text{Bu}}$	510 (sh, 200) 660 (90)	1112 (50)	550 (18) 554(20)	η_2	[45]
$^{i\text{Pr}}$Tp^{Ad}	452 (300) 700 (sh, 40) 975 (20) 2380 (220)	1058 (50)	542 (24)	η_2	[45]

1.5.3 Reactivity of Mononuclear End-on Superoxocopper(II) Complexes

Given that end-on superoxocopper(II) complexes are evidenced to be the active oxidants in several biological systems responsible for synthetically interesting organic transformations, the reactivity of the synthetic complexes are of significant interest. Thus far, few synthetic

complexes have been shown to be able to oxidize C-H bonds. One example is $[Cu^{II}(\eta^1\text{-}O_2^{\bullet-})(MMPA)]^+$, which was shown to be able to abstract a hydrogen atom from substrates with weak C-H bonds, BNAH or BzImH (**Figure 1.22)**.[52] Unfortunately, no reaction was observed with substrates containing moderately strong C-H bonds, such as DHA. Oxidation of C-H bonds was also reported for superoxocopper(II) complexes supported by ^{N3S}DMA and a cyclic tridentate system. The former was able to oxidize C-H bonds of *N*-methyl-9,10-dihydroacridine to 10-methyl-9-acridone,[53] while the latter displayed intramolecular ligand hydroxylation of the benzylic position of a phenylethyl substituent (**Figure 1.23**).[57]

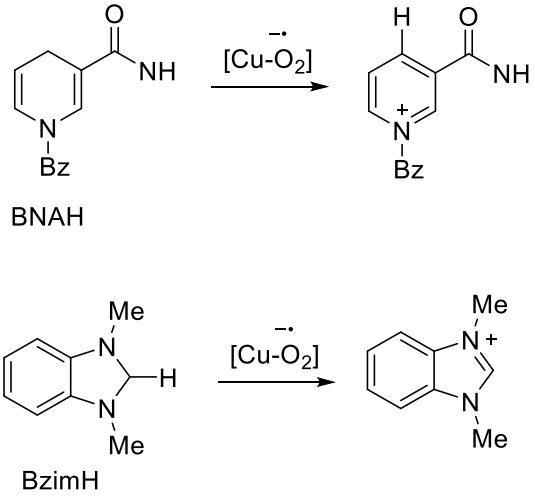

Figure 1.22: C-H bond oxidation of BNAH (top) and BzImH (bottom) using $[Cu^{II}(\eta^1\text{-}O_2^{\bullet-})(MMPA)]^+$

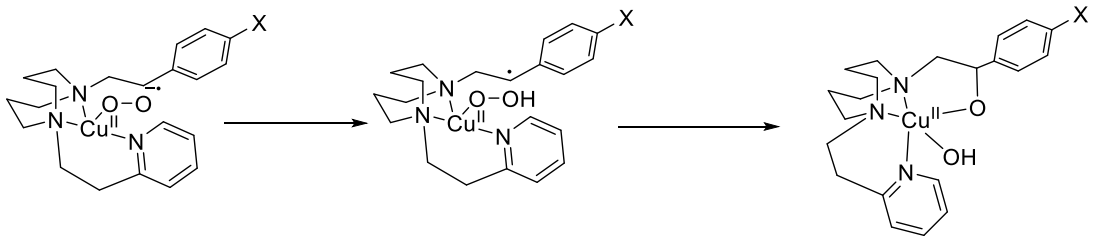

Figure 1.23: Intramolecular ligand oxidation in $[Cu^{II}(\eta^1\text{-}O_2^{\bullet-})(cyclic)]^+$

More commonly, η^1-superoxocopper(II) complexes are able to abstract hydrogen atoms from compounds with comparatively weak O-H bonds, such as *para*-substituted-2,6-ditertbutylphenols and TEMPO-H.[43,44] Karlin and co-workers demonstrated that

intramolecular hydrogen bonding can enhance reactivity and showed that the complex $[Cu^{II}(\eta^1\text{-}O_2^{\bullet-})(F_5BA)]^+$ could react with *para*-methoxyphenol, which contains an O-H bond that has a bond dissociation energy of 87.6 kcal mol^{-1}.[55] This is strongest O-H bond oxidized thus far. A summary of reactivity of some prominent superoxocopper(II) complexes with phenols is given in **Table 1.6**.

The somewhat disappointing reactivity of superoxocopper(II) complexes reported, thus far, can (in part) be attributed to the low temperature at which they were studied. This stems from the fact that most are stable only at low temperatures of < -80°C. On the other hand, superoxocopper(II) complexes that are stabilized against dimerization by bulky ligands, such as $[Cu^{II}(\eta^1\text{-}O_2^{\bullet-})TMG_3tren)]^+$ and $[Cu^{II}(\eta^1\text{-}O_2^{\bullet-})(HIPT_3tren)]^+$, exhibit low electrophilic reactivity, even with phenols.[47,50] The reason for this has not been addressed and although steric bulk is a likely factor, the donor properties of the ligands may also contribute. To clarify this situation, incorporation of steric bulk into commonly used donors (i.e., pyridine) would be beneficial. Constructing such ligand systems would allow for the possibility of stabilizing superoxocopper(II) complexes, whilst retaining the higher reactivity of the parent complexes.

Table 1.6: Reported second order rate constants (k_2) for reaction of superoxocopper(II) complexes with phenolic substrate.

$[Cu^{II}(\eta^1\text{-}O_2^{\bullet-})(L)]^+$ where L =	k_2 (Temp)		ref
	p-OMe-2,6,-ditertbutylphenol	*p*-OMe-phenol	
TMG_3tren	Not reported. Reaction left for 48 h	No reaction	[56]
$HIPT_3$tren	No reaction	No reaction	[50]
^{DMM}TPA	23 (-92)	No reaction	[54]
MMPA	0.988 (-135)	0.0233 (-135)	[55]
F5BA	1.147 (- 135)	Unable to identify kinetic pattern with reaction	[55]
^{N3S}DMA	Fast reaction with half life of 3 min	No reaction	[53]

1.6 Conclusions and Aims of the Thesis

Despite several high-spin oxoiron(IV) complexes having been reported, most of them, specifically those possessing a trigonal bipyramidal geometry, have lower reactivity towards C-H bonds than mnay of their intermediate-spin counterparts. It is assumed that the steric bulk of the ligand used to enforce C_3 symmetry is the main reason behind their low reactivity, which seems to defy predictions from biological precedents and theoretical studies. However, since intermediate-spin oxoiron(IV) complexes have been shown to possess comparable or higher reactivity, the possibility that the donor properties of the ligands might be a major contributing factor should be considered. To resolve this question, we targeted trigonal bipyramidal oxoiron(IV) complexes supported by ligands containing the donor groups that predominate in $S = 1$ oxoiron(IV) complexes.

Similarly, studies of superoxcopper(II) complexes reveal a trade-off of reduced reactivity towards substrates for increased stability. Low temperatures are, overwhelmingly, required for stabilization of superoxocopper(II) complexes. This kinetically limits reaction to easily oxidized substrates and, thus, the scope of substrates that have been studied is limited. Bulky ligands have been used to stabilize superoxocopper(II) complexes against dimerization. Unfortunately, the resulting systems are, often, still prone to self-decay and, more crucially, display greatly reduced reactivity towards substrates. The latter can attributed to steric inhibition of reaction, but the donor properties of the ligand may well be a contributing factor. Ideally, therefore, we would want to stabilize the superoxocopper(II) moiety using donors similar to those that predominate in the field, such that reactivity studies can be performed at higher temperatures but without loss of reactivity. This can, in principle, be done by strategic incorporation of steric bulk into known ligand systems. However, it must be done without weakening ligand field, which would increase the Cu^{II}/Cu^{I} redox potential and prevent successful O_2 binding.

The aims for both the oxoiron(IV) and superoxocopper(II) complexes can be accommodated by a common set of ligand properties, through the incorporation of steric bulk onto ligands containing pyridine and tertiary amines. To this end, we synthesized the ^{Ar3}TPA ligands (**Figure 1.24**), which are based around the well-studied tris(2-pyridylmethyl)amine (TPA) ligand framework, and explored their coordination chemistry (Chapter 2). In addition, we translated our strategy to the tridentate analogues ^{Ar2}RBPA (**Figure 1.24**), which are based around the bis(2-pyridylmethyl)amine moiety, and examined their chemistry with late first-row transition metal (Chapter 3). The hope was that the selected method of introducing steric bulk into these ligand frameworks would not significantly weaken their ligand field, so that their copper(I) complexes would still react with O_2, and that the resulting superoxocopper(II) species would be stable against dimerization, whilst also retaining reactivity with substrates (Chapter 4). In addition, we sought to use the same set of ligands to reinforce trigonal bipyramidal geometries in iron complexes, such that high-spin oxoiron(IV) species could be obtained (Chapter 5). An important criteria once again is that the steric bulk should not significantly perturb the ligand field, so that there is minimal impact upon the reduction potential of the oxoiron(IV) moiety. Clearly, achieving all of these goals requires a fine balance between conflicting steric effects. We felt that incorporating bulk aryl substituents onto the 5-position of the pyridine donors would achieve these ends by promoting steric clashes between the donors groups, while its relative remoteness from the metal centre would minimize its unwanted impacts.

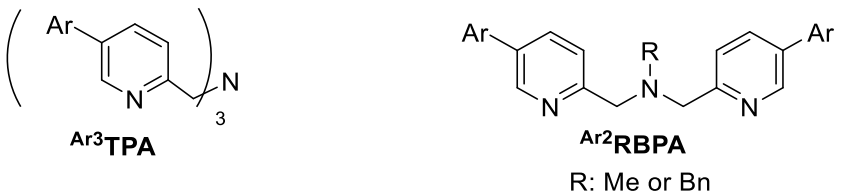

Figure 1.24: Structure of ^{Ar3}TPA and ^{Ar2}RBPA used in this thesis.

1.7 References

(1) Höft, E. In *Organic Peroxygen Chemistry*; Herrmann, W. A., Ed.; Springer Berlin Heidelberg: Berlin, Heidelberg, 1993; pp 63–77.

(2) Kolb, H. C.; VanNieuwenhze, M. S.; Sharpless, K. B. *Chem. Rev.* **1994**, *94*, 2483–2547.

(3) Borden, W. T.; Hoffmann, R.; Stuyver, T.; Chen, B. *J. Am. Chem. Soc.* **2017**, *139*, 9010–9018.

(4) Que Jr, L.; Tolman, W. B. *Nature* **2008**, *455*, 333.

(5) Guengerich, F. P. *J. Biochem. Mol. Toxicol.* **2007**, *21*, 163–168.

(6) Guengerich, F. P. *ACS Catal.* **2018**, *8*, 10964–10976.

(7) Denisov, I. G.; Makris, T. M.; Sligar, S. G.; Schlichting, I. *Chem. Rev.* **2005**, *105*, 2253–2278.

(8) Yoshioka, S.; Takahashi, S.; Hori, H.; Ishimori, K.; Morishima, I. *Eur. J. Biochem.* **2001**, *268*, 252–259.

(9) Yosca, T. H.; Rittle, J.; Krest, C. M.; Onderko, E. L.; Silakov, A.; Calixto, J. C.; Behan, R. K.; Green, M. T. *Science (80-.).* **2013**, *342*, 825–829.

(10) Hausinger, R. P. *Crit. Rev. Biochem. Mol. Biol.* **2004**, *39*, 21–68.

(11) McDonald, A. R.; Que, L. *Coord. Chem. Rev.* **2013**, *257*, 414–428.

(12) Price, J. C.; Barr, E. W.; Hoffart, L. M.; Krebs, C.; Bollinger, J. M. *Biochemistry* **2005**, *44*, 8138–8147.

(13) Bollinger, J. M.; Krebs, C. *Curr. Opin. Chem. Biol.* **2007**, *11*, 151–158.

(14) Krebs, C.; Galonić Fujimori, D.; Walsh, C. T.; Bollinger, J. M. *Acc. Chem. Res.* **2007**,

40, 484–492.

(15) Grapperhaus, C. A.; Mienert, B.; Bill, E.; Weyhermüller, T.; Wieghardt, K. *Inorg. Chem.* **2000**, *39*, 5306–5317.

(16) Rohde, J.-U.; In, J.-H.; Lim, M. H.; Brennessel, W. W.; Bukowski, M. R.; Stubna, A.; Münck, E.; Nam, W.; Que, L. *Science (80-.).* **2003**, *299*, 1037–1039.

(17) Monte Pérez, I.; Engelmann, X.; Lee, Y.-M.; Yoo, M.; Kumaran, E.; Farquhar, E. R.; Bill, E.; England, J.; Nam, W.; Swart, M.; et al. *Angew. Chemie Int. Ed.* **2017**, *56*, 14384–14388.

(18) Shaik, S. *Nat. Chem.* **2010**, *2*, 347.

(19) Klinker, E. J.; Shaik, S.; Hirao, H.; Que Jr., L. *Angew. Chemie Int. Ed.* **2009**, *48*, 1291–1295.

(20) Price, J. C.; Barr, E. W.; Tirupati, B.; Bollinger, J. M.; Krebs, C. *Biochemistry* **2003**, *42*, 7497–7508.

(21) Seo, M. S.; Kim, N. H.; Cho, K.-B.; So, J. E.; Park, S. K.; Clémancey, M.; Garcia-Serres, R.; Latour, J.-M.; Shaik, S.; Nam, W. *Chem. Sci.* **2011**, *2*, 1039–1045.

(22) Kaizer, J.; Klinker, E. J.; Oh, N. Y.; Rohde, J.-U.; Song, W. J.; Stubna, A.; Kim, J.; Münck, E.; Nam, W.; Que, L. *J. Am. Chem. Soc.* **2004**, *126*, 472–473.

(23) Martinho, M.; Banse, F.; Bartoli, J.-F.; Mattioli, T. A.; Battioni, P.; Horner, O.; Bourcier, S.; Girerd, J.-J. *Inorg. Chem.* **2005**, *44*, 9592–9596.

(24) McDonald, A. R.; Guo, Y.; Vu, V. V; Bominaar, E. L.; Münck, E.; Que, L. *Chem. Sci.* **2012**, *3*, 1680–1693.

(25) Company, A.; Prat, I.; Frisch, J. R.; Mas-Ballesté, D. R.; Güell, M.; Juhász, G.; Ribas,

X.; Münck, D. E.; Luis, J. M.; Que Jr., L.; et al. *Chem. – A Eur. J.* **2011**, *17*, 1622–1634.

(26) Bautz, J.; Bukowski, M. R.; Kerscher, M.; Stubna, A.; Comba, P.; Lienke, A.; Münck, E.; Que Jr., L. *Angew. Chemie Int. Ed.* **2006**, *45*, 5681–5684.

(27) Lim, M. H.; Rohde, J.-U.; Stubna, A.; Bukowski, M. R.; Costas, M.; Ho, R. Y. N.; Münck, E.; Nam, W.; Que, L. *Proc. Natl. Acad. Sci.* **2003**, *100*, 3665–3670.

(28) Paine, T. K.; Costas, M.; Kaizer, J.; Que, L. *JBIC J. Biol. Inorg. Chem.* **2006**, *11*, 1098–1099.

(29) Pestovsky, O.; Stoian, S.; Bominaar, E. L.; Shan, X.; Münck, E.; Que, L.; Bakac, A. *Angew. Chemie Int. Ed.* **2005**, *44*, 6871–6874.

(30) Biswas, A. N.; Puri, M.; Meier, K. K.; Oloo, W. N.; Rohde, G. T.; Bominaar, E. L.; Münck, E.; Que, L. *J. Am. Chem. Soc.* **2015**, *137*, 2428–2431.

(31) Puri, M.; Biswas, A. N.; Fan, R.; Guo, Y.; Que, L. *J. Am. Chem. Soc.* **2016**, *138*, 2484–2487.

(32) England, J.; Martinho, M.; Farquhar, E. R.; Frisch, J. R.; Bominaar, E. L.; Münck, E.; Que, L. *Angew. Chemie - Int. Ed.* **2009**, *48*, 3622–3626.

(33) Lacy, D. C.; Gupta, R.; Stone, K. L.; Greaves, J.; Ziller, J. W.; Hendrich, M. P.; Borovik, A. S. *J. Am. Chem. Soc.* **2010**, *132*, 12188–12190.

(34) Harman, W. H.; Chang, C. J. *J. Am. Chem. Soc.* **2007**, *129*, 15128–15129.

(35) England, J.; Guo, Y.; Van Heuvelen, K. M.; Cranswick, M. A.; Rohde, G. T.; Bominaar, E. L.; Münck, E.; Que, L. *J. Am. Chem. Soc.* **2011**, *133*, 11880–11883.

(36) Bigi, J. P.; Harman, W. H.; Lassalle-Kaiser, B.; Robles, D. M.; Stich, T. A.; Yano, J.;

Britt, R. D.; Chang, C. J. *J. Am. Chem. Soc.* **2012**, *134*, 1536–1542.

(37) Wong, S. D.; Bell III, C. B.; Liu, L. V; Kwak, Y.; England, J.; Alp, E. E.; Zhao, J.; Que Jr., L.; Solomon, E. I. *Angew. Chemie Int. Ed.* **2011**, *50*, 3215–3218.

(38) Rohde, J.-U.; Stubna, A.; Bominaar, E. L.; Münck, E.; Nam, W.; Que, L. *Inorg. Chem.* **2006**, *45*, 6435–6445.

(39) Crespo, A.; Martí, M. A.; Roitberg, A. E.; Amzel, L. M.; Estrin, D. A. *J. Am. Chem. Soc.* **2006**, *128*, 12817–12828.

(40) Yoshizawa, K.; Kihara, N.; Kamachi, T.; Shiota, Y. *Inorg. Chem.* **2006**, *45*, 3034–3041.

(41) Klinman, J. P. *J. Biol. Chem.* **2006**, *281*, 3013–3016.

(42) Prigge, S. T.; Eipper, B. A.; Mains, R. E.; Amzel, L. M. *Science (80-.).* **2004**, *304*, 864–867.

(43) Cramer, C. J.; Tolman, W. B. *Acc. Chem. Res.* **2007**, *40*, 601–608.

(44) Elwell, C. E.; Gagnon, N. L.; Neisen, B. D.; Dhar, D.; Spaeth, A. D.; Yee, G. M.; Tolman, W. B. *Chem. Rev.* **2017**, *117*, 2059–2107.

(45) Mirica, L. M.; Ottenwaelder, X.; Stack, T. D. P. *Chem. Rev.* **2004**, *104*, 1013–1046.

(46) Würtele, C.; Gaoutchenova, E.; Harms, K.; Holthausen, M. C.; Sundermeyer, J.; Schindler, S. *Angew. Chemie Int. Ed.* **2006**, *45*, 3867–3869.

(47) Maiti, D.; Lee, D.-H.; Gaoutchenova, K.; Würtele, C.; Holthausen, M. C.; Narducci Sarjeant, A. A.; Sundermeyer, J.; Schindler, S.; Karlin, K. D. *Angew. Chemie Int. Ed.* **2007**, *47*, 82–85.

(48) Maiti, D.; Lee, D.-H.; Narducci Sarjeant, A. A.; Pau, M. Y. M.; Solomon, E. I.;

Gaoutchenova, K.; Sundermeyer, J.; Karlin, K. D. *J. Am. Chem. Soc.* **2008**, *130*, 6700–6701.

(49) Ginsbach, J. W.; Peterson, R. L.; Cowley, R. E.; Karlin, K. D.; Solomon, E. I. *Inorg. Chem.* **2013**, *52*, 12872–12874.

(50) Kobayashi, Y.; Ohkubo, K.; Nomura, T.; Kubo, M.; Fujieda, N.; Sugimoto, H.; Fukuzumi, S.; Goto, K.; Ogura, T.; Itoh, S. *Eur. J. Inorg. Chem.* **2012**, No. 29, 4574–4578.

(51) Donoghue, P. J.; Gupta, A. K.; Boyce, D. W.; Cramer, C. J.; Tolman, W. B. *J. Am. Chem. Soc.* **2010**, *132*, 15869–15871.

(52) Peterson, R. L.; Himes, R. A.; Kotani, H.; Suenobu, T.; Tian, L.; Siegler, M. A.; Solomon, E. I.; Fukuzumi, S.; Karlin, K. D. *J. Am. Chem. Soc.* **2011**, *133*, 1702–1705.

(53) Kim, S.; Lee, J. Y.; Cowley, R. E.; Ginsbach, J. W.; Siegler, M. A.; Solomon, E. I.; Karlin, K. D. *J. Am. Chem. Soc.* **2015**, *137*, 2796–2799.

(54) Lee, J. Y.; Peterson, R. L.; Ohkubo, K.; Garcia-Bosch, I.; Himes, R. A.; Woertink, J.; Moore, C. D.; Solomon, E. I.; Fukuzumi, S.; Karlin, K. D. *J. Am. Chem. Soc.* **2014**, *136*, 9925–9937.

(55) Bhadra, M.; Lee, J. Y. C.; Cowley, R. E.; Kim, S.; Siegler, M. A.; Solomon, E. I.; Karlin, K. D. *J. Am. Chem. Soc.* **2018**, *140*, 9042–9045.

(56) Maiti, D.; Fry, H. C.; Woertink, J. S.; Vance, M. A.; Solomon, E. I.; Karlin, K. D. *J. Am. Chem. Soc.* **2007**, *129*, 264–265.

(57) Kunishita, A.; Kubo, M.; Sugimoto, H.; Ogura, T.; Sato, K.; Takui, T.; Itoh, S. *J. Am. Chem. Soc.* **2009**, *131*, 2788–2789.

Chapter 2

Metal Complexes of TPA Ligands

2.1 Introduction

Tris(2-pyridylmethyl)amine(TPA), first described in 1967[1], is a well-known tripodal tetradentate ligand that has been widely used in coordination chemistry (**Figure 2.1**). This can in large part be attributed to its moderately strong donor ability, resistance to oxidation, and comparative ease of derivatization.[2] Most pertinently, it (and derivatives thereof) have been used to support 6-coordinate oxoiron(IV) complexes and superoxocopper(II) chemistry. The former are, primarily, generated by reaction of complexes of general formula $[Fe^{II}(L)(NCMe)_2]^{2+}$ with oxo-transfer agents; and the latter are derived from reaction of copper(I) complexes with O_2 gas.

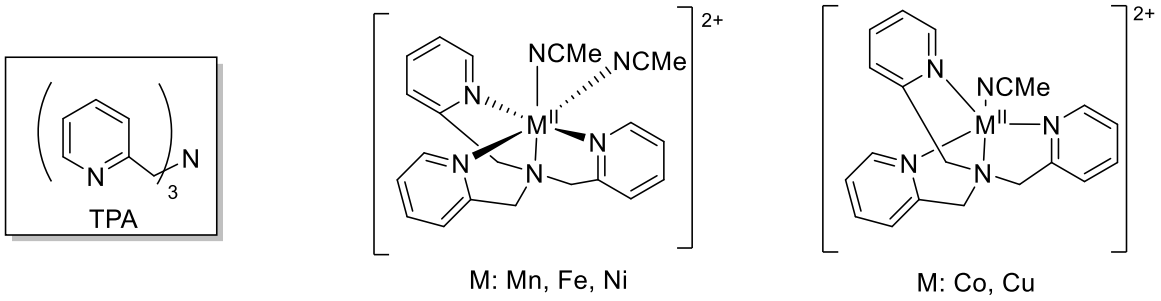

Figure 2.1: Structure of TPA ligand and the most commonly observed geometries of its first-row late transition metal(II) complexes.

In most cases, first-row late transition metal complexes bearing TPA-type ligands adopt octahedral or, where Jahn-Teller distortions are likely (Co and Cu), trigonal bipyramidal geometries (**Figure 2.1**).[3] The predominance of 6-coordinate geometries for TPA reflects the limited steric bulk associated with its pyridine donor, which in turn has an impact upon its chemical and electronic properties. For instance, complexes of the type $[Fe^{II}(TPA)X_2]$ have particular prominence in the field of spin-crossover compounds. An example would be $[Fe^{II}(TPA)(NCMe)_2]^{2+}$, which in MeCN solution is high-spin (S = 2) at elevated temperatures and can be converted to a low-spin (S = 0) complex as sub-ambient temperatures. In contrast, weak field co-ligands, such as TfO^- (**Figure 2.2**), yield high-spin complexes.

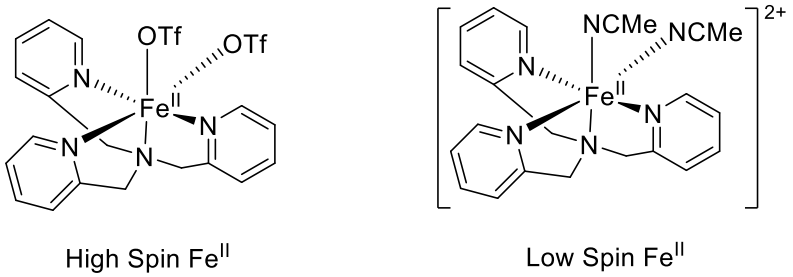

Figure 2.2: Structure of high-spin [Fe(TPA)(OTf)$_2$] and low-spin [Fe(TPA)(NCMe)$_2$](OTf)$_2$.

In addition to use of weak-field co-ligands, introduction of substituents onto the sixth position of the pyridyl ring can induce a high-spin state. For example, introduction of methyl substituents into the α-position of the pyridyl rings of TPA affords the high-spin complex [Fe(^{Me3}TPA)(NCMe)$_2$]$^{2+}$ (**Figure 2.3**).[4] In fact, introduction of only a single methyl substituent, to give [Fe(^{Me}TPA)(NCMe)$_2$]$^{2+}$, is sufficient to cause formation of a high-spin iron(II) centre. The change in the spin-state associated with introduction of α-pyridine substituents is attributed to weakening of the ligand field due to steric repulsion between the substituent and the metal centre. Moving to higher oxidation states mitigates the reduced ligand field resulting from α-substitution of the pyridine rings and weak-field co-ligands, such that low-spin states dominate. This is evident in oxoiron(IV) chemistry, where the overwhelming majority of examples supported by TPA-derived ligands have, thus far, been found to be intermediate-spin (S = 1).

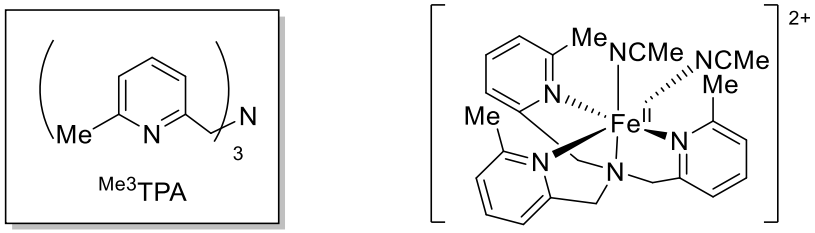

Figure 2.3: Structure of ^{Me3}TPA ligand and the complex [Fe(^{Me3}TPA)(MeCN)$_2$]$^{2+}$.

A complication arising from incorporation of substituents onto the 6-position of pyridine rings is that their close proximity to the metal centre renders them oxidatively susceptible. This is clearly demonstrated by reaction of [Fe(^{Ph}TPA)(NCMe)$_2$]$^{2+}$ with ^{t}BuOOH, which proceeds with hydroxylation of the phenyl substituent to yield a phenolate ligand (**Figure 2.4**). This is

believed to proceed via the hydrogen atom abstraction of the phenyl group by of intermediate-spin oxoiron(IV) intermediate.[5]

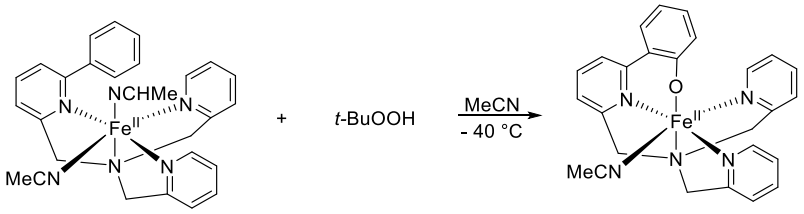

Figure 2.4: Reaction of $[Fe(^{Ph}TPA)(NCMe)_2]^{2+}$ with $^{t}BuOOH$ that yield phenolate ligand.

Similarly, Kitagawa and co-workers reported that reaction of $[Cu^{I}(^{Me3}TPA)(NCMe)]^{+}$, with O_2, in acetone solution at -80°C, resulted in oxidation of a methyl substituent to a carboxylate donor (**Figure 2.5**).[6]

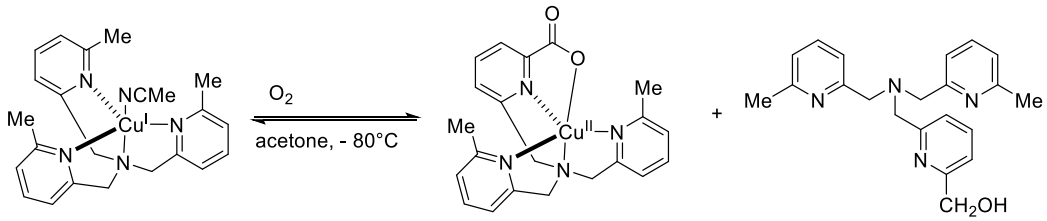

Figure 2.5: Reaction of $[Cu^{I}(^{Me3}TPA)(NCMe)]^{+}$ with dioxygen that which yield the oxidation of methyl substituent to a carboxylate donor.

Interestingly, the inclusion of bulky phenyl substituents onto the 6-position of more than one pyridyl arms of TPA is able to induce a reduction of coordination number of its complexes. However, this can be associated with non-consistent binding to the metal center, as the ligand failed to coordinate as tetradentate ligand due to partial coordination of pyridine donors. More specifically, whereas the complex $[Co^{II}(^{Ph2}TPA)(NCMe)]^{2+}$ displays a trigonal bipyramidal geometry in which all pyridine donors are coordinated, but, one of the pyridyl arm remained uncoordinated for the iron analog of the same ligand (**Figure 2.6**). This non-consistent binding of the ligands is likely due to the presence of excessive steric repulsion between ligand and metal and the associated weakening of donor strength of the ligand.

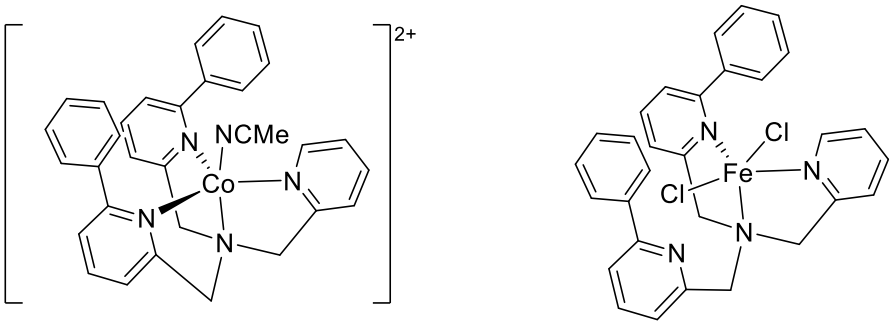

Figure 2.6: Structure of $[Co(^{Ph2}TPA)(NCMe)]^{2+}$ and $[Fe(^{Ph2}TPA)Cl_2]$.

The weakening of the donor strength associated with incorporation of 6-substituents into the pyridine rings also manifests in increased reduction potentials of its complexes. The reduction potential of $[Cu^{II}(^{Me3}TPA)(NCMe)]^{2+}$ and $[Cu^{II}(^{Ph3}TPA)(NCMe)]^{2+}$ was found to be +0.07 V and – 0.10 V vs Fc as compared to $[Cu^{II}(TPA)]^{+}$ with a $E_{1/2}$ value of – 0.40 V. This indicated the stabilization of $[Cu^{I}(^{R3}TPA)]^{+}$ complexes. As a consequence, the comparatively hard to oxidize complex $[Cu^{I}(^{Ph3}TPA)(NCMe)]^{+}$ (**Figure 2.7**) was found to be unreactive towards dioxygen binding.[7] In addition, the phenyl ring might be expected to sterically hinder approach of dioxygen to the copper centre or, indeed, any other substrate.

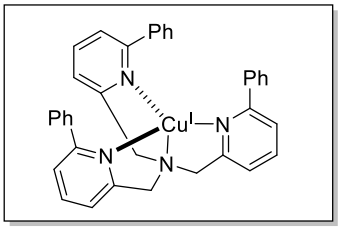

Figure 2.7: Structure of the complex $[Cu^{I}(^{Ph3}TPA)]^{+}$

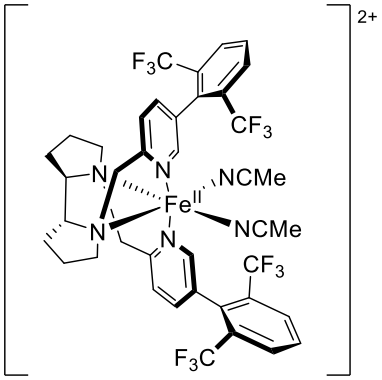

(*R*,*R*)-[Fe(CF3-PDP)]$^{2+}$

Figure 2.8: Structure of the complex (R,R)-[Fe(CF_3-PDP)].

More recently, it has been shown that installation of bulky substituents at the 5-position of pyridine rings in iron and manganese complexes of TPA (and related linear tetradentate ligands) can influence their reactivity in oxidation catalysis. Notably, they do so without compromising the oxidative stability of the ligands or causing a reduction in coordination number of the complexes. The earliest demonstration of this was by White and co-workers, who reported the use of the complex [(*R*,*R*)-Fe(CF_3-PDP)][$B(C_6F_5)_4$] (**Figure 2.8**) as a catalyst for C-H bond oxidation using H_2O_2 as a terminal oxidant.[8] They showed that the presence of 2,6-bis(trifluoromethyl)phenyl substituents on the pyridine donors of the linear tetradentate ligand directed the site of oxidation away from thermodynamically favoured tertiary C-H bonds to less sterically hindered secondary C-H bonds. This observation was rationalized through discussion of approach trajectories of the substrate and the increased effective cone angles of the pyridine donors.[8–10]

Spurred by this success, Costas and co-workers reported C-H bond and olefin oxidation catalysis using Mn and Fe complexes supported by mcp ligands and TPA ligands incorporating bulky Si($^{i}Pr_3$) substituents at the 5th position of pyridyl ring (**Figure 2.9**).[11] Importantly, all catalysts showed high reactivity, which indicates that installation at the 5-position of the pyridine rings does not hinder reactivity. The average Fe-N bond length of [Fe^{II}(^{tips3}TPA)$(OTf)_2$] was found to be 2.20 Å which was similar to high-spin, octahedral

[Fe(TPA)(OTf)$_2$]. Despite obtaining high-spin iron(II) complex with octahedral geometry, this complex showed good reactivity toward olefin epoxidation and C-H bond oxidation.

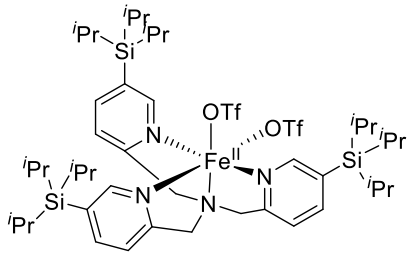

[Fe^{II}(^{tips3}TPA)(OTf)$_2$]

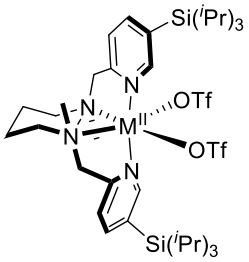

[(*S,S*)-[M(^{tips2}mcp)(OTf)$_2$]
M: Fe, Mn

Figure 2.9: Structure of [Fe(5^{tips3}TPA)(OTf)$_2$] and [(*S,S*)-M(^{tips}mcp)(OTf)$_2$]

We reasoned that introduction of judiciously selected bulky substituents at the 5th position of the pyridine rings in TPA would not only promote stabilization of trigonal bipyramidal geometries, it would also allow inhibition of formation of bimetallic complexes. Furthermore, we felt that the distal nature of the substituents relative to the metal centre would reduce the probability of their oxidation, and leave the metal centre relatively uncrowded, thereby, minimizing their impact upon reaction with substrates and donor strength of the constituent pyridine rings. Such ligand design features would be expected to be of benefit in formation of high-spin complexes and in stabilization of reactive species, both of which we have sought to exploit in this thesis work. With these objectives in mind, we prepared the series of aryl-substituted TPA ligands given in **Figure 2.10**. Their synthesis, complexation and coordinative properties are discussed in the subsequent sections.

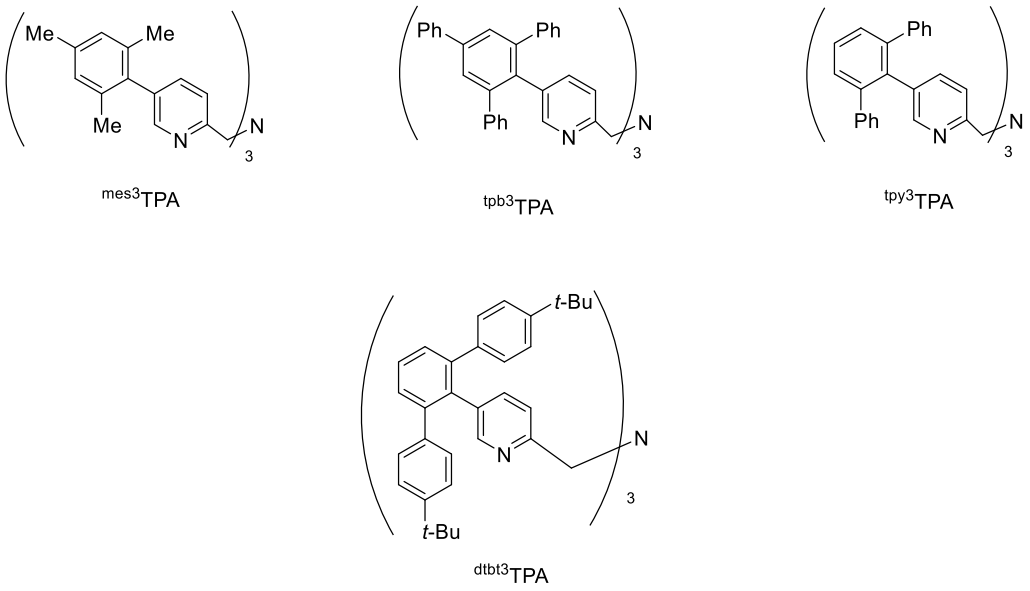

Figure 2.10: Tris(5-aryl-2-pyridylmethyl)amine (^{Ar3}TPA) ligands prepared in this study.

2.2 Results and Discussion

2.2.1 Ligand synthesis

2.2.1.1 Route A

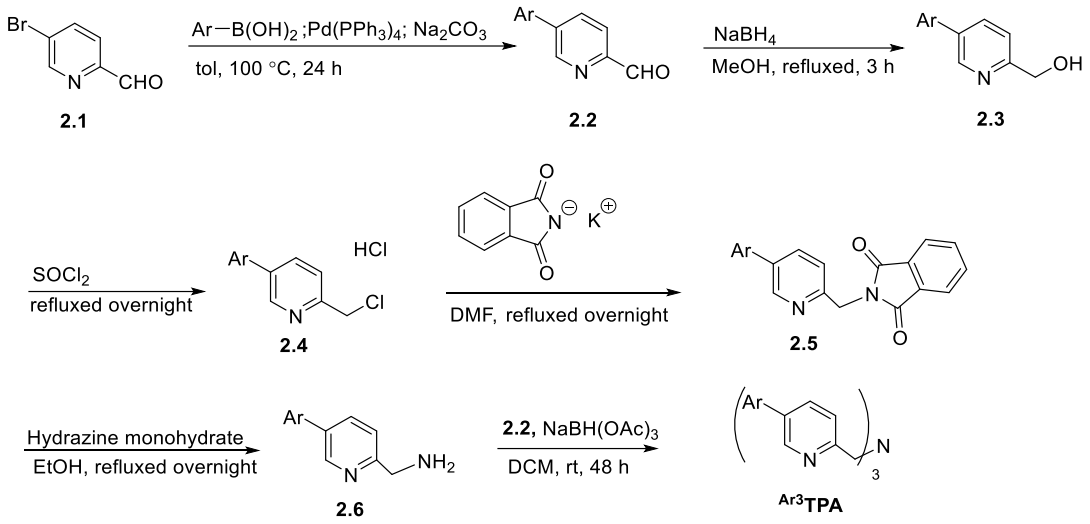

Scheme 2.1: Initial synthetic route for the formation of ^{Ar3}TPA.

Our initial efforts to synthesize ^{Ar3}TPA ligands utilized the general synthetic approach reported by Canary and his co-workers for preparation of ^{Ph3}TPA.[7] This is shown in **Scheme 2.1** and involved synthesis of 5-aryl-2-pyridinecarboxaldehydes, **2.2**, via palladium catalysed Suzuki cross-coupling of the 5-bromo-2-pyridinecarboxaldehyde and aryl boronic acids. Subsequent to reduction of the aldehydes to form the corresponding alcohols (**2.3**) using sodium borohydride, chlorination using thionyl chloride was used to provide 5-aryl-2-chloromethylpyridines (**2.4**). Reaction with potassium phthalimide and deprotection using hydrazine monohydrate afforded compounds **2.5** and **2.6**, respectively. Finally, reductive amination of (5-aryl-pyridin-2-yl)methanamine, **2.6**, using compounds **2.2** and sodium triacetoxyborohydride was attempted.

Using this synthetic route, the target ligand bearing comparatively small mesityl groups, ^{mes3}TPA, was obtained in an overall yield of 24 %. However, when attempting to form 5^{tpb3}TPA, which has much larger substituents, partial reaction occured in the final reductive amination step, which yield **^{tpb2}2.7** as the major product. In an effort to promote this reaction, various

reaction conditions were attempted (**Table 2.1**) but none were able to provide the target ligand. This included addition of acetic acid, which is known to catalyze reductive amination reactions, and vigorous heating. In all cases, incomplete reaction was observed via NMR spectroscopy with dominant products being ^{tpb2}**2.7** (**Scheme 2.2**).

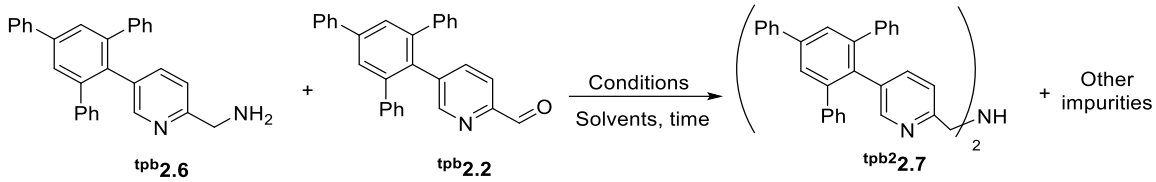

Scheme 2.2: Outcome of reductive amination of ^{tpb}**2.6** and ^{tpb}**2.2** under all reducing conditions tested.

Table 2.1: Various reaction conditions tested for attempted synthesis of ^{tpb3}TPA ligand via reductive amination and their outcomes.

Reagents	Solvent	Temperature	Reaction Time	Results
$Na(OAc)_3BH$, AcOH	DCM	Room temperature	1 Week	Incomplete reaction
$Na(OAc)_3BH$, AcOH	MeCN	Refluxed	1 Week	Incomplete Reaction

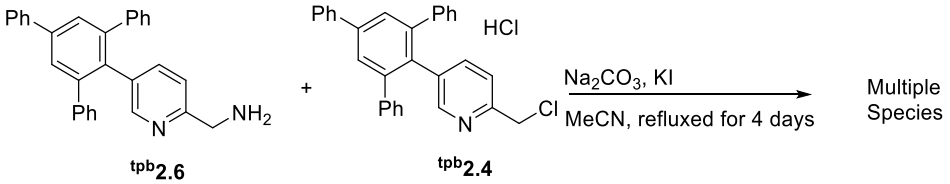

Scheme 2.3 Proposed scheme for S_N^2 reaction of ^{tpb}pyridylmethylamine, ^{tpb}**2.6** and ^{tpb}pyridylmethylchloride, ^{tpb}**2.4**.

Thus, an alternative S_N2 alkylation route involving reaction of **2.6** with 2 equiv of **2.4** was pursued (**Scheme 2.3**) using sodium carbonate and potassium iodide as a base and catalyst in acetonitrile. The reaction was refluxed for 4 days. However, multiple species were observed, none of which were the target compound, according to NMR spectroscopy and mass

spectrometry. At this point, it was concluded that early stage installation of the very bulky 2,4,6-triphenylbenzene substituent renders such traditional routes to TPA ligands unworkable. As such, we sought an alternative reaction pathway involving installation of the aryl substituent *after* construction of the TPA ligand framework (**Scheme 2.4**).

2.2.1.2 Route B

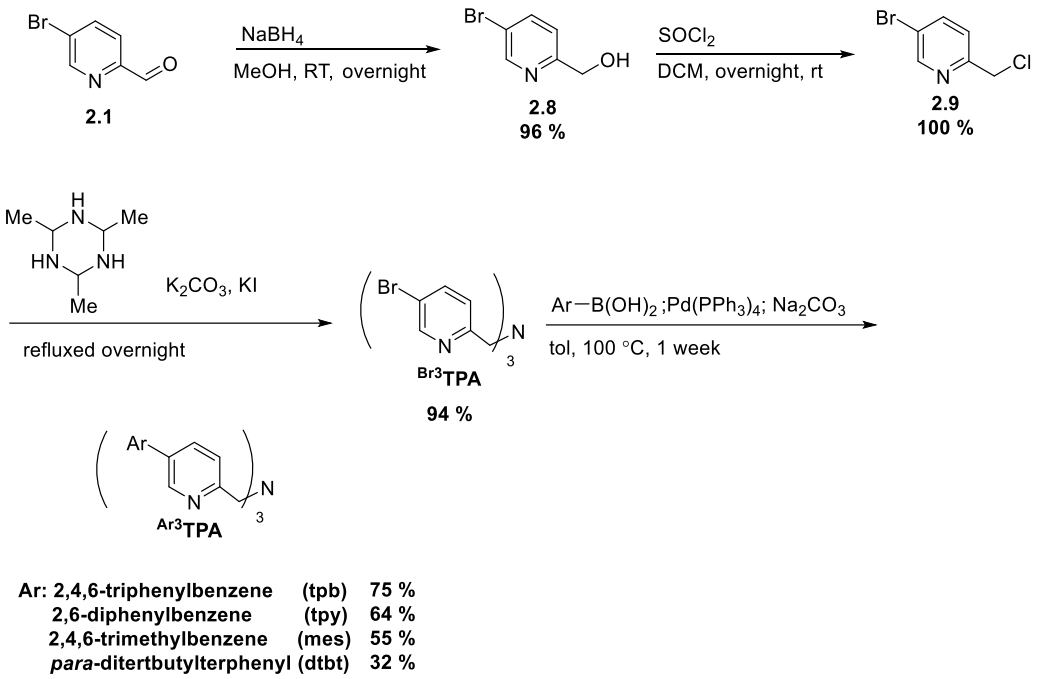

Scheme 2.4: Alternative synthetic route for the ^{Ar3}TPA ligand, in which Suzuki cross-coupling is the final step.

The late-stage arylation synthetic route is summarized in **Scheme 2.4**. The first step involves $NaBH_4$ reduction of 5-bromo-pyridinecarboxaldehyde (**2.1**) to the corresponding alcohol (**2.8**) which was treated with thionyl chloride to give 5-bromo-2-(chloromethyl)pyridine (**2.9**). Reaction of the latter via an S_N2 reaction with acetaldehyde ammonia trimer, via a general procedure reported by Hideo and coworkers, afforded ^{Br3}TPA.[12] Lastly, palladium catalysed Suzuki cross-coupling reactions were performed using a series of aryl boronic acids, which were themselves synthesized via metalation of arylbromides using *n*-BuLi or magnesium and subsequent reaction with trimethylborate (**Scheme 2.5**). Gratifyingly, this approach provided the target ^{Ar3}TPA ligands in good to excellent overall yields (^{mes3}TPA: 50 %; ^{tpy3}TPA: 51 %;

^{tpb3}TPA: 63 %; and ^{dtbt3}TPA: 25 %). It is worth noting that ^{tpb3}TPA and ^{tpy3}TPA have poor solubility in most organic solvents, except chlorinating solvents, which allowed for straightforward purification. In contrast, 5^{dtbt3}TPA was highly soluble in most organic solvents and not straightforward to purify by column chromatography. This, and not the cross-coupling reaction, was the cause of its comparatively low yield. Given the success of the late-stage arylation synthetic route, it was used as a default in all subsequent thesis work.

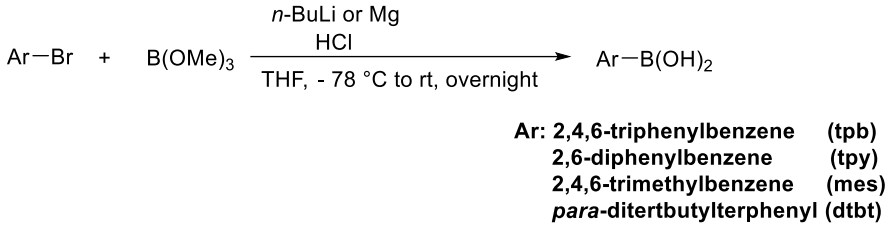

Scheme 2.5: Reaction pathway used in synthesis of arylboronic acids.

2.2.2 Complexation

In addition to synthesis of iron and copper complexes of all ^{Ar3}TPA ligands prepared, which are the focus of this thesis work, ^{tpy3}TPA and ^{tpb3}TPA were used in complexation with all first row transition metals ranging from manganese to copper. The latter was undertaken in order to provide a better understanding of the general coordinative properties of the TPA ligands synthesized.

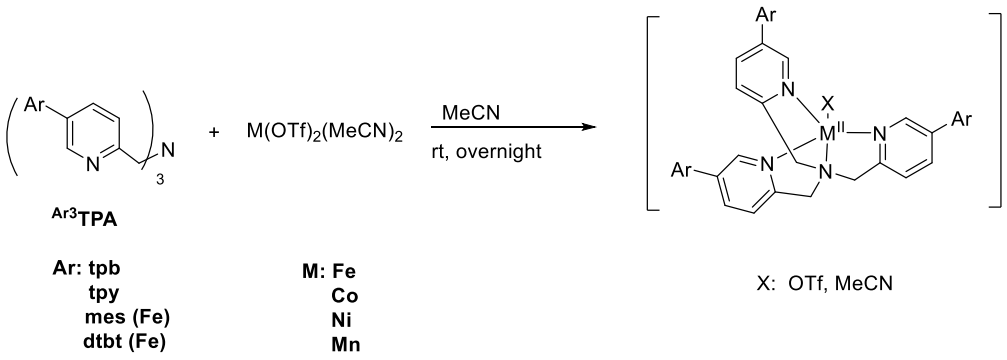

Scheme 2.6: Complexation of ^{Ar3}TPA with $[M^{II}(OTf)_2(NCMe)_2]$ to obtain metal complex with proposed trigonal bipyramidal geometry.

The ^{Ar3}TPA ligands were first employed in complexation with metal(II) triflate salts (metal = Mn, Fe, Co and Ni) using acetonitrile as solvent (**Scheme 2.6**), in which the ligands have poor solubility. The yield of the complexes was, uniformly, about 70 % after purification. As detailed below, they were characterized by combinations of ^{1}H and ^{19}F NMR spectroscopies, mass spectrometry, cyclic voltammetry and X-ray crystallography.

Interestingly, the complexes $[Fe^{II}(^{mes3}TPA)(NCMe)_2](OTf)_2$, $[Fe^{II}(^{tpb3}TPA)(OTf)](OTf)$, $[Fe^{II}(^{tpy3}TPA)(OTf)]$ complex formed red solutions in MeCN, whereas that of $[Fe^{II}(^{dtbt3}TPA)(OTf)](OTf)$ was yellow in colour. Note, the complexes form solvates of the type $[Fe^{II}(^{Ar3}TPA)(NCMe)_2]^{2+}$ in acetonitrile solution. The red colour of the former derives from an absorption centred at 520 nm (ε = 170 M^{-1} cm^{-1}) (**Figure 2.11**) and is characteristic of a metal-to-pyridine charge transfer (CT) band, which is particularly intense for *low-spin* iron(II) complexes. The low intensity of this CT band in the case of $[Fe^{II}(^{dtbt3}TPA)(OTf)](OTf)$ suggests that $[Fe^{II}(^{dtbt3}TPA)(NCMe)_2]^{2+}$ is high-spin. As previously reported, all the iron(II) triflate complexes form yellow solutions in DCM and this is because they are triflate coordinated and, consequently, high-spin.

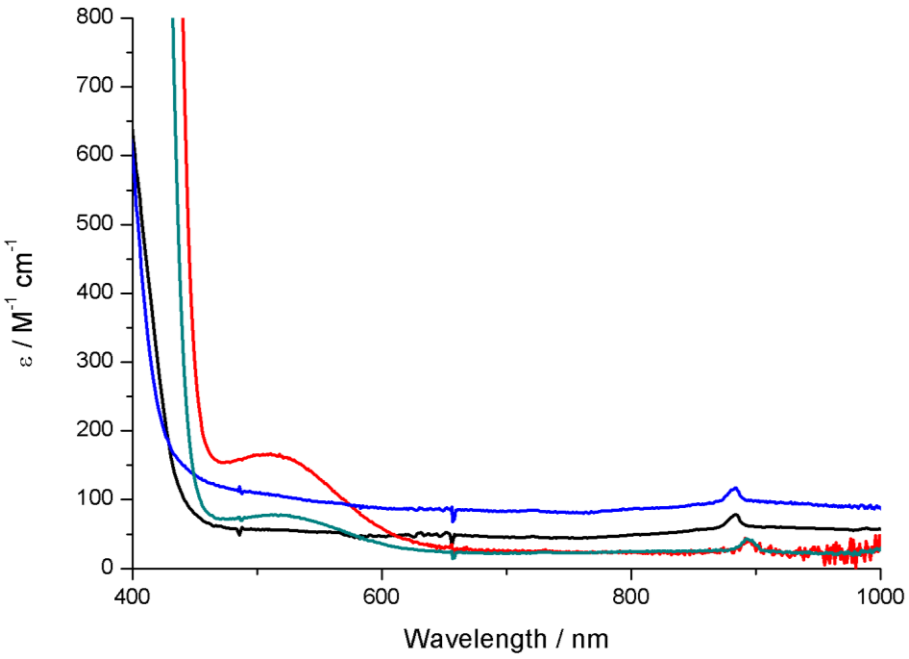

Figure 2.11: UV-vis plot for [Fe^{II}(^{tpb3}TPA)(OTf)](OTf) (2 mM) (black in DCM) and (red in MeCN) and [Fe^{II}(^{dtbt3}TPA)(OTf)](OTf) (2 mM) (blue in DCM) and (green in MeCN).

Despite numerous attempts, recrystallizing the full series of metal triflate complexes prepared, with triflate or MeCN coordinated, was not successful. This appears to be due to the bulkiness of the complex, making it too soluble in most of the solvent. In response, we sought to prepare $[Fe^{II}(^{Ar3}TPA)(NCMe)_n]^{2+}$ (n = 1 or 2) complexes with counterions that engender high crystallinity. To this end, we synthesised metal(II) bromide complexes of the ^{Ar3}TPA ligands and then performed silver salt metathesis using $AgClO_4$ and $AgSbF_6$ in MeCN solution (**Scheme 2.7**). Single crystals suitable for X-ray crystallographic studies were obtained via vapour diffusion of MeCN/Et_2O. Despite all our efforts, only the X-ray crystallographic structure of $[Co^{II}(^{tpb3}TPA)(MeCN)](SbF_6)_2$ and $[Fe^{II}(^{dtbt3}TPA)(MeCN)(ClO_4)](ClO_4)$ was obtained.

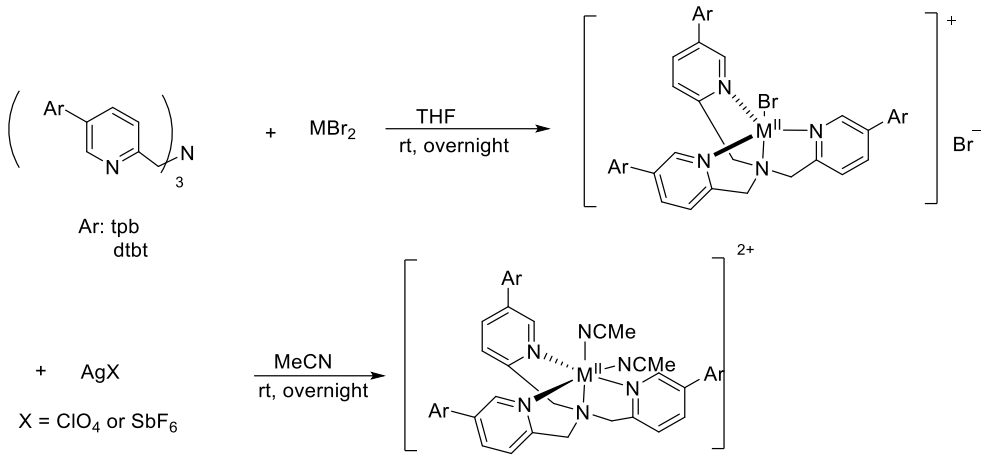

Scheme 2.7: Complexation with $M^{II}Br_2$ salts and subsequent silver salt metathesis.

The reaction of $[Fe^{II}(^{dtbt3}TPA)(Br)]Br$ with $Na[B(C_6F_5)_4]$ in THF would allow the formation of $[Fe^{II}(^{dtbt3}TPA)Br][B(C_6F_5)_4]$complex which were trigonal bipyramidal geometry, as proven by X-ray crystallographic analysis (**Scheme 2.8**). This was done to ensure that the anion was not coordinated to the metal complex, like $[Fe^{II}(^{dtbt3}TPA)(MeCN)(ClO_4)](ClO_4)$ This result suggests that at least one weakly coordinating anion is required to obtain successful tetradentate coordination of this ligand. However, more studies are required (and pending) before a full understanding of the coordinative properties of our bulky TPA ligands is obtained.

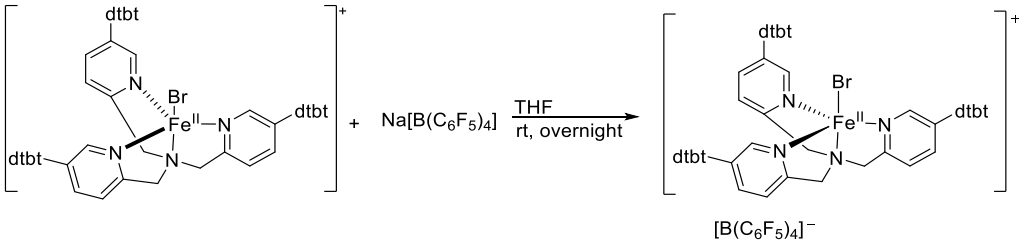

Scheme 2.8: Counterion exchange of $[Fe^{II}(^{dtbt3}TPA)(Br]](Br)$ with $Na[B(C_6F_5)_4)$.

On the other hand, $[Cu^{II}(^{tpb3}TPA)(NCMe)](ClO_4)_2$ and $[Cu^{II}(5^{py3}TPA)(NCMe)](ClO_4)_2$ were obtained in yields of 68 and 65 %, respectively, by reacting the ligand with $Cu(ClO_4)_2.xH_2O$ (**Scheme 2.9**). These complexes were characterized by mass spectrometry, x-ray crystallography and elemental analysis.

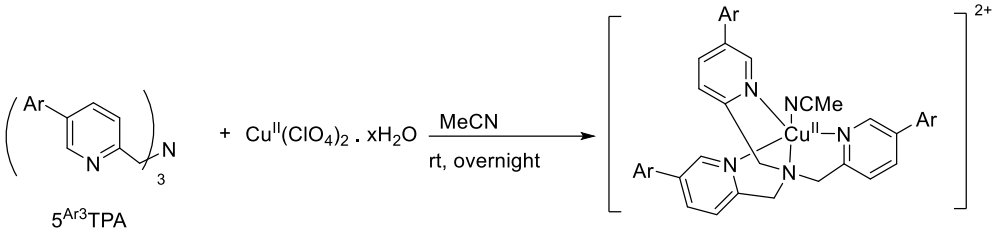

Scheme 2.9: Formation of $[Cu^{II}(^{Ar3}TPA)MeCN][ClO_4]_2$.

2.2.3 Characterization of Complexes

2.2.3.1 ^{1}H NMR Spectroscopy

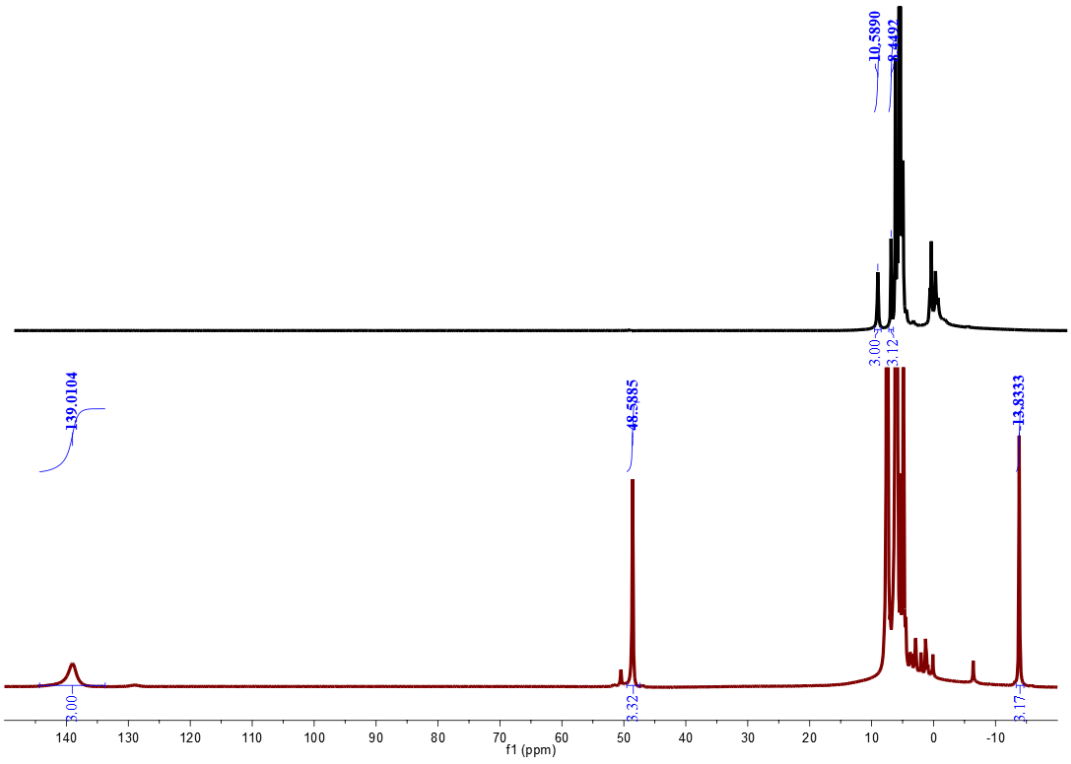

Figure 2.12: ^{1}H NMR spectra of $[Fe^{II}(^{tpb3}TPA)(OTf)](OTf)$ recorded in CD_3CN (black) and CD_2Cl_2 (red) solution, at room temperature.

^{1}H NMR spectroscopic studies of transition metal complexes can provide a more detailed understanding of their spin-states and geometries, whilst also giving an indication of impurity. As the ^{1}H NMR spectra of $[Fe^{II}(^{tpy3}TPA)(OTf)](OTf)$ and $[Fe^{II}(^{tpb3}TPA)(OTf)](OTf)$ exhibit similar solvent dependent behaviour, we will discuss only the latter here (**Figure 2.12**). The spectra of the former will appear in the appendices (**Figure S1** and **S2**). When the ^{1}H NMR spectrum of $[Fe^{II}(^{tpb3}TPA)(OTf)](OTf)$ (**Figure 2.12**) is recorded in CD_3CN solution, the

resonances are confined to the diamagnetic region, which indicates that $[Fe^{II}(^{tpb3}TPA)(NCMe)_n]^{2+}$ is low-spin (S = 0). This is consistent with this complex being 6-coordinate (i.e., having 2 MeCN ligands), but the apparent C_3 symmetry of the spectrum suggests the complex is highly fluxional. The observation of low-spin ground states for the aforementioned complexes is of significant note because it indicates the bulk aryl substituents in question do not significantly weaken the donor strength of the pyridine rings. This should be contrasted with introduction of a single methyl substituent at the 6-position of a pyridine ring in TPA, which causes the complex $[Fe^{II}(^{Me3}TPA)(NCMe)_2]^{2+}$ to be high-spin.

In contrast, when CD_2Cl_2 is used as a solvent, there are peaks that are strongly paramagnetically shifted. This is consistent with expectations of coordinated triflate ligands, which would engender a high-spin state (S = 2). Consistent with time-averaged C_3 symmetry, 3 peaks are observed. By comparison with published spectra, the 3 paramagnetically shifted signals at 139, 48.5 and -13.8 ppm can tenatively be assigned as H_α, H_β and H_γ of the pyridine rings, respectively.[13] Unfortunately, the ^1H NMR spectral data recorded in CD_2Cl_2 does not distinguish between the possibility of an octahedral versus a trigonal bipyramidal geometry. In other words, between $[Fe^{II}(^{tpb3}TPA)(OTf)_2]$ and $[Fe^{II}(^{tpb3}TPA)(OTf)](OTf)$. However, given that the former contains 2 coordinated triflate anions and the latter 1 free triflate and 1 coordinated triflate, one would expect to be able to differentiate between these 2 options using ^{19}F NMR spectroscopy.

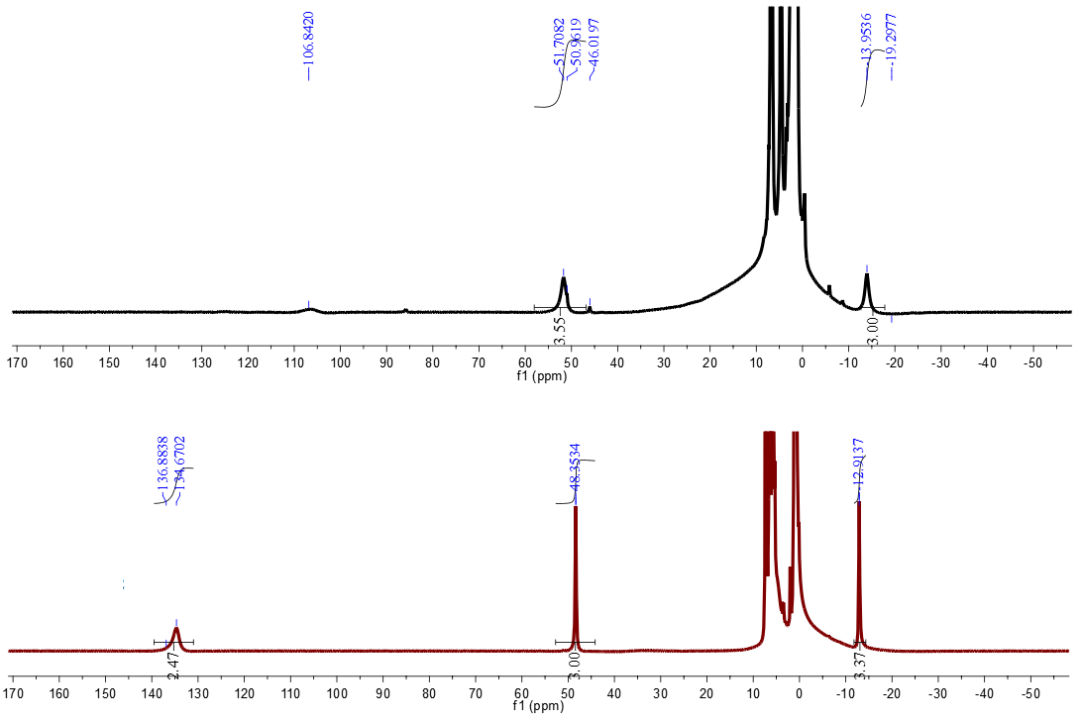

Figure 2.13: ^{1}H NMR spectra of [Fe^{II}(^{dtbt3}TPA)(OTf)](OTf) recorded in CD_3CN (black) and CD_2Cl_2 (red) solution, at room temperature.

On the other hand, the ^{1}H NMR spectrum of [Fe^{II}(^{dtbt3}TPA)(OTf)](OTf) differs from the other iron complexes in that strongly paramagnetically shifted peaks are observed in CD_3CN, as well as CD_2Cl_2, solution (**Figure 2.13**). More specifically, in CD_3CN the peaks corresponding to the α-, β- and γ-pyridyl protons appear at 106, 51.0 and -14.0 ppm, respectively; and at 136.8, 48.3 and -12.9 ppm, respectively when the spectrum is recorded in CD_2Cl_2 solution. On this basis, it is not possible to discern whether this ligand enforces trigonal bipyramidal geometries in solution or if the large dtbt substituents weaken the donor strength of the pyridine rings.

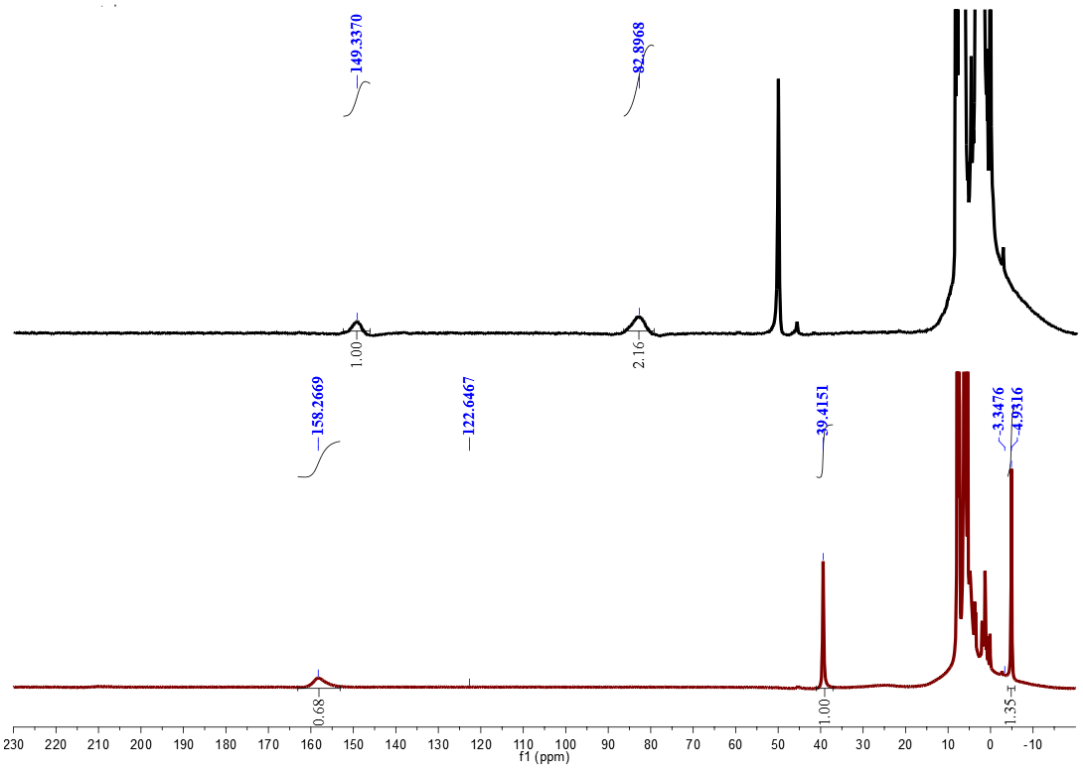

Figure 2.14: ^{1}H NMR spectra of [Co^{II}(^{tpb3}TPA)(OTf)](OTf) recorded in CD_3CN (black) and CD_2Cl_2 (red) solution, at room temperature.

As anticipated, the peaks in the ^{1}H NMR spectra of the complex [Co^{II}(^{tpb3}TPA)(OTf)](OTf) in both CD_3CN and CD_2Cl_2 solution were strongly paramagnetically shifted and broadened (**Figure 2.14**), features that are consistent with an S = 3/2 spin-state. For both spectra, the peaks corresponding to the α-, β- and γ-pyridyl protons of the pyridine ring appear at 158, 39 and – 5 ppm, respectively. A peak corresponding to the methylene protons could only be seen in CD_3CN solution, where they appear at 82 ppm. Similar ^{1}H NMR spectra were observed for [Co^{II}(^{tpy3}TPA)OTf](OTf) (**Figure S3** and **Figure S4**).

Generally speaking, copper(II), and high-spin manganese(II) and nickel(II) ions show electronic relaxation rates incompatible with ^{1}H NMR spectroscopy. As such it is no surprise that the resonances in the ^{1}H NMR spectra of the complexes [Ni^{II}(^{Ar3}TPA)]$^{2+}$, [Mn^{II}(^{Ar3}TPA)]$^{2+}$ and [Cu^{II}(^{Ar3}TPA)]$^{2+}$ were too severely broadened to be of any diagnostic value. As a result, other methods are required for their characterization.

2.2.3.2 ^{19}F NMR Spectroscopy

As mentioned earlier, ^{19}F NMR spectroscopic measurements performed in CD_2Cl_2 should allow us to distinguish between the possibility of the complexes being 6-coordinate, with 2 coordinated triflate anions, and trigonal bipyramidal, wherein we would expect 1 coordinated and 1 free triflate anion. Generally speaking, uncoordinated triflate should be located somewhere between -77 and -79 ppm, while coordinated triflate anion can range from -40 to 100 ppm.

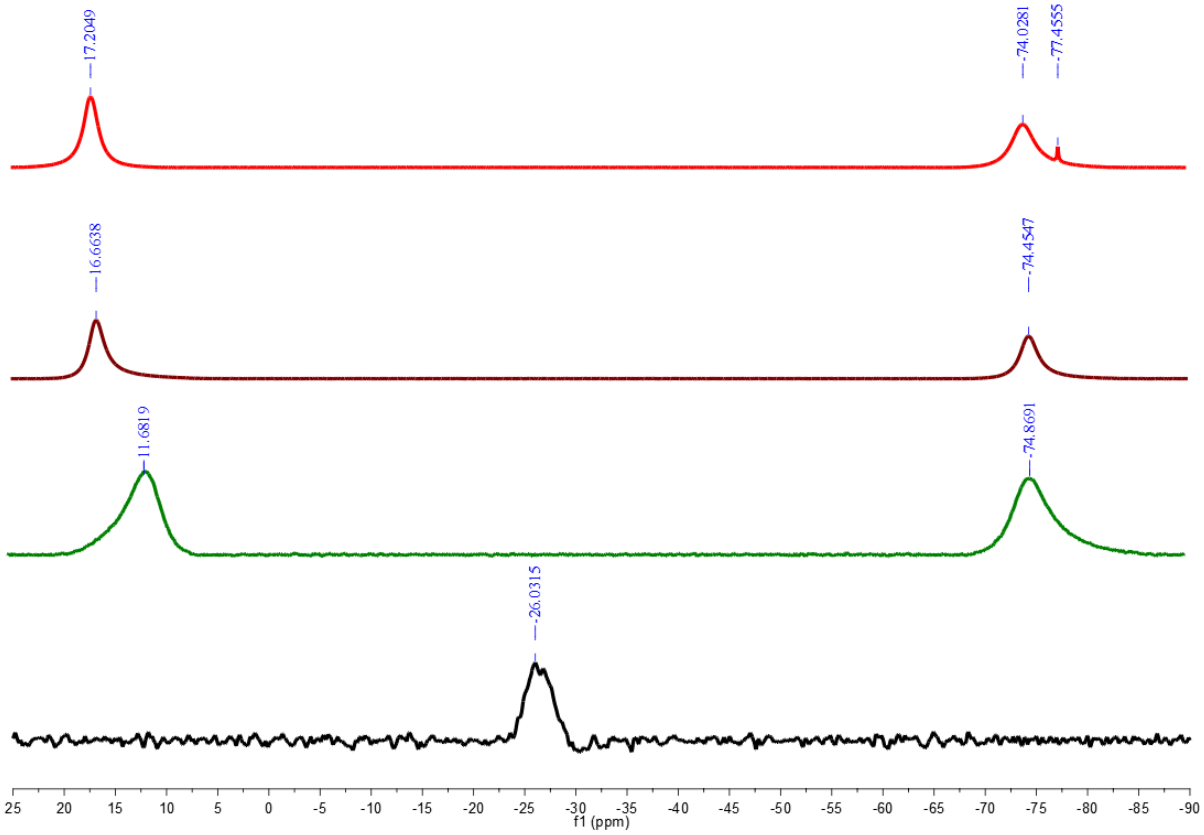

Figure 2.15: ^{19}F NMR spectra of [Fe^{II}(^{tpb3}TPA)(OTf)](OTf) (red), [Fe^{II}(^{tpy3}TPA)(OTf)](OTf) (maroon), [Fe^{II}(^{dtbt3}TPA)(OTf)](OTf) (green) and [Fe^{II}(^{mes3}TPA)(OTf)$_2$](black), recorded in CD_2Cl_2 solution at room temperature.

The ^{19}F NMR spectrum of a CD_2Cl_2 solution of [Fe^{II}(^{mes3}TPA)(OTf)$_2$] contains a single peak at -26 ppm (**Figure 2.15, black**), which can be assigned as coordinated triflate. On this basis, we expect [Fe^{II}(^{mes3}TPA)(OTf)$_2$] to exhibit an octahedral geometry in solution, regardless of

whether coordinatin or non-coordinating solvents are used. This is similar to the octahedral parent complex [Fe(TPA)(OTf)$_2$], for which a single peak at -34 ppm was observed in the same solvent.[4] In contrast, two chemically different types of triflate anion are observed in the ^{19}F NMR spectra of the other iron complexes when they were recorded in non-coordinating NMR solvents (e.g., CD_2Cl_2). In all these complexes, the most upfield peak at -75 ppm can be attributed to non-coordinated triflate, with the remaining downfield peak at > 10 ppm being due to coordinated triflate (**Figure 2.15, red**). Thus, it is clear that all the iron complexes, other than [Fe^{II}(^{mes3}TPA)(OTf)$_2$], exhibit a trigonal bipyramidal geometry when dissolved in non-coordinating solvents. It should be noted that only non-coordinated triflate, denoted by a peak at -78 ppm, is observed when coordinating CD_3CN was used as a solvent.

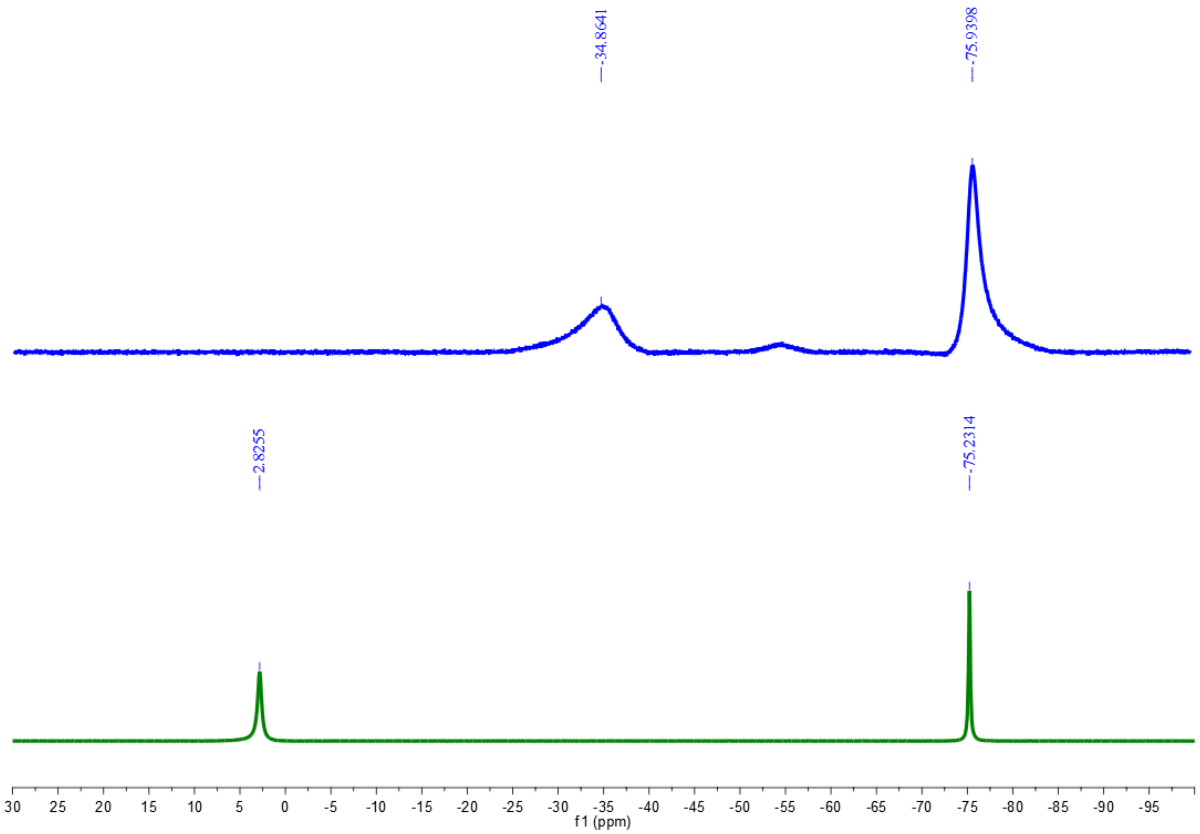

Figure 2.16: ^{19}F NMR for [Ni^{II}(^{tpb3}TPA)(OTf)](OTf) (blue) and [Co^{II}(^{tpb3}TPA)(OTf)](OTf) (green), recorded in CD_2Cl_2 solution at room temperature.

The ^{19}F NMR spectra of the corresponding Co and Ni complexes of the ^{tpb3}TPA ligand both exhibit a peak at -76 ppm, which corresponds to non-coordinating triflate, and peaks at -35 and 2.8 ppm, respectively, which represent coordinated triflate ligands (**Figure 2.16**). This confirms that these complexes possess trigonal bipyramidal geometries in non-coordinating solvents. Similar results were observed for the corresponding complexes supported by 5^{tpy3}TPA. As expected, peaks could not be resolved in the ^{19}F NMR spectra of the Mn and Cu complexes.

2.2.3.3 Solution State Evans' NMR

The solution-state magnetic moments (μ_{eff}) of all the complexes have been determined using Evans' NMR method and are summerized in **Table 2.2**. The μ_{eff} values of [Fe^{II}(^{tpb3}TPA)(OTf)](OTf), [Fe^{II}(^{tpy3}TPA)(OTf)$_2$] and [Fe^{II}(^{dtbt3}TPA)(OTf)](OTf) were measured in CD_2Cl_2 solution to be 5.2, 4.9 and 5.7 μ_B, respectively. The latter value is a little high but, regardless, it can be concluded that they all contain a high-spin (S = 2) iron(II) ion. Interestingly, in CD_3CN solution [Fe(^{dtbt3}TPA)(OTf)](OTf) was found to have a μ_{eff} of 4.66 μB, which suggests that this complex is also high-spin. This result is in agreement with the paramagnetically shifted ^{1}H NMR spectrum of [Fe^{II}(^{dtbt3}TPA)(OTf)](OTf). The fact that the observed μ_{eff} is lower than the spin-only expectation value of 4.90 is either due to the presence of impurities or close proximity to a spin-crossover domain. This is in contrast with [Fe^{II}(^{tpb3}TPA)(OTf)](OTf) and [Fe^{II}(^{tpy3}TPA)(OTf)$_2$], for which a ^{1}H NMR spectrum diagnostic of an S = 0 spin-state was observed.

The μ_{eff} values of 4.3 and 3.9 μB measured for the complexes [Co^{II}(^{tpb3}TPA)(OTf)](OTf) and [Co^{II}(^{tpy3}TPA)(OTf)](OTf), respectively, in CD_2Cl_2 solution indicates they contain S = 3/2 Co^{II} centers. Similar μ_{eff} values were measured in CD_3CN solution, so their spin states are not solvent dependent. Lastly, μ_{eff} of 2.7 and 3.30 μ_B were obtained for [Ni^{II}(^{tpb3}TPA)(OTf)](OTf) and [Ni^{II}(^{tpy3}TPA)(OTf)$_2$], from which S = 1 spin-state assignments for the Ni^{II} centers can be deduced.

Table 2.2: Comparison of the solution-state magnetic moment (μ_{eff}) values and spin-states for the metal(II) complexes in this study, with either CD_2Cl_2 or CD_3CN as a solvent.

Complex	Solvent	μ_{eff}	Spin-state
$[Fe^{II}(^{tpb3}TPA)(OTf)](OTf)$	CD_2Cl_2	5.2	2
$[Fe^{II}(^{tpy3}TPA)(OTf)_2]$	CD_2Cl_2	4.9	2
$[Fe^{II}(^{dtbt3}TPA)(OTf)](OTf)$	CD_2Cl_2	5.7	2
$[Fe^{II}(^{dtbt3}TPA)(OTf)](OTf)$	CD_3CN	4.7	2
$[Co^{II}(^{tpb3}TPA)(OTf)](OTf)$	CD_2Cl_2	4.3	3/2
$[Co^{II}(^{tpb3}TPA)(OTf)](OTf)$	CD_3CN	4.4	3/2
$[Co^{II}(^{tpy3}TPA)(OTf)](OTf)$	CD_2Cl_2	3.9	3/2
$[Ni^{II}(^{tpb3}TPA)(OTf)](OTf)$	CD_2Cl_2	2.7	1
$[Ni^{II}(^{tpy3}TPA)(OTf)](OTf)$	CD_2Cl_2	3.3	1

2.2.3.4 X-ray Crystallographic Studies

Efforts were made to obtain X-ray structures of the iron complexes with both triflate and MeCN ligands, by growing crystals from non-coordinating solvents and MeCN, respectively. A full series of both proved difficult to obtain. This was in large part due to disorder in the structures, which seemed to mostly derive from extensive incorporation of solvent into the crystals. All structures that were successfully obtained and their structural parameters are provided in **Figure 2.17, Figure 2.18, Table 2.3** and **Table 2.4** respectively. Unfortunately, no single crystals of the nickel complexes supported by ^{tpy3}TPA or ^{tpb3}TPA could be obtained, despite numerous attempts using various counterions and solvent mixture

The used of mesityl group onto the ligand was first used as it was the least hindered. Single crystal of $[Fe^{II}(^{mes3}TPA)(NCMe)_2][ClO_4]_2$ was obtained via vapour diffusion of diethyl ether into a concetration acetoniritile solution of it and the X-ray crystallographic analysis showed that the resulting complex was octahedral, similar to the low-spin $[Fe(TPA)(NCMe)_2]^{2+}$ complex and agreed with its ^{19}F NMR spectrum (**Figure 2.15 and Table 2.3**). The Fe-N_{am} bond length was found to be 1.985(2) Å (vs 1.98 Å for $[Fe^{II}(TPA)(NCMe)_2]^{2+}$) and the average Fe-$N_{py}$ bond length was 1.962(2) Å (vs 1.96 Å for $[Fe^{II}(TPA)(NCMe)_2]^{2+}$). The N_{am}-Fe-N_{py} was found to be 84.19(9)°, all these bond lengths and bond angles are similar to the low-spin $[Fe^{II}(TPA)(MeCN)_2]^{2+}$ complex. This might suggest that the mesityl group was not bulky enough to enforce a trigonal bipyramidal geometry. Thus, it implied that the used of sterically bulky phenyl group was important to obtain iron(II) complexes with trigonal bipyramidal, as suggested in ^{19}F NMR spectroscopic studies.

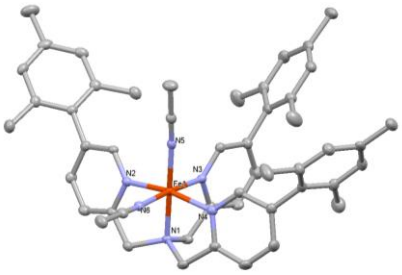

$[Fe^{II}(^{mes3}TPA)(NCMe)_2](ClO_4)_2$

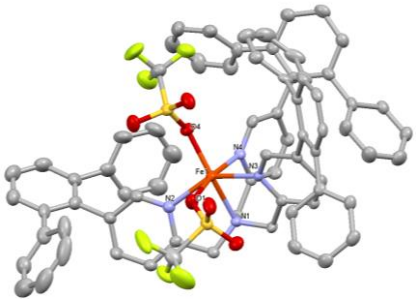

$[Fe^{II}(^{tpy3}TPA)(OTf)_2]$

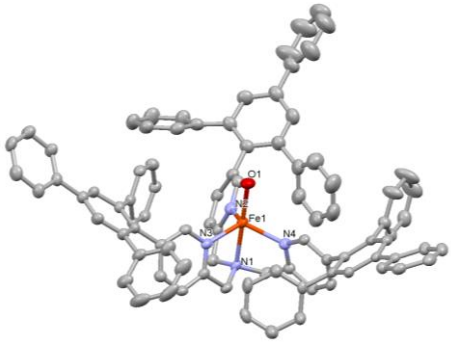

$[Fe^{II}(^{tpb3}TPA)(OH_2)](OTf)_2$

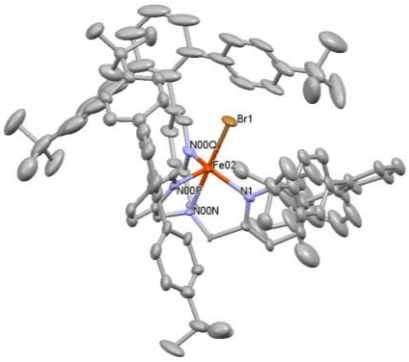

$[Fe^{II}(^{dtbt3}TPA)(Br)][B(C_5F_6)_4]$

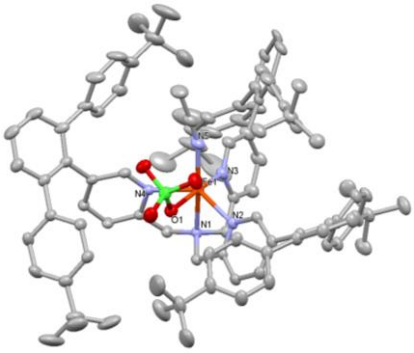

$[Fe^{II}(^{dtbt3}TPA)(ClO_4)(NCMe)][ClO_4]$

Figure 2.17: Crystal structures of the Fe^{II} complexes bearing ^{Ar3}TPA ligands, depicted with thermal ellipsoids of 50 %. Atom colour scheme: carbon, gray; nitrogen, purple; oxygen, red; sulfur, yellow; fluorine, yellowish green; chlorine, green; bromine, brown; iron, orange. All hydrogen atom, solvent molecules and counteranions are omitted for clarity.

Table 2.3: Selected bond lengths (Å) and bond angles (°) of the iron(II) complexes.

	$[Fe^{II}(^{mes3}TPA)(NCMe)_2][ClO_4]_2$	**$[Fe^{II}(^{tpy3}TPA)(OTf)_2]$**	**$[Fe^{II}(^{tpb3}TPA)(OH_2)](OTf)_2$**	**$[Fe^{II}(^{dtbt3}TPA)(Br)][B(C_5F_6)_4]$**	**$[Fe^{II}(^{dtbt3}TPA)(ClO_4)(NCMe)](ClO_4)$**
M-N1 (N_{amine})	1.985(2)	2.180(4)	2.194(4)	2.276	2.2074(17)
M-N2 (N_{py})	1.961(2)	2.138(4)	2.103(4)	2.127	2.1690(17)
M-N3 (N_{py})	1.958(2)	2.124(4)	2.127(4)	2.096	2.1429(19)
M-N4 (N_{py})	1.966(2)	2.262(4)	2.111(4)	2.086	2.1405(18)
M-N_{MeCN}/O_{OTf}	1.931(2)	2.286(4)	2.031(3)	2.422	2.0935(19)
M-N_{MeCN}/O_{ClO4}	1.940(2)	2.015(8)	2.031(3)	-	2.3933(16)
N1-M-N2	83.36(9)	76.00(15)	76.92(13)	77.09	74.95(6)
N1-M-N3	85.35(9)	80.16(15)	76.90(13)	76.32	76.57(7)
N1-M-N4	83.87(9)	76.58(15)	76.99(13)	75.73	78.30(6)
N4-M-N3	86.34(9)	89.35(15)	114.05(13)	113.14	102.21(7)
N4-M-N2	167.19(9)	108.23(16)	115.97(14)	117.02	137.20(7)
N2-M-N3	91.63(9)	145.81(16)	115.12(14)	113.73	103.28(7)

Even though ^{19}F NMR spectroscopy suggested that there was only 1 triflate coordinated to $[Fe^{II}(^{tpy3}TPA)]^{2+}$, surprisingly, the X-ray structure revealed a distorted octahedral $[Fe^{II}(^{tpy3}TPA)(OTf)_2]$ complex, which was obtained from vapour diffusion of diethyl ether into concentrated DCM solution. The Fe-N_{amine} bond length was found to be 2.180(4) Å and the average Fe-N_{py} was found to be 2.175 Å, which was similar to the average Fe-N bond length of 2.220 Å found in $[Fe^{II}(^{tips3}TPA)(OTf)_2]$.[11] Despite that, one of the N_{py}-Fe-N_{py} bond angles of 108.23(16)° was found to be larger than 90°, hence, suggesting that the increase in steric bulk on the phenyl substituent might be able to obtain Fe^{II} complex with trigonal bipyramidal geometry.

Thus, the addition of phenyl groups on the ligand would form $[Fe^{II}(^{tpb3}TPA)(H_2O)](OTf)_2$, that was obtained from vapour diffusion of Et_2O into a concentrated DCM solution of the complex. Its structure exhibited a trigonal bipyramidial geometry (τ-value = 1)[14], with the tertiary amine and adventitious water ligand filling the axial positions. Consistent with it being high-spin, the average Fe-N_{py} bond length was found to be 2.113 Å, while the Fe-N_{am} bond length was 2.194(4) Å. This contrasts with most iron(II) complexes supported by the parent TPA ligand, which tend to exhibit octahedral geometry. Efforts to obtain an X-ray structure corresponding to the ^1H NMR spectrum measured in CD_2Cl_2, wherein one triflate anion coordinates to the metal centre, have been unsuccessful. Nevertheless, the structure obtained highlights the ability of this ligands to enforce trigonal bipyramidal geometries in iron(II) complexes.

Since the ^1H NMR of $[Fe^{II}(^{dtbt3}TPA)]^{2+}$ in CD_3CN was paramagnetic, it raised a question on whether the complex exhibits 5-coordinate geometry due to steric bulk or there was binding of weak co-ligand. Thus, to answer this question, the X-ray crystallographic analysis was performed. A distorted octahedral $[Fe^{II}(^{dtbt3}TPA)(ClO_4)(MeCN)][ClO_4]$ was obtained from the vapour diffusion of Et_2O into a concentrated MeCN solution. The Fe-N_{am} bond length was 2.2074(17) Å and the average Fe-N_{py} bond length was 2.1508 Å. A slightly elongated Fe-N_{py}

bond length was observed, which could be due to the binding of weak-field co-ligand. This might suggest that the paramagnetic features in ^{1}H NMR spectroscopy was due to the binding of weak-field co-ligand. However, the average N_{py}-Fe-N_{py} bond angle of 102.75° suggested a distortion in the geometry and approaching of trigonal bipyramidal geometry, which was probably due to the steric bulk that the ligand might play a part.

Thus, to access this possibility, the use of non-coordinating counteranions, $[B(C_6F_5)_4]$ would be needed to prevent such interaction. A trigonal bipyramidal $[Fe^{II}(^{dtbt3}TPA)(Br)][B(C_6F_5)_4]$ was obtained from the vapour diffusion of Et_2O into a concentration DCM solution. However, the crystal quality of this complex was not good, thus, the corresponding bond lengths and bond angles are not discussed, even though the average N_{py}-Fe-N_{py} bond angle was 114.63°

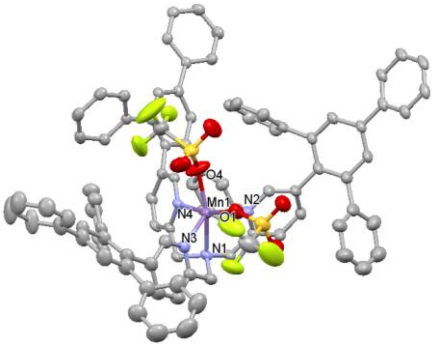

$[Mn^{II}(^{tpb3}TPA)(OTf)_2]$

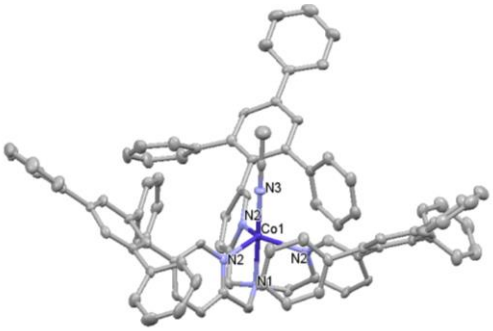

$[Co^{II}(^{tpb3}TPA)(NCMe)](SbF_6)_2$

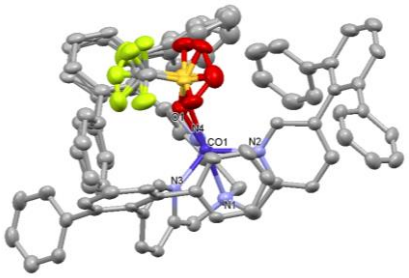

$[Co^{II}(^{tpy3}TPA)(OTf)](OTf)$

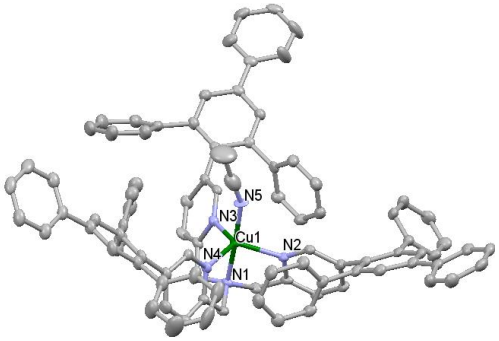

$[Cu^{II}(^{tpb3}TPA)(NCMe)](ClO_4)_2$

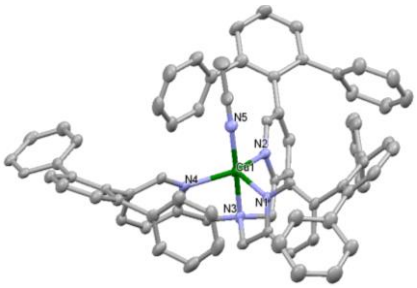

$[Cu^{II}(^{tpy3}TPA)(MeCN)](ClO_4)_2$

Figure 2.18: Crystal structures of Mn(II), Co(II) and Cu(II) complexes supported by ^{Ar3}TPA, depicted with thermal ellipsoids of 50 %. Atom colour scheme: carbon, gray; nitrogen, purple; oxygen, red; sulfur, yellow; fluorine, yellowish green; manganese, violet; cobalt, dark purple; copper, green. All hydrogen atoms, solvent molecules and counteranions are omitted for clarity.

Table 2.4: Selected bond lengths (Å) and bond angles (°) of the Mn(II), Co(II) and Cu(II) complexes

	$[Mn^{II}(^{tpb3}TPA)(OTf)_2]$	**$[Co^{II}(^{tpb3}TPA)(MeCN)](SbF_6)_2$**	**$[Co^{II}(^{tpy3}TPA)(OTf)](OTf)$**	**$[Cu^{II}(^{tpb3}TPA)(MeCN)](ClO_4)_2$**	**$[Cu^{II}(^{tpy3}TPA)(MeCN)](ClO_4)_2$**
M-N1 (N_{amine})	2.315(2)	2.165(16)	2.153	1.997(3)	2.011(5)
M-N2 (N_{py})	2.217(3)	2.055(8)	2.044	2.077(3)	2.052(5)
M-N3 (N_{py})	2.230(3)	2.055(8)	2.056	2.066(3)	2.100(5)
M-N4 (N_{py})	2.293(2)	2.055(8)	2.044	2.058(3)	2.062(5)
M-O_{OTf}/N_{MeCN}	2.224(2)	2.007(15)	2.029	1.952(3)	1.955(5)
M-O_{OTf}	2.102(3)	-	-	-	-
N1-M-N2	75.04(8)	78.5(2)	79.18	81.85(14)	82.30(19)
N1-M-N3	73.70(9)	78.5(2)	77.16	81.31(14)	81.46(19)
N1-M-N4	72.75(8)	78.5(2)	78.36	81.65(13)	80.46(19)
N4-M-N3	107.84(9)	116.15(14)	117.96	119.45(13)	112.31(18)
N4-M-N2	92.78(9)	116.15(14)	116.90	118.82(14)	129.1(2)
N2-M-N3	134.88(9)	116.15(14)	113.37	115.44(13)	111.83(19)

Single crystals of $[Mn^{II}(^{tpb3}TPA)(OTf)_2]$ were obtained via vapour diffusion of diethyl ether into a concentration solution of it. The structure was found to exhibit an octahedral geometry (**Figure 2.18**), with a Mn-N_{amine} bond length of 2.315(2) Å and an average Mn-N_{py} bond length of 2.247 Å (**Table 2.4**). Consistent with expectations, these distances are significantly elongated relative to those in the high-spin iron(II) complexes (*vide infra*). These long bond lengths, in turn, cause a contraction of the bite angles of the chelate rings, N_{amine}-Mn-N_{py}, to an average value of 73.83°. The aforementioned bond lengths and bond angles are very similar to $[Mn^{II}(TPA)(OTf)_2]$ with Mn-N_{amine} bond length of 2.289(2) Å, average Mn-N_{py} bond length of 2.243 Å and N_{amine}-Mn-N_{py} of 75.77°, as reported by Arnold and co-workers.[3] From observation of a 6-coordinate geometry, it can be concluded that either the 2,4,6-triphenylbenzene subsituent is not bulky enough to enforce a trigonal bipyramidal geometry or the comparitively large ionic radius of maganese(II) can accommodate an octahedral geometry with relative ease.

In contrast, the crystal structures of $[Co^{II}(^{tpb3}TPA)(NCMe)](SbF_6)_2$, $[Co^{II}(^{tpy3}TPA)(OTf)](OTf)$, $[Cu^{II}(^{tpb3}TPA)(NCMe)](ClO_4)_2$ and $[Cu^{II}(^{tpy3}TPA)(MeCN)](ClO_4)_2$ all exhibit trigonal bipyramidal geometries (**Figure 2.18** and **Table 2.4**), which is reflected by all of them having approximately τ-values close to 1.[14] The strong preference for formation of 5-coordinate geometries in these complexes can be attributed to contraction of the ionic radius of metal ions as you move across a period. An additional contributing factor for copper(II) complexes is their tendency to undergo Jahn-Teller distortions, which can be mitigated by decreasing coordination number.

Single crystals of $[Co^{II}(^{tpb3}TPA)(MeCN)](SbF_6)_2$ were obtained via vapour diffusion of Et_2O to a concentration MeCN solution containing the complex. The Co-N_{amine} bond length in $[Co^{II}(^{tpb3}TPA)(MeCN)](SbF_6)_2$ was found to be 2.165(16) Å, while the average Co-N_{py} bond length was found to be 2.055 Å. As expected for the smaller ionic radius of Co^{II}, the latter

distance is notably shorter than the corresponding bonds in the high-spin iron complexes. In addition, the average N_{eq}-Co-N_{eq} bond angle was 116.15(14)° and the average N_{ax}-Co-N_{eq} was 78.5(2)° (**Table 2.4**). Similar structural parameters were observed for $[Co^{II}(^{tpy3}TPA)(OTf)](OTf)$, which was obtained from vapour diffusion of Et_2O to a concentration DCM solution containing the complex. However, poor crystal data was obtained for discussion. As the reported $[Co^{II}(TPA)(OTf)](OTf)$ had a Co-N_{amine} bond length of 2.162(5) Å and average Co-N_{py} bond length of 2.039, it was fair to conclude that $[Co^{II}(^{tpb3}TPA)(MeCN)](SbF_6)_2$ and $[Co^{II}(^{tpy3}TPA)(OTf)](OTf)$ had similar bond lengths and bond angles.[3] Given that a trigonal bipyramidal geometry is observed with MeCN and TfO co-ligands, we feel it is safe to assume that all of our cobalt(II) complexes possess trigonal bipyramidal geometries in all of the organic solvents used in this thesis work.

Trigonal bipyramidal $[Cu^{II}(^{tpb3}TPA)(MeCN)][ClO_4]_2$ and $[Cu^{II}(^{tpy3}TPA)(MeCN)][ClO_4]_2$ were obtained from the vapour diffusion of Et_2O into a concentration MeCN solution of the complex. In the former case, the Cu-N_{amine} bond length was found to be 1.997 (3) Å, while the average Cu-N_{py} bond length was 2.067(3) Å. The average N_{amine}-Cu-N_{py} was found to be 81.60° and the average N_{py}-Cu-N_{py} bond angles were 117.90° (**Table 2.4**). Similar bond lengths and bond angles were observed in $[Cu(^{tpy3}TPA)(MeCN)][ClO_4]_2$. Once again, these results are comparable to previously reported copper(II) complexes supported by TPA.[3] As compared to the rest of the metal complexes, all of the copper(II) complexes were the shortest due the smallest ionic radii that Cu^{2+} possessed.

2.2.3.5 Cyclic Voltammetry (CV) Studies

The cyclic voltammograms of the metal complexes detailed in this chapter were measured in acetonitrile solution, at room temperature, using tetrabutylammomium hexafluorophosphate as an electrolyte. All potentials are referenced against the ferrocenium/ferrocene (Fc^+/Fc) redox couple. As confirmed by ^{19}F NMR spectroscopy, in MeCN solution all complexes exist as

solvates of general formula $[M^{II}(^{Ar3}TPA)(NCMe)_n]^{2+}$ (n = 1 or 2). Despite our best efforts, we were unable to measure the potential of Mn^{III}/Mn^{II} redox couple supported by our ligands. This is presumably due to the very high potential of this couple in MeCN solution. For reference, this redox couple for the parent complex $[Mn^{II}(TPA)(NCMe)_2]^{2+}$ was reported, by Arnold and his co-workers, to be at 1.79 V.[3]

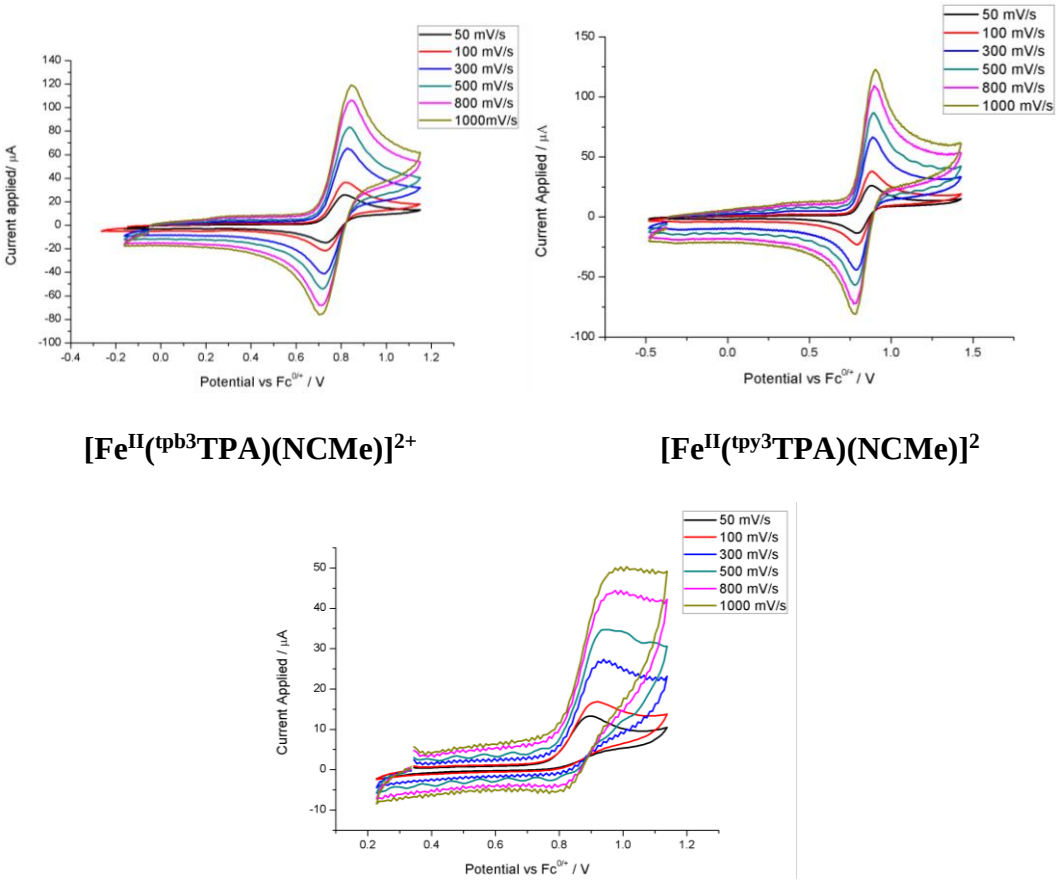

$[Fe^{II}(^{tpb3}TPA)(NCMe)]^{2+}$ **$[Fe^{II}(^{tpy3}TPA)(NCMe)]^{2}$**

$[Fe^{II}(^{dtbt3}TPA)(NCMe)]^{2}$

Figure 2.19: Cyclic Voltammograms of $[Fe^{II}(^{tpb3}TPA)(NCMe)]^{2+}$ (a), $[Fe^{II}(^{tpy3}TPA)(NCMe)]^{2+}$ (b) and $[Fe^{II}(^{dtbt3}TPA)(NCMe)]^{2+}$ (c) at various scan rates.

Table 2.5: A comparison of $E_{1/2}$ values for the Fe^{III}/Fe^{II} redox couple of $[Fe^{II}(^{Ar3}TPA)(NCMe)_n]^{2+}$ and selected reported complexes.

Complex	$E_{1/2}$ / V	Reference
$[Fe^{II}(^{tpb3}TPA)(NCMe)]^{2+}$	+0.77	This work
$[Fe^{II}(^{tpy3}TPA)(NCMe)]^{2+}$	+0.84	This work
$[Fe^{II}(^{dtbt3}TPA)(NCMe)]^{2+}$	+0.91[a]	This work
$[Fe^{II}(TPA)(MeCN)_2]^{2+}$	+0.75	4
$[Fe^{II}(^{Ph}TPA)(MeCN)_2]^{2+}$[b]	+1.24	15
$[Fe^{II}(^{Me3}TPA)(MeCN)_n]$[b]	+0.94[a]	4

a. Only E_{ox} potential is reported

b. Substitution on the 6th position of the pyridyl ring.

When performed under air-free conditions, the cyclic voltammograms of $[Fe^{II}(^{tpb3}TPA)(NCMe)]^{2+}$ and $[Fe^{II}(^{tpy3}TPA)(NCMe)]^{2+}$ contained reversible one electron Fe^{III}/Fe^{II} redox couples at $E_{1/2}$ values of +0.77 and +0.84 V, respectively (**Figure 2.19** and **Table 2.5**). These values are very similar to that of the parent complex, $[Fe^{II}(TPA)(NCMe)_2]^{2+}$, which further reinforces our assertion that the aryl substituents of the 5-ArTPA ligands have a minimal impact upon the donor strength of their constituent pyridine rings.[3] On the other hand, the CV trace of $[[Fe^{II}(^{dtbt3}TPA)(NCMe)]^{2+}$displayed an irreversible oxidation wave at +0.91 V, which is very similar to that of the high-spin complex $Fe(^{Me3}TPA)(NCMe)_2]^{2+}$ (+0.94 V) reported by Que and co-workers.[4] We postulate that the irreversibility of this redox process derives from conversion of a high-spin iron(II) complex to its low-spin iron(III) congener. Such large spin-state changes have been shown, in some cases, to engender electrochemical irreversibility.[4]

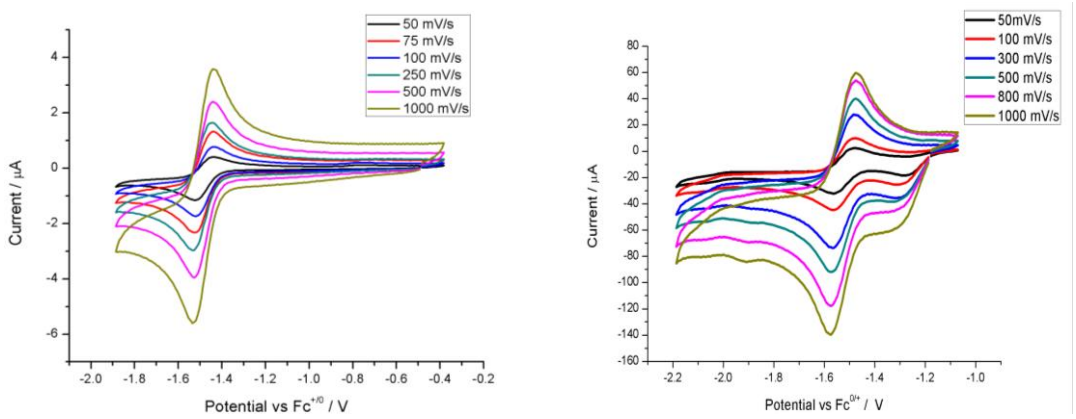

$[Co^{II}(^{tpb3}TPA)(NCMe)]^{2+}$ **$[Co^{II}(^{tpy3}TPA)(NCMe)]^{2+}$**

Figure 2.20: Cyclic voltammograms of $[Co^{II}(^{tpb3}TPA)(NCMe)]^{2+}$ (a) and $[Co^{II}(^{tpy3}TPA)(NCMe)]^{2+}$ (b) at various scan rates.

Table 2.6: A comparison of $E_{1/2}$ values for the Co^{II}/Co^{I} redox couples of $[Co^{II}(^{Ar3}TPA)(NCMe)]^{2+}$ and selected complexes.

Complex	$E_{1/2}$ / V	Reference
$[Co^{II}(^{tpb3}TPA)(NCMe)]^{2+}$	-1.50	This work
$[Co^{II}(^{tpy3}TPA)(NCMe)]^{2+}$	-1.53	This work
$[Co^{II}(TPA)(MeCN)]^{2+}$	-1.54	3
$[Co^{II}(^{Ph2}TPA)(MeCN)]^{2+a}$	-1.01	15

a. Substitution on the 6th position of the pyridyl ring.

Consistent with observations for the parent complex $[Co^{II}(TPA)(MeCN)]^{2+}$, the cyclic voltammograms of $[Co^{II}(^{tpb3}TPA)(NCMe)]^{2+}$ and $[Co^{II}(^{tpy3}TPA)(NCMe)]^{2+}$ both displayed only a single one electron redox process at -1.50 and -1.53 V, respectively, which is assigned to the Co^{II}/Co^{I} redox couple (**Figure 2.20** and **Table 2.6**). These $E_{1/2}$ values are very similar to that measured for $[Co^{II}(TPA)(MeCN)]^{2+}$(-1.54 V), which reinforces the notion that the bulky aryl substituents do not significantly weaken the donor strength of the pyridine rings. Features associated with the oxidative Co^{III}/Co^{II} couple could not be located. This contrasts with introduction of aryl substituents in the 6-position, which greatly weaken the donor strength of

the pyridine rings and destabilize higher oxidation states, thereby, leading to large shifts to more positive redox potentials. This is exemplified by $[Co^{II}(^{Ph2}TPA)(MeCN)]^{2+}$, for which the $E_{1/2}$ of the Co^{II}/Co^{I} redox couple appears at -1.01 V (i.e., 500 mV higher than for TPA). Significantly, in the case of $[Co^{II}(^{tpb3}TPA)(NCMe)]^{2+}$ and $[Co^{II}(^{tpy3}TPA)(NCMe)]^{2+}$, the Co^{II}/Co^{I} redox couple was reversible at all scan rates. This differs from $[Co^{II}(^{t}TPA)(NCMe)]^{2+}$ for which this couple showed irreversibility at low scan rates, which associated with disproportionation of the Co^{I} complex to the corresponding Co^{II} complex and Co^{0} metal. The latter is deposited on the electrode and upon oxidation shows a feature typical of stripping. The absence of such disproportionation in the ^{Ar3}TPA complexes can be attributed to the steric bulk of the aryl groups, which will inhibit intermolecular interaction of the cobalt centres. It is should be noted that there is an additional reduction wave in the CV trace of $[Co^{II}(^{tpy3}TPA)(NCMe)]^{2+}$ at -1.2 V, which is more prominent at low scan rates. The identity of this feature is currently unknown.

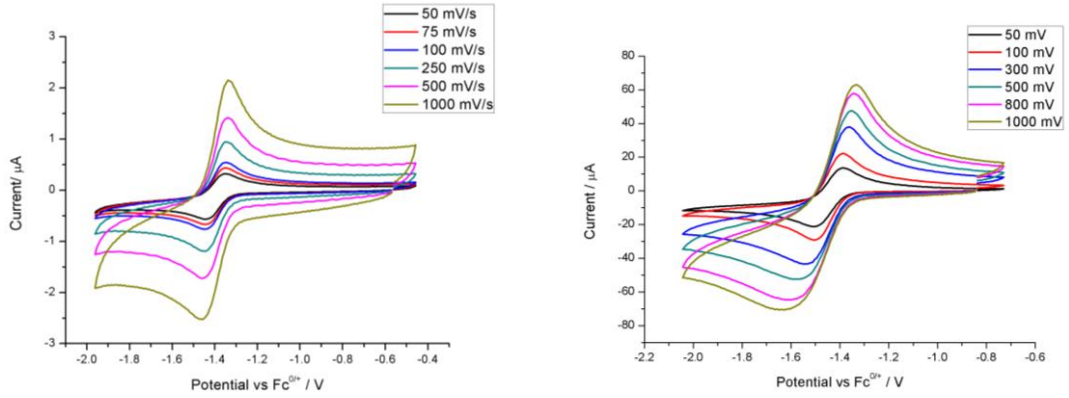

$[Ni^{II}(^{tpb3}TPA)(NCMe)]^{2+}$ **$[Ni^{II}(^{tpy3}TPA)(NCMe)]^{2+}$**

Figure 2.21: Cyclic voltammograms of $[Ni^{II}(^{tpb3}TPA)(NCMe)]^{2+}$ (a) and $[Ni^{II}(^{tpy3}TPA)(NCMe)]^{2+}$ (b) at various scan rates.

Table 2.7: A comparison of $E_{1/2}$ values for the Ni^{II}/Ni^{I} redox couples of $[Ni^{II}(^{Ar3}TPA)(NCMe)]^{2+}$ and selected complexes.

Complex	$E_{1/2}$ / V	Reference
$[Ni^{II}(^{tpb3}TPA)(MeCN)]^{2+}$	-1.40	This work
$[Ni^{II}(^{tpy3}TPA)(MeCN)]^{2+}$	-1.45	This work
$[Ni^{II}(TPA)(MeCN)_2]^{2+}$	-1.48	3
$[Ni^{II}(^{Ph2}TPA)(MeCN)_2]^{2+a}$	-0.89	15

a. Substitution on the 6th position of the pyridyl ring.

Analogous to their cobalt congeners, the CV data for complexes $[Ni^{II}(^{tpb3}TPA)(NCMe)]^{2+}$and $[Ni^{II}(^{tpy3}TPA)(NCMe)]^{2+}$ displays only a reductive electrochemical process (**Figure 2.21** and **Table 2.7**), associated with the Ni^{II}/Ni^{I} redox, in this case at -1.40 and -1.45 V, respectively. This behaviour and the redox potential of the couple is very similar to that seen for $[Ni^{II}(TPA)(NCMe)_2]^{2+}$ (-1.48 V) but much more negative than that of $[Ni^{II}(^{Ph2}TPA)(NCMe)_2]^{2+}$ (-0.89 V) which further reinforces the belief that the bulky aryl substituents are not significantly influencing the donor strength of the 5-arylpyridines.

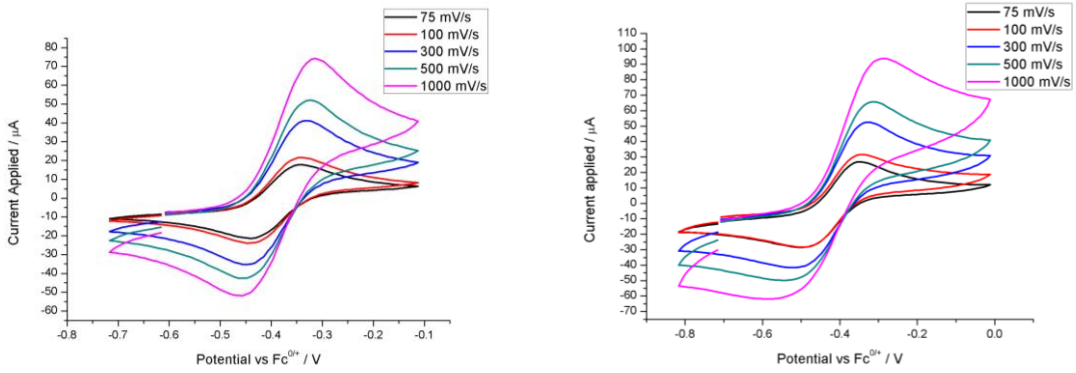

$[Cu^{II}(^{tpb3}TPA)(NCMe)]^{2+}$ **$[Cu^{II}(^{tpy3}TPA)(NCMe)]^{2+}$**

Figure 2.22: Cyclic voltammograms of $[Cu^{II}(^{tpb3}TPA)(NCMe)]^{2+}$ (a) and $[Cu^{II}(^{tpy3}TPA)(NCMe)]^{2+}$ (b) at various scan rates.

Table 2.8: A comparison of $E_{1/2}$ values for the Cu^{II}/Cu^{I} redox couples of $[Cu^{II}(^{Ar3}TPA)(NCMe)]^{2+}$ and selected complexes.

Complex	$E_{1/2}$ / V	Reference
$[Cu^{II}(^{tpb3}TPA)(NCMe)]^{2+}$	-0.40	This work
$[Cu^{II}(^{tpy3}TPA)(NCMe)]^{2+}$	-0.46	This work
$[Cu^{II}(TPA)(NCMe)]^{2+}$	-0.40	[7]
$[Cu^{II}(^{Ph3}TPA)(NCMe)]^{2+a}$	-0.10	[7]
$[Cu^{II}(^{Me3}TPA)(NCMe)]^{2+a}$	+0.070	[6]

a. Substitution on the 6th position of the pyridyl ring.

As with the corresponding cobalt and nickel complexes, the complexes $[[Cu^{II}(^{tpb3}TPA)(NCMe)]^{2+}$ and $[Cu^{II}(^{tpb3}TPA)(NCMe)]^{2+}$ show reversible Cu^{II}/Cu^{I} redox couples with $E_{1/2}$ values of -0.40 and -0.46 V, respectively, which are very similar to that of $[Cu^{II}(TPA)(NCMe)]^{2+}$ (**Figure 2.22** and **Table 2.8**). As with their Co and Ni analogues, the presence of substituents on the 6th position of the pyridine rings causes significant positive shifts of the redox couples due to a reduction of the electron donating ability of the ligand.

From all of the above electrochemical data, we can conclude that the inclusion of substituents at the 5th position of the TPA does not weaken the donor strength of the pyridine rings, which would manifest as shifts of their redox couples to more positive potentials. This contrasts with incorporation of substituents at the 6th position, where there was a reduction of the donor ability of the ligand is observed due to steric hindrance of coordination. As such, we would expect the redox reactivity of complexes of the 5-Ar3TPA ligands to be similar to those of the parent TPA ligand.

2.3 Conclusion

TPA ligand bearing bulky substituent at the 5th position, as well as it's respective metal(II) complexes was synthesized. The metal(II) complexes bearing bulky aryl group could potentially exhibit trigonal bipyramidal geometry in solution state due to the presence of two triflate anion signals in ^{19}F NMR studies using CD_2Cl_2. In addition, the used of weak field co-ligand would enable high-spin metal(II) complexes to be obtained. Strong field co-ligand and the used of small aryl group on the ligand would cause the formation of low-spin metal(II) complex. This was largely confirmed by X-ray crystallographic experiments. The electrochemicals studies suggested that the introduction of bulky substituents in this position would not weaken the ligand field of the complex, thus, intermolecular reaction would not be inhibited. As such, we could explore the reactivity of the copper and iron complexes using this ligand, which will further be discussed in Chapters 4 and 5, respectively. As ^{dtbt3}TPA ligand was not extensively explored, further complexation would be needed to expand the chemistry. Furthermore, some of the atom connectivity of the complexes, especially Ni^{2+} complex, was not observed, further X-ray crystallographic studies would be needed. In addition, since $[Fe^{II}(^{dtbt3}TPA)(NCMe)_n]^{2+}$ showed a different reactivity as the rest of the $[Fe^{II}(^{Ar3}TPA)(NCMe)_n]^{2+}$, ^{dtbt3}TPA ligand should coordinated to form $[Cu^{II}(^{Ar3}TPA)(NCMe)_n]^{2+}$ so to understand ligand field exerted on the complex.

2.4 Reference

(1) Anderegg, G.; Wenk, F. *Helv. Chim. Acta.* **1967**, *50*, 2330–2332.

(2) Blackman, A. G. *Eur. J. Inorg. Chem. 2008*, 2633–2647.

(3) Ward, A. L.; Elbaz, L.; Kerr, J. B.; Arnold, J. *Inorg. Chem.* **2012**, *51*, 4694–4706.

(4) Zang, Y.; Kim, J.; Dong, Y.; Wilkinson, E. C.; Appelman, E. H.; Que, L. *J. Am. Chem. Soc.* **1997**, *119*, 4197–4205.

(5) Jensen, M. P.; Lange, S. J.; Mehn, M. P.; Que, E. L.; Que, L. *J. Am. Chem. Soc.* **2003**, *125*, 2113–2128.

(6) Hayashi, H.; Uozumi, K.; Fujinami, S.; Nagatomo, S.; Shiren, K.; Furutachi, H.; Suzuki, M.; Uehara, A.; Kitagawa, T. *Chem. Lett.* **2002**, *31*, 416–417.

(7) Chuang, C.; Lim, K.; Chen, Q.; Zubieta, J.; Canary, J. W. *Inorg. Chem.* **1995**, *34*, 2562–2568.

(8) Howell, J. M.; Feng, K.; Clark, J. R.; Trzepkowski, L. J.; White, M. C. *J. Am. Chem. Soc.* **2015**, *137*, 14590–14593.

(9) Osberger, T. J.; Rogness, D. C.; Kohrt, J. T.; Stepan, A. F.; White, M. C. *Nature* **2016**, *537*, 214.

(10) Nanjo, T.; de Lucca, E. C.; White, M. C. *J. Am. Chem. Soc.* **2017**, *139*, 14586–14591.

(11) Borrell, M.; Costas, M. *J. Am. Chem. Soc.* **2017**, *139*, 12821–12829.

(12) Mikata, Y.; Nodomi, Y.; Ohnishi, R.; Kizu, A.; Konno, H. *Dalt. Trans.* **2015**, *44*, 8021–8030.

(13) Diebold, A.; Hagen, K. S. *Inorg. Chem.* **1998**, *37*, 215–223.

(14) Yang, L.; Powell, D. R.; Houser, R. P. *Dalt. Trans.* **2007**, No. 9, 955–964.

(15) Makowska-Grzyska, M. M.; Szajna, E.; Shipley, C.; Arif, A. M.; Mitchell, M. H.; Halfen, J. A.; Berreau, L. M. *Inorg. Chem.* **2003**, *42*, 7472–7488.

Chapter 3

Metal Complexes of BPA Ligands

3.1 Introduction

Bis(2-pyridylmethyl)amine (BPA, **Figure 3.1**) is a tridentate analogue of TPA that was first reported in 1968 by Bunds and co-workers.[1] The central amine is usually alkylated, to give RBPA (most commonly, R = Me and Bn), and the ligand is able to coordinate to transition metals in either a facial (*fac*) or meridional (*mer*) manner. There are multiple factors that can influence binding mode of the ligand (*mer* versus *fac*), with overall geometry of the complex, nature of the co-ligands, and identity of the R group on the tertiary amine centre being amongst them.[2] In fact, the highly flexible nature of the ligand often allows both binding modes to be accessible.

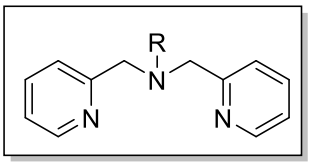

R =H, Me, *t*Bu, Bn

Figure 3.1: Structures of common variants of BPA, referred to herein as RBPA.

Out of all the available *N*-alkyl substituents, the methyl group (MeBPA) has been investigated the longest. Rodgers and co-workers reported the first iron(II) and nickel(II) complexes supported by MeBPA ligand in 1968.[3] From a combination of magnetochemical and UV-Vis spectroscopic measurements, both complexes were proposed to be bischelate compounds. These conclusion were later confirmed by X-ray crystallography, with the MeBPA ligand binding in a *cis-fac* manner in both $[Ni^{II}(MeBPA)_2]^{2+}$ and $[Fe^{II}(MeBPA)_2]^{2+}$ (**Figure 3.2**).[2,4]

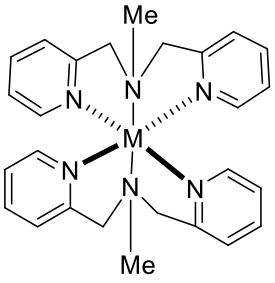

M: Fe, Ni

Figure 3.2: *Cis-fac* coordination in $[M^{II}(MeBPA)_2]^{2+}$ (M = Fe and Ni).

In addition, the used of benzyl group was still not bulky enough to inhibit the formation of bis-chelate complex, as evident in $[Ni(BnBPA)_2]^{2+}$ (**Figure 3.3**).[5] Thus, the use of sterically bulky *t*Bu group was investigated to prevent formation of bischelate complex and mononuclear $[Ni(tBuBPA)s_3]^{2+}$ complex was formed (**Figure 3.3**). However, it was bound in a 'fac' fashion rather than the 'mer' fashion. This might imply that by changing the alkyl R group of the BPA ligand, bischelate metal(II) complexes could still have the potential to be formed. Bischelate formation has been observed for many other transition metals and, also, for other RBPA ligands, including BnBPA.[2,4,5] In many senses, the tendency of BPA ligands to form bischelate complexes have limited their utility and, as such, they are much less studied that the closely related tetradentate TPA ligands (Chapter 2).

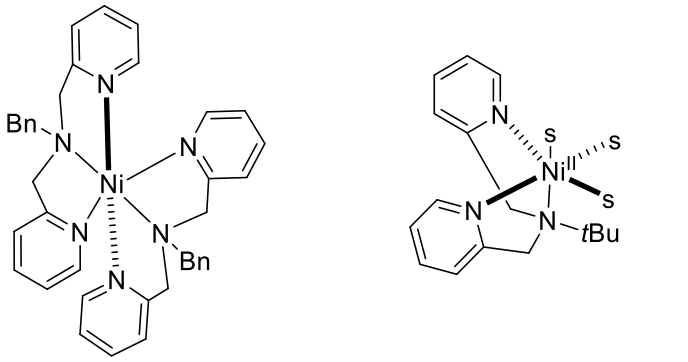

$[Ni(BnBPA)_2]^{2+}$ $[Ni(tBuBPA)s_3]^{2+}$

Figure 3.3: Reported structure of $[Ni(BnBPA)_2]^{2+}$ and $[Ni(tBuBPA)s_3]^{2+}$ complexes

To inhibit the formation of bischelate metal(II) complexes, the incorporation of substituents on the 6th position of the pyridyl was performed by various groups. This would reduce the electron donor ability of the ligand due to steric clashes of the substituent and the metal centre as seen from the TPA analog.[6] In addition, it could provide steric hindrance to prevent bischelation, thus, the incorporation of phenyl group was performed on the BnBPA ligand. This was seen in $[Ni(^{Ph2}BnBPA)(OH)_2(NCMe)]^{2+}$ complex where a square pyramidal geometry with ligand bound in the 'mer' fashion was observed (**Figure 3.4a**).[7,8] However, the phenyl group was able

to be oxidized by oxidant to form phenoxonickel complex (**Figure 3.4b).** Similar chemistry was also observed in the copper complex bearing the same ligand (**Figure 3.4**).

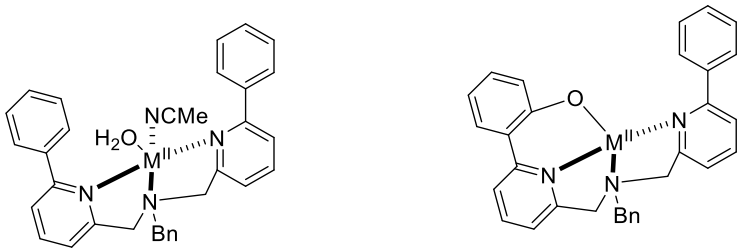

Figure 3.4: Structure of [Ni(^{Ph2}BnBPA)H_2O(MeCN)] complexes (**a**) and its oxidized form after exposing to oxidant(**b**).

Despite the limited application on most first row transition metals, copper in the +1 and +2 oxidation states readily forms complexes displaying coordination numbers of less than 6 and, as such, there are many examples of it forming monochelate complexes with RBPA ligands. Mukherjee and co-workers, reported the formation square pyramidal geometry of [Cu^{II}(MeBPA)Cl_2] complex (**Figure 3.5a**).[9] However, *pseudo*-dimeric complex was also observed with the ligand bound in a 'mer' fashion if one of the chloride ions was replaced with a weakly coordinating anion (**Figure 3.5b**). Fortunately, Poli and co-workers reported that the used of weakly coordinating anions, triflate anions, would form *pseudo*-octahedral [Cu^{II}(MeBPA)$(OTf)_2$(NCMe)] complex with one of the triflate anions weakly coordinated due to Jahn-Teller distortion (**Figure 3.5c**).[10] On the other hand, the solid state structure of [Cu^{I}(MeBPA)]$^+$ was not obtained which might be due to disproportionation and bubbling of dioxygen does not form any Cu-dioxygen adducts.[9] Thus, it was rarely used in dioxygen chemistry.

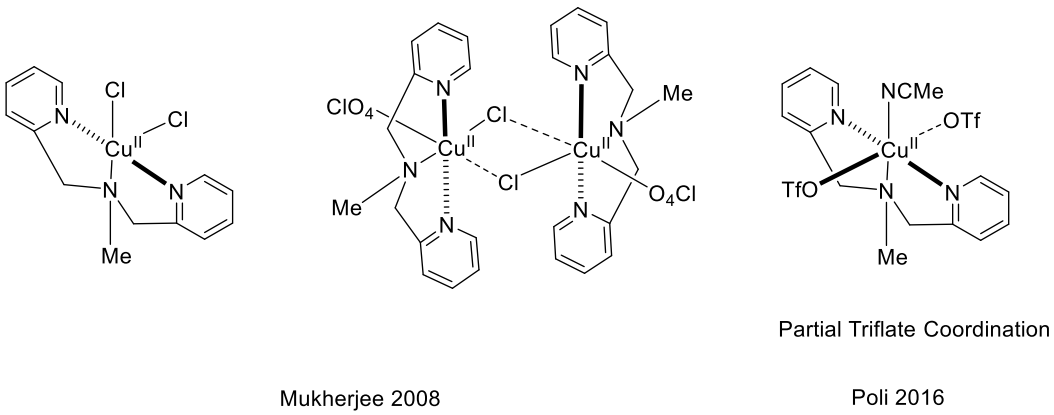

Figure 3.5: Known structure of $[Cu^{II}(MeBPA)Cl_2]$(**a**), *pseudo*-dimeric copper(II) complex(**b**) and $[Cu^{II}(MeBPA)(OTf)_2(NCMe)]$(**c**).

On the other hand, BnBPA ligand was more commonly used in copper chemistry. Tetrahedral $[Cu^{I}(BnBPA)(CO)](PF_6)$ and monomeric square pyramidal $[Cu^{II}(BnBPA)(NCMe)_2](ClO_4)_2$ was first studied by Itoh and co-worker (**Figure 3.6**)[7,11,12]. It was noted that the presence of CO is important for the copper(I) complex as it tends to disproportionate easily.

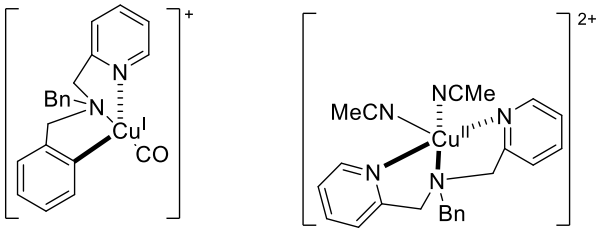

Figure 3.6: Reported structure of $[Cu^{I}(BnBPA)(CO)](PF_6)$ and $[Cu^{II}(BnBPA)(NCMe)_2](ClO_4)_2$

However, it was until recently, Karlin and co-workers reported that the bubbling of dioxygen into the solution of $[Cu^{I}(BnBPA)(CO)]^{+}$ would cause dimerization which results in bis(*u*-oxo)dicopper(III) complex, through a postulate superoxocopper(II) intermediate (**Figure 3.7**).[13] Thus, to prevent the dimerization process, the inclusion of substituent (phenyl and methyl group) on the 6th position of the pyridyl ring was conducted, since it could stabilize low-valent metal complex as well as steric hindrance (**Figure 3.8**).[12]

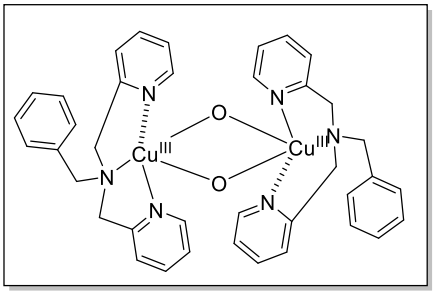

Figure 3.7: Structure of bis(*u*-oxo)dicopper(III) complex supported by BnBPA ligand.

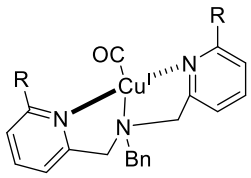

R: Me. Ph

Figure 3.8: Structure of $[Cu^{I}(^{R2}BnBPA)(CO)](PF_6)$ complex.

It was found that on $[Cu^{I}(^{Me2}BnBPA)(CO)](PF_6)$ ($E_{1/2}$ = 0.15 V vs $Ag/AgNO_3$) and on $[Cu^{I}(^{Ph2}BnBPA)(CO)](PF_6)$ ($E_{1/2}$ = 0.24 V vs $Ag/AgNO_3$) would weaken the ligand of the result copper(I) complex, comparing to $[Cu^{I}(BnBPA)(CO)]^{+}$ ($E_{1/2}$ = -0.15 V vs $Ag/AgNO_3$), suggesting a stabilization of +1 oxidation state.[12] Furthermore, the phenyl group on $[Cu^{I}(^{Ph2}BnBPA)(CO)](PF_6)$ could provide steric hindrance towards the metal center, as evident from the lengthening of Cu-N_{py} bond in the X-ray crystal structure.[12] However, no oxygenation reaction was observed for $[Cu^{I}(^{Ph2}BnBPA)(CO)](PF_6)$, suggesting that the copper center could either be block by the phenyl group or copper(I) complex are more stable due to high reduction potential. Furthermore, similar chemistry was also observed in the monomeric square pyramidal $[Cu(^{Ph2}BnBPA)(OH)_2(NCMe)]^{2+}$, as the nickel(II) analog(**Figure 3.4**) when react with hydrogen peroxide and triethylamine as the base. Thus, it suggested that the ligand was no longer oxidatively robust. Thus, it was not ideal to include substituent on the 6th position of the pyridyl donor despite the ability to inhibit the formation of bischelate metal complex.

As an extension of our TPA work, detailed in Chapter 2, we decided to install bulky 2,4,6-triphenylbenzene (tpb) substituents on the 5th position of the pyridyl donors of the MeBPA and

BnBPA ligand frameworks (**Figure 3.9**), with the aim to prevent the formation of bischelate and bimetallic metal complexes. In addition, it could serve as a comparison with the tetradentate analog. We chose to focus primarily upon the chemistry of ^{tpb2}MeBPA, as benzyl substituents are less oxidatively robust than methyl and could, therefore, limit utility of the ^{tpb2}BnBPA ligand. It was anticipated that the tpb substituents would inhibit the formation of bischelate and bimetallic complexes, and that their steric bulk would be sufficiently remote from the metal centre to have a minimal impact upon donor donor strength of the ligands.

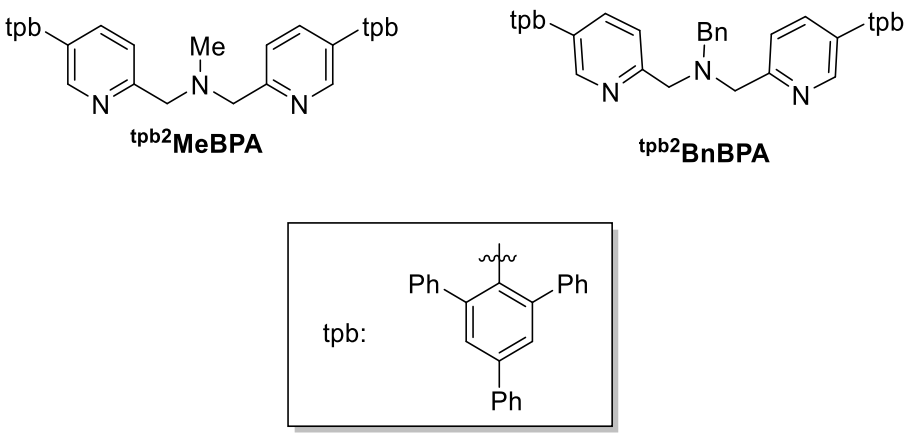

Figure 3.9: Structures of the 5^{tpb2}MeBPA and 5^{tpb2}BnBPA synthesized in this work

3.2 Results and Discussion

3.2.1 Ligand Synthesis

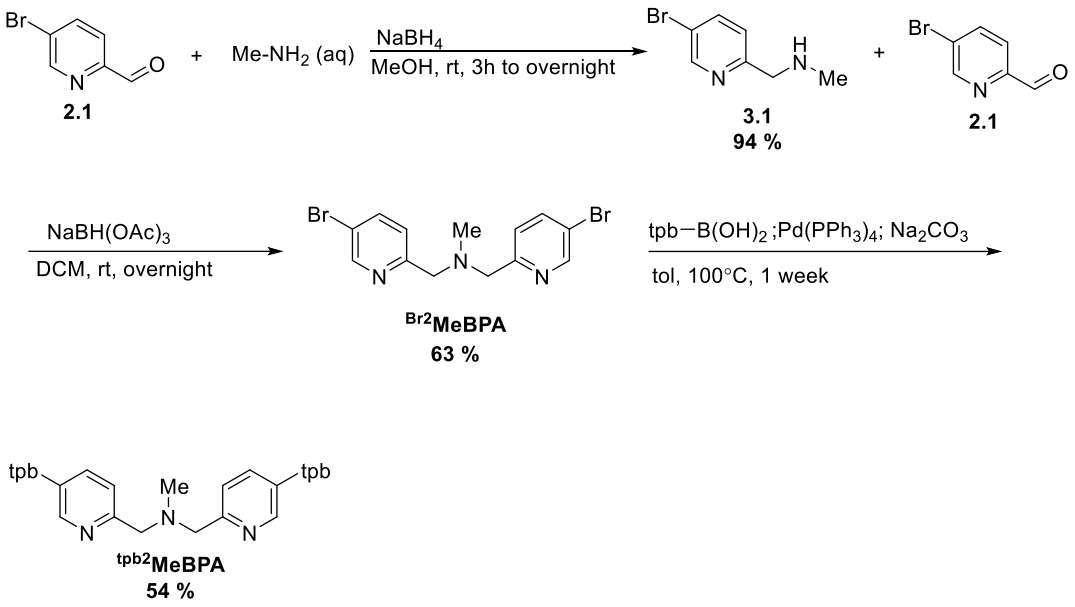

Scheme 3.1: Synthetic route used for preparation of ^{tpb2}MeBPA.

The approach we used to synthesise the ^{Ar2}RBPA ligands mirrored the late-state arylation procedure successfully used for synthesis of the ^{Ar3}TPA ligands. As such, our initial targets were ^{Br2}MeBPA and ^{Br2}BnBPA.

The synthetic pathway to the former involved initial reductive amination of methylamine with 5-bromo-2-pyridinecarboxaldehyde (**2.1**) using sodium borohydride as a reducing agent. This provided compound **3.1**, which was subjected to a second reductive amination with **2.1** but using sodium triacetoxyborohydride as a reductant (**Scheme 3.1**). To maximize the yield of product, an excess of **2.1** was required. A single reductive amination of methylamine and **2.1** for the formation of ^{Br2}MeBPA was not achieved. As a consequence, the reaction as accompanied by formation of the by-product 5-bromo-2-hydroxymethylpyridine (**2.8**). Removal of **2.8** was most conveniently achieved by treatment with potassium hydride, which yields compound **3.2**, and extraction of product ^{Br2}MeBPA and washing using hot hexanes (**Scheme 3.2**).

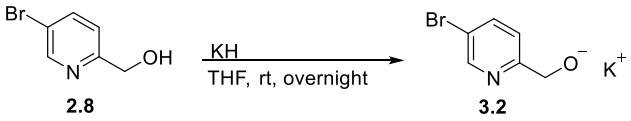

2.8 3.2

Scheme 3.2: Deprotonation of 5-bromo2-hydroxymethylpyridine using KH.

The target ligand ^{tpb2}MeBPA was then obtained by Suzuki cross-coupling of ^{Br2}MeBPA with 2,4,6-triphenylbenzene boronic acid, tpb-B(OH)$_2$, using Pd(PPh$_3$)$_4$ as a catalyst. The overall yield of ligand, across the three steps of the synthesis, was 32 %. This disappointing yield can be attributed to difficulties in purification, rather than incomplete reaction, in the second and third steps. The high solubility of the final product and its tendency to "drag" during column chromatography proved very problematic.

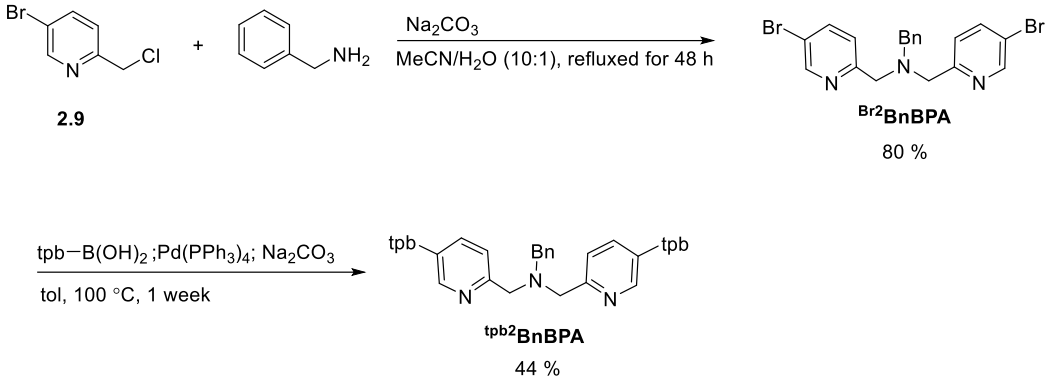

2.9

^{Br2}BnBPA

80 %

^{tpb2}BnBPA

44 %

Scheme 3.3: Synthetic route used for preparation of ^{tpb2}BnBPA.

An alternative two-step synthetic route (**Scheme 3.3**) was used in preparation of ^{Br2}BnBPA, which was not successful for ^{Br2}MeBPA, due to the low boiling point of the methylamin. It involved an S_N2 alkylation of benzylamine using 5-bromo-2-(chloromethyl)pyridine (**2.9**), with sodium carbonate as a base. The target product was obtained by Suzuki cross-coupling of ^{Br2}BnBPA with TPB-B(OH)$_2$, using Pd(PPh$_3$)$_4$ as a catalyst. The poor overall yield of 35 % yield of ^{tpb2}BnBPA does not reflect an unsuccessful cross-coupling reaction and can, instead, be attributed to the same difficulties that were experienced in purification of ^{tpb2}MeBPA.

3.2.2 Complexation

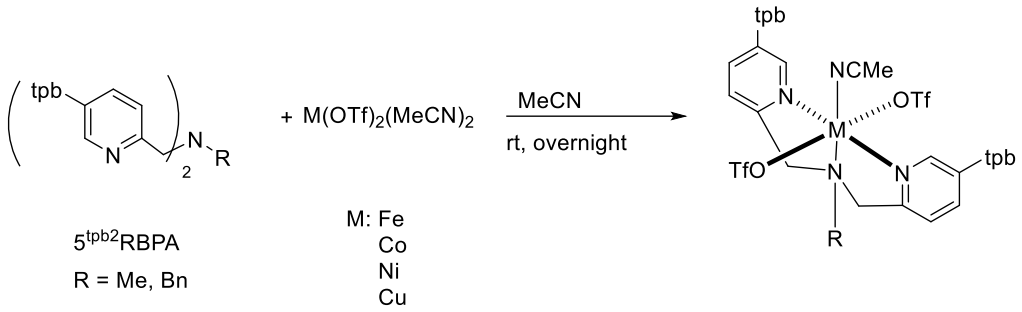

Scheme 3.4: Complexation of ^{tpb2}MeBPA and ^{tpb2}BnBPA with $M^{II}(OTf)_2(MeCN)_2$.

The ^{tpb2}MeBPA and ^{tpb2}BnBPA ligands were first reacted with metal(II) triflate salts (**Scheme 3.4**) to give the target complexes in yields of about 70 %, after recrystallization. Single crystals of complexes suitable for X-ray crystallography were grown by vapour diffusion of Et_2O in concentrated MeCN or DCM solutions of complex. The crystals were of the following colours: iron, yellow; cobalt, pink; Ni and Cu (for both ^{tpb2}MeBPA and ^{tpb2}BnBPA), blue. All of the complexes synthesized were characterized by combinations of electrospray ionization mass spectrometry (ESI-MS), elemental analysis (with the exception of $[Co^{II}(^{tpb2}MeBPA)(OTf)_2(NCMe)]$), solution state Evans' NMR and X-ray crystallography. It should be noted that no evidence for formation of bischelate complexes were obtained. As illustrated for $[Fe^{II}(^{tpb2}MeBPA)(OTf)_2(NCMe)]$ (**Figure 3.10**), only ion fragments associated with monochelate species were observed in their ESI mass spectra.

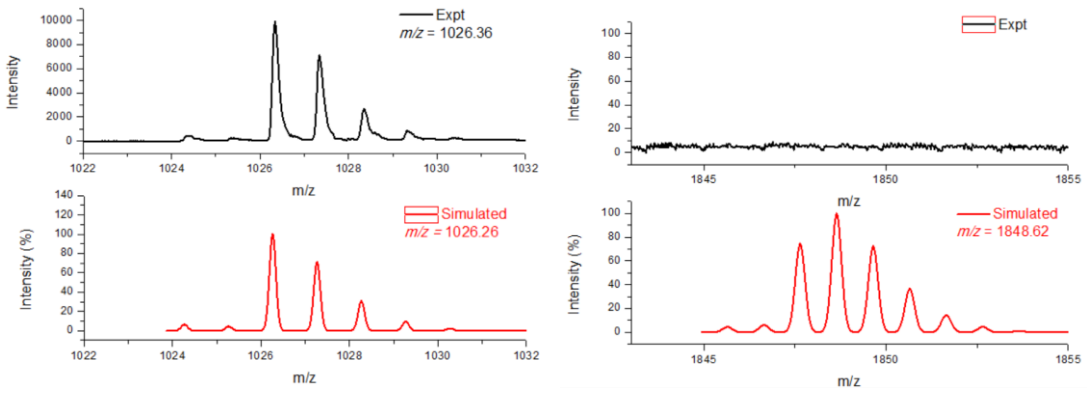

a **b**

Figure 3.10: Experimental mass spectrometry spectrum (black) and simulated mass spectrometry spectrum (red) of $[Fe^{II}(^{tpb2}MeBPA)(OTf)]^{+}$ (a) and hypothetical $[Fe^{II}(^{tpb2}MeBPA)_2]^{2+}.(OTf)$ (b).

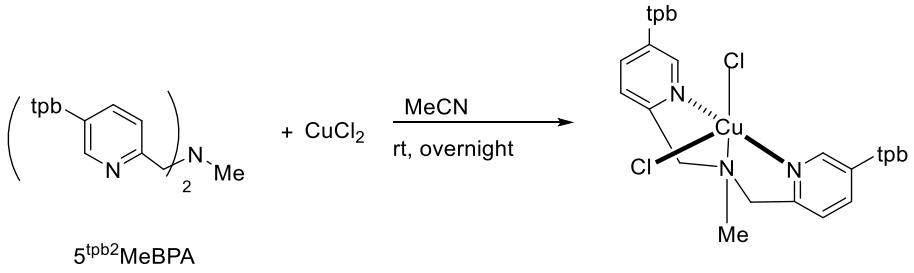

$5^{tpb2}MeBPA$

Scheme 3.5: Complexation of $^{tpb2}MeBPA$ by $CuCl_2$ in MeCN.

Although single crystals of $[Cu^{II}(5^{tpb2}MeBPA)(OTf)_2]$ could be grown, crystallographic analysis was complicated by disorder associated with a weakly coordinated triflate anion, which was observed due to Jahn-Teller distortions. To probe the geometric features of complexes of this particular tridentate ligand we also synthesized the complex $[Cu^{II}(^{tpb2}MeBPA)Cl_2]$ (**Figure 3.10**). It was obtained in 80 % yield and recrystallization of the complex was obtain via vapour diffusion of pentane into a concentrate dichloroethane solution of it. Blue crystals that were suitable for suitable for X-ray crystallography were yielded blue crystals. It was possible to verify the purity of $[M^{II}(^{tpb2}RBPA)(OTf)_2(NCMe)]$ using elemental analysis, with the exception of the two complexes $[Co^{II}(^{tpb2}MeBPA)(OTf)_2MeCN]$ and

$[Cu^{II}(5^{tpb2}MeBPA)Cl_2]$. The exact reason for this is unclear, but we suspect that severe Jahn-Teller distortion of these complexes render them particularly unstable.

3.2.3 Characterization of the Complexes

3.2.3.1 NMR Spectroscopy

Attempts were made to characterize the iron(II) and cobalt(II) complexes using ^{1}H NMR spectroscopy. However, severe broadening of resonances was observed in both coordinating and non-coordinating solvents, which rendered interpretation impossible. We attribute this broadening due to a high degree of coordinative flux resulting from the high lability of the co-ligands and the flexible coordination properties of the BPA ligand.

Our suspicion of a high degree of coordinative flux was seemingly confirmed by ^{19}F NMR spectroscopic measurements. For $[Fe^{II}(^{tpb2}MeBPA)(OTf)_2]$, only a single high broadened resonance at -47 is observed in CD_2Cl_2 solution (**Figure 3.11**). This observation is consistent with both triflates being coordinated to the metal centre, but the degree of peak broadening and their moderate paramagnetic shifts suggest a high degree of lability. Furthermore, the single high broadened resonance of -73 ppm was observed in CD_2Cl_2 solution for $[Co^{II}(^{tpb2}MeBPA)](OTf)_2$ (**Figure 3.11**), suggesting that both triflates are uncoordinated from the metal centre. However, this data does not provide information regarding the geometry of the complexes, as they could be either 5- or 6-coordinate and have two bound triflate ligands. On the other hand, uncoordinated triflate, at – 78 ppm, was observed for all iron and cobalt complexes when CD_3CN was used as a solvent. Thus, X-ray crystallographic studies would be needed for more analysis. It should be noted that unlike with the corresponding TPA complex, the ^{19}F NMR spectrum of $[Ni^{II}(^{tpb2}MeBPA)(OTf)_2]$ was featureless, presumably due severe line broadening associated with fluxionality.

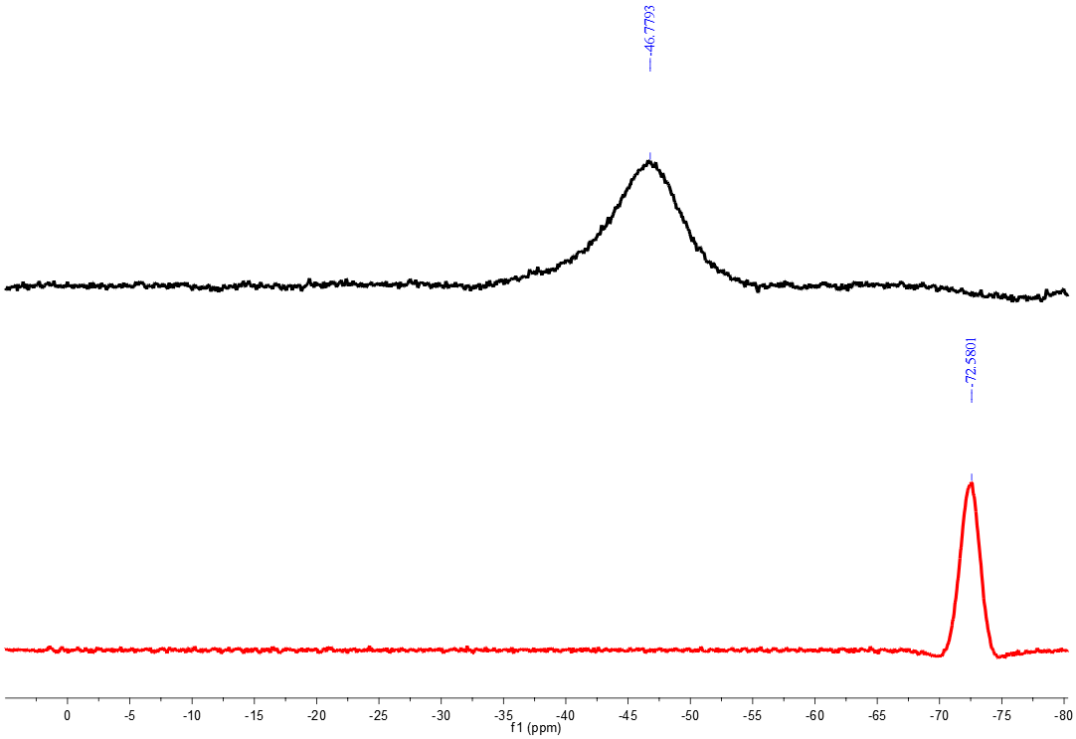

Figure 3.11: ^{19}F NMR spectra of [Fe^{II}(^{tpb2}MeBPA)(OTf)$_2$] (black) and [Co^{II}(^{tpb2}MeBPA)](OTf)$_2$ (red), recorded in CD_2Cl_2 solution at room temperature.

3.2.3.2 Solution State Evans' NMR

The solution-state effective magnetic moments, μ_{eff}, of [Fe(^{tpb2}MeBPA)(OTf)$_2$], [Co^{II}(^{tpb2}MeBPA)](OTf)$_2$ and [Ni^{II}(^{tpb2}MeBPA)(OTf)$_2$]were found to be 4.47, 4.23 and 2.52 μ_B, respectively, in non-coordinating CD_2Cl_2. The cobalt(II) complex clearly has an S = 3/2 spin state but, although the values for iron(II) and Ni(II) complexes are suggestive of high-spin (S = 2 and 1, respectively) ground states, they are on the low-side. This is suggestive of the presence of impurities or a high degree of instability. As for [Cu^{II}(^{tpb2}MeBPA)(OTf)$_2$(NCMe)] and [Cu^{II}(^{tpb2}BnBPA)(OTf)$_2$(NCMe)], respective solution-state μ_{eff} values of 1.66 and 1.71 μ_B were measured, which are consistent the expected S = 1/2 spin-state.

3.2.3.3 X-ray Crystallographic Studies

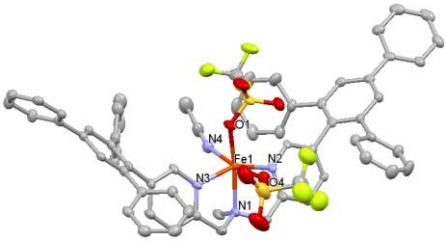

[Fe^{II}(^{tpb2}MeBPA)(OTf)2(NCMe)]

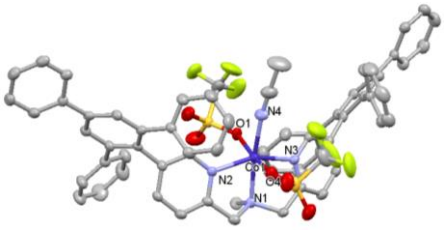

[Co^{II}(^{tpb2}MeBPA)(OTf)$_2$(NCMe)]

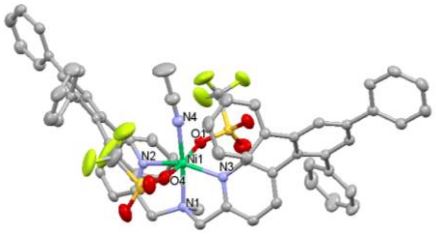

[Ni^{II}(^{tpb2}MeBPA)(OTf)$_2$(NCMe)]

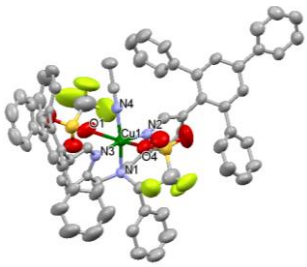

[Cu^{II}(^{tpb2}BnBPA)(OTf)$_2$(NCMe)]

Figure 3.12: Crystal Structures of metal(II) complexes bearing ^{Ar2}MeBPA or ^{Ar2}BnBPA ligands, depicted with thermal ellipsoids of 50 %. Atom colour scheme: carbon, gray; nitrogen, purple; oxygen, red; sulfur, yellow; fluorine, yellowish green; iron, orange; cobalt, dark purple; nickel, green; copper, dark green. All hydrogen atoms, solvent molecules and counteranions are omitted for clarity.

Table 3.1: Selected bond lengths (Å) and bond angles (°) for the metal complexes bearing ^{tpb2}MeBPA and ^{tpb2}BnBPA ligands

	[Fe^{II}(^{tpb2}MeBPA)$(OTf)_2$(NCMe)]	**[Co^{II}(^{tpb2}MeBPA)$(OTf)_2$(NCMe)]**	**[Ni^{II}(^{tpb2}MeBPA)$(OTf)_2$(NCMe)]**	**[Cu^{II}(^{tpb2}BnBPA)$(OTf)_2$(NCMe)]**
M-N1 (N_{amine})	2.224(6)	2.147(5)	2.0899(17)	2.027(4)
M-N2 (N_{py})	2.185(3)	2.126(5)	2.0998(17)	1.997(4)
M-N3 (N_{py})	2.155(3)	2.147(5)	2.0846(17)	1.972(4)
M-N4(N_{MeCN})	2.177(7)	2.082(5)	2.0522(19)	2.000(5)
M-O1	2.067(6)	2.148(4)	2.1282(15)	2.394(10)
M-O4	2.152(11)	2.167(4)	2.1571(15)	2.412(8)
N1-M-N2	75.6(2)	77.93(18)	80.04(7)	82.34(18)
N1-M-N3	76.2(2)	78.93(18)	80.40(7)	83.25(17)
N2-M-N3	151.6(2)	156.57(18)	160.32(7)	165.53(18)
N1-M-N4	151.6(2)	173.7(2)	174.91(7)	168.50(19)
N2-M-N4	89.5(3)	106.3(2)	97.22(7)	95.19(18)
N3-M-N4	92.3(3)	97.0(2)	102.45(7)	99.19(18)
N1-M-O1	170.1(3)	98.75(17)	97.34(6)	100.3(5)
N2-M-O1	113.6(3)	96.72(17)	83.53(6)	83.4(4)
N3-M-O1	94.7(2)	83.21(17)	96.94(6)	98.0(4)
N1-M-O4	87.2(5)	90.07(18)	90.74(7)	104.8(3)
N2-M-O4	87.0(5)	84.44(17)	97.85(7)	98.7(3)
N3-M-O4	94.4(4)	99.23(18)	84.45(6)	83.8(3)

The X-ray structures of $[M^{II}(^{tpb2}RBPA)(OTf)_2(NCMe)]$ (R = Me: Fe, Co and Ni; R = Bn: Cu) all exhibit an octahedral geometry, in which the tridentate BPA ligand coordinates in a meridional (*mer*) fashion and the coordination sphere is completed by three monodentate ligands, two triflates and one MeCN (**Figure 3.12** and **Table 3.1**). The triflate anions coordinate *trans* to one another, which leaves the MeCN ligand *trans* to the tertiary amine centre, in all cases except for the iron(II) complex. In the latter, 1 triflate ligand coordinates *trans* to the MeCN ligand, which leaves the other *trans* to the tertiary amine donor.

Consistent with the decrease in M^{2+} ionic radius upon moving across the period, the respective M-N_{amine} and average M-N_{py} bond distances sequentially decrease from 2.224(6) and 2.169(3) Å for Fe through to 2.027(4) and 1.984(4) Å for Cu. This resulted in a commensurate increase in average 5-membered chelate ring bite angle from 75.9° in the Fe complex through to 82.8° in the Cu complex. Trends in the M-OTf bond lengths are not so easy to rationalize. This is because the 2 triflate ligands are *cis* to one another in the Fe complex are *trans* to one another elsewhere, and the M-OTf bond distances in the copper(II) complex are highly elongated due to the Jahn-Teller effect. What is apparent is that the monodentate ligands *trans* to one another exhibit comparatively long bond lengths. The reason for this is not clear, but one possibility is that the triflate anions exert a strong *trans* influence. Alternatively, the steric bulk of the aryl substituents on the pyridine rings may exert a labilizing influence on these coordination sites, which they are orientated towards.

Comparison of our X-ray structures with published data is not straightforward due to the comparatively limited scope of BPA coordination chemistry. For instance, for cobalt 1 example, $[Co(BPA)(H_2O)_3]^{2+}$, was reported in 1977 without any discussion of its X-ray structure,[14] and the complex $[Co(^{Me2}BnBPA)Cl_2]$ possesses a trigonal bipyramidal geometry, so is not suitable for direct comparison with our 6-coordinate complex $[Co^{II}(^{tpb2}MeBPA)(OTf)_2(NCMe)]$ (**Figure 3.13**).[15]

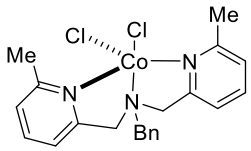

Figure 3.13: Structure of [Co(^{Me2}BnBPA)Cl_2]

[Ni^{II}(^{tpb2}MeBPA)$(OTf)_2$(NCMe)] has an average Ni-N bond length of 2.090 Å which was similar to [Ni^{II}(*t*BuBPA)$(OH_2)_3]^{2+}$ (with an average Ni-N bond length of 2.101 Å)[5], which could imply that the electron donating ability was not affected by the substituent. Installation of aryl substituents at the 6th position of the pyridine ring has a much more marked effect upon M-N bond distances. For instance, [Ni^{II}($^{Ph(NO2)2}$BnBPA)$(OH_2)(NCMe)_2]^{2+}$ by Itoh and co-workers (**Figure 3.14**) had average Ni-N bond length of 2.143 Å.[8] That is not to say the bulky aryl substituents in the ^{tpb2}RBPA ligands do not have structural implications. We suspect that it is likely that one of the main driving forces for their *mer* coordination is minimization of steric conflict between the bulky tpb groups. This should be contrasted with the complex [Ni^{II}(*t*BuBPA)$(OH_2)_3]^{2+}$, in which the BPA ligand coordinates in a facial (*fac*) fashion (**Figure 3.14**).

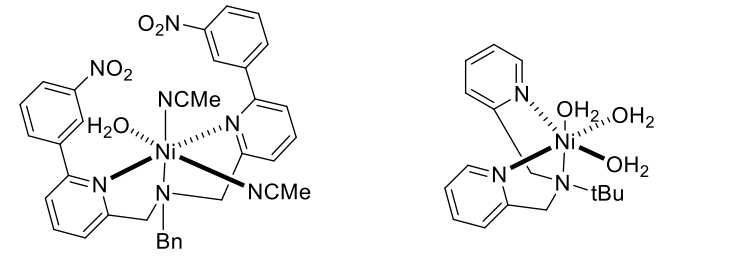

[Ni($^{Ph(NO2)2}$BnBPA)$(OH_2)(NCMe)_2$]
Itoh, 2009

[Ni(*t*BuBPA)$(OH_2)_3](ClO_4)_2$
Rybak-Akimova, 2010

Figure 3.14: Known nickel complex with BPA ligand

Plentiful examples of copper(II) complexes bearing BPA ligands have been reported. However, many of them exhibit a square pyramidal geometry. For example, [Cu^{II}(BnBPA)$(NCMe)_2](ClO_4)_2$ and [Cu^{II}(^{Ph2}BnBPA$(NCMe)_2)](ClO_4)_2$.[7,16] This difference in coordination geometry could be due to the use of coordinating triflate anions in our complex,

rather than the weakly coordinating perchlorate anions. Regardless of the difference in geometry, the average Cu-N bond lengths of 1.997 Å found in $[Cu^{II}(BnBPA)(NCMe)_2](ClO_4)_2$ display close similarity to those of $[Cu^{II}(^{tbp2}BnBPA)(OTf)_2(NCMe)]$ with a Cu-N bond length of 1.999 Å

In contrast, the average Cu-N_{py} bond lengths of 1.985 Å in $[Cu^{II}(^{tpb2}BnBPA)(OTf)_2(NCMe)]$ are shorter than those reported for the aforementioned 6th-substituted complex, $[Cu^{II}(^{6Ph2}BnBPA)(NCMe)_2](ClO_4)_2$, with an average Cu-$N_{py}$ bond length of 2.020 Å.[7] Taken together, these comparisons imply that placing bulky aryl substituents at the 5th position of the pyridine rings does not greatly weaken the ligand field of the ligand.

As previously mentioned, crystals of $[Cu^{II}(^{tpb2}MeBPA)(OTf)_2(NCMe)]$ were successfully grown but disorder associated with partial coordination of one of the triflate anions to the copper centre (**Figure 3.15**) led to suboptimal data. Thus, although atom connectivity could be discerned, the structure could not be solved. Such a problem was also reported for the parent complex $[Cu^{II}(MeBPA)(OTf)_2(NCMe)]$.[10]

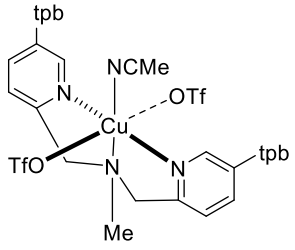

Figure 3.15: Structure of $[Cu(5^{tpb2}MeBPA)(OTf)_2MeCN]$ showing partial coordination of 1 triflate anion.

The X-ray structure of $[Cu^{II}(^{tpb2}MeBPA)Cl_2]$ exhibited a square pyramidal geometry, denoted by a τ value of 0, with the tridentate ligand binding in a *mer* fashion (**Figure 3.16**). The average Cu-N_{py} bond length was found to be 2.000 Å, while that of Cu-N_{amine} was found to be 2.038(4) Å. These values are similar to those reported for the $[Cu^{II}(MeBPA)Cl_2]$ complex[10], where

average Cu-N_{py} bond length of 2.006 Å and Cu-N_{amine} was found to be 2.0837(13) Å . The apparent lack of perturbation of the metal-ligand bonds resulting from installation of the bulky tbp substituents reaffirms our belief that they have minimal impact upon pyridine donor strength.

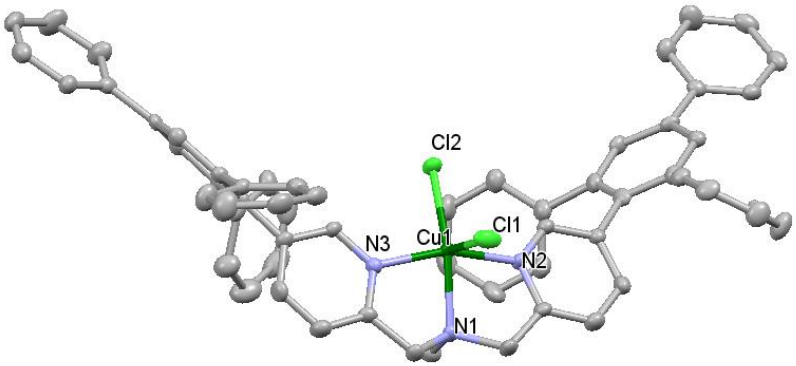

Figure 3.16: Crystal Structure of [Cu^{II}(^{tpb2}MeBPA)Cl_2], depicted with thermal ellipsoids of 50 %. Atom colour scheme: carbon, gray; nitrogen, purple; chlorine, light green; copper, dark green. All hydrogen atoms, solvent molecules and counteranions are omitted for clarity. Selected bond lengths (Å) and bond angles (°): Cu-N1 2.038(4), Cu-N2, 1.996(4), Cu-N3 1.993(4), Cu-Cl1 2.5188(14), Cu-Cl2 2.2495(13); N1-Cu-N2 80.66(17), N1-Cu-N3 80.92(17), N2-Cu-N3 160.93(15); N2-Cu-Cl1 94.62(13), N3-Cu-Cl1 91.91(13), N1-Cu-Cl1 95.05(12), N2-Cu-Cl2 96.75(12), N3-Cu-Cl2 98.56(13), N1-Cu-Cl2 158.56(12).

3.2.3.4 Cyclic Voltammetry (CV) Measurements

The cyclic voltammograms of the metal complexes detailed in this chapter were measured in acetonitrile solution, at room temperature, using tetrabutylammomium hexafluorophosphate as an electrolyte. All potentials are referenced against the ferrocenium/ferrocene (Fc^+/Fc) redox couple. As confirmed by ^{19}F NMR spectroscopy, in MeCN solution all complexes exist as solvates of general formula [M^{II}(^{tpb2}RBPA)(NCMe)]$^{2+}$

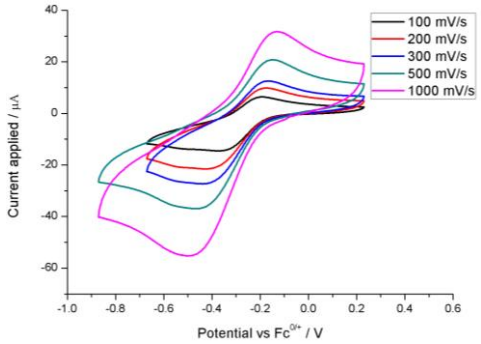

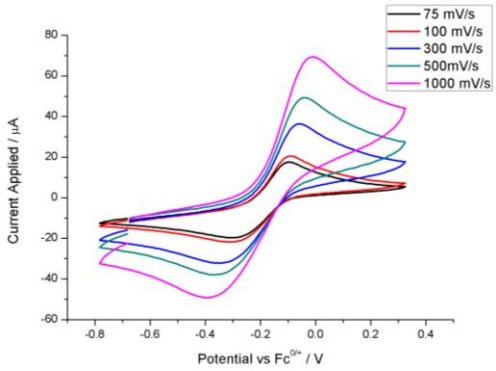

$Cu^{II}(^{tpb2}MeBPA)(NCMe)]^{2+}$ **$[Cu^{II}(^{tpb2}BnBPA)(NCMe)]^{2+}$**

Figure 3.17: Cyclic voltammogram of $[Cu^{II}(^{tpb2}MeBPA)(NCMe)]^{2+}$ (**a**) and $[Cu^{II}(^{tpb2}BnBPA)(NCMe)]^{2+}$ (**b**) measured at various scan rates.

Table 3.2: Comparison of $E_{1/2}$ value of $[Cu^{II}(^{tpb2}RBPA)(NCMe)]^{2+}$ with those of selected $[Cu(RBPA)(NCMe)]^{2+}$ compounds

Complex	$E_{1/2}$ / V	Reference
$[Cu^{II}(^{tpb2}MeBPA)(MeCN)]^{2+}$	-0.28	This work
$Cu^{II}(^{tpb2}BnBPA)(MeCN)]^{2+}$	-0.21	This work
$[Cu^{II}(MeBPA)(NCMe)]^{2+}$	-0.26	10
$[Cu^{II}(BnBPA)(NCMe)_2]^{2+}$	-0.14	7
$[Cu^{II}(^{Ph2}BnBPA)(NCMe)_2]^{2+}$	+0.070	6

As can be seen from **Figure 3.17**, the cyclic voltammogram of $[Cu^{II}(^{tpb2}BnBPA)(MeCN)]^{2+}$ contains a reversible redox process with a $E_{1/2}$ value of -210 mV (**Table 3.2**), which is assigned to the Cu^{II}/Cu^{I} redox couple. It appears at a slightly lower potential than $[Cu^{II}(BnBPA)(NCMe)_2]^{2+}$ with a $E_{1/2}$ value of -140 mV. The reason for this is unclear and we can only speculate that it is associated with slight deviations in geometry. In contrast, the potential of the corresponding redox couple in the complex $[Cu^{II}(^{6Ph2}BnBPA)(NCMe)_2](ClO_4)_2$ is more than 400 mV higher than that of the ^{tpb2}BnBPA complex. This is a consequence of the weakening ligand field in the former due to introduction of phenyl substituents on the 6th

position of the pyridine donors, which destabilizes the high oxidation state. From this, we can conclude that as with TPA, the ligand field of the complex is not significantly weakened by inclusion of substituents on the 5th position of the pyridine rings, unlike 6-pyridyl substituents. Similarly to $[Cu^{II}(^{tpb2}BnBPA)(NCMe)]^{2+}$, $[Cu^{II}(^{tpb2}MeBPA)(NCMe)]^{2+}$ had a redox potential of – 278 mV, which was similar to the $[Cu^{II}(MeBPA)(NCMe)]^{2+}$ complex (**Figure 3.17** and **Table 3.2**). This redox potential resembled the Cu^{I}/Cu^{II} redox couple.

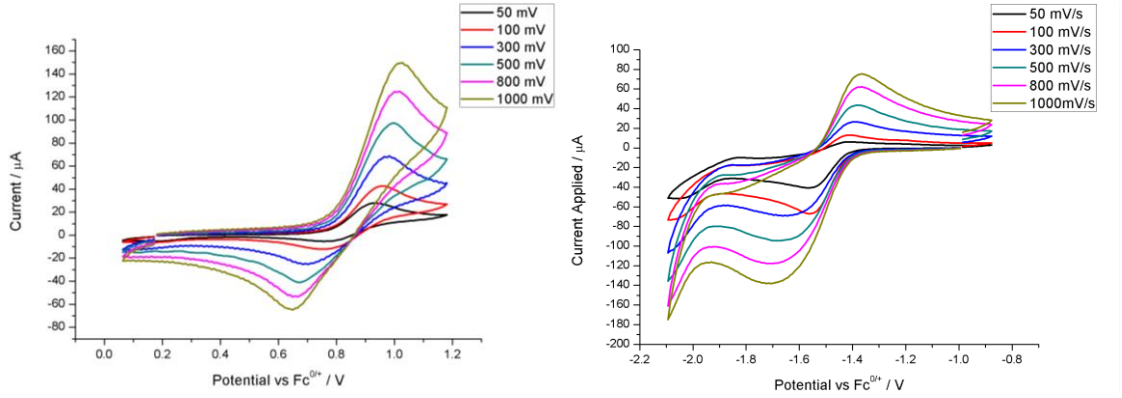

$[Fe^{II}(^{tpb2}MeBPA)(NCMe)]^{2+}$ **$[Co^{II}(^{tpb2}MeBPA)((NCMe)]^{2+}$**

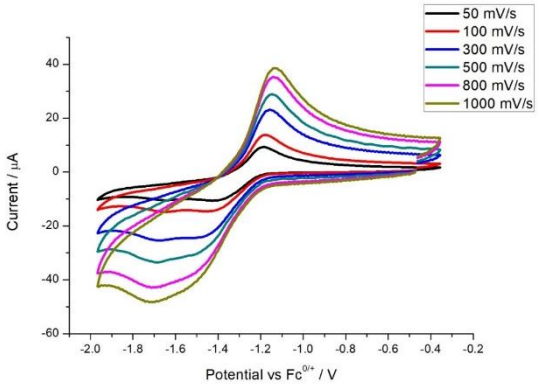

$[Ni^{II}(^{tpb2}MeBPA)(NCMe)]^{2+}$

Figure 3.18: Cyclic voltammograms of $[Fe^{II}(^{tpb2}MeBPA)(NCMe)]^{2+}$ (**a**), $[Co^{II}(^{tpb2}MeBPA)((NCMe)]^{2+}$ (**b**) and $[Ni^{II}(^{tpb2}MeBPA)(NCMe)]^{2+}$ (**c**), measured at various scan rates.

Whereas a reversible oxidative redox process was observed for $[Fe^{II}(5^{tpb2}MeBPA)(NCMe)]^{2+}$ at an $E_{1/2}$ value of +840 mV, which is assigned to the $Fe^{III/II}$ redox couple (**Figure 3.18)**, only events associated with the +1 oxidation state were observed for the corresponding Co and Ni

complexes (**Figure 3.18**). Well-defined anodic waves were observed for [Co(5^{tpb2}MeBPA)$(OTf)_2$MeCN] and [Ni(5^{tpb2}MeBPA)$(OTf)_2$MeCN] at -1.40 and -1.13 V, respectively, which are associated with the M^I/M^{II} redox couple. However, there is clearly 2 cathodic features in the Ni complex at around -1.40 and -1.60 V. The latter becomes more prominent at faster scan rates, which is consistent with these features corresponding to 2 species in equilibrium. Given the highly fluxional nature of these complexes, which is clear from the NMR studies, one might imagine the 2 species differ in terms of the composition of their coordination sphere.

There is a paucity of reports for monochelate BPA complexes of Fe, Co and Ni complexes and, consequently, there is no direct point of comparison for this data. However, according to the metal(II) TPA complexes and the copper(II) BPA complex, the ligand field of these complexes should not be weakened as compared to the 6^{th} substituted TPA analog.

3.3 Conclusion

In conclusion**,** RBPA ligands bearing bulky substituents at the 5th position of the pyridyl ring, as well as its respective metal(II) complexes have been synthesized. The characterization of the complexes is relatively complicated as poor ^{1}H and ^{19}F NMR data was obtained. It suggested that the complexes are either highly fluxional or the presence of impurity. The X-ray crystallographic studies suggested that no bischelate metal(II) complex was obtained, which agreed with the data from mass spectrometry and elemental analysis. Furthermore, the ligand was coordinated in a 'mer' fashion, suggesting the bulkiness of the ligand used. In addition, the CV data of the copper(II) complexes suggested that the donor properties of the ligand was similar to the copper(II) complex of the parent ligand. As such, similar reactivity would be expected, suggesting the potential of this ligand for dioxygen chemistry in Chapter 5. Even though the characterization of monochelate BPA complexes is currently quite limited, the copper(II) complex was the main focus for reactivity studies, which is relatively well characterized.

.

3.4 Reference

(1) Romary, J. K.; Barger, J. D.; Bunds, J. E. *Inorg. Chem.* **1968**, *7*, 1142–1145.

(2) Hazell, A.; McKenzie, C. J.; Nielsen, L. P. *Polyhedron* **2000**, *19*, 1333–1338.

(3) Nelson, S. M.; Rodgers, J. *J. Chem. Soc. A Inorg., Phys. Theor.* **1968**, No. 0, 272–276.

(4) Butcher, R. J.; Addison, A. W. *Inorgan. Chim. Acta* **1989**, *158*, 211–215.

(5) Wikstrom, J. P.; Filatov, A. S.; Staples, R. J.; Guifarro, C. R.; Rybak-Akimova, E. V. *Inorg. Chim. Acta* **2010**, *363*, 884–890.

(6) Zang, Y.; Kim, J.; Dong, Y.; Wilkinson, E. C.; Appelman, E. H.; Que, L. *J. Am. Chem. Soc.* **1997**, *119*, 4197–4205.

(7) Kunishita, A.; Scanlon, J. D.; Ishimaru, H.; Honda, K.; Ogura, T.; Suzuki, M.; Cramer, C. J.; Itoh, S. *Inorg. Chem.* **2008**, *47*, 8222–8232.

(8) Kunishita, A.; Doi, Y.; Kubo, M.; Ogura, T.; Sugimoto, H.; Itoh, S. *Inorg. Chem.* **2009**, *48*, 4997–5004.

(9) Astner, J.; Weitzer, M.; Foxon, S. P.; Schindler, S.; Heinemann, F. W.; Mukherjee, J.; Gupta, R.; Mahadevan, V.; Mukherjee, R. *Inorg. Chim. Acta* **2008**, *361*, 279–292.

(10) Ribelli, T. G.; Wahidur Rahaman, S. M.; Daran, J.-C.; Krys, P.; Matyjaszewski, K.; Poli, R. *Macromolecules* **2016**, *49*, 7749–7757.

(11) Osako, T.; Ueno, Y.; Tachi, Y.; Itoh, S. *Inorg. Chem.* **2003**, *42*, 8087–8097.

(12) Kunishita, A.; Osako, T.; Tachi, Y.; Teraoka, J.; Itoh, S. *Bull. Chem. Soc. Jpn.* **2006**, *79*, 1729–1741.

(13) Lucas, H. R.; Li, L.; Sarjeant, A. A. N.; Vance, M. A.; Solomon, E. I.; Karlin, K. D. *J. Am. Chem. Soc.* **2009**, *131*, 3230–3245.

(14) Walker, J. K.; Nakon, R. *J. Am. Chem. Soc.* **1977**, *99*, 8359–8360.

(15) Kooistra, T. M.; Hekking, K. F. W.; Knijnenburg, Q.; de Bruin, B.; Budzelaar, P. H. M.; de Gelder, R.; Smits, J. M. M.; Gal, A. W. *Eur. J. Inorg. Chem.* **2003**, No. 4, 648–655.

(16) Kunishita, A.; Teraoka, J.; Scanlon, J. D.; Matsumoto, T.; Suzuki, M.; Cramer, C. J.; Itoh, S. *J. Am. Chem. Soc.* **2007**, *129*, 7248–7249.

Chapter 4

Mononuclear End-On Superoxocopper(II) Complexes

4.1 Introduction

Mononuclear 'end-on' (η^1) superoxocopper(II) intermediates have been postulated to be the active oxidant for C-H bond hydroxylation in a number of enzymes, including the copper monoxygenases PHM and DβM.[1,2] In support of this supposition, Amzel and co-workers reported an X-ray structure of PHM containing an end-on superoxide bound to one of the copper centres (Cu_B) in the active site. The copper centres were not coupled to each other due to the long Cu-Cu bond distance of 11 Å. (**Figure 4.1)**. It is believed that these complexes were involved in hydrogen atom abstraction from the substrate.

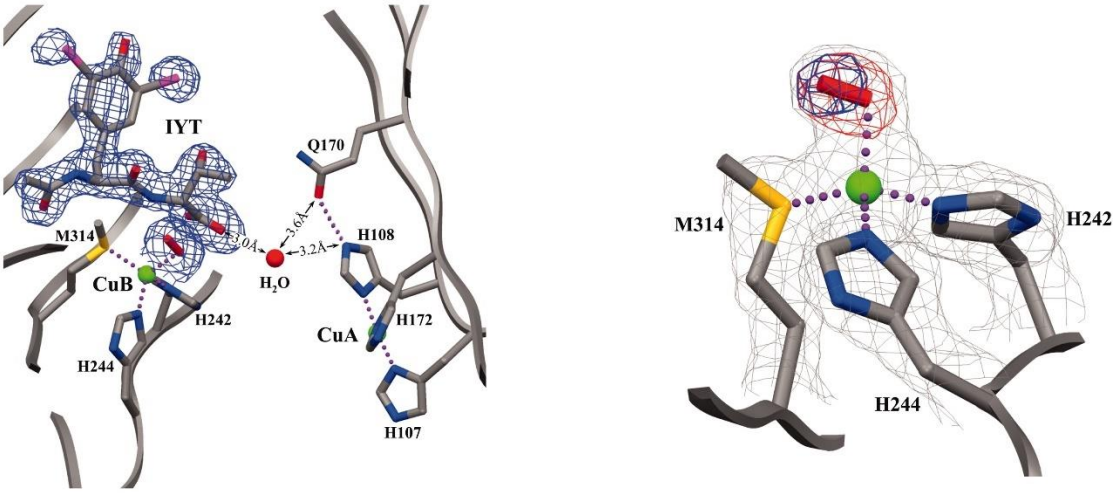

Figure 4.1: Simulated X-ray structure of the active site of PHM (left) and expansion of Cu_B showing binding of an 'end-on' superoxo moiety (right).[3]

However, there are theoretical studies[4] and mechanistic analyses that have questioned whether a superoxocopper(II) species is the oxidant responsible for C-H hydroxylation in PHM and DβM and have suggested that a oxylcopper(II) complex (**Figure 4.2**), which is predicted to be a more powerful oxidant, is a more likely candidate.[2] Despite vigorous efforts, oxylcopper(II) species have remained elusive in both synthetic and biological systems. In contast, more than 15 mononuclear 'end-on' superoxocopper(II) complexes, $Cu^{II}(\eta^1\text{-}O_2^{\bullet-})$, have been reported to date.[5–8]

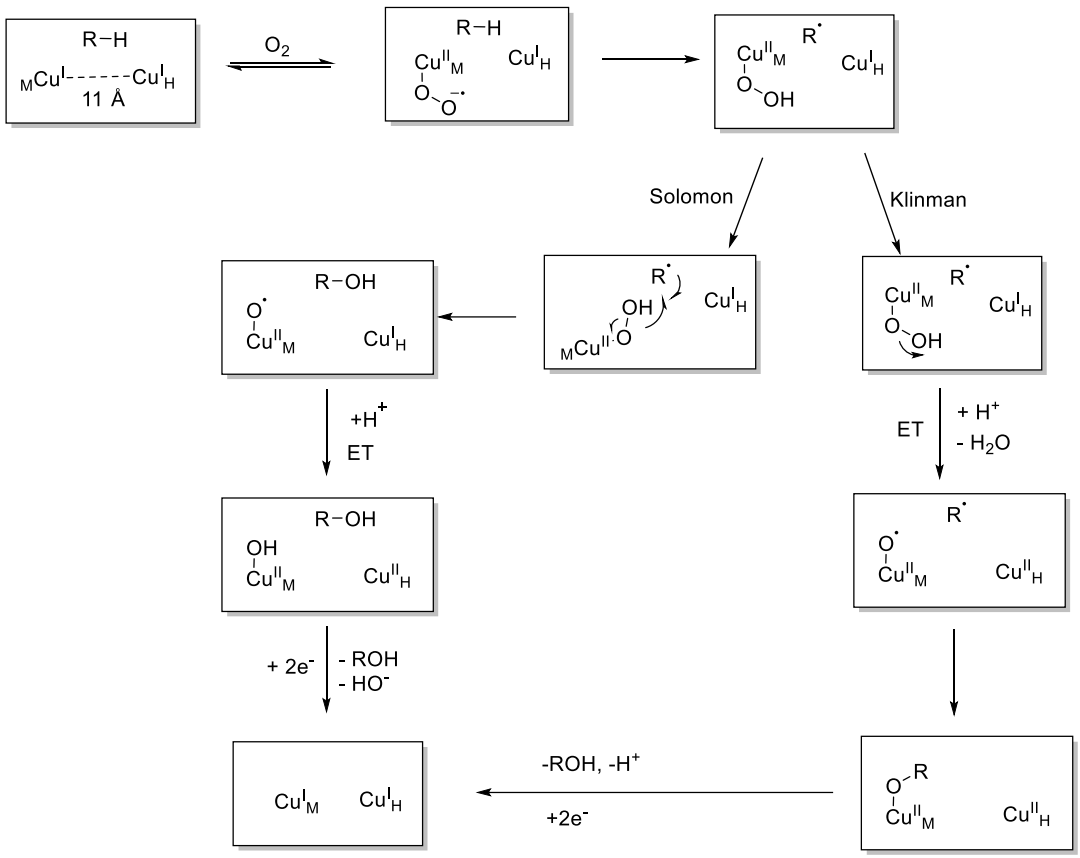

Figure 4.2: Proposed general mechanism of DβM and PHM by Klinder and Solomon.[2]

Superoxocopper(II) complexes are, inexorably, the first species formed upon reaction of O_2 with a copper(I) complex. However, they tend be very unstable with respect to reaction with further copper(I) centres, which yields peroxo-bridged dicopper(II), $Cu^{II}_2(\mu\text{-}O_2)$, complexes. Depending upon the denticity of the supporting ligands and other factors, the latter may well convert to oxo-atom bridged species, with some of the more common moieties being $Cu^{III}_2(\mu\text{-}O)_2$ and $Cu^{II}_2Cu^{III}(\mu\text{-}O)_2$. Even when superoxocopper(II) complexes do not react to form dicopper complexes, they will, usually, decompose to yield poorly-defined copper(II). The aforementioned stability issues have hampered their study, which is routinely conducted at very low temperatures (≤ -80°C), and our understanding of their reactivity of superoxocopper(II) complexes is limited.

Most of the ligand systems that have been used to support end-on superoxocopper(II) complexes are tetradentate, with only a few examples of tridentate ligands being shown to be

fit for this purpose. Of the ligand systems that have been used to support end-on superoxocopper(II) complexes, the tetradentate tris(2-pyridyl)methylamine (TPA) ligand framework, used in the seminal work of Karlin and co-workers, is the most widely studied. Introduction of dioxygen into solutions of $[Cu^{I}(TPA)(NCMe)]^{+}$ at -90°C causes a very rapid reaction to give the corresponding peroxo-bridged dicopper(II) complex, $[(TPA)Cu^{II}(\mu\text{-}O_2)Cu^{II}(TPA)]^{2+}$, which is the thermodynamically favoured product (**Figure 4.3**).[9] However, conducting the same reaction at -135°C afforded mixtures of the peroxo-bridged complex and the superoxocopper(II) complex $[Cu^{II}(\eta^1\text{-}O_2^{\bullet-})(TPA)]^{+}$.

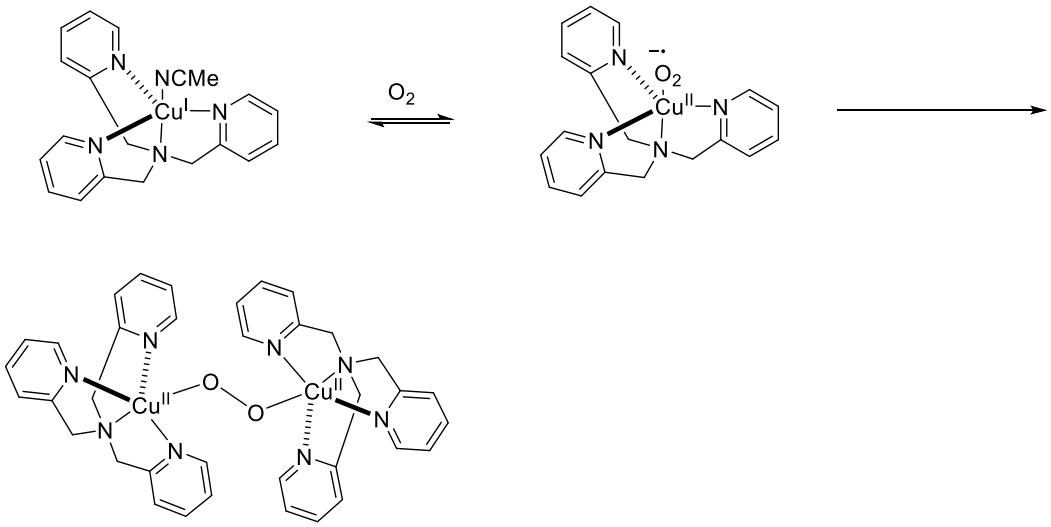

Figure 4.3: Reaction of $[Cu^{I}(TPA)(NCMe)]^{+}$ with O_2.

Karlin and co-workers found out that the use of electron dontating substituents, $^{(OMe)3}$TPA and ^{DMA}TPA ligands were able to stabilize the superoxocopper(II) complexes, such that the peroxo-bridged complex was observed in a small quantity. (**Figure 4.4**). The used of electron-donating OMe group on the ligand as well as performing the oxygenation reaction in a non-coordinating solvent, THF, would help to enhance the thermodynamic stability of the superoxocopper(II) complex, as well as peroxo-bridiged dicopper(II) complex at – 90 °C. In addition, the oxygenation of $[Cu^{I}(CO)(^{DMA}TPA)]$ complex would form the superoxocopper(II) species at low temperature with a half-life of more than 4 h (**Figure 4.4**) at – 85 °C.[10,11] It showed to be

good hydrogen atom donor toward 2,6-di-*tert*-butyl-*para*-R-phenol. Similarly, the rate of decomposition would increase at higher temperature.

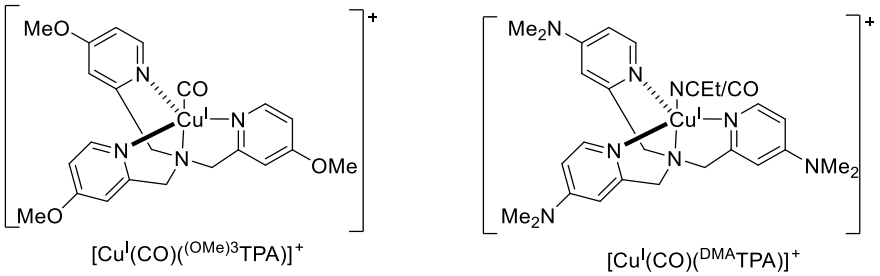

Figure 4.4: Structures of the copper(I) complexes ligated by *para*-substituted TPA ligands that have been studied in reaction with O_2.

Addition of methyl groups on the 3,5-position of the pyridyl ring of the $^{(OMe)3}$TPA ligand to give ^{DMM}TPA (**Figure 4.5**) resulted in an increase in the lifetime of the superoxocopper(II) complex ($t_{1/2}$ > 3h) at -90°C. This superoxocopper(II) species was found to have good reactivity toward a much wider variety of substituted phenols than was previously possible. Furthermore, unlike preceding and following examples, the reactivity of this $Cu^{II}(\eta^1\text{-}O_2^{\bullet-})$complex could be studied over an, albeit very narrow, temperature range of -85 to -100°C. Use of higher temperatures caused rapid self-decay, while lower temperatures resulted in freezing of the solvent. In addition, to limit side-reactions, such as dispropotionation, the CO adduct $[Cu^{I}(CO)(TPA)]^{+}$ had to be used as the starting complex and only in low concentration. Regardless, this allowed measurement of the only set of kinetic and thermodynamic parameters, thus far, for reactivity of an 'end-on' superoxocopper(II) complex with substrate and confirmed that reaction of this complex with phenol proceeded via a hydrogen atom transfer (HAT) mechanism.[12]

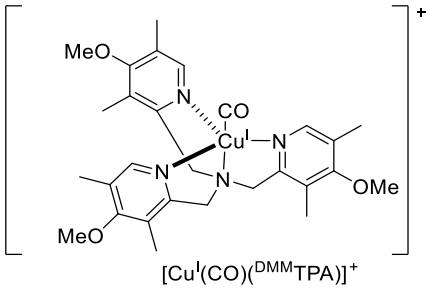

Figure 4.5: Structure of the complex $[Cu^{I}(CO)(^{DMM}TPA)]^{+}$.

As an alternative to electron donating functionality, Karlin and co-workers recently reported that inclusion of a hydrogen bond donor group on the 6-position of a pyridine ring in TPA (**Figure 4.6**) led to stabilization of superoxocopper(II) complexes relative to the corresponding peroxo-bridged species.[13] This was evidenced to be due to intramolecular H-bonding with the superoxo O-atom bound to the metal centre and allowed synthesis of $Cu^{II}(\eta^{1}\text{-}O_2^{\bullet-})$, at -135°C, without conversion to $Cu^{II}(\mu\text{-}O_2)Cu^{II}$. As an added bonus, the hydrogen bonding appeared to enhance the reactivity of the superoxocopper(II) complex towards phenols and allowed reaction with *para*-methoxy-phenol, which has the highest bond dissociation energy (88 kcal mol^{-1}) of any phenol successfully reacted with such a complex. Despite stabilizing the $Cu^{II}(\eta^{1}\text{-}O_2^{\bullet-})$ moiety, dimerization to give peroxo-bridged complexes was still observed at temperatures > -80°C.

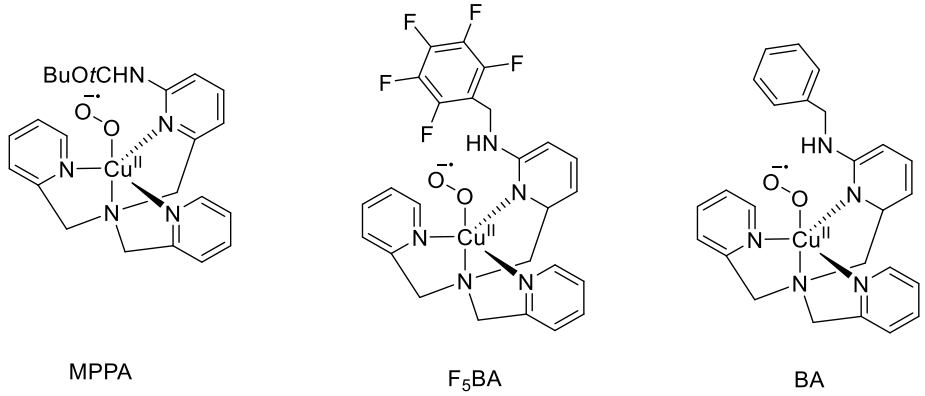

Figure 4.6: Superoxocopper(II) complexes supported by TPA ligand with hydrogen bond donor functionality.

In an effort to explain the crucial role of the His_2Met coordination sphere of the copper ion in the active site of the PHM (**Figure 4.1**), Karlin and co-workers reported a TPA derivative in which one pyridylmethyl arm had been replaced by a thioether donor to give $^{DMA}N_3S$. The copper(I) complex of this ligand reacted with O_2 at -100°C to afford the complex $[Cu^{II}(\eta^1\text{-}O_2^{\bullet-})(^{DMA}N_3S)]^+$ (**Figure 4.7**).[14] It was found to have significantly enchanced reactivity in hydrogen atom abstraction. For example it reacted with 2,6-di-*tert*-butyl-*para*-methoxyphenol at -100°C, where the complex $[Cu^{II}(O_2^{\bullet-})(^{DMA}TPA)]^+$ did not. It is worth mentioning that $[Cu^{II}(\eta^1\text{-}O_2^{\bullet-})(^{DMA}N_3S)]^+$ was only stable at -100°C in the presence of polar or hydrogen bonding solvent additives. Without them, dimerization to form the corresponding peroxo-bridged dicopper(II) complex would form rather than the equilibrium mixture of superoxo and peroxo-bridged dicopper(II) complex.

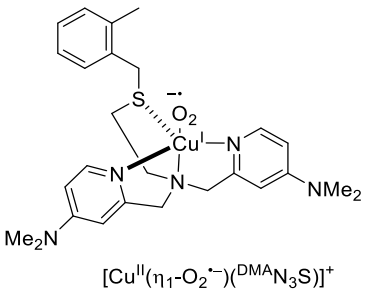

$[Cu^{II}(\eta_1\text{-}O_2^{\bullet-})(^{DMA}N_3S)]^+$

Figure 4.7: Structure of $[Cu^{II}(\eta^1\text{-}O_2^{\bullet-})(^{DMA}N_3S)]^+$

Despite significant efforts to stabilize mononuclear superoxocopper(II) complexes supported by TPA ligands, all of them tend to either dimerize or decompose at temperatures greater than -80°C. On the other hand, Schindler, Itoh and Tolman have reported 'end-on' superoxocopper(II) complexes, $[Cu^{II}(\eta^1\text{-}O_2^{\bullet-})(TMG_3tren)]^+$, $[Cu^{II}(\eta^1\text{-}O_2^{\bullet-})(HIPT_3tren)]^+$ and $[Cu^{II}(\eta^1\text{-}O_2^{\bullet-})$(*N*,*N*′-bis(2,6-diisopropylphenyl)-2,6-pyridinedicarboxamide)$]^+$ (**Figure 4.8**), that are stable against dimerization. This stability is a consequence of the sterically hindered nature of the ligands, which prohibits intermolecular reaction.[15,16] For $[Cu^{II}(\eta^1\text{-}O_2^{\bullet-})(TMG_3tren)]^+$, oxygenation process was found to be fully reversible, such that warming to room temperature regenerated the copper(I) precursor without any decay, and the only X-

ray structure of end-on superoxocopper(II) complex was obtained. However, its reactivity was found to be very sluggish as compared to the TPA complexes. For instance, it required 48 h for it to react with 2,6-di-*tert*-butyl-*para*-methoxyphenol at -80°C.[17] Even lower reactivity was reported for $[Cu^{II}(\eta^1\text{-}O_2^{\bullet-})(^{HIPT3}tren)]^+$. At -90°C, it did not react with phenols and hydroxylamine derivatives, which have a very weak O-H bond, and addition of triphenylphospine, thioanisole and 1,4-cyclohexadiene caused loss of the bound O_2 and copper(I) complex coordinated by the additive. It is natural to assume that the low reactivity of the complexes in Figure 4.8 is due to the steric bulk of their ligands, but their donor strength is greater than TPA, which might be expected to impair reactivity, and that prevents any firm conclusions. Furthermore, $[Cu^{II}(\eta^1\text{-}O_2^{\bullet-})$(N,N'-bis(2,6-diisopropylphenyl)-2,6-pyridinedicarboxamide)$]^+$, that was synthesized from the reaction of the copper(II) starting material and potassium superoxide, possessed no reactivity towards phenols at -80°C. It could only act as a base or nucleophile due to its anionic properties.

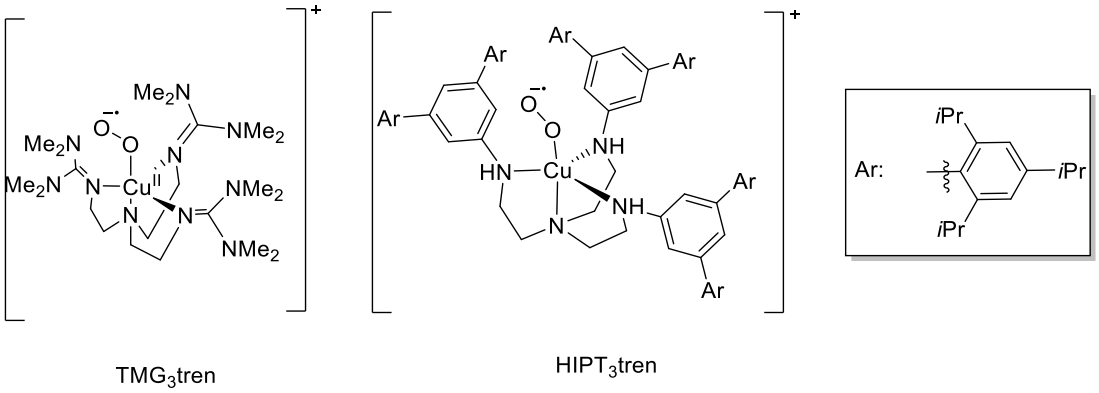

TMG_3tren $HIPT_3tren$

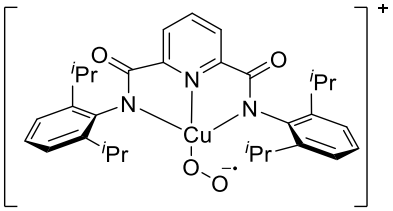

N,N'-bis(2,6-diisopropylphenyl)-2,6-pyridinedicarboxamide

Figure 4.8: Superoxocopper(II) complexes supported by super bulky ligands

End-on superoxocopper(II) complexes supported by tridentate ligands are relatively rare, with only a few having been reported so far. However, they have significance because the copper ions in the active sites of many oxygenases have tetrahedral coordination geometries and it is possible that this is key to the high reactivity shown by these enzymes. Thus it should be noted that the only tetrahedral end-on superoxocopper(II) complex, presently known, was reported by Itoh and co-workers **(Figure 4.9)**.[18] The tridentate ligand that supports it contains a 1,5-diazacyclooctane ring with the constituent *N*-atoms bearing 2-ethylpyridyl and ethylphenyl side arms respectively. Interestingly, the superoxocopper(II) decays via hydroxylation of the ethylphenyl side arm, even at - 60°C. This is one of the few examples of a synthetic superoxocopper(II) complex that can perform C-H oxidation, which implies high reactivity. In addition, it was shown to perform oxo-transfer to PPh_3 and to react with one-electron redunctants, from which a reduction potential of 0.19±0.07 V vs SCE was estimated.[19] These

unusual reactivity features mark out tridentate ligand systems that can support tetrahedral geometries as important targets for future superoxocopper(II) complex research.

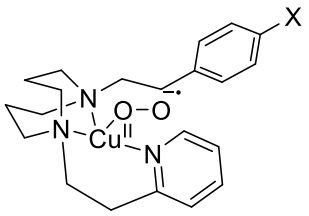

X= H, OMe, NO_2

Cyclic complex

Figure 4.9: Structure of Itoh's mononuclear 'end-on' superoxocopper(II) complex supported by a tridentate ligand.

We felt that the steric bulk provided by the aryl substituents of the ^{Ar3}TPA ligands described in Chapter 2 of this thesis would be sufficient to prevent dimerization of any end-on superoxocopper(II) complex formed. Furthermore, the close similarity of the $E_{1/2}$ values of the Cu^{II}/Cu^{I} redox couples of the $[Cu^{II}(^{Ar3}TPA)(NCMe)]^{2+}$ and parent TPA complexes suggest that the copper(I) complexes of the ^{Ar3}TPA ligands would also react with O_2. In addition, we postulated that the remote nature of the bulky aryl substituents, relative to the metal centre, would minimize steric hindrance of reactivity of any η^1-$O_2^{\bullet-}$ complex formed with substrates.

As a separate point of interest, we were also intrigued by the possibility of observing a superoxocopper(II) complex supported by a tridentate BPA derivative. Oxygenation of copper(I) complexes of the BPA ligands, such $[Cu^{I}(BnBPA)(NCMe)]^{+}$, with O_2 yields only bis(μ-oxo)dicopper(III) complexes (**Figure 4.10**).[20] Thus, we were keen to explore the O_2 reactivity of copper(I) complexes supported by ^{tpb2}Me/BnBPA ligand and hope it will provide a means to learn more about the reactivity of 4-coordinate superoxocopper(II) complexes.

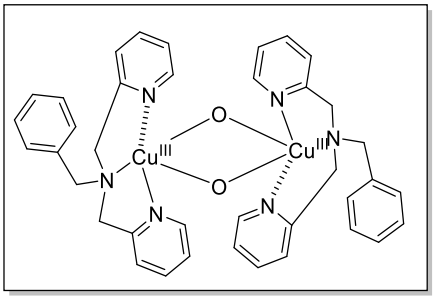

Figure 4.10: Structure of $[(BnBPA)Cu^{III}(\mu\text{-}O)_2Cu^{III}(BnBPA)]^{2+}$.

4.2 Result and Discussion

4.2.1 Synthesis of Cu^{I} Complexes

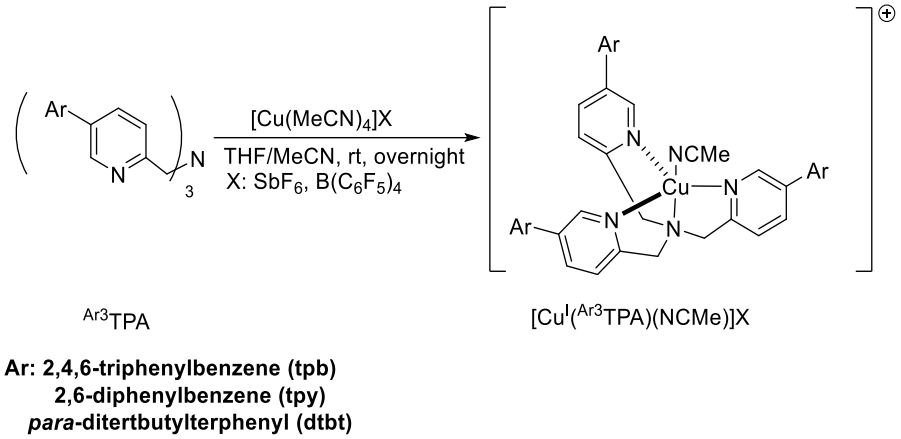

Scheme 4.1: Complexation of the ^{Ar3}TPA ligands by $[Cu^{I}(MeCN)_4][B(C_6F_5)_4]$

Initially, copper(I) complexes of the ^{Ar3}TPA ligands detailed in Chapter 2 were synthesized, in yields of around 80%, by reaction with $[Cu^{I}(MeCN)_4][B(C_6F_5)_4]$ in THF (**Scheme 4.1**). The purity of all complexes was confirmed by ^{1}H NMR spectroscopy. However, difficulties were met in trying to grow single crystals of these complexes suitable for X-ray crystallography. In an effort to obviate this problem, copper(I) complexes with various, alternative counteranions were also synthesized. Unfortunately, this did not resolve the issue.

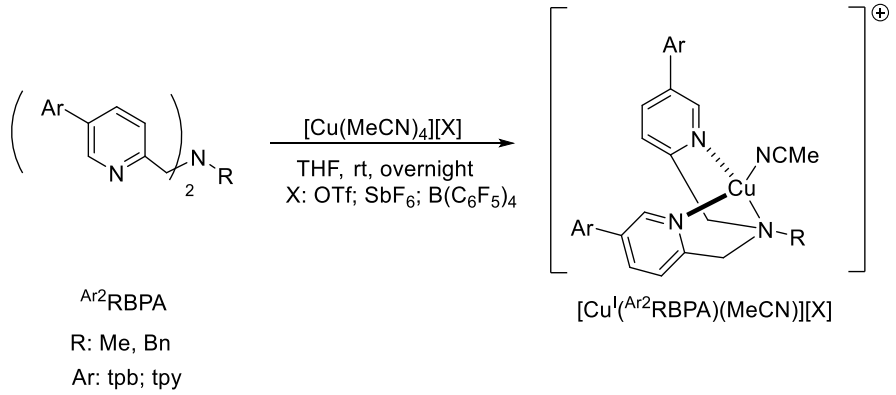

Scheme 4.2: Complexation of the ^{Ar2}RBPA ligands by $[Cu^{I}(MeCN)_4][B(C_6F_5)_4]$.

Similarly, the ligands ^{tpb2}MeBPA and ^{tpb2}BnBPA were also reacted with the salt $[Cu^{I}(MeCN)_4][B(C_6F_5)_4]$ to form the corresponding $[Cu^{I}(^{tpb2}RBPA)(NCMe)][B(C_6F_5)_4]$ complexes (**Scheme 4.2**) in yields of about 90%. Once again, the purity of the complexes was

confirmed by ^{1}H NMR spectroscopy. To facilitate growth of single crystals of complexes suitable for X-ray crystallographic studies, the corresponding triflate, [Cu^{I}(^{tpb2}RBPA)(NCMe)][OTf], and SbF_6^- salts, [Cu^{I}(^{tpb2}RBPA)(NCMe)][SbF_6], was prepared. This strategy proved to be successful for the ^{tpb2}BnBPA ligated complex. In the hope of obtaining high-quality single crystals for a ^{Ar2}MeBPA complex, we also synthesized the ligand ^{tpy2}MeBPA (in an overall yield of 32%) via the general synthetic route described in Chapter 3. Pleasingly, recrystallization of the resultant copper(I) complex [Cu^{I}(^{tpy2}MeBPA)MeCN][SbF_6] was successful.

4.2.2 X-ray Crystallographic Studies

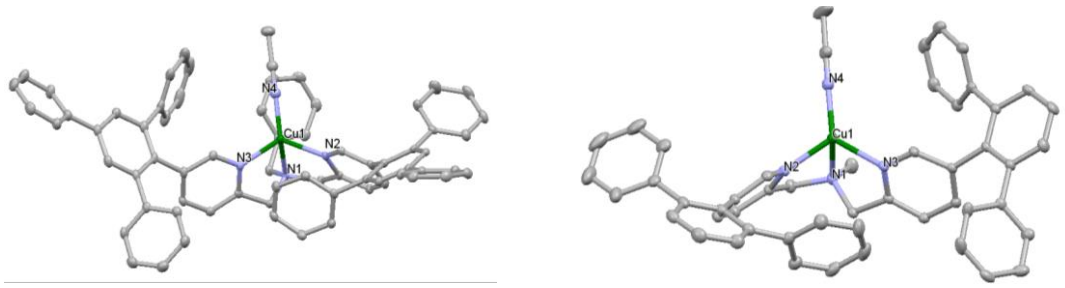

[Cu^{I}(^{tpb2}BnBPA)(NCMe)](OTf) **[Cu^{I}(^{tpy2}MeBPA)(MeCN)](SbF_6)**

Figure 4.11: Crystal structures of copper(I) complexes bearing ^{Ar2}RBPA ligands, depicted with thermal ellipsoids of 50 %. Atom colour scheme: carbon, gray; nitrogen, purple; copper, dark green. All hydrogen atoms, solvent molecules and counteranions are omitted for clarity.

As judged by a τ_4 value of 0.77, the structure of [Cu^{I}(^{tpb2}BnBPA)(NCMe)](OTf) displays a distorted tetrahedral geometry (**Figure 4.11**).[21] The average Cu-N_{py} bond length was found to be 2.030(2) Å and the Cu-N_{amine} bond was 2.213(2) Å (**Table 4.1**). In addition, the Cu-NCMe bond length was 1.891(2) Å. The bond lengths obtained were similar to the [Cu^{I}(BnBPA)(NCMe][$B(C_6F_5)_4$] complex that was reported by Karlin and co-workers,[22] which possessed respective Cu-N_{amine}, average Cu-N_{Py} and Cu-NCMe bond lengths of 2.309(4) Å, 2.016 Å and 1.900(4) Å. Furthermore, the Cu-N bond lengths in the aforementioned complexes are shorter than those in [Cu^{I}(CO)(^{Ph2}BnBPA)]$^{+}$, whose average Cu-N_{py} bond lengths were

reported to be 2.109 Å. Cumulatively, this data is consistent with the aryl substituents in the ^{tpb2}BnBPA ligand having little impact upon the donor strength of the pyridine rings.

Similarly, a τ_4 value of 0.81 was obtained for [Cu^{I}(^{tpy2}MeBPA)(MeCN)][SbF_6], which indicates that it possesses a tetrahedral geometry. The Cu-N_{amine} bond length was was 2.206(2) Å, while the average Cu-N_{py} bond length was found to be 2.030(2) Å. Furthermore, Cu-NCMe bond length was 1.891(2) Å. These values are very similar to [Cu^{I}(^{tpb2}BnBPA)(MeCN)][OTf] and, this combined the cyclic voltammetry results detailed in chapter 3, reinforce our conclusion that putting bulky substituents at the 5th position of the pyridine donors does not perturb the ligand field strength of the BPA ligands.

Table 4.1: Selected bond lengths (Å) and bond angles (°) for the copper(I) complexes bearing ^{Ar2}RBPA ligands

	[Cu^{I}(^{tpb2}BnBPA)(NCMe)](OTf)	**[Cu^{I}(^{tpy2}MeBPA)(NCMe)](SbF_6)**
Cu-N1 (N_{amine})	2.213(2)	2.206(2)
Cu-N2 (N_{py})	2.026(2)	2.049(2)
Cu-N3 (N_{py})	2.034(3)	2.020(2)
Cu-N4 (NCMe)	1.891(2)	1.891(2)
N1-Cu-N2	80.46(8)	79.49(8)
N1-M-N3	82.08(8)	81.42(8)
N2-Cu-N3	121.07(8)	113.18(8)
N1-Cu-N4	129.97(9)	116.64(9)
N2-Cu-N4	116.95(9)	120.56(9)
N3-Cu-N4	117.31(9)	125.29(9)

4.2.3 Dioxygen Activation

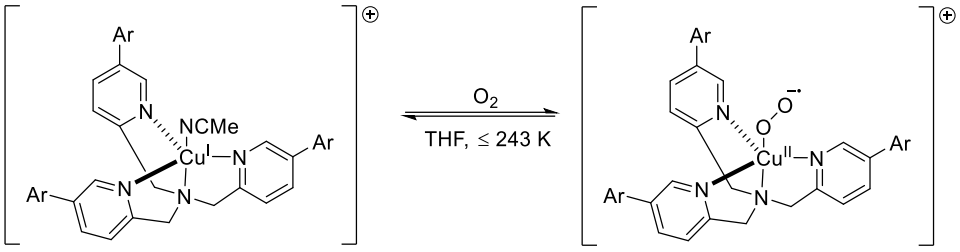

Scheme 4.3: Reaction of $[Cu^{I}(^{Ar3}TPA)(MeCN)][B(C_6F_5)_4]$ with O_2.

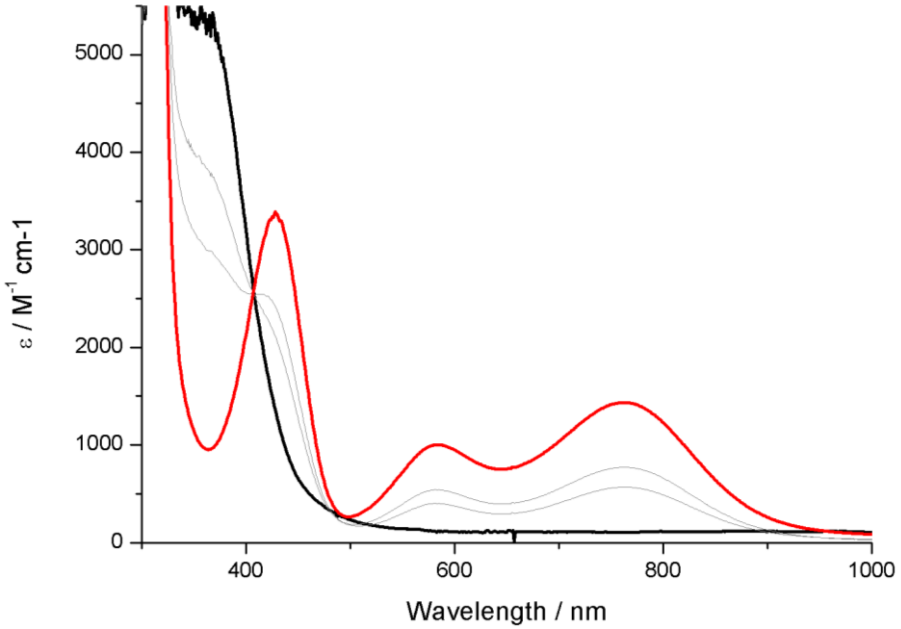

Figure 4.12: UV-vis spectra of $[Cu^{I}(^{tpb3}TPA)(NCMe)][B(C_6F_5)_4]$ (black line) and product of oxygenation (red line). Measurements performed at -80°C, in THF solution, using 0.5 mM solution of complex.

Bubbling oxygen through a THF solution of $[Cu^{I}(^{tpb3}TPA)(NCMe)][B(C_6F_5)_4]$ (0.5 mM) at -80°C (**Scheme 4.3**) yields a green species with a UV-vis spectrum containing three distinct absorbance features centred at 420 nm (ε_{max} = 3100 M^{-1} cm^{-1}), 580 nm (ε_{max} = 1100 M^{-1} cm^{-1}) and 765 nm (ε_{max} = 1330 M^{-1} cm^{-1}) (**Figure 4.12**). This spectrum is very similar to all other 'end-on' superoxocopper(II) complexes supported by neutral N-donor atom ligands reported, thus far (**Table 4.2**),[8,23,24] and is diagnostic for successful formation of $[Cu^{II}(\eta^1\text{-}O_2^{\bullet-})(^{tpb3}TPA)]^{+}$. The maximum wavelength and extinction coefficient of $[Cu^{II}(\eta^1$-

$O_2^{\bullet-}$)(^{tpb3}TPA)]$^+$ was found to be similar to the stable mononuclear 'end-on' superoxocopper(II) complex supported by TMG$_3$tren, with a peak at 444 nm (ε_{max} = 3500 M^{-1} cm^{-1}) near UV region.[11] Although it had similar λ_{max} as [Cu^{II}(η^1-$O_2^{\bullet-}$)(^{DMA}TPA)]$^+$ at 418 nm (ε_{max} = 4300 M^{-1} cm^{-1}) and [Cu^{II} (η^1-$O_2^{\bullet-}$)(^{DMM}TPA)]$^+$ at 409 nm (ε_{max} = 4250 M^{-1} cm^{-1}), a lower extinction co-efficient was observed. The reason for this is not apparent, it may be due to inherent electron features of our system but we cannot exclude the possibility of solvent impurities, which reduced the yield of the oxygenated product.

Similar results were obtained for the corresponding ^{Ar3}TPA complexes when Ar = tpy and dtbt (**Figure 4.13**), but somewhat lower extinction coefficients were observed. In particular, those superoxocopper(II) complex formed from [Cu^I(^{dtbt3}TPA)(NCMe)] were significally reduced. The absorption maxima and extinction coefficients of our ^{Ar3}TPA-supported superoxocopper(II) complexes are summerized in **Table 4.2** alongside prominent examples taken from the literarure. Studies intended to investigate the origin of the suppressed extinction coefficients are underway. It was worth mentioning that no decay of the complex or dimerization to form a binuclear copper complex was observed, suggesting its stability.

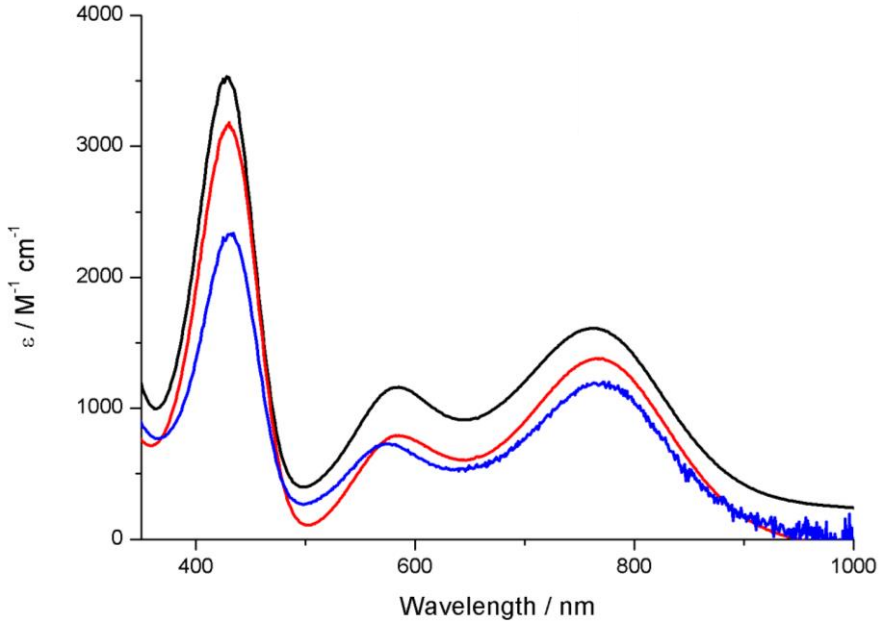

Figure 4.13: UV-vis spectra of $[Cu^{II}(\eta^1\text{-}O_2^{\bullet-})(^{tpb3}TPA)]^+$ (black), $[Cu^{II}(\eta^1\text{-}O_2^{\bullet-})(^{tpy3}TPA)]^+$ (red) and $[Cu^{II}(\eta^1\text{-}O_2^{\bullet-})(^{dtbt3}TPA)]^+$ (blue), recorded in THF (0.5 mM) solution at -80°C.

Table 4.2: UV-vis spectroscopic data for selected mononuclear end-on superoxocopper(II) complexes

$[Cu^{II}(\eta^1\text{-}O_2^{\bullet-})(L)]^+$, where L =	λ_{max}/nm (ε_{max}/M^{-1} cm^{-1})	References
^{tpb3}TPA	420 (3200) 680 (1100) 780 (1330)	This work
^{tpy3}TPA	430 (3200) 680 (800) 770 (1400)	This work
^{dtbt3}TPA	430 (2300) 680 (770) 770 (1170)	This work
TMG_3tren	444 (3500) 680 780	15
^{DMA}TPA	418 (4300) 615 (1100) 767 (840)	11
^{DMM}TPA	409 (4250) 587 (1100) 743 (1030)	12

To probe whether the binding of dioxygen was reversible, an oxygenated THF solution of $[Cu^{I}(^{tpb3}TPA)(NCMe)][B(C_6F_5)_4]$ was cycled between -80°C and room temperature thrice (**Figure 4.14**). Warming of $[Cu^{II}(\eta^1\text{-}O_2^{\bullet-})(^{tpb3}TPA)]^+$ resulted in dissociation of O_2 and reformation of the copper(I) starting complex, while subsequent recooling led to regeneration of $[Cu^{II}(\eta^1\text{-}O_2^{\bullet-})(^{tpb3}TPA)]^+$. This behaviour is consistent with entropically disfavoured reversibile O_2 binding. Such behaviour has yet to be reported for any TPA ligand, as warming invariably leads them to either dimerize to form a thermodynamically favoured peroxo-bridged dicopper(II) complex or to undergo decomposition.

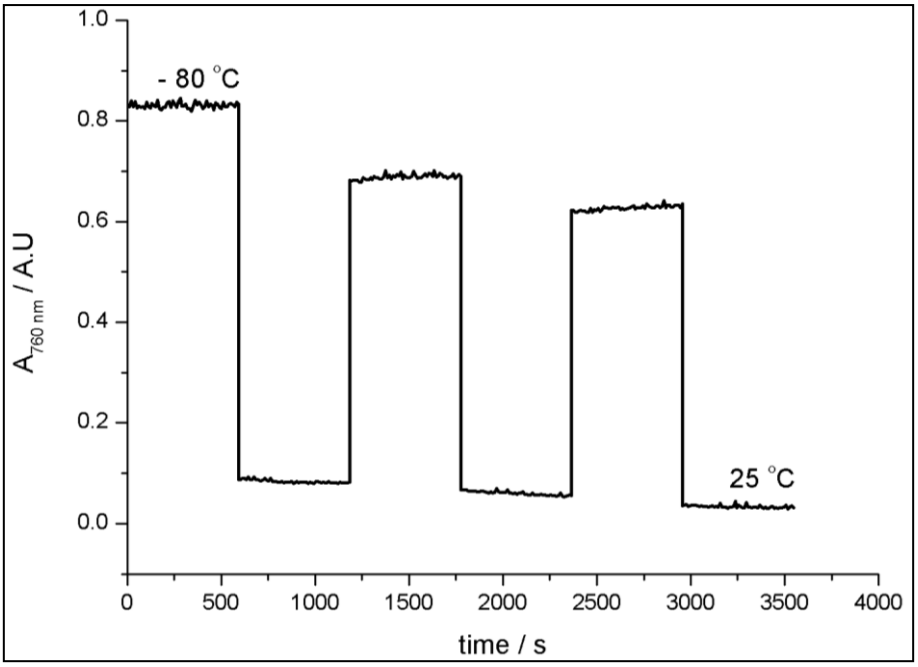

Figure 4.14: Plot of absorption coefficient at 760 nm ($A_{760\ nm}$) versus time for cycling of an O_2 saturated solution of $[Cu^{I}(^{tpb3}TPA)(NCMe)]^+$, in THF (0.5 mM), between -80 and 25 °C.

Such temperature-dependent reversibile binding of O_2 has only been observed for one other superoxocopper(II) complex, namely $[Cu^{II}(\eta^1\text{-}O_2^{\bullet-})(TMG_3tren)]^+$ where its bulky ligand also prevents self-decomposition and dimerization. The above observations imply that the aryl substituents of the ^{Ar3}TPA ligands sterically prohibit formation of the corresponding thermodynamically favoured peroxo-bridged dicopper(II) complex, even at high temperatures. However, the extinction coefficient of $[Cu^{II}(\eta^1\text{-}O_2^{\bullet-})(^{tpb3}TPA)]^+$ did decrease during every

cycle. The reason(s) for this is unclear, but it is possible that there was some reaction of the superoxocopper(II) complex with solvent (or impurities) or outer sphere electron transfer reactivity of the copper(I) complex with O_2 at higher temperatures. Alternatively, there may have been condensation of moisture in the high humdity atmosphere of Singapore, which is known to interfere with O_2 binding. To probe these possibilities, ESI-MS measurements were conducted after warming of solutions of the superoxocopper(II) complex and only $[Cu^{I}(5^{tpb3}TPA)]^{+}$ was seen. However, this is not conclusive and further studies are required. Regardless, this is the first example of a TPA-supported superoxocopper(II) complex not showing any observable dimerization or self-decay.

Furthermore, $[Cu^{II}(\eta^{1}\text{-}O_2^{\bullet-})(^{tpb3}TPA)]^{+}$ could also be formed using acetone, Et_2O and 2-methyltetrahydrofuran (MeTHF) as solvents, although the extinction coefficients did differ between solvents (**Figure 4.15**). The latter could be due to poor solubility of the superoxocopper(II) complexes in certain solvents and/or poor baselines in others.

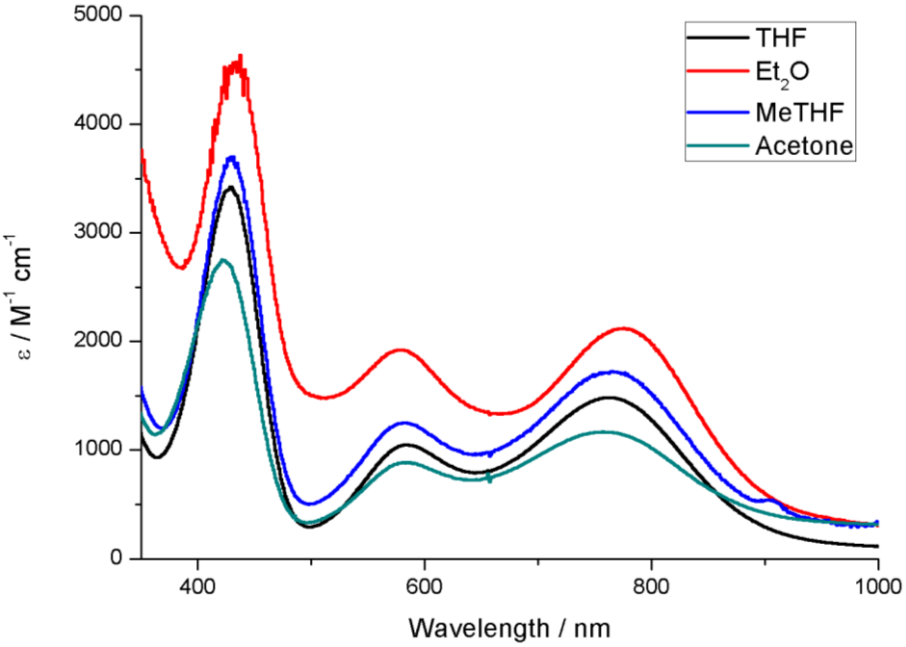

Figure 4.15: UV-Vis spectra of $[Cu^{II}(\eta^1\text{-}O_2^{\bullet-})(^{tpb3}TPA)]^+$ (0.5 mM) in various solvents, at -80°C.

It was worth mentioning that bubbling Ar gas into solutions of $[Cu^{II}(\eta^1\text{-}O_2^{\bullet-})(^{tpb3}TPA)]^+$ did not cause it to revert back to Cu^I complex, which implies that dioxygen binds strongly to the complex. This combined with rapid rate of oxygenation of the copper(I) starting complex (within 10 s), especially at low temperatures, made efforts to measure the corresponding rate constants and equilibrium constants unworkable. As was the case for $[Cu^{II}(\eta^1\text{-}O_2^{\bullet-})(^{DMA}TPA)]^+$,[10,17] this would require stop-flow kinetics, which we do not have access to.

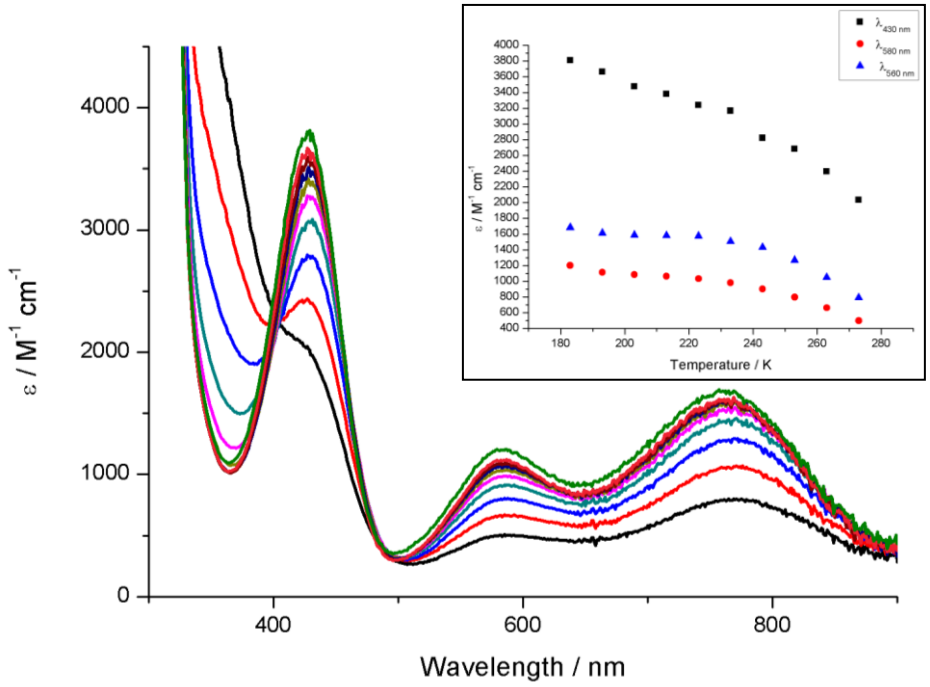

Figure 4.16: Temperature-dependence of the UV-vis spectrum of an oxygen saturated THF solution of $[Cu^{I}(^{tpb3}TPA)(NCMe)]^{+}$ (0.5 mM). **Inset:** Plot of absorption maxima vs temperature with black square, $\lambda_{430\ nm}$; red dot, $\lambda_{580\ nm}$; blue triangle, $\lambda_{760\ nm}$.

To further investigate the effects of temperature upon the formation of $[Cu^{II}(\eta^{1}\text{-}O_2^{\bullet-})(^{tpb3}TPA)]^{+}$, dioxygen was bubbled into a THF solution of $[Cu^{I}(^{tpb3}TPA)(NCMe)]^{+}$ at various temperatures from 0 to -90°C (**Figure 4.16**). As expected for entropically disfavoured binding of O_2, the absorption coefficients of the features at 430, 580 and 760 nm increase as the temperature is incrementally decreased. In addition, it was worth noting that the superoxocopper(II) intermediate could be clearly observed at temperatures as high as 0°C. This is truly remarkable and contrasts starkly with superoxocopper(II) complexes supported by other TPA-based ligands (and all other neutral N-donor ligands), none of which were stable at temperatures exceeding -80°C. This remarkable stability affords the opportunity to study the reactivity of superoxocopper(II) complexes at higher temperatures, where study of reaction with substrates containing stronger O-H, N-H or C-H bonds is a more feasible prospect.

Despite the high stability of the $[Cu^{II}(\eta^{1}\text{-}O_2^{\bullet-})(^{Ar3}TPA)]^{+}$ complexes, and the use of many different solvent mixture and counterions, thus far, we have been unable to grow single crystals

of this complex suitable for X-ray crystallographic studies. This problem was also encountered for the copper(I) complexes and can be attributed to the high solubility of the ^{Ar3}TPA complexes in most organic solvents and the large void spaces generated by the bulky aryl groups, which leads to extensive incorporation of solvent molecules.

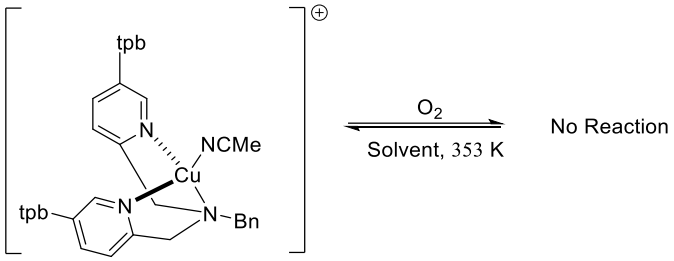

Scheme 4.4: Attempted oxygenation of $[Cu^{I}(^{tpb2}BnBPA(NCMe)][B(C_6F_5)_4]$ (0.5 mM)

By comparison, oxygenation studies of the $[Cu^{I}(^{Ar2}RBPA)(NCMe)]^{+}$ complexes proved more troublesome. For instance, no reaction was observed when dioxygen was bubbled into solutions of $[Cu^{I}(^{tpb2}BnBPA)(NCMe)]^{+}$ in both acetone and THF solution (**Scheme 4.4**). This was unexpected as $[Cu^{I}(BnBPA)(NCMe)]^{+}$ has been reported to exhibit reaction with O_2 to yield a $Cu^{III}_2(\mu\text{-}O)_2$ species.[10,22,25] Efforts to reproduce this literature precedent also met with difficulties, which suggests that our current experimental set-up is imperfect. This could be due to adventitious moisture, which is a major problem in highly humid Singapore, or the presence of solvent impurifies. Efforts to resolve this problem are ongoing.

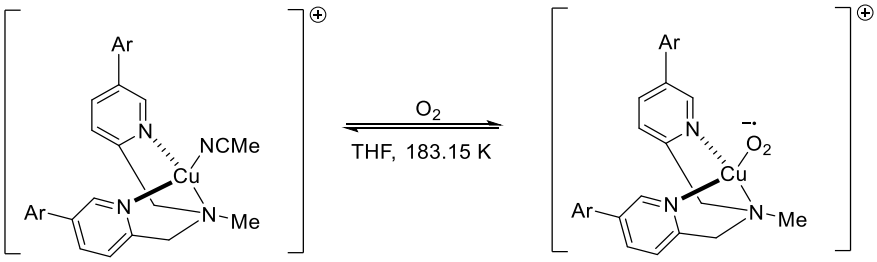

Scheme 4.5: Oxygenation of $[Cu^{I}(^{tpb2}MeBPA)(NCMe)][B(C_6F_5)_4]$ in THF (0.5 mM)

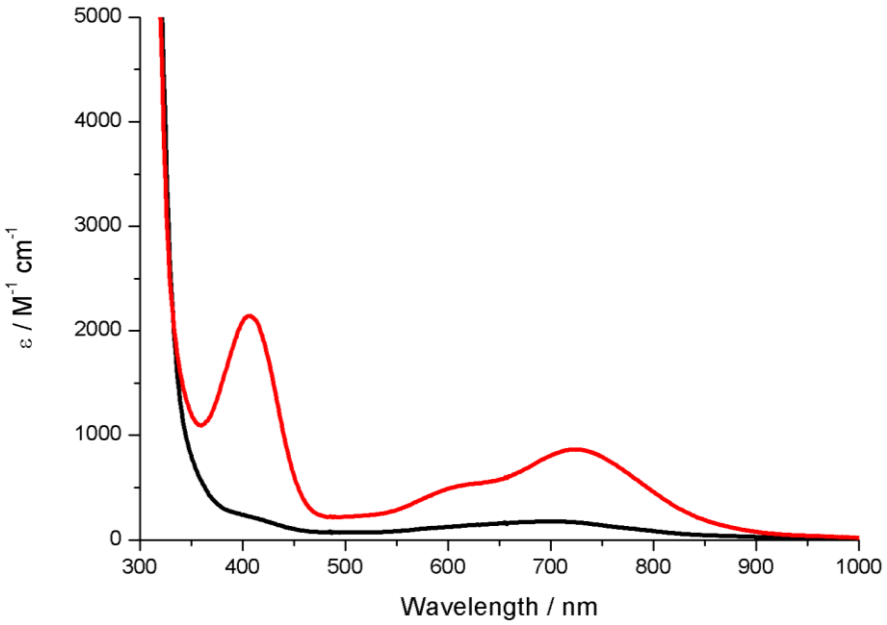

Figure 4.17: UV-vis spectrum of [Cu^{I}(^{Ar2}MeBPA)(MeCN)][$B(C_6F_5)_4$] (black line) and its oxygenated product (red line), recorded in THF solution (0.5 mM) at -85°C.

In contrast, introducing dioxygen into THF solutions of [Cu^{I}(^{tpb2}MeBPA)]$^{+}$ (0.5 mM) at -90°C afforded a green species (**Scheme 4.5**), whose UV-vis spectrum (**Figure 4.15**) displayed absorption maxima at 410 nm (ε_{max} = 2150 M^{-1} cm^{-1}) and 730 nm (ε_{max} = 850 M^{-1} cm^{-1}), plus a shoulder at 600 nm (ε = 490 M^{-1} cm^{-1}). These features are diagnostic of successful superoxocopper(II) complex formation and are very similar to those of Itoh's tridentate ligand system, but lower extinction coefficients are observed in our case (**Table 4.3)**.[18] In contrast, it differed from the [Cu^{II}(η^1-$O_2^{\bullet-}$)(*N*,*N*′-bis(2,6-diisopropylphenyl)-2,6-pyridinedicarboxamide)]$^{+}$, suggesting which could due to a difference in the nature of the complex. A similar result was also observed for [Cu^{I}(^{tpy2}MeBPA)(NCMe)]$^{+}$. The superoxocopper(II) complex supported by the ^{tpy2}MeBPA ligand is stable only at temperatures lower than -85°C. Upon moving to higher temperatures, these intermediates decayed to unidentified species that did not resemble any known copper-oxygen adducts.

Table 4.3: UV-vis spectroscopic data for mononuclear end-on superoxocopper(II) complex supported by tridentate ligands

$[Cu^{II}(\eta^1\text{-}O_2^{\bullet-})(L)]^+$ where L =	λ_{max}/nm (ε_{max}/M^{-1} cm^{-1})	Reference
^{tpb2}MeBPA	410 (2150) 600 (490) 730 (850)	This work
^{tpy2}MeBPA	400 (2580) 600 (550) 720 (860)	This work
N,N'-bis(2,6-diisopropylphenyl)-2,6-pyridinedicarboxamide	627 (1700)	[26]
Cyclic tridentate	397 (4200) 570 (850) 705 (1150)	[18]

4.2.4 Reactivity Studies of Superoxocopper(II) Complex

Thus far, only the reactivity of $[Cu^{II}(\eta^1\text{-}O_2^{\bullet-})(^{tpb3}TPA)]^+$ and $[Cu^{II}(\eta^1\text{-}O_2^{\bullet-})(^{tpy3}TPA)]^+$ with the O-H bond bonds of a variety of substrates has been studied. We chose to focus on O-H containing substrates because they predominate in the literature, and this allows us to benchmark the reactivity of our complexes. The progress of all reactions was monitored using UV-vis spectroscopy.

4.2.4.1 Reaction with TEMPO-H

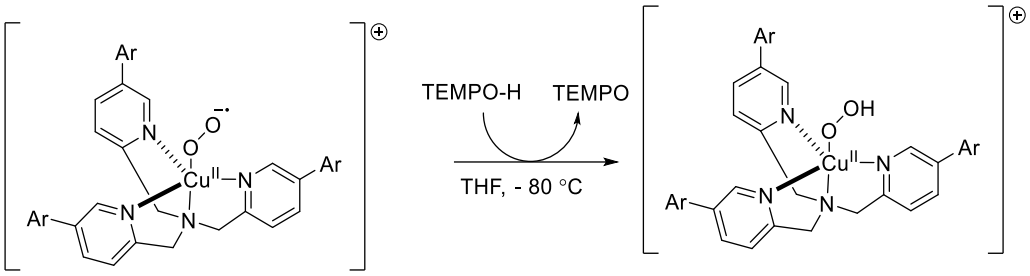

Scheme 4.6: Reaction of $[Cu^{II}(\eta^1\text{-}O_2^{\bullet-})(^{tpb3}TPA)]^+$ with TEMPO-H.

Initially, $[Cu^{II}(\eta^1\text{-}O_2^{\bullet-})(^{tpb3}TPA)]^+$ was treated with TEMPO-H (10 eq) at -80 °C, which contains a weak O-H possessing a bond dissociation energy (BDE) of 66.5 kcal mol^{-1} (**Scheme 4.6**). The resulting reaction caused the UV-vis features of the superoxocopper(II) complex, at 420, 580 and 760 nm, to rapidly decay (k_{obs} was found to be 0.141 ± 0.004 s^{-1}) and commensurately a peak at 412 nm ($\varepsilon = 2200$ M^{-1} cm^{-1}) to grow (**Figure 4.18**). The latter feature was assigned to the hydroperoxocopper(II) complex $[Cu^{II}(OOH)(^{tpb3}TPA)]^+$. Similar reactivity was observed for $[Cu^{II}(\eta^1\text{-}O_2^{\bullet-})(^{tpb3}TPA)]^+$ (**Figure S5**).

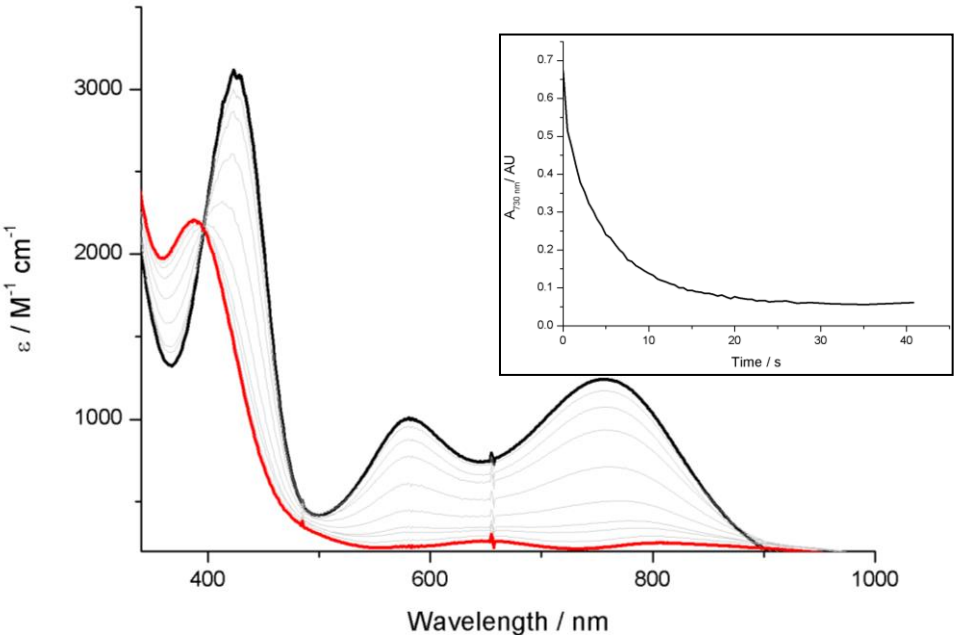

Figure 4.18: Reaction of $[Cu^{II}(\eta^1\text{-}O_2^{\bullet-})(^{tpb3}TPA)]^+$ (0.5 mM) with 10 eq of TEMPO-H at -80°C in THF. **Inset:** Time trace for decay of asorption maxima at 370 nm ($A_{730\ nm}$).

For comparison, reaction of $[Cu^{II}(\eta^1\text{-}O_2^{\bullet-})(TMG_3tren)]^+$ with TEMPO-H to give $[Cu^{II}(OOH)(TMG_3tren)]^+$ required 1 h for full conversion,[17] whereas reaction for the ^{Ar3}TPA supported complexes was complete within 20 s. The complex $[Cu^{II}(OOH)(^{tpb3}TPA)]^+$ generated via this means was found to display good stability at -80°C, but underwent full decay at -40°C within 10 s. This high instability of a hydroperoxocopper(II) complex relative to the corresponding superoxocopper(II) complex has previously been observed for the TMG_3tren ligand system, where $[Cu^{II}(\eta^1\text{-}O_2^{\bullet-})(TMG_3tren)]^+$ was also found to be stable at -80°C, while $[Cu^{II}(OOH)(^{tpb3}TPA)]^+$ would cause ligand hydroxylation. Our observation, seemingly, supports the notion that hydroperoxocopper(II) species are more reactive than their superoxocopper(II) congeners. However, more studies are needed to confirm this suggestion for the ^{tpb3}TPA systems.

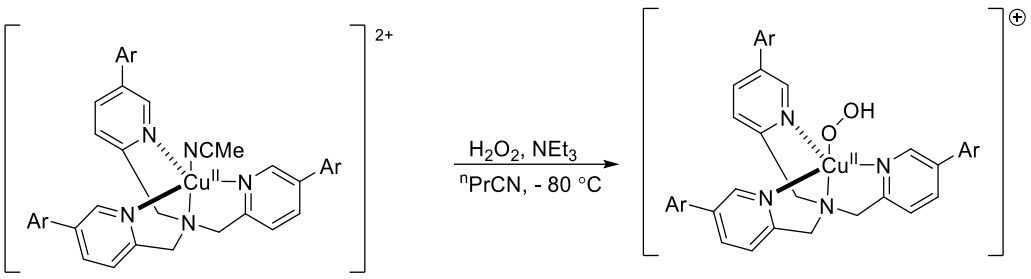

Scheme 4.7: Formation of $[Cu^{II}(OOH)(^{Ar3}TPA)]^+$ from copper(II) starting complexes using a combination of hydrogen peroxide and triethylamine.

To confirm formation of a hydroperoxocopper(II) complex, an independent synthesis was conducted by reacting $[Cu^{II}(^{tpb3}TPA)(NCMe)]^{2+}$ with hydrogen peroxide and the base triethylamine (**Scheme 4.7**), in ^{n}PrCN solution at -80°C. This yielded a species with an absorption centred at 400 nm (ε = 1600 M^{-1} cm^{-1}), which is very similar to the species formed by reaction of TEMPO-H with $[Cu^{II}(\eta^1\text{-}O_2^{\bullet-})(^{tpb3}TPA)]^+$ (**Figure 4.19**) and, thereby, supports the notion that the latter is a hydroperoxocopper(II) complex. It is worth mentioning that the baseline in the reaction conducted in ^{n}PrCN is elevated and this is likely due to the poor

solubility of one of the reaction components in this solvent at low temperatures. We suspect ice formation, as our original H_2O_2 solution was aqueous.

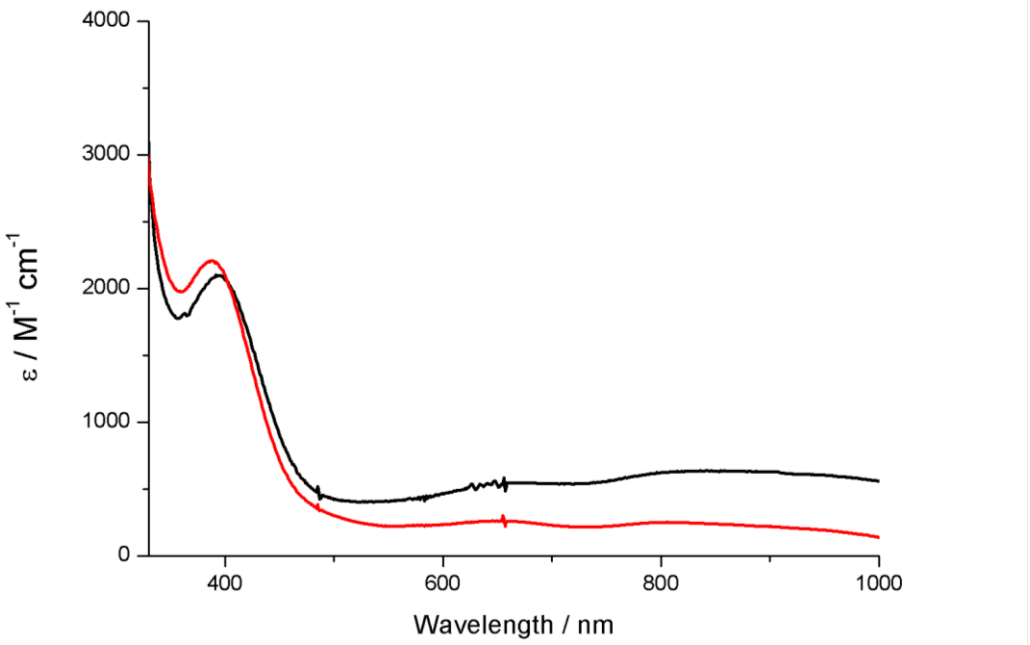

Figure 4.19: UV-vis spectra of $[Cu^{II}(OOH)(^{tpb3}TPA)]^+$ (0.5 mM) generated by the methods described in **Scheme 4.6** (red line) and **Scheme 4.7** (black line).

4.2.4.2 Reaction with Phenols

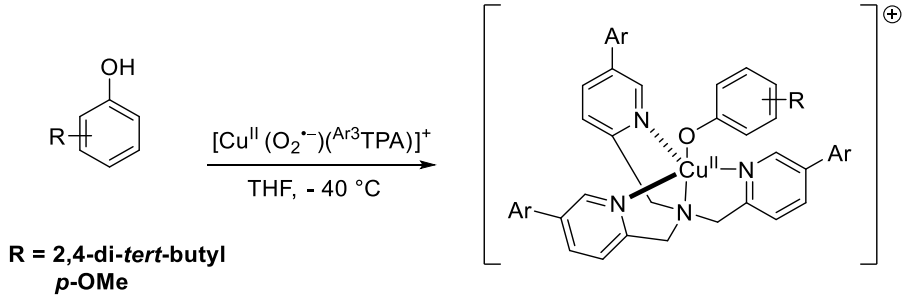

R = 2,4-di-*tert*-butyl
***p*-OMe**

Scheme 4.8: Reaction of 2,4-di-*tert*-butylphenol with superoxocopper(II) complex (0.5 mM), in THF solution at -40°C.

Initially, attempts were made to react the superoxocopper(II) complex supported by ^{tbp3}TPA with 2,4-di-*tert*-butylphenol (**Scheme 4.8**). This led to slow decay of $[Cu^{II}(\eta^1\text{-}O_2^{\bullet-})(^{tpb3}TPA)]^+$ and formation of a UV-vis feature at 580 nm (ε_{max} = 1500 M^{-1} cm^{-1}, **Figure 4.20**). However, no homo-coupled 2,4-di-*tert*-butylphenol product was observed, but phenoxide complex

$[Cu^{II}(^{tpb3}TPA)(OAr)]^+$ was identified using ESI-MS. Similar results were observed when *para*-methoxyphenol, which has a BDE of 85.2 kcal mol^{-1}, was used as a substrate. This indicates that the bulky aryl substituents in this ligand allow significant access to the copper centre, despite them being sufficient to prevent dicopper complex formation. To avoid phenoxide complex formation, reaction with 2,6-disubstituted phenols was investigated.

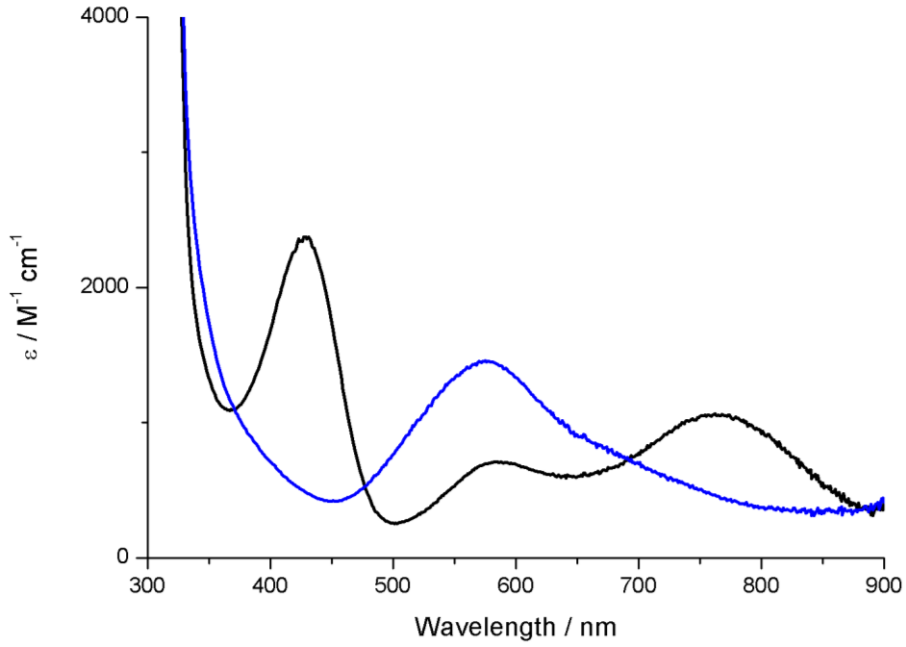

Figure 4.20: UV-Vis spectra of product (blue line) of reaction of $[Cu^{II}(\eta^1\text{-}O_2^{\bullet-})(^{tpb3}TPA)]^+$ (black line) with 2,4-di-*tert*-butylphenol in THF solution (0.5 mM), as illustrated in **Scheme 4.8**.

As a consequence of its relatively weak O-H bond, reaction of 2,6-di-*tert*-buty-4-methoxyphenol with $[Cu^{II}(\eta^1\text{-}O_2^{\bullet-})(^{Ar3}TPA)]^+$ could be performed from -40°C to -85°C (**Figure 4.21** and **Figure S6**), whereas reaction kinetics for the rest of the phenol substrates could only be performed at -40 °C. In all cases, addition of phenol substrates caused the features of the superoxocopper(II) complexes to undergo pseudo-first order decay. The observed rate constants, k_{obs}, obtained show a linear dependence upon substrate concentration (**Figure S6 – S15**). This indicates that the reaction is first order in both phenol and superoxocopper(II)

complex. Fitting of the data yielded second order rate constansts, k_2, and they are listed alongside those of known superoxocopper(II) complexes in **Table 4.4**.

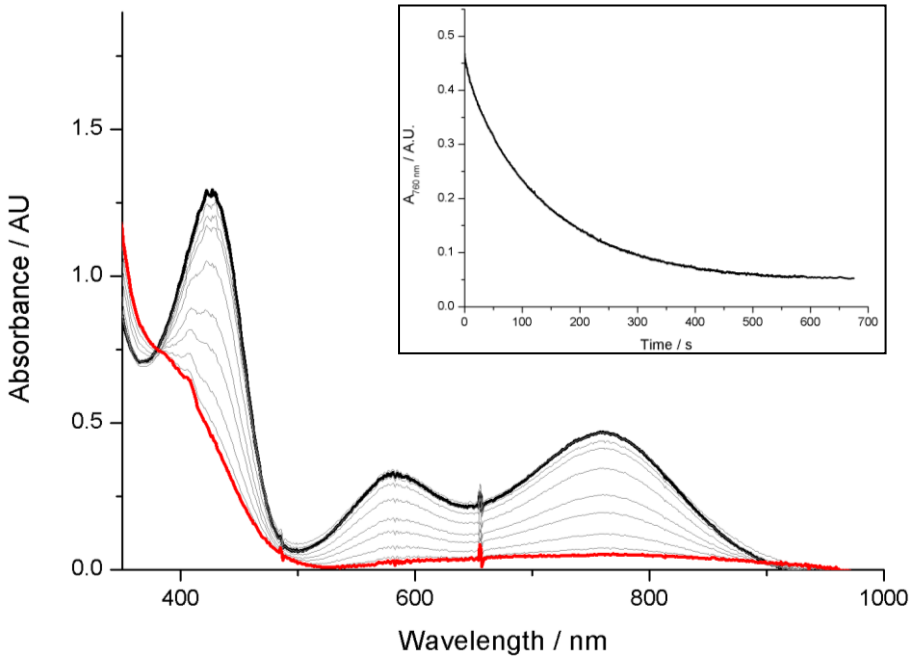

Figure 4.21: UV-vis plot showing reaction of $[Cu^{II}(\eta^1\text{-}O_2^{\bullet-})(^{tpb3}TPA)]^+$ with 2,6-di-*tert*-buty-*para*-methoxyphenol at -40 °C. **Inset:** Time trace for decay of the 760 nm UV-vis feature.

Table 4.4: Comparion of the second order rate constants (k_2) of reaction of superoxocopper(II) complexes supported TPA ligands with 2,6-di-*tert*-butylphenols.

2,6-di-*tert*-butyl-*para*-R-phenol (OH BDE)	k_2 / M^{-1} s^{-1}				
	^{tpy3}TPA -40°C	^{tpb3}TPA -40°C	TPA -135°C[13]	F_3BA -135°C[13]	^{DMM}TPA -92°C[12]
OMe (79.6 kcal mol^{-1})	6.54 ± 6.5 x 10^{-2}	8.48 ± 1.7 x 10^{-1}	3.11 x 10^{-1}	11.47 x 10^{-1}	23
OCH_2CF_3	Not performed	8.02 x 10^{-1} ± 1.7 x 10^{-1}	Not reported	Not reported	0.81
Me (80.1 kcal mol^{-1})	7.99 x 10^{-2} ± 5.65 x 10^{-3}	1.19 x 10^{-1} ± 6.79 x 10^{-3}	Not reported	Not reported	4.2 x 10^{-2}
Et (80.0 kcal mol^{-1})	Not performed	1.02 x 10^{-1} ± 5.12 x 10^{-3}	Not reported	Not reported	2.7 x 10^{-2}
t-Bu (82.3 kcal mol^{-1})	5.01 x 10^{-2} ± 3.48 x 10^{-3}	6.29 x 10^{-2} ± 3.48 x 10^{-3}	Not reported	Not reported	8.00 x 10^{-3}

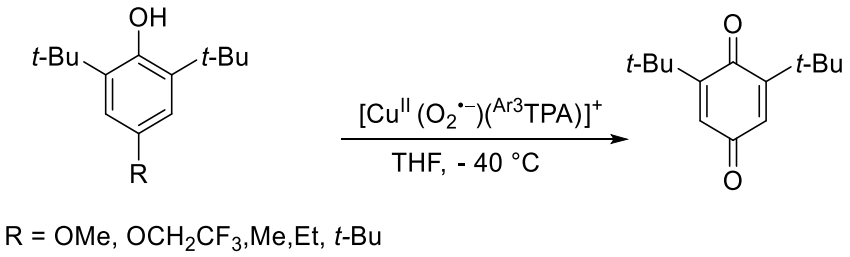

R = OMe, OCH_2CF_3,Me,Et, *t*-Bu

Scheme 4.9: Reaction upon treatment of $[Cu^{II}(\eta^1\text{-}O_2^{\bullet-})(^{Ar3}TPA)]^+$ with 2,6-di-*tert*-butylphenol, with various substituents at the para position.

Reaction of $[Cu^{II}(\eta^1\text{-}O_2^{\bullet-})(^{Ar3}TPA)]^+$ with 2,6-di-*tert*-butyl-4-R-phenols, at -40°C, was found (by GC-MS) to yield 2,6-di-*tert*-butylbenzoquinone as the final organic product (**Scheme 4.9**). In the case of both $[Cu^{II}(\eta^1\text{-}O_2^{\bullet-})(^{tpb3}TPA)]^+$ and $[Cu^{II}(\eta^1\text{-}O_2^{\bullet-})(^{tpy3}TPA)]^+$, the yields obtained for the phenols with R = OMe, Me and ^{t}Bu were 34, 40 and 50 %, respectively. The observation of a maximum yield of only 50 % was rationalized, by Karlin and co-workers, on the basis that 2 equiv of superoxocopper(II) complex are required to react with 1 equiv of phenol, thus, superoxocopper(II) complexes are potentially 1 electron oxidant.[12] They also suggested that two electron oxidation was observed from the reaction of superoxocopper(II) complex with

2,6-di-*tert*-butyl-*para*-alkoxy substrate, coupled with hydrolysis. On the other hand, 2,6-ditertbutyl-*para*-alkyl-phenol would react with superoxocopper(II) complex via four-electron transfer. Interestingly, as was previously reported by Karlin and co-workers,[12] no reaction was observed upon addition of 2,6-di-*tert*-butylphenol (BDE = 82.7 kcal mol^{-1}) to $[Cu^{II}(\eta^1\text{-}O_2^{\bullet-})(^{Ar3}TPA)]^+$, even though the BDE is only marginally higher than of 2,4,6-tri-*tert*-butylphenol.

From the data in **Table 4.4**, it is clear that although both $[Cu^{II}(\eta^1\text{-}O_2^{\bullet-})(^{tpb3}TPA)]^+$ and $[Cu^{II}(\eta^1\text{-}O_2^{\bullet-})(^{tpy3}TPA)]^+$ display significant reactivity towards phenols, it is more sluggish than that of other TPA-ligated systems. For instance, a k_2 value of 23 M^{-1} s^{-1} was reported for reaction of $[Cu^{II}(\eta^1\text{-}O_2^{\bullet-})(^{DMM}TPA)]^+$ with 4-methoxy-2,6-di-*tert*-butylphenol at -92°C,[12] while a k_2 value of 6.54 ± 6.5 x 10^{-2} M^{-1} s^{-1} at -40°C was recorded for the reaction of the same substrate with $[Cu^{II}(\eta^1\text{-}O_2^{\bullet-})(^{tpb3}TPA)]^+$. Taking the temperature difference into account, we can conclude that the reactivity of the $[Cu^{II}(\eta^1\text{-}O_2^{\bullet-})(^{Ar3}TPA)]^+$ complexes are greatly supressed. The obvious inference would be that the bulky aryl groups sterically inhibits approach of the 2,6-di-*tert*-butylphenol substrates. However, the thermodynamic effects of substitution of the pyridine donors upon superoxocopper(II) complex reactivity are not clear.

On the other hand, the $[Cu^{II}(\eta^1\text{-}O_2^{\bullet-})(^{Ar3}TPA)]^+$ complexes are clearly more reactive than $[Cu^{II}(\eta^1\text{-}O_2^{\bullet-})(TMG_3tren)]^+$, for which reaction with 4-methoxy-2,6-di-*tert*-butylphenol required 48 h, and $[Cu^{II}(\eta^1\text{-}O_2^{\bullet-})(HIPT_3tren)]^+$, for which did not react at all with phenols. Of course the latter two systems have different donor atoms and steric profiles, which greatly complicates any comparison. It shoud be noted that the reaction rate of $[Cu^{II}(\eta^1\text{-}O_2^{\bullet-})(^{tpb3}TPA)]^+$ and $[Cu^{II}(\eta^1\text{-}O_2^{\bullet-})(^{tpy3}TPA)]^+$ towards 2,6-di-*tert*-butyl-*para*-R-phenol were comparable to each other (i.e., their k_2 values are effectively identical). This indicates that the additional *para* phenyl group in the tpb substituent, relative to tpy, does not inhibit reaction. This is a little surprising and, combined with the unknown impact of pyridine ring substituents

on reactivity of superoxocopper(II) complexes, spurred us to investigate the mechanistic properties of our complexes.

4.2.4.3 Activation Parameters for Reaction With Phenol Substrates

Since our $[Cu^{II}(\eta^1\text{-}O_2^{\bullet-})(^{Ar3}TPA)]^+$ complexes are stable over a much wider temperature range than other TPA-ligated superoxocopper(II) complexes, the activation parameters for reaction with the substrate 2,6-di-*tert*-butyl-*para*-methoxyphenol could be investigated by constructing Eyring plots (**Figure 4.22**). Comparison was made with $[Cu^{II}(\eta^1\text{-}O_2^{\bullet-})(^{DMM}TPA)]^+$, the only other superoxocopper(II) complex for which such studies have been performed.[12] As previously mentioned, the reactivity of $[Cu^{II}(\eta^1\text{-}O_2^{\bullet-})(^{DMM}TPA)]^+$ could only be studied over a 15°C temperature range, which limits the accuracy of the kinetic parameters obtained.

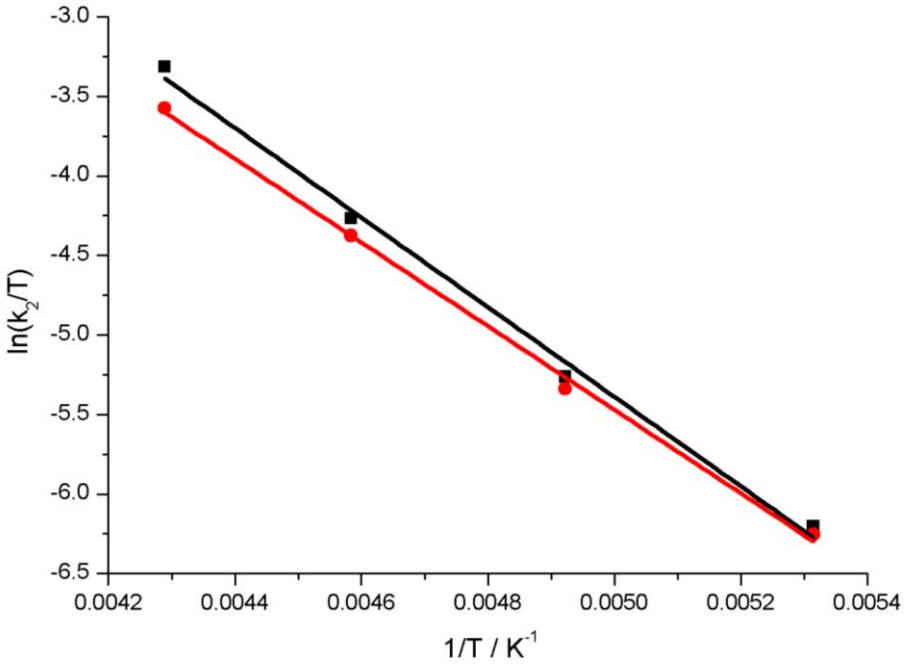

Figure 4.22: Erying plots for reaction of $[Cu^{II}(\eta^1\text{-}O_2^{\bullet-})(^{tpb3}TPA)]^+$ (black line) and $[Cu^{II}(\eta^1\text{-}O_2^{\bullet-})(^{tpy3}TPA)]^+$ (red line) with 2,6-di-*tert*-butyl-*para*-methoxyphenol.

Table 4.5: Activation parameters extracted from Eyring plots for reaction of $[Cu^{II}(\eta^1\text{-}O_2^{\bullet-})(^{Ar3}TPA)]^+$ with 2,6-di-*tert*-butyl-*para*-methoxy-phenol.

	$[Cu^{II}(\eta^1\text{-}O_2^{\bullet-})(^{tpy3}TPA)]^+$	$[Cu^{II}(\eta^1\text{-}O_2^{\bullet-})(^{tpb3}TPA)]^+$	$[Cu^{II}(\eta^1\text{-}O_2^{\bullet-})(^{DMM}TPA)]^+$
$\Delta H^{\neq}$ (kJ mol^{-1})	+ 21.9	+ 23.4	+15.1
$\Delta S^{\neq}$ (J mol^{-1} K^{-1})	-133.95	-125.24	-133.98

We studied the rate of reaction of $[Cu^{II}(5^{tpb3}TPA)O_2^{\bullet-}]^+$ and $[Cu^{II}(5^{tpy3}TPA)O_2^{\bullet-}]^+$ with 4-methoxy-2,6-di-*tert*-butylphenol over the temperature range 188 to 233 K. Fitting of the resulting Erying plots of $[Cu^{II}(5^{tpb3}TPA)O_2^{\bullet-}]^+$ and $[Cu^{II}(5^{tpy3}TPA)O_2^{\bullet-}]^+$ (**Figure 4.22**) yielded respective enthalpies of activation, $\Delta H^{\neq}$, of +23.4 and +21.9 kJ mol^{-1} and entropies of activation, $\Delta S^{\neq}$, of -125.24 and -133.95 J mol^{-1} K^{-1} (**Table 4.5**). Remarkably, despite differences in steric profile of the ligands, the $\Delta S^{\neq}$ for $[Cu^{II}(5^{tpb3}TPA)O_2^{\bullet-}]^+$ and $[Cu^{II}(5^{tpy3}TPA)O_2^{\bullet-}]^+$ are not only *very* similar to one another, they are effectively identical to values reported for $[Cu^{II}(^{DMM}TPA)O_2^{\bullet-}]^+$.[12] If steric factors were the source of lower reactivity of the former two superoxocopper(II) complexes, one might expect to see larger entropic barriers to reaction. However, this was not the case. Instead, the major differences between the activation parameters derived from enthalpic barriers to reaction, with that for $[Cu^{II}(^{DMM}TPA)O_2^{\bullet-}]^+$ being much smaller. Although steric inhibition of reaction can have enthalpic consequences, differences in redox potential of the superoxocopper(II) complexes and proton affinity of their 1 electron reduced products cannot be disregarded.

4.2.4.4 Mechanistic Analysis on Reaction With Phenols

To gain insight into the rate determining step for reaction of $[Cu^{II}(\eta^1\text{-}O_2^{\bullet-})(^{tpb3}TPA)]^+$ with phenols, this superoxocopper(II) complex was reacted with the O-D deuterated 4-methoxy-2,6-di-*tert*-butylphenol. From measurement of the k_2 for this reaction (k_H of 8.48 and k_D of 0.666 M^{-1} s^{-1}) at -40°C, a kinetic isotope effect (KIE) value of 13 was obtained (**Figure 4.23**). This is similar to that reported by Karlin and co-workers for $[Cu^{II}(\eta^1\text{-}O_2^{\bullet-})(^{DMM}TPA)]^+$,[12] and is

indicative of a rate determining hydrogen atom transfer (HAT) to yield a phenoxyl radical, rather than rate determining electron transfer or proton transfer. Consistent with previous suggestions for $[Cu^{II}(\eta^1\text{-}O_2^{\bullet-})(^{DMM}TPA)]^+$, the KIE for this reaction was found to be effectively temperature independent (**Table 4.6** and **Figure S16**).

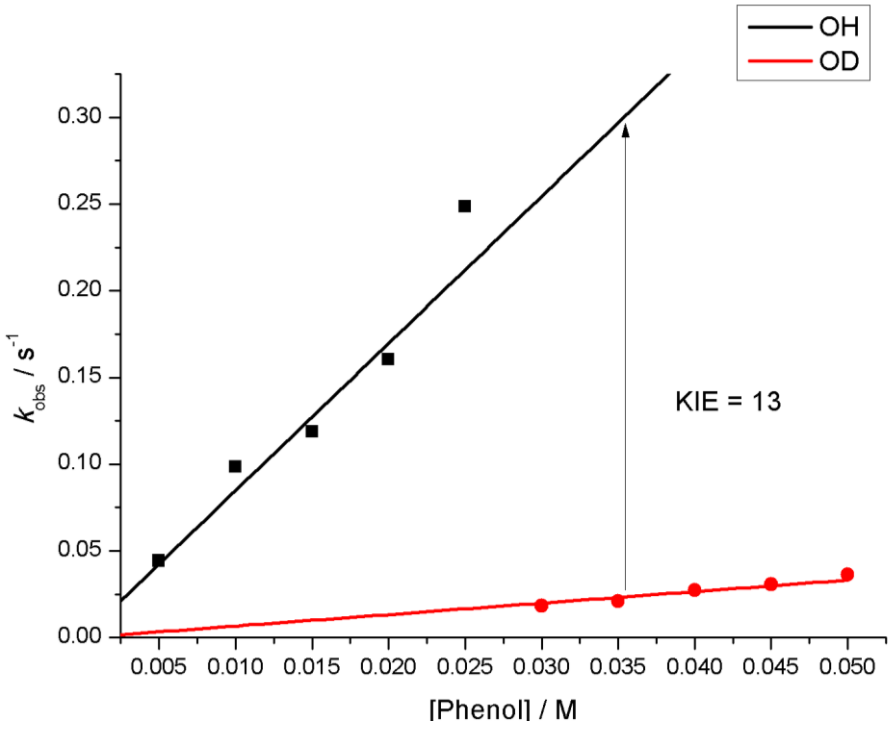

Figure 4.23: Plot of k_{obs} (at -40°C) for reaction of $[Cu^{II}(\eta^1\text{-}O_2^{\bullet-})(^{tpb3}TPA)]^+$ with 2,6-di-*tert*-butyl-*para*-methoxyphenol (black line) and its O-D deuterated analog (red line), from which a KIE (k_H/k_D) of 13 was obtained.

Table 4.6: Temperature dependent second order rate constants and KIE for reaction of $[Cu^{II}(\eta^1\text{-}O_2^{\bullet-})(^{tpb3}TPA)]^+$ 2,6-di-*tert*-butyl-*para*-methoxyphenol (k_H) and its O-D deuterated analog (k_D).

Temperature / K	k_H / M^{-1} cm^{-1}	k_D / M^{-1} cm^{-1}	KIE
233.15	8.48	6.66 x 10^{-1}	13
218.15	3.06	2.76 x 10^{-1}	11
203.15	1.05	7.79 x 10^{-2}	13
188.15	3.81 x 10^{-1}	3.32 x 10^{-2}	12

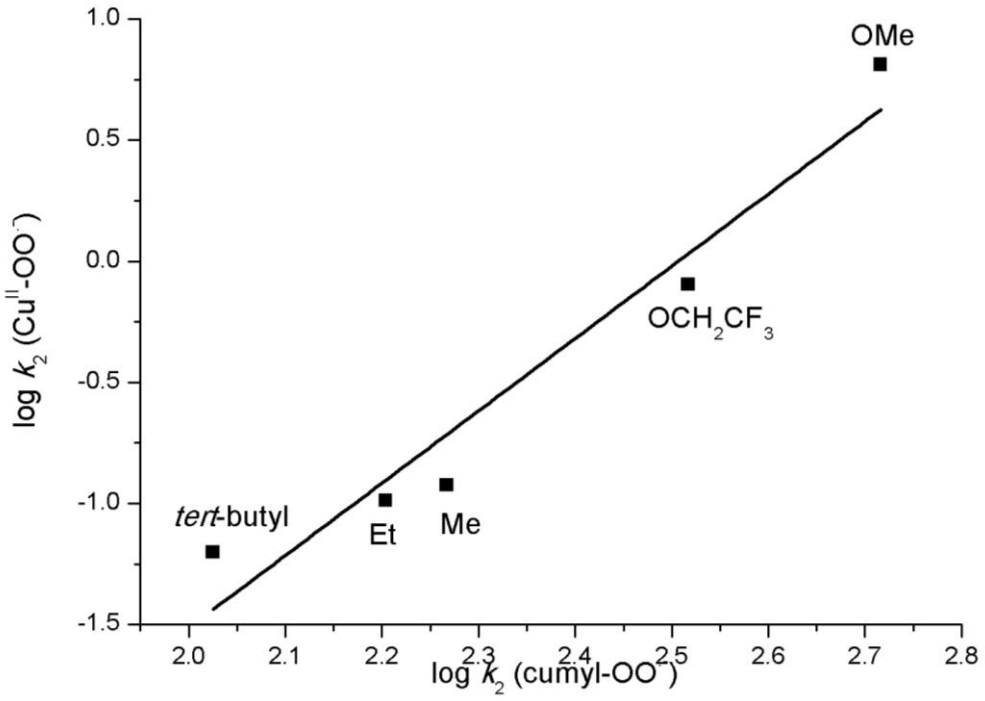

Figure 4.24: Correlation of log k_2 of $[Cu^{II}(\eta^1\text{-}O_2^{\bullet-})(^{tpb3}TPA)]^+$ against log k_2 of $[cumyl\text{-}O_2^{\bullet-}]^+$ on the 2,6-di-*tert*-butyl-*para*-R-phenol.

To further explore the nature of rate determining HAT step, a plot of k_2 of the $[Cu^{II}(\eta^1\text{-}O_2^{\bullet-})(^{tpb3}TPA)]^+$ for reaction with a series of phenols vs published k_2 values for reaction of cumylperoxyl radical with the same phenols has been constructed (**Figure 4.24**).[27,28] A comparison with the reactivity of cumylperoxyl radical was made because it is known to react with phenols via a pure, fully concerted HAT. Additionally, the relatively large variation in the acidity and oxidation potentials of phenols complicates any attempts to correlate the k_2 values for their reaction with superoxocopper(II) complexes versus phenol O-H BDE. Thus, an indirect approach is required to examine the nature of the HAT step.

In any case, the plot in **Figure 4.24** is linear and has slope of 2.98. This is significantly larger than the value of 1 expected for a fully concerted HAT reaction between $[Cu^{II}(\eta^1\text{-}O_2^{\bullet-})(^{tpb3}TPA)]^+$ and phenol. This implies that the HAT is asynchronous. However, this value is significantly lower than that obtained for $[Cu^{II}(\eta^1\text{-}O_2^{\bullet-})(^{DMM}TPA)]^+$, where the

correposnding slope was 4.85. The larger value for the latter would seem to imply greater asynchronicity in the HAT reaction.

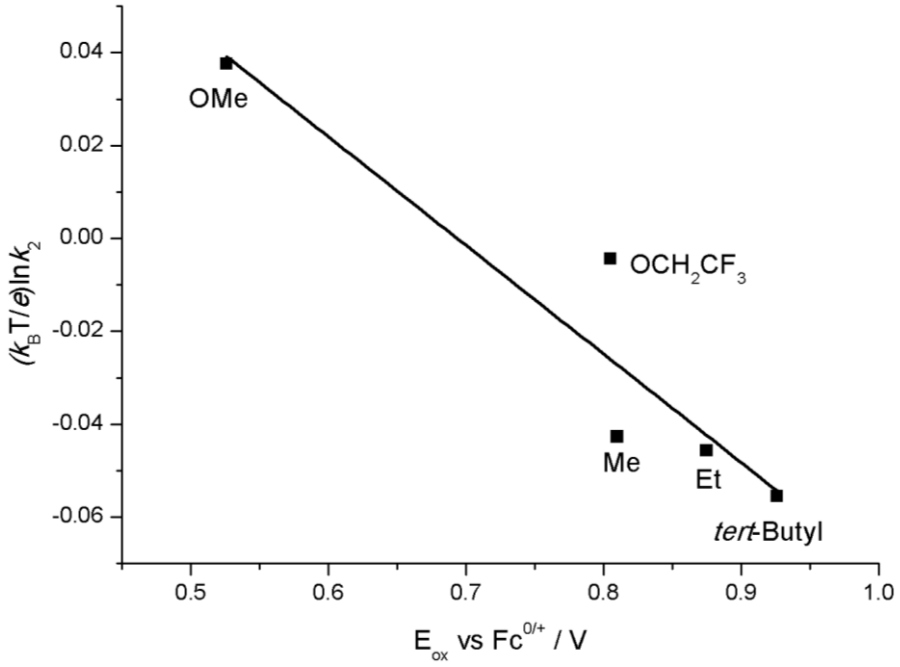

Figure 4.25: Plot of $(k_BT/e)\ln k_2$ against oxidation potential of the phenols.

To examine the origin of the asynchronicity of the rate determining HAT step, a plot of $(k_BT/e)\ln k_2$ versus oxidation potential of the phenol substrates was constructed (**Figure 4.25**). A linear plot with a slope of -0.23 was obtained. If a proton transfer step preceded the electron transfer step (a PT-ET reaction), a positive slope would be obtained for such a plot. This is because more electron deficient phenols are more acidic and in such a scenario they would exhibit faster reaction. Instead, given that a slope greater than 0.5 is expected for an initial discrete electron transfer step (in a ET-PT reaction), a slope of -0.23 implies that we have a true HAT reaction for which electron transfer is more advanced than proton transfer in the transition state. A similar negative slope of – 0.29 was observed by Karlin and co-workers for $[Cu^{II}(\eta^1\text{-}O_2^{\bullet-})(^{DMM}TPA)]^+$.[12] The slightly more negative value obtained in their case can be interpreted as reflecting a greater degree of charge transfer in the HAT transition state relative to $[Cu^{II}(\eta^1\text{-}O_2^{\bullet-})(^{tpb3}TPA)]^+$. This is consistent with the suggestion of greater asynchronicity in the reaction of $[Cu^{II}(\eta^1\text{-}O_2^{\bullet-})(^{DMM}TPA)]^+$ with phenols that was made above. Either way, the

k_2 values for reaction of superoxocopper(II) complexes with phenols are, as previously asserted,[12] highly sensitive to the redox potential of the phenols.

4.3 Conclusion

The installation of bulky triphenylbenzene or terphenyl substituents on the 5th position of the pyridine donors of TPA and BPA ligand systems allowed end-on superoxocopper(II) complexes to be cleanly formed (i.e., without any evidence of dicopper complex formation). The $[Cu^{I}(^{Ar3}TPA)(MeCN)]^{+}$ complexes displayed temperature-dependent reversible binding of O_2, superoxocomplex formation was observed as high as 0°C, and at no point was self-decay observed, either to thermodynamically favoured peroxo-bridged dicopper(II) complexes or other species. The resulting $[Cu^{II}(\eta^1\text{-}O_2^{\bullet-})(^{Ar3}TPA)]^{+}$ species retained many of the reactivity features of the TPA supported congeners. For instance, exposure to TEMPO-H yielded the corresponding hydroperoxocopper(II) complexes and they exhibited appreciable reactivity towards phenols. More specifically, $[Cu^{II}(\eta^1\text{-}O_2^{\bullet-})(^{Ar3}TPA)]^{+}$ was found to react with 2,6-di-*tert*-butyl-*para*-R-phenols at rates faster than other sterically encumbered systems, such $[Cu^{II}(\eta^1\text{-}O_2^{\bullet-})(TMG_3tren)]^{+}$, but appreciably slower than Karlin's published TPA systems.

The large temperature range over which our $[Cu^{II}(\eta^1\text{-}O_2^{\bullet-})(^{Ar3}TPA)]^{+}$ systems can be studied opens a lot of possibilities and allowed Eyring parameters be be measured for reaction with 4-methoxy-2,6-di-*tert*-butylphenol. Remarkably, the bulky aryl substituents of $[Cu^{II}(\eta^1\text{-}O_2^{\bullet-})(^{Ar3}TPA)]^{+}$ did not significantly alter the entropy of activation from $[Cu^{II}(\eta^1\text{-}O_2^{\bullet-})(^{DMM}TPA)]^{+}$, the only point of comparison. However, the enthalpic barrier to reaction was found to be significantly larger in the former. To a first approximation, this does not seem to be consistent with steric retardation of reactivity and, instead, differences in electronic properties can be inferred as the origin of the difference in reactivity. The greater asynchronicity in the rate determining HAT step, resulting from more extensive charge transfer, in reaction of $[Cu^{II}(\eta^1\text{-}O_2^{\bullet-})(^{DMM}TPA)]^{+}$ with phenols, suggested by our mechanistic studies for $[Cu^{II}(\eta^1\text{-}O_2^{\bullet-})(^{tpb3}TPA)]^{+}$, seemingly supports this notion. However, given that steric effects can have thermodynamic consequences, these conclusions are only tentative. It is likely that

theoretical calculations and/or electrochemical measurements will be required to clarify the origin of the comparatively low reactivity of the $[Cu^{II}(\eta^1\text{-}O_2^{\bullet-})(^{tpb3}TPA)]^+$ complexes.

In this chapter we also disclosed that $[Cu^{I}(^{tpb2}MeBPA)(MeCN)]^+$ reacts with O_2 to yield a superoxocopper(II) intermediate. However, this species formed with low extinction coefficients, which might imply low yields, and proved to be highly solvent sensitive. Furthermore, difficulties were met when trying to reproduce published chemistry for the BnBPA ligand (i.e., no reaction with dioxygen was observed). Taken together, we suspect solvent impurities and/or high humidity of Singapore are hampering our efforts to trap $[Cu^{II}(\eta^1\text{-}O_2^{\bullet-})(^{tpb2}MeBPA)]^+$ in high yield. Thus, we are trying to optimize and improve our methods for generation of this superoxocopper(II) complex, so that we probe its reactivity with substrates. This will help elucidate geometric effects upon reactivity of such species and, as such, provide insight into the coordinative preferences of the enzymatic systems.

4.4 Reference

(1) Bollinger, J. M.; Krebs, C. *Curr. Opin. Chem. Biol.* **2007**, *11*, 151–158.

(2) Klinman, J. P. *J. Biol. Chem.* **2006**, *281*, 3013–3016.

(3) Prigge, S. T.; Eipper, B. A.; Mains, R. E.; Amzel, L. M. *Science.*. **2004**, *304*, 864–867.

(4) Yoshizawa, K.; Kihara, N.; Kamachi, T.; Shiota, Y. *Inorg. Chem.* **2006**, *45*, 3034–3041.

(5) Cramer, C. J.; Tolman, W. B. *Acc. Chem. Res.* **2007**, *40*, 601–608.

(6) Elwell, C. E.; Gagnon, N. L.; Neisen, B. D.; Dhar, D.; Spaeth, A. D.; Yee, G. M.; Tolman, W. B. *Chem. Rev.* **2017**, *117*, 2059–2107.

(7) Que Jr, L.; Tolman, W. B. *Nature* **2008**, *455*, 333.

(8) Mirica, L. M.; Ottenwaelder, X.; Stack, T. D. P. *Chem. Rev.* **2004**, *104*, 1013–1046.

(9) Wei, N.; Murthy, N. N.; Chen, Q.; Zubieta, J.; Karlin, K. D. *Inorg. Chem.* **1994**, *33*, 1953–1965.

(10) Zhang, C. X.; Kaderli, S.; Costas, M.; Kim, E.; Neuhold, Y.-M.; Karlin, K. D.; Zuberbühler, A. D. *Inorg. Chem.* **2003**, *42*, 1807–1824.

(11) Maiti, D.; Fry, H. C.; Woertink, J. S.; Vance, M. A.; Solomon, E. I.; Karlin, K. D. *J. Am. Chem. Soc.* **2007**, *129*, 264–265.

(12) Lee, J. Y.; Peterson, R. L.; Ohkubo, K.; Garcia-Bosch, I.; Himes, R. A.; Woertink, J.; Moore, C. D.; Solomon, E. I.; Fukuzumi, S.; Karlin, K. D. *J. Am. Chem. Soc.* **2014**, *136*, 9925–9937.

(13) Bhadra, M.; Lee, J. Y. C.; Cowley, R. E.; Kim, S.; Siegler, M. A.; Solomon, E. I.; Karlin, K. D. *J. Am. Chem. Soc.* **2018**, *140*, 9042–9045.

(14) Kim, S.; Lee, J. Y.; Cowley, R. E.; Ginsbach, J. W.; Siegler, M. A.; Solomon, E. I.;

Karlin, K. D. *J. Am. Chem. Soc.* **2015**, *137*, 2796–2799.

(15) Würtele, C.; Gaoutchenova, E.; Harms, K.; Holthausen, M. C.; Sundermeyer, J.; Schindler, S. *Angew. Chem. Int. Ed.* **2006**, *45*, 3867–3869.

(16) Kobayashi, Y.; Ohkubo, K.; Nomura, T.; Kubo, M.; Fujieda, N.; Sugimoto, H.; Fukuzumi, S.; Goto, K.; Ogura, T.; Itoh, S. *Eur. J. Inorg. Chem.* **2012**, No. 29, 4574–4578.

(17) Maiti, D.; Lee, D.-H.; Gaoutchenova, K.; Würtele, C.; Holthausen, M. C.; Narducci Sarjeant, A. A.; Sundermeyer, J.; Schindler, S.; Karlin, K. D. *Angew. Chem. Int. Ed.* **2007**, *47*, 82–85.

(18) Kunishita, A.; Kubo, M.; Sugimoto, H.; Ogura, T.; Sato, K.; Takui, T.; Itoh, S. *J. Am. Chem. Soc.* **2009**, *131*, 2788–2789.

(19) Tano, T.; Okubo, Y.; Kunishita, A.; Kubo, M.; Sugimoto, H.; Fujieda, N.; Ogura, T.; Itoh, S. *Inorg. Chem.* **2013**, *52*, 10431–10437.

(20) Tahsini, L.; Kotani, H.; Lee, Y.-M.; Cho, J.; Nam, W.; Karlin, K. D.; Fukuzumi, S. *Chem. A Eur. J.* **2011**, *18*, 1084–1093.

(21) Yang, L.; Powell, D. R.; Houser, R. P. *Dalt. Trans.* **2007**, No. 9, 955–964.

(22) Lucas, H. R.; Li, L.; Sarjeant, A. A. N.; Vance, M. A.; Solomon, E. I.; Karlin, K. D. *J. Am. Chem. Soc.* **2009**, *131*, 3230–3245.

(23) Karlin, K. D.; Wei, N.; Jung, B.; Kaderli, S.; Zuberbuehler, A. D. *J. Am. Chem. Soc.* **1991**, *113*, 5868–5870.

(24) Karlin, K. D.; Kaderli, S.; Zuberbühler, A. D. *Acc. Chem. Res.* **1997**, *30*, 139–147.

(25) Kunishita, A.; Osako, T.; Tachi, Y.; Teraoka, J.; Itoh, S. *Bull. Chem. Soc. Jpn.* **2006**, *79*,

1729–1741.

(26) Donoghue, P. J.; Gupta, A. K.; Boyce, D. W.; Cramer, C. J.; Tolman, W. B. *J. Am. Chem. Soc.* **2010**, *132*, 15869–15871.

(27) Osako, T.; Ohkubo, K.; Taki, M.; Tachi, Y.; Fukuzumi, S.; Itoh, S. *J. Am. Chem. Soc.* **2003**, *125*, 11027–11033.

(28) Fukuzumi, S.; Shimoosako, K.; Suenobu, T.; Watanabe, Y. *J. Am. Chem. Soc.* **2003**, *125*, 9074–9082.

Chapter 5

Oxoiron(IV) Complexes Supported by ^{tpb3}TPA Ligand

5.1 Introduction

Oxoiron(IV) intermediates have been proposed to be the active oxidants responsible for substrate oxidation in a wide variety of non-heme iron-containing oxygenase enzymes, particularly those responsible for C-H bond oxidation. Several examples of such species have been trapped and spectroscopically characterized and shown in all instances to contain high-spin (S = 2) iron(IV). The most longstanding and thoroughly studied example is "Intermediate J" (**Figure 5.1**), the active oxidant of the enzyme α-ketoglutarate-dependent taurine dioxygenase (TauD), which is responsible for hydroxylation of taurine to aminoacetaldehye.[1,2] Nominally, Intermediate J has a trigonal bipyramidal geometry. However, this is uncertain and a distorted 6-coordinate geometry is possible if the succinate co-ligand binds in a bidentate fashion.

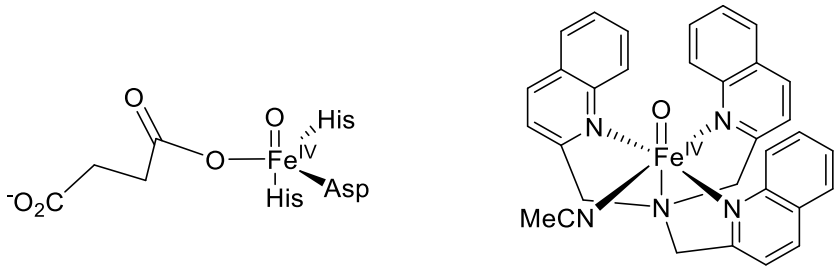

Figure 5.1: High-spin oxoiron(IV) complexes Intermediate J, from the enzyme TauD, and the synthetic complex $[Fe^{IV}(O)(TQA)(NCMe)]^{2+}$.

In parallel to characterization of the enzymatic oxoiron(IV) intermediates, a wide range of synthetic oxoiron(IV) complexes have been synthesized and characterized in terms of spectroscopic and reactivity properties.[3] Although the majority of the synthetic systems are intermediate-spin (S = 1), there are now several examples of high-spin oxoiron(IV) complexes. Computational studies predict that high-spin oxoiron(IV) complexes are more reactive than their intermediate-spin congeners. However, with the exception of $[Fe^{IV}(O)(TQA)(NCMe)]^{2+}$ (**Figure 5.1**), most of the high-spin systems reported (**Figure 5.2**) possess low reactivity

towards substrates containing strong C-H bonds.[4,5] This is because, unlike 6-coordinate $[Fe^{IV}(O)(TQA)(NCMe)]^{2+}$, whose spin-state is a consequence of a weak equatorial ligand field, most of the complexes achieve an $S = 2$ spin-state by using a bulky ligand to impose a trigonal bipyramidal (TBP) geometry at the metal centre (**Figure 5.3**).[3] The latter leads to degeneracy of the d_{xy} and d_{x2-y2} orbitals, which leads inexorably to a high-spin state. Unfortunately, the steric bulk required to enforce a TBP geometry appears to hinder reaction with substrates.[6]

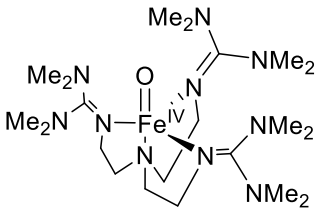

TMG$_3$tren
Que 2009

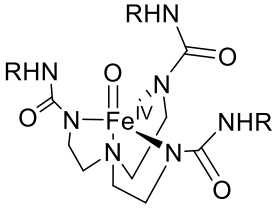

H_3buea
Borovik 2010

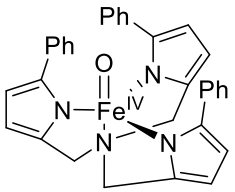

tpa^{Ph}
Chang 2010

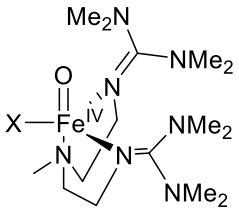

TMG$_2$dien
X=NCCH$_3$, N$_3$, Cl
Que 2010

Figure 5.2: Published trigonal bipyramidal high-spin ($S = 2$) oxoiron(IV) complexes

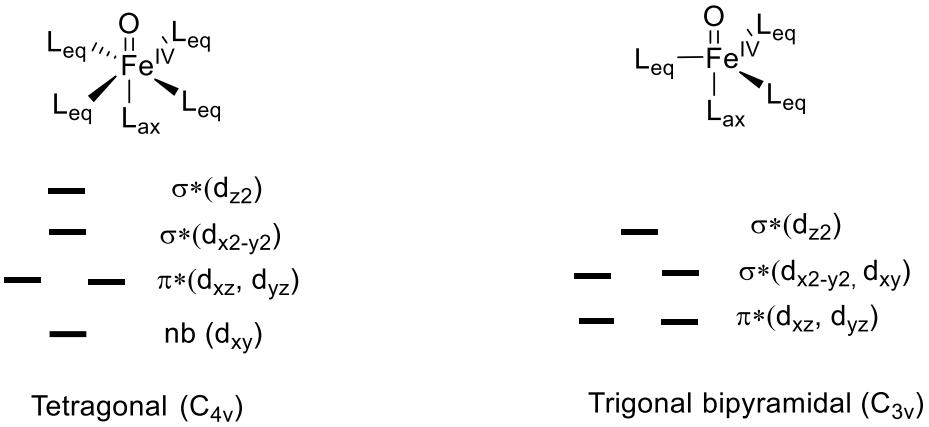

Figure 5.3: Ligand-field splitting diagram for oxoiron(IV) complexes with tetragonal and trigonal bipyramidal geometries.

It should be noted that some of the intermediate-spin oxoiron(IV) complexes supported by strong neutral N-donor atom ligands, such as N4Py, Me_3NTB and BnTPEN (**Figure 5.4**), possess good reactivity towards substrates with strong C-H bonds. In some cases, even comparable to the high-spin system $[Fe^{IV}(O)(TQA)(NCMe)]^{2+}$, which is the most reactive synthetic non-heme oxoiron(IV) complex that has been reported thus far.[3] The high reactivity of the intermediate-spin oxoiron(IV) complexes is, normally, attributed to the presence of a low-lying $S = 2$ reaction surface, on which the barrier for the rate determining hydrogen atom abstraction (HAA) reaction is calculated lower than that on the intermediate-spin reaction surface. [4] Spin crossover is believed to occur during the course of reaction and led to the phrase "two-state reactivity" being coined.

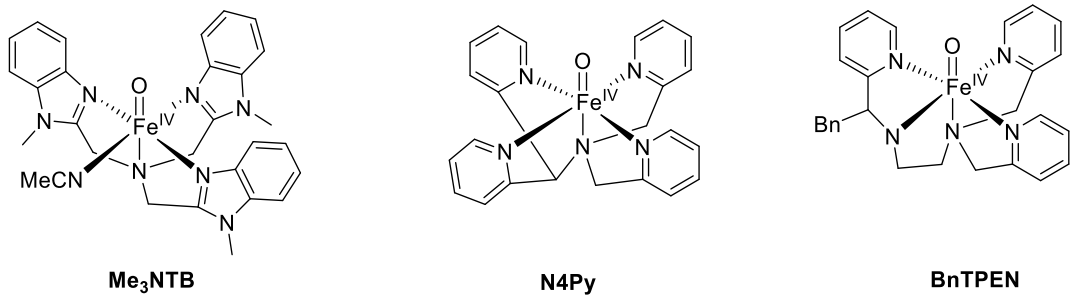

Figure 5.4: Selected S =1 oxoiron(IV) complexes that possess good reactivity towards substrates with strong C-H bonds

It is worth noting that the TQA ligand that supports the super reactive high-spin oxoiron(IV) complex $[Fe^{IV}(O)(TQA)(NCMe)]^{2+}$ is a derivative of tris(2-pyridylmethyl)amine, TPA. The parent TPA ligand was, itself, used to support the 6-coordinate complex $[Fe^{IV}(O)(TPA)(NCMe)]^{2+}$ (**Figure 5.5**), which was one of the earliest examples of a synthetic oxoiron(IV) complex and was prepared by reaction of $[Fe^{II}(TPA)(NCMe)_2]^{2+}$ with stoichiometric peracetic acid in MeCN solution.[7] Despite it being stable at -40℃ for days, this species decayed to a diferic complex upon warming.[8] It showed O-atom transfer reactivity with thioanisole and cyclooctene, performed HAA from substrates containing C-H bonds of moderate strenght, and the MeCN co-ligand could be substituted by a variety of anions to yield complexes of general formulation $[Fe^{IV}(O)(TPA)(X)]^{+}$ (**Figure 5.5**). Introduction of anions did not alter the spin-state (they complexes remained $S = 1$), but was found to decrease stability and slightly enhance substrate reactivity relative to $[Fe^{II}(TPA)(NCMe)_2]^{2+}$.[9]

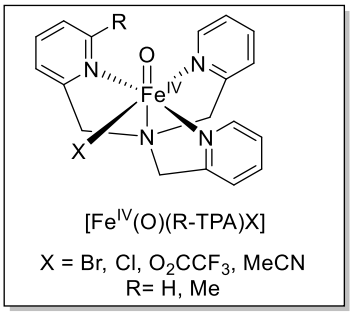

Figure 5.5: Oxoiron(IV) complexes supported by TPA

In the hope of accessing a high-spin oxoiron(IV) complex, efforts were made to weaken the equatorial ligand field exerted by TPA via inclusion of substituents at the 6th position of its pyridine donors. Initial work involved methyl substituents, for instance $[Fe^{IV}(O)(^{Me}TPA)]^{2+}$ (**Figure 5.5**), but yielded intermediate-spin complexes only.[10] Inclusion of a phenyl substituent on TPA was also performed, but reaction of the iron(II) precursor $[Fe^{II}(^{Ph}TPA)(NCMe)]^{2+}$ with oxidants, such as *tert*-butyl hydroperoxide, resulted in oxidation of the phenyl substituent to phenolate and its ligation in an oxo-bridged diiron(III) product (**Figure 5.6**).[11] Evidence

showed that an Fe^{IV}=O complex was initially formed, but rapidly decays via intramolecular oxidation of the phenyl substituent.[12] The general strategy of weakening equatorial ligand field in the hope of obtaining high-spin oxoiron(IV) complex was, ultimately, successful. This is because it led to use of the TQA ligand and formation of $[Fe^{IV}(O)(TQA)(NCMe)]^{2+}$, which does have an $S = 2$ spin-state.

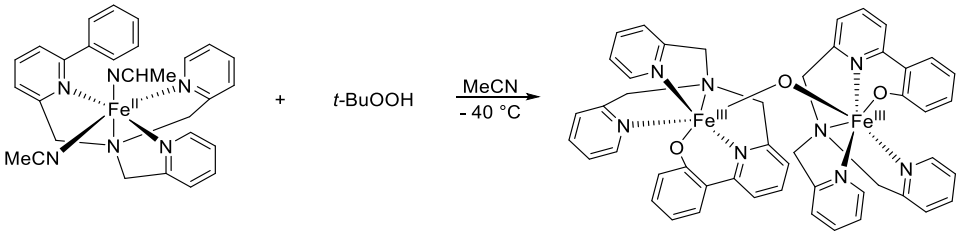

Figure 5.6: Reaction of $[Fe^{II}(^{Ph}TPA)(NCMe)]^{2+}$ with *tert*-butyl hydroperoxide.

Attributing the comparatively low reactivity of TBP high-spin oxoiron(IV) complexes to steric factors is an intuitively obvious thing to do. However, the ligands that have been used to support these TBP geometries contain strongly basic σ-donors, such as guanidine and pyrrolide, which would be expected to significantly decrease the reduction potentials of the oxoiron(IV) complexes and, thereby, reduce their reactivity. As such, the cause of the low reactivity seen for these complexes cannot be easily discerned.[13] To resolve this question, we sought to develop a ligand system with sufficient bulk to impose a TBP geometry at an oxoiron(IV) complex, but using the pyridine and tertiary amine donors that predominate for the $S = 1$ systems, whilst also minimizing steric impediment to reaction with substrates. As shown by the work in Chapter 2, installation of bulky 2,4,6-triphenylbenzene substituents onto the 5th position of the pyridine donors of tripodal tetradentate tris(2-pyridylmethyl)amine (TPA) to yield the ligand ^{tpb3}TPA (**Figure 5.7**) provided an excellent candidate for our purposes. The remote nature of the steric bulk, relative to the metal centre, in these ligands provides a number of advantages. Not only should it limit steric impediment to reaction with substrates, it would also be expected to minimize impact upon ligand field, which will simplify comparison with published systems, and inhibit intramolecular oxidative degradation of the ligand.

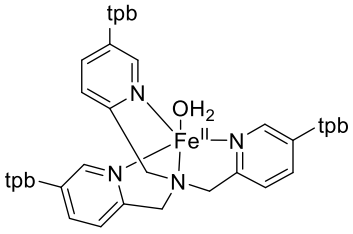

$[Fe^{II}(^{tpb3}TPA)(OH_2][OTf]_2$

tpb: 2,4,6-triphenylbenzene

Figure 5.7: Structure of $[Fe^{II}(^{tpb3}TPA)H_2O][OTf]_2$ (use in this study).

5.2 Result and Discussion

5.2.1 Synthesis of Oxoiron(IV)

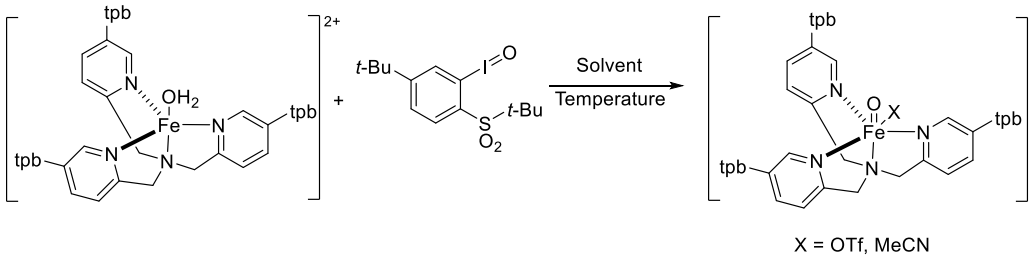

Scheme 5.1: Formation of oxoiron(IV) complex by reaction of $[Fe(^{tpb3}TPA)(OH_2)][OTf]_2$ with an organic solvent soluble iodosylbenzene.

The reaction of $[Fe^{II}(^{tpb3}TPA)(OH_2)][OTf]_2$ with organic solvent soluble oxidant 2-(*tert*-butylsulfonyl)-5-*tert*-butyl-iodosylbenzene (sArIO) in DCM or acetone solution at -80°C (**Scheme 5.1**) forms a reactive green complex whose UV-vis spectrum (**Figure 5.8**) contained a absorption feature at a λ_{max} of 760 nm (ε_{max} = 350 M^{-1} cm^{-1}). Such near infrared (NIR) features derive from ligand field (d-d) transitions and are diagnostic of formation of intermediate-spin oxoiron(IV) complexes. Titration of oxidant into 2 mM solution of iron(II) starting complex indicated that around 1.5 equiv is required to maximize yield of oxoiron(IV) complex (**Figure 5.9**).

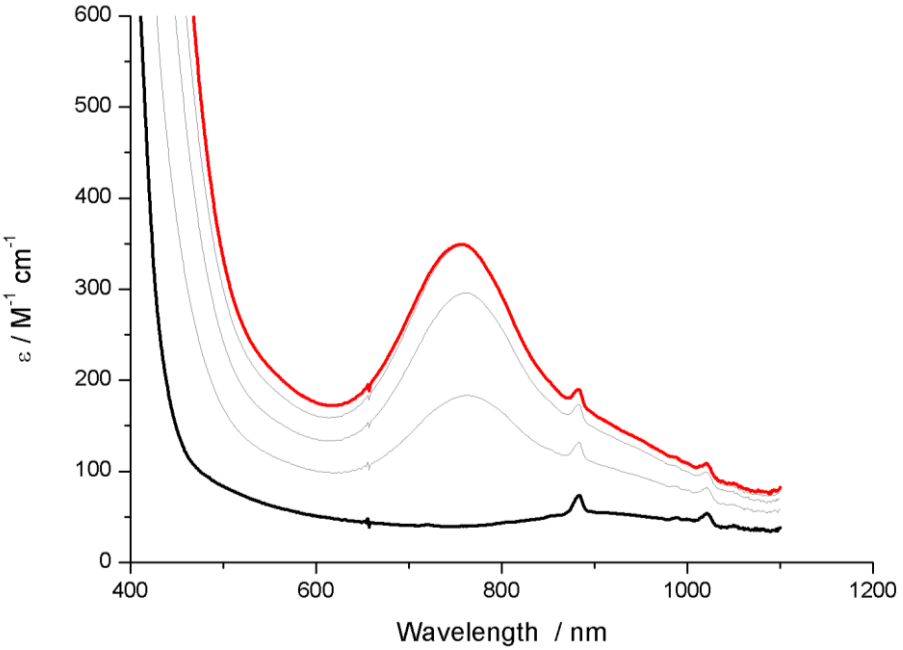

Figure 5.8: UV-vis spectra for the formation of $[Fe^{IV}(O)(5^{tpb3}TPA)(OTf)]^{+}$ by reaction of $[Fe^{II}(^{tpb3}TPA)(OH_2)][OTf]_2$ with 1.5 equiv sArIO, in DCM solution at -80°C.

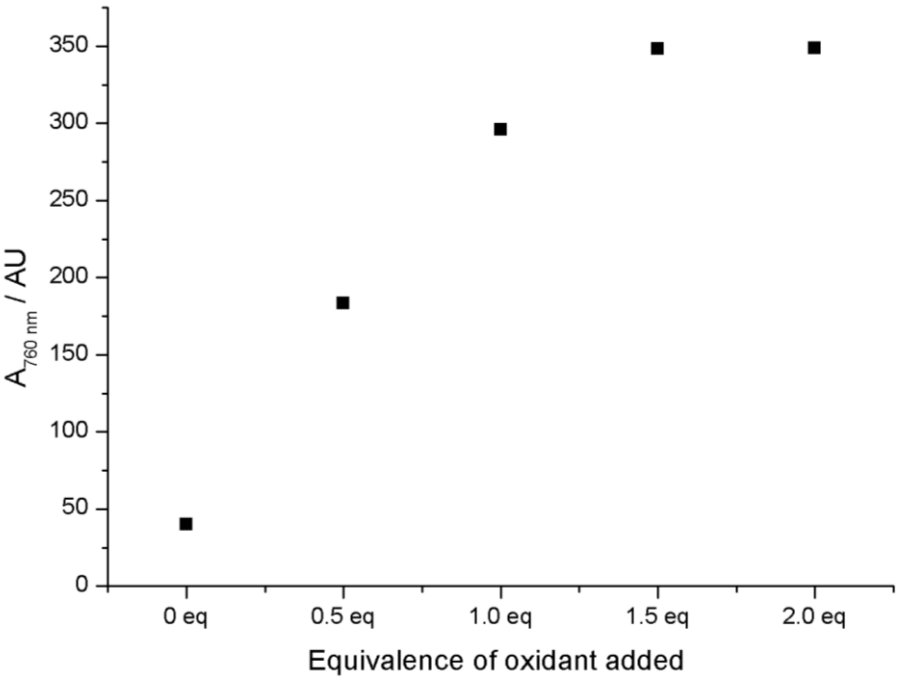

Figure 5.9: Intensity of the absorption at 760 nm ($A_{760\ nm}$) plotted against equiv of sArIO added to $[Fe^{II}(^{tpb3}TPA)(OH_2)][OTf]_2$, in DCM at – 80 °C.

Support for formulation of the green species as an oxoiron(IV) complex was provided by coldspray ionization mass spectrometry (CSI-MS), which showed an ion fragment with an *m/z* ratio (1424.50) and isotopic distribution pattern corresponding to $[Fe^{IV}(O)(^{tpb3}TPA)(OTf)]^{+}$

(**Figure 5.10**). Despite of the high stability at -80°C, it had a half-life of 10 min at -60°C. It is worth mentioning that, unlike for the parent complex $[Fe^{IV}(O)(TPA)(NCMe)]^{2+}$, there was no indication that the synthesis of $[Fe^{IV}(O)(^{tpb3}TPA)(OTf)]^{+}$ was accompanied by formation of any oxo-bridged diiron(III) complex, which is known to be the thermodynamically stable product of decay of the parent complex.[9] Thus, it appears that the steric hindrance provided by aryl substituents inhibits intermolecular reaction of $[Fe^{IV}(O)(^{tpb3}TPA)(OTf)]^{+}$.

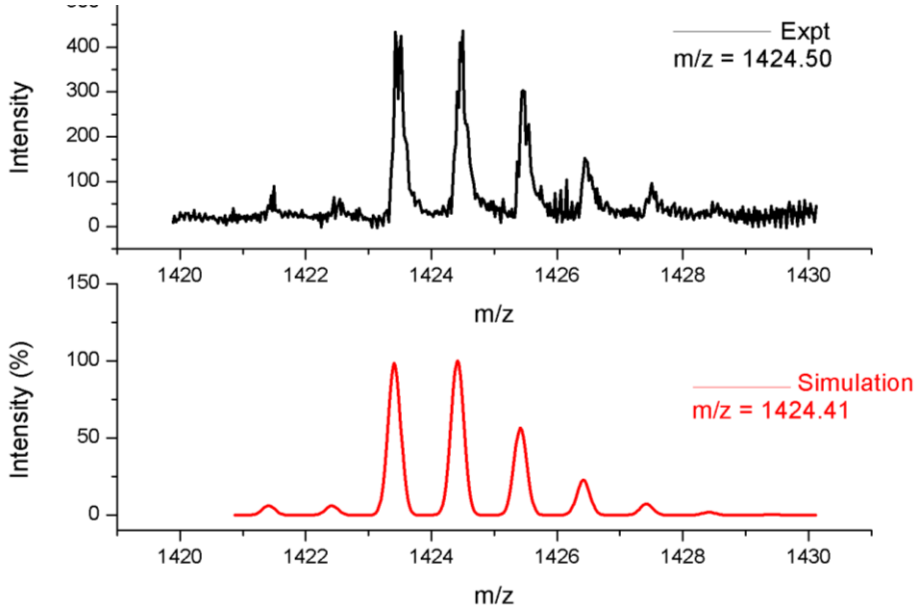

Figure 5.10: CSI-MS experimental data (black line) and simulation (red line) for the ion fragment $[Fe^{IV}(O)(^{tpb3}TPA)(OTf)]^{+}$. DCM solution; -40°C.

Reaction of $[Fe^{II}(^{tpb3}TPA)(OH_2)][OTf]_2$ with 2-(*tert*-butylsulfonyl)-5-*tert*-butyl-iodosylbenzene was also performed in MeCN solution at 0 °C (**Scheme 5.1**). In this case, this reaction yielded a UV-vis spectrum (**Figure 5.11**) with an absorption maxima at 740 nm (ε = 300 M^{-1} cm^{-1}), which is slightly different to the reaction in DCM and $[Fe^{IV}(O)(TPA)(MeCN)]^{2+}$ (**Table 5.1**), and 2 equiv of oxidant was needed to maximize the yield of oxoiron(IV) complex (**Figure 5.12**). A half-life of approximately 20 min was measured for $[Fe^{IV}(O)(^{tpb3}TPA)(NCMe)]^{2+}$ at room temperature.

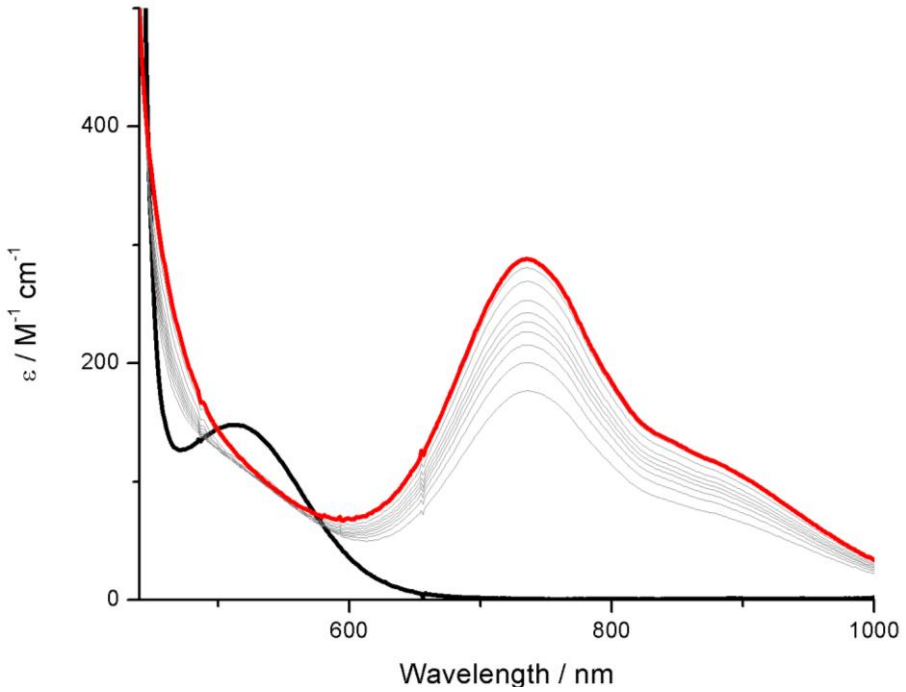

Figure 5.11: UV-Vis spectrum for the formation of $[Fe^{IV}(O)(^{tpb3}TPA)(MeCN)]^{2+}$ by reaction of $[Fe^{II}(^{tpb3}TPA)(OH_2)][OTf]_2$ with 2 equiv of sArIO, in MeCN solution at 0 °C.

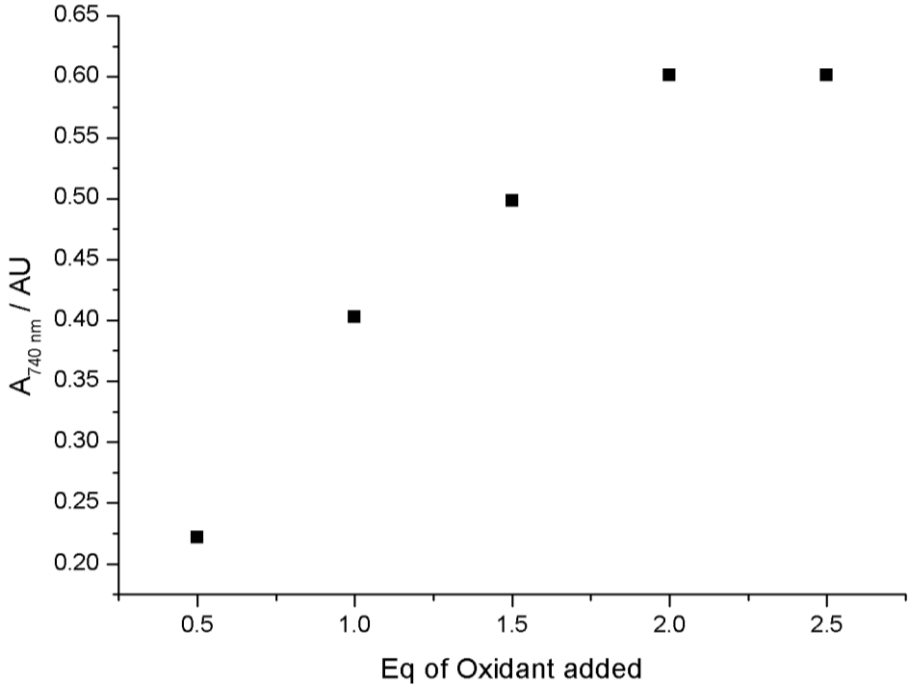

Figure 5.12: Intensity of the absorption at 740 nm ($A_{740\ nm}$) plotted against equiv of sArIO added to $[Fe^{II}(^{tpb3}TPA)(OH_2)][OTf]_2$, in MeCN at 0°C.

It contrast to $[Fe^{II}(^{tpb3}TPA)(OH_2)][OTf]_2$, attempts to generate of $[Fe^{IV}(O)(TPA)(MeCN)]^{2+}$ using 2-(*tert*-butylsulfonyl)-5-*tert*-butyl-iodosylbenzene as oxidant was unsuccessful in both MeCN and DCM solution. Traditionally, $[Fe^{IV}(O)(TPA)(MeCN)]^{2+}$ was synthesized using either peracetic acid, mCPBA or *tert*-butyl hydroperoxide and at a temperature of -40°C high stability was observed. However, these oxidants contain mixtures of compounds, which in some cases react with the oxoiron(IV) complex, facilitate dimerization and decay (where acidic), and can promote diiron complex formation. All of this can affect half-life, so comparisons of stability between the parent complex and $[Fe^{IV}(O)(^{tpb3}TPA)(MeCN)]^{2+}$ are not meaningful.

To confirm coordination of MeCN in $[Fe^{IV}(O)(^{tpb3}TPA)(MeCN)]^{2+}$, small amounts of MeCN were added into solutions of $[Fe^{IV}(O)(^{tpb3}TPA)(OTf)]^{+}$ in DCM (**Figure 5.13**). This yielded a blue-shifted UV-vis spectrum that was identical to the oxoiron(IV) complex generated in MeCN. From this we can conclude that a 6-coordinate complex, $[Fe^{IV}(O)(^{tpb3}TPA)(MeCN)]^{2+}$, is obtained in the presence of coordinating solvents and not the desired TBP geometry. Furthermore, addition of small amounts of MeCN caused the half-life ($t_{1/2}$) of the complex generated in DCM, $[Fe^{IV}(O)(^{tpb3}TPA)(OTf)]^{+}$, to increase massively from 10 min at -60°C to 20 min, at room temperature. This behaviour is consistent with observations for $[Fe^{IV}(O)(TPA)(NCMe)]^{2+}$, where substitution of MeCN with anions caused a large decrease in the thermal stability of the complex.[9]

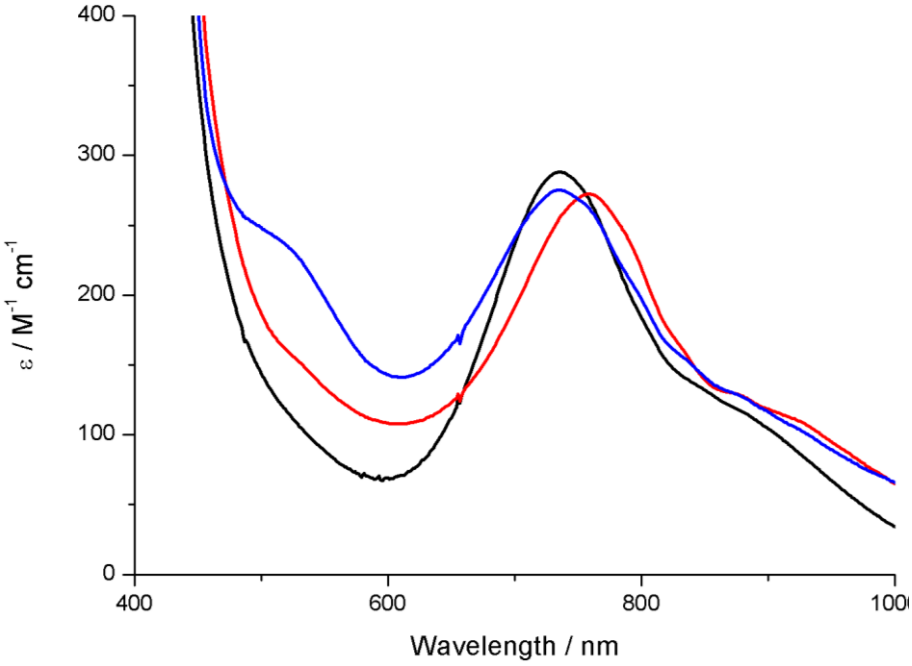

Figure 5.13 UV-vis spectra for $[Fe^{IV}(O)(^{tpb3}TPA)(NCMe)]^{2+}$ (blue line) generated by addition of MeCN to a DCM solution of $Fe^{IV}(O)(^{tpb3}TPA)(OTf)]^{+}$ (red line) at -80°C, and $[Fe^{IV}(O)(^{tpb3}TPA)(NCMe)]^{2+}$ generated in MeCN solution at 0°C (black line).

Mössbauer spectroscopic data for $[^{57}Fe^{IV}(O)(^{tpb3}TPA)(NCMe)]^{2+}$, measured in frozen MeCN solution, revealed the presence of S=1 iron(IV) center. More specifically, the zero-field spectrum contained a doublet with an isomer shift, δ, of 0.01 mm s^{-1} and a quadrupole splitting, ΔE_Q, of 0.66 mm s^{-1} (**Figure 5.14**). The presence of the doublet in the spectrum is consistent with an integer spin ground state, and the low δ value is indicative of the presence of an iron(IV) centre. For comparison, the parent TPA complex had similar isomer shift, δ, of 0.01 mm s^{-1} and quadrupole splitting, ΔE_Q, of 0.92mm s^{-1} Unfortunately, only 53 % of the ^{57}Fe present was associated with the target complex $[Fe^{IV}(O)(^{tpb3}TPA)(NCMe)]^{2+}$, with the majority of the balance (30 %) displaying spectral properties characteristic of a diiron(III) complex.

A similar scenario was observed when weakly-coordinating solvent acetone was used in place of MeCN. Here, it is assumed that a triflate anion is coordinated in place of MeCN, affording the complex $[Fe^{IV}(O)(^{tpb3}TPA)(OTf)]^{+}$. In this case, the quadrupole doublet had δ and ΔE_Q values of 0.09 and 0.85 mm s^{-1}, respectively (**Figure S17)**. These values are distinct to those

of the aformentioned MeCN-ligated complex, but characteristic of intermediate-spin oxoiron(IV) complexes (**Table 5.1**).

Fitting of the paramagnetic hyperfine structure observed in spectra of these oxoiron(IV) complexes recorded in applied magnetic fields with an $S = 1$ spin Hamiltonian, yielded D-values of between 20 and 30 cm^{-1} (E/D was assumed to be 0). This is very similar to values obtained for previously reported for $S = 1$ oxoiron(IV) complexes. Efforts to fit the data assuming an S = 2 ground state afforded unreasonable zero-field splitting parameters. , rather than the targeted $S = 2$ spin-state. As a consequence, we can conclude that the oxoiron(IV) complexes supported by ^{tpb3}TPA have $S = 1$, rather than the targeted $S = 2$, spin-state configuration. By extension, we can assume that a 6-coordinate geometry was obtained in both MeCN and DCM/acetone solution, with a solvent ligand and triflate anion, respectively, filling the sixth coordination site.

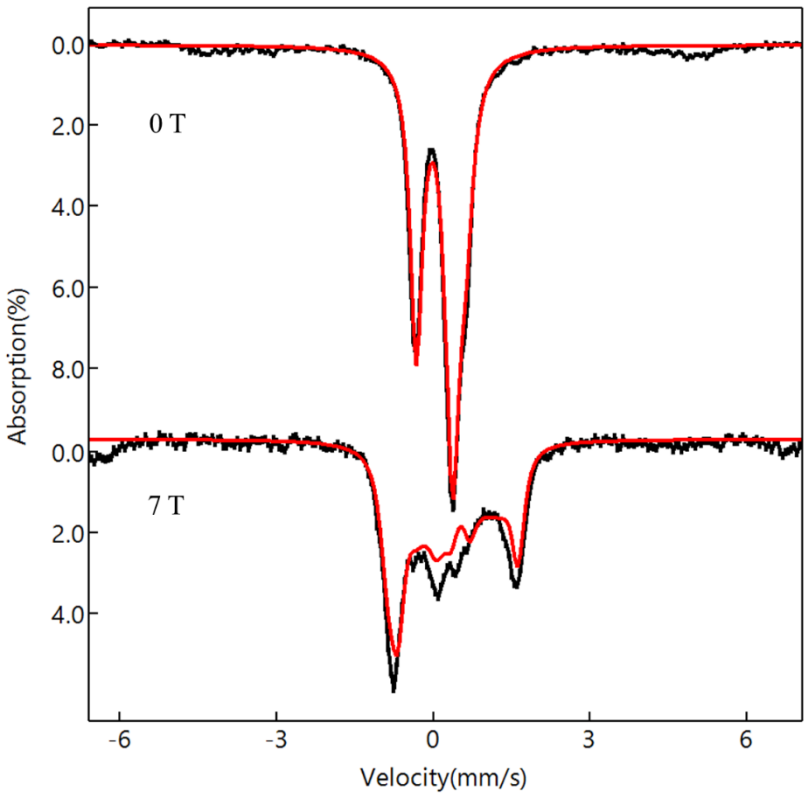

Figure 5.14: Mössbauer spectra (black lines) of $[^{57}Fe^{IV}(O)(^{tpb3}TPA)(NCMe)]^{2+}$, in CH_3CN solution, were recorded at 4.2 K in the parallel applied magnetic fields (B) indicated. Contributions from differic impurities (30% of Fe), fits of which are provided in the SI, have been substracted from the data. Spectral simulations (red lines) were generated by fitting the $S = 1$ spin Hamiltonian ($H = D\left[S_{z^2} - \frac{2}{3}\right] + E\,[S] + \beta S.B + S.A.I - g_n\beta_n B.I + H_Q$) using the following parameters: $D = 25\ cm^{-1}$; $\eta = 0.9$; $E/D = 0$; $A_{x,y}/g_nB_n = -23.5$ T; A_z/g_nB_n was not determined experimentally.

Table 5.1: Comparison of the spectral properties and geometry of [Fe^{IV}(O)(^{tpb3}TPA)] with selected published oxoiron(IV) complexes

[Fe^{IV}(O)(L) where L =	λmax/nm (ε/M^{-1} cm^{-1})	δ (mm/s)	ΔE_Q (mm s^{-1})	Spin State	Geometry	ref
^{tpb3}TPA DCM/Acetone	760 (270)	0.09	0.85	1	Octahedral	This work
^{tpb3}TPA MeCN	740 (288)	0.01	0.66	1	Octahedral	This work
TPA MeCN	724 (300)	0.01	0.92	1	Octahedral	[3]
$^{6\text{-Me}}$TPA MeCN	770 (300)	-	-	1	Octahedral	[3]
TauD	318 (15000)	0.33	-0.88	2	-	[3]
TQA MeCN	400 (sh), 650 (300), 900 (75)	0.24 (2)	-1.05 (2)	2	Octahedral	[5]
TMG_3tren	400 (9800), 825 (260)	0.09	−0.29	2	Trigonal bipyramidal	[14]

5.2.2 Alternative Oxidants Used for the Generation of Oxoiron(IV)

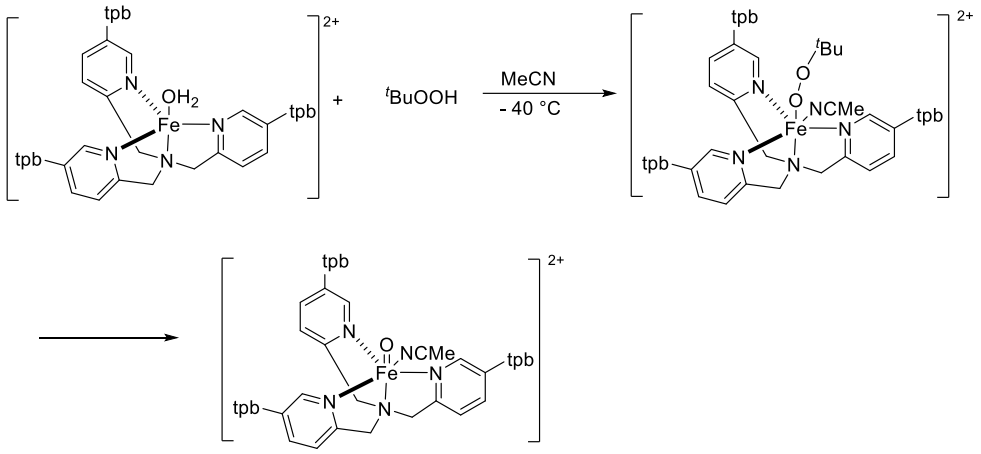

Scheme 5.2: Reaction of $[Fe^{II}(^{tpb3}TPA)(OH_2)][OTf]_2$ with tBuOOH

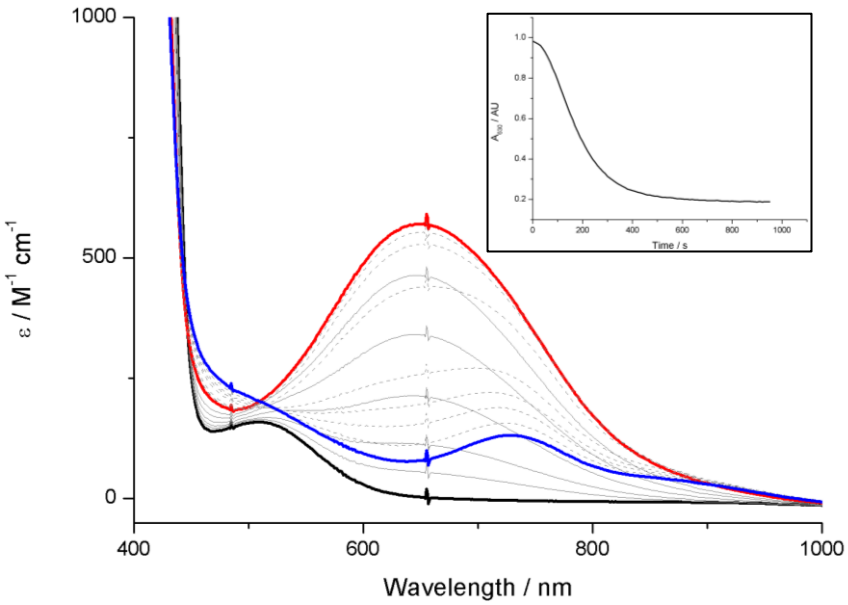

Figure 5.15: UV-Vis spectra showing formation of $[Fe^{III}(OO^tBu)(^{tpb3}TPA)]^{2+}$ (red and solid grey lines), in MeCN at -40°C, by reaction of $[Fe^{II}(^{tpb3}TPA)(OH_2)][OTf]_2$ with 5 eq of ^{t}BuOOH and subsequent decay to $[Fe^{IV}(O)(^{tpb3}TPA)]^{2+}$ (blue and dotted grey lines). **Inset**: Plot of intensity of absorption at 630 nm vs time (s) for decay of $[Fe^{III}(OO^tBu)(^{tpb3}TPA)]^{2+}$.

Reaction of $[Fe^{II}(^{tpb3}TPA)]^{2+}$ (2mM) with 5 eq of ^{t}BuOOH yielded a violet species whose UV-vis spectrum contained a broad signal with a λ_{max} of 630 nm (ε = 570 M^{-1} cm^{-1}) (**Figure 5.15**). On the basis of similarity to literature precedents, this purple species was assigned as the *tert*-butylperoxoiron(III) complex $[Fe^{III}(OO^tBu)(^{tpb3}TPA)]^{2+}$. This species proved to be transient

and decayed to a new species with a λ_{max} of 740 nm (ε = 130 M^{-1} cm^{-1}), which can be assigned as $[Fe^{IV}(O)(^{tpb3}TPA)(NCMe)]^{2+}$. This was confirmed by ESI-MS. $[Fe^{III}(OO^{t}Bu)(^{tpb3}TPA)]^{2+}$ has similar UV-vis spectral features as the low-spin complex $[Fe^{III}(OO^{t}Bu)(TPA)(OH_2)]^{2+}$, whose λ_{max} = 600 nm (2200 M^{-1} cm^{-1}), but with much lower extinction coefficients.[15] This can be attributed to more rapid decay of $[Fe^{III}(OO^{t}Bu)(^{tpb3}TPA)]^{2+}$. Assignment of spin state for this complex would require EPR or resonance Raman studies. However, the yield of oxoiron(IV) complex, $[Fe^{IV}(O)(^{tpb3}TPA)(NCMe)]^{2+}$, obtained using this oxidant is very low and also the reaction was slower than when using 2-(*tert*-butylsulfonyl)-5-*tert*-butyl-iodosylbenzene as an oxidant. As such, there is little merit in performing further studies using TBHP as an oxidant.

5.2.3 Halide-coordinated Oxoiron(IV) Complex

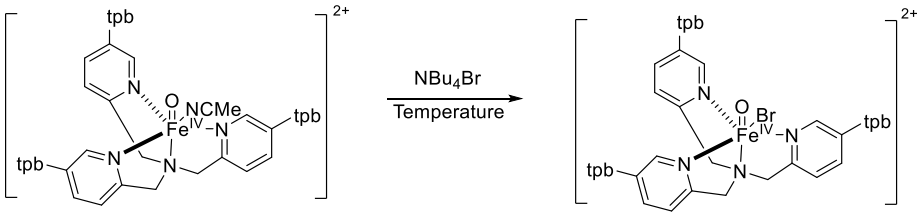

Scheme 5.3: Reaction of $[Fe^{IV}(O)(^{tpb3}TPA)(NCMe)]^{2+}$ with NBu_4Br.

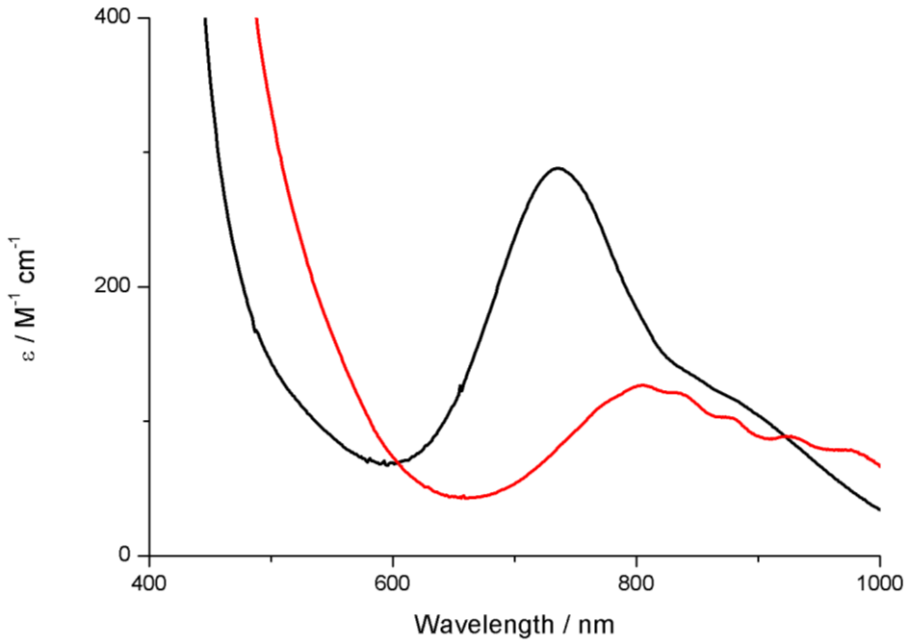

Figure 5.16: UV spectra of $[Fe^{IV}(O)(^{tpb3}TPA)(NCMe)]^{2+}$ (black line) and $[Fe^{IV}(O)(^{tpb3}TPA)(Br)]^{+}$ (red line).

The possibility of substitution of the labile MeCN ligand in $[Fe^{IV}(O)(^{tpb3}TPA)(NCMe)]^{2+}$ by anions was probed by addition of NBu_4Br at -60°C in DCM/MeCN (9:1) solution (**Scheme 5.3**). UV-vis spectral changes were observed that are consistent with formation of the complex $[Fe^{IV}(O)(^{tpb3}TPA)(Br)]^{+}$. More specifically, the NIR feature at 740 nm shifted to 800 nm and did so with a clean isobestic point (**Figure 5.16**). Apart from being significantly less intense, the red shifted NIR band associated with bromide complex display much more prominent vibronic fine structure. In addition, $[Fe^{IV}(O)(^{tpb3}TPA)(Br)]^{+}$ is unstable and tends to decay fully

(within 2 min). Similar spectral changes were also seen in octahedral $[Fe^{IV}(O)(TPA)Br]^{+}$ complex.[3]

The ligand field NIR bands move to lower energy as follows $[Fe^{IV}(O)(^{tpb3}TPA)(NCMe)]^{2+}$ > $[Fe^{IV}(O)(^{tpb3}TPA)(OTf)]^{+}$ > $[Fe^{IV}(O)(^{tpb3}TPA)(Br)]^{+}$. This is simply a consequence of theligand field strength of the equatorial anion. As proposed by Que and co-workers[16], the replacement of MeCN, which is bound in the equatorial plane, by weaker field ligands causes the energy level of $3d_{x^2-y^2}$ antibonding orbital to decrease. As such, the transition between the $3d_{xy/yz/xz}$ and $3d_{x^2-y^2}$ orbitals shifts to lower energy (i.e., higher wavelengths) in accordance with the spectrochemical series. This lowering of the $3d_{x^2-y^2}$ antibonding orbital with decreasing field strength would, also, be expected to decrease the energy of the high-spin state. According to two-state reactivity theory, this should make the complexes more reactive and, indeed, that is what is observed in terms of relative stability of the oxoiron(IV) complexes.

Similar to $[Fe^{IV}(O)(^{tpb3}TPA)(NCMe)]^{2+}$, the zero field Mössbauer spectrum of $[^{57}Fe^{IV}(O)(^{tpb3}TPA)(Br)]^{+}$ (**Figure 5.17**), recorded in frozen acetonitrile solution, displayed a doublet with δ and ΔE_Q being 0.07 mm and 1.01 mm s^{-1}, respectively, that accounts for 30% of the iron present. (Differic species account for another 30% of the iron present, with the balance being unreacted iron(II) complex.) The close resemeblance of these spectral parameters to those of the acetonitrile solvate and published S = 1 oxoiron(IV) complexes, suggest that the S = 1 ground state was retained upon introduction of halide ion. Fitting of the paramagnetic hyperfine structure, observed in the applied magnetic fields, confirm this supposition. Thus, introduction of the weak field bromide ligand was insufficient to elicit a change in ground spin-state of the complex.

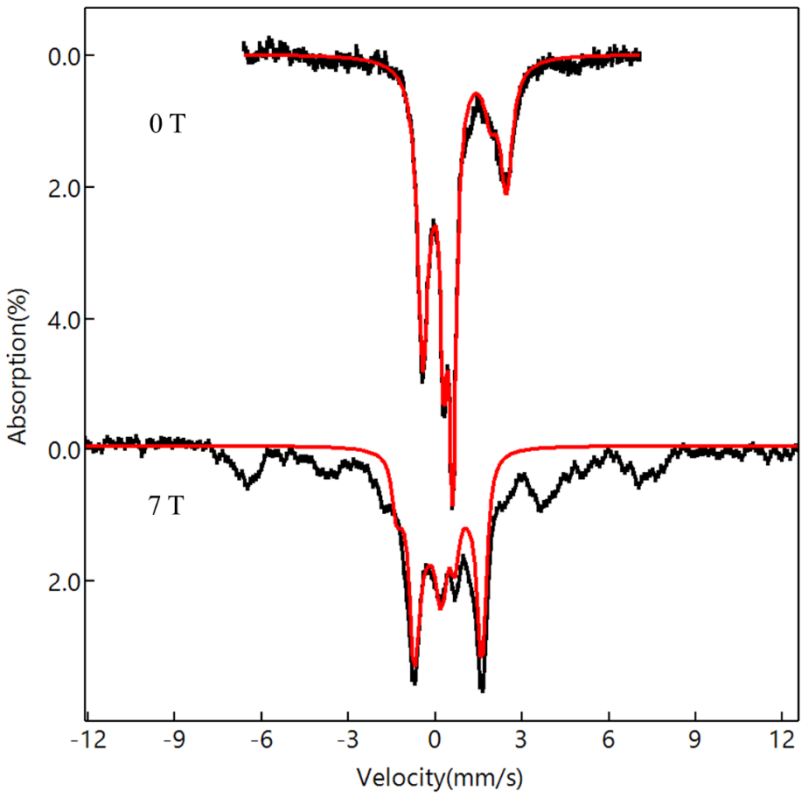

Figure 5.17: Mössbauer spectra (black lines) of $[^{57}Fe^{IV}(O)(5^{tpb3}TPA)(Br)]^{+}$, recorded in CH_3CN solution at 4.2 K, in the parallel applied magnetic fields (B) indicated. Contributions from differic impurities (30% of Fe), fits of which are provided in the SI, have been substracted from the data. Spectral simulations (red lines) were generated by fitting the $S = 1$ spin Hamiltonian ($H = D\left[S_z^2 - \frac{2}{3}\right] + E\,[S] + \beta S.B + S.A.I - g_n\beta_n B.I + H_Q$) using the following parameters: $D = 25\ cm^{-1}$; $\eta = 0.0$; $E/D = 0$; $A_{x,y}/g_nB_n = -22.0$ T; A_z/g_nB_n was not determined experimentally.

5.2.4 Reactivity of Oxoiron(IV) with Substrate

All the evidence gathered suggests that intermediate-spin oxoiron(IV) complexes have been exclusively obtained, which indicates that an octahedral, rather than trigonal bipyramidal, geometry is obtained. However, we felt that study of the reactivity of $[Fe^{IV}(O)(^{tpb3}TPA)(NCMe)]^{2+}$ with substrates was worthwhile, as it provides an indication of accessibility of the reactive site to substrates and is a good point of comparison for any ^{Ar3}TPA-

supported trigonal bipyramidal oxoiron(IV) complexes we prepare in future. As expected, kinetic measurements for reaction of $[Fe^{IV}(O)(^{tpb3}TPA)(NCMe)]^{2+}$ with excess substrate (i.e., under pseudo-first order conditions) yielded a first order rate dependence upon both concentration of complex and substrate, from which second order rate constants (k_2) could be extracted. A compilation of these k_2 values is provided in **Table 5.2**.

Table 5.2: Second order rate constants (k_2) obtained from kinetic measurements of reaction of $[Fe^{IV}(O)(^{tpb3}TPA)(NCMe)]^{2+}$, in DCM/MeCN (9:1) with selected substrates. Temperature of measurement is provided in parentheses.

complex	Spin State	k_2 [M^{-1} s^{-1}] (temp, °C)		
		PPh_3	CHD	DHA
$[Fe^{IV}(O)(^{tpb3}TPA)]^{2+}$	1	0.802 ± 0.04 (–60)	5.91 ± 0.134 (–40)	0.040 ± 0.0041 (–40)
$[Fe^{IV}(O)(TPA)NCMe]^{2+}$	1	Not reported	1.9 (–40)	Not reported
$[Fe^{IV}(O)(N4Py)]^{2+}$	1	Not reported	0.07 (–40)	18 (25)
$[Fe^{IV}(O)(Me_3NTB)]^{2+}$	1	17 (-40)	940 (-40)	310 (-40)
$[Fe^{IV}(O)(TMG_3tren)]^{2+}$	2	1.1 (–30)	1.2 (– 30)	0.090 (–30)

Successful reaction of $[Fe^{IV}(O)(^{tpb3}TPA)(NCMe)]^{2+}$ with triphenylphospine (PPh_3) to form triphenylphosphine oxide ($Ph_3P=O$) demonstrated that the complex was capable of oxo transfer (**Figure S18**). It was necessary to obtain the rate of reaction (k_2 = 0.802 ±0.04 M^{-1} s^{-1}) at -60°C in mixed solvents because it was too fast to accurately measure at -40°C. Interestingly, at –40 °C, reaction with 1,4-cyclohexadiene, CHD, was found to proceed 120 orders of magnitude faster than with dihydroanthrance, DHA (k_2 of 5.91 ± 0.134 and 0.040 ± 0.0041 M^{-1} s^{-1}, respectively, **Figure S19**, **Figure S20** and **Table 5.2**). The ultimate respective products of reaction were benzene and anthracene. Given that the C-H BDEs for CHD (76.0 kcal mol^{-1}) [16] and DHA (76.3 kcal mol^{-1}) [17] are very similar to one another, this can only stem from steric

retardation of reaction of the larger DHA substrate. Such behaviour was also seen in the TBP high-spin complexes $[Fe^{IV}(O)(TMG_3tren)]^{2+}$.[7,18]

It should also be noted that, $[Fe^{IV}(O)(^{tpb3}TPA)(NCMe)]^{2+}$ appears to be more reactive than the parent compound $[Fe^{IV}(O)(TPA)(NCMe)]^{2+}$. This is evident from the second order rate constant for reaction with CHD, which is 5.91 ± 0.134 M^{-1} s^{-1} for the former and 1.9 M^{-1} s^{-1} for the latter. This suggests the bulky aryl substituents in $[Fe^{IV}(O)(^{tpb3}TPA)(NCMe)]^{2+}$ do not significantly hinder reaction with small substrates, and may in fact improve it, which raises the prospect of shape/size selective reaction with substrates. Such a notion has been exploited in iron catalysed oxidation of C-H bond and olefin, using H_2O_2 as an oxidant, by the groups of White and Costas.[19–21]

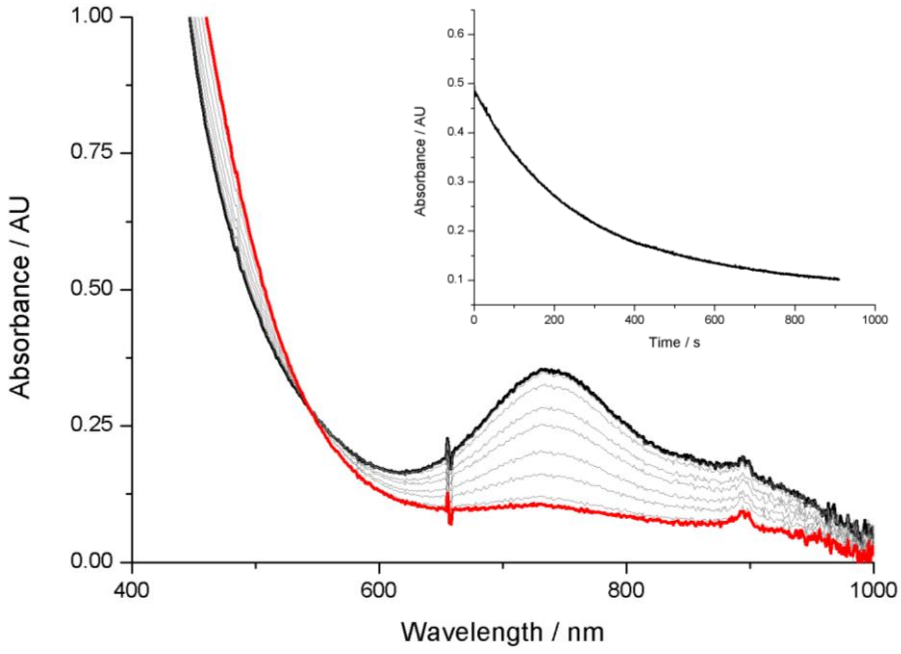

Figure 5.18: Reaction of $[Fe^{IV}(O)(^{tpb3}TPA)(NCMe)]^{2+}$ (2mM) with cyclohexane (200 eq) at room temperature, monitored by UV-Vis spectroscopy. **Inset:** Intensity of the absorption band at 740 nm (A_{740}) during the course of the reaction (time in s).

Since there are no reports of reaction of $[Fe^{IV}(O)(TPA)(NCMe)]^{2+}$ with substrates with strong C-H bonds, we decided to perform kinetic studies for reaction of $[Fe^{IV}(O)(^{tpb3}TPA)(NCMe)]^{2+}$ with a series of substrates with moderate to strong C-H bonds at room temperature. In all cases,

reaction was observed and its progress was monitored by UV-vis spectroscopy, an example of which is provided for cyclohexane in **Figure 5.18**. Plot of pseudo-first order rate constants versus substrate concentration, from which k_2 values can be extracted are provided in the **Appendix** (**Figure S21 – S29**). The k_2 values obtained are summarized in **Table 5.3**. The products of oxidation of cyclohexane and ethylbenzene by $[Fe^{IV}(O)(^{tpb3}TPA)(NCMe)]^{2+}$ were found to be cyclohexanone and acetophenone (**Table 5.3**), respectively.

As observed for other oxoiron(IV) complexes, a plot of log k_2', which is the k_2 value divided by the number of oxidizable C-H bonds, versus C-H BDEs for the substrates was found to yield a linear plot with a slope of -0.095 (**Figure 5.19**). This indicates that the rate determining step of reaction of $[Fe^{IV}(O)(^{tpb3}TPA)(NCMe)]^{2+}$ with the substrates involves C-H bond cleavage. Given the varying steric profile of the substrates, it suggests that reaction for these compounds was not *heavily* impacted by the bulk of the aryl substituents $[Fe^{IV}(O)(^{tpb3}TPA)(NCMe)]^{2+}$. That is not to say there is no influence. For instance, despite cumene having a BDE of 85 kcal mol^{-1}, which is lower than ethylbenzene, it has a similar k_2' rate constant as toluene, which has a comparatively high BDE of 90 kcal mol^{-1}. The reason for this is not entirely clear, but suggestion of steric hindrance of reaction of comparatively bulky cumene seems a reasonable proposition.[5]

Table 5.3: Second order rate constants (k_2) for reaction of $[Fe^{IV}(O)(^{tpb3}TPA)(NCMe)]^{2+}$ with substrates containing moderate to strong C-H bonds..

Substrate (BDE)/ kcal mol^{-1}	BDE/ kcal mol^{-1}	k_2 [M^{-1} s^{-1}]	Product
Triphenylmethane	81	0.10839 ± 0.00501	-
Cumene	85	0.00876 ± 0.00134	-
Ethylbenzene	87	0.06035 ± 0.00931	Acetophenone
Toluene	90	0.0217 ± 0.00363	-
THF	92	0.28864 ± 0.01961	-
Cyclooctane	95	0.0667 ± 0.00904	-
2,3-diemethylbutane	96	0.00758 ± 0.0317	-
Cyclopentane	97	0.0103 ± 0.0037	-
Cyclohexane	99	0.01146 ± 0.00379	Cyclohexanone

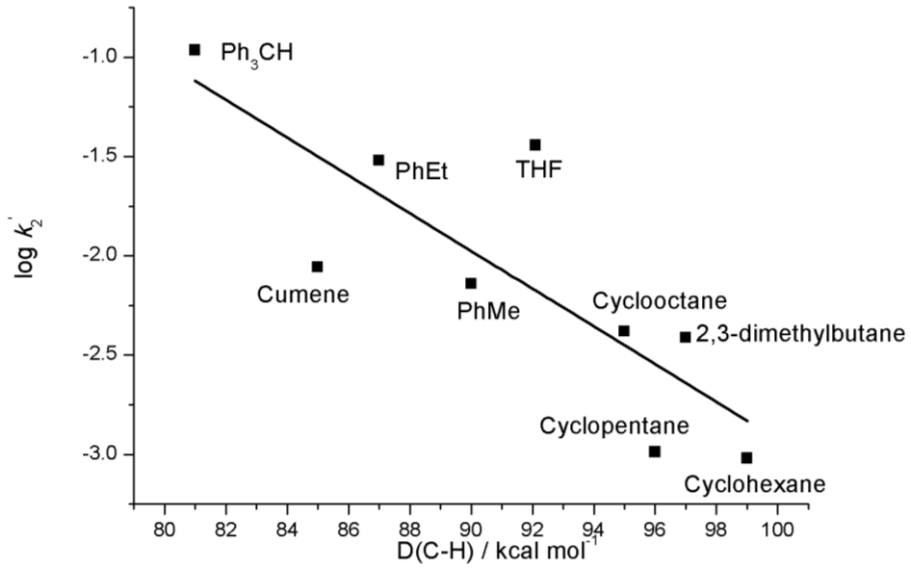

Figure 5.19: Plot of log k_2' values, which are obtained by dividing k_2 by the number of C-H bonds available for HAA, for the reaction of $[Fe^{IV}(O)(^{tpb3}TPA)(NCMe)]^{2+}$ with substrate versus the C-H BDEs of the substrates.

A further point of note is that THF displays a significant positive deviation away from the best fit line. More specifically, it has a C-H BDE of 92 kcal mol^{-1} but displays a comparable (or higher) k_2' value to ethylbenzene, whose C-H BDE is 87 kcal mol^{-1}. We attribute this to the activated nature of C-H adjacent to heteroatoms, which is associated with hyperconjugation. Alternatively, it could be due to the potential pre-coordination of THF to the oxoiron(IV) species, thus weakening it's C-H bond strength. However, this phenomenon is currently under investigation. Regardless, a kinetic isotope effect (KIE) of 28 was obtained from a ratio of the k_2 values of THF with its perdeuterated analog THF-d8 (**Figure S24**). This indicates that that the rate determining step involves hydrogen atom abstraction via a hydrogen atom tunnelling mechanism.

Table 5.4: Comparison of k_2 values observed in reaction of selected oxoiron(IV) complexes, of various spin state, with toluene and cyclohexane.

Entry	Substrate (BDE)/ kcal mol^{-1}	k_2 [M^{-1} s^{-1}] LFe^{IV}(O), where L =			
		S=1			S=2
		^{tpb3}TPA 25°C	N4Py 25°C	Me$_3$NTB -40°C[22]	TQA -40°C[2]
1	Toluene (90)	0.0217 ± 0.00363	0.0063	0.47	0.64
2	Cyclohexane (99)	0.0115 ± 0.00379	0.0005	0.25	0.37

The k_2 values for hydrogen atom abstraction (HAA) from cyclohexane and toluene by [Fe^{IV}(O)(^{tpb3}TPA)(NCMe)]$^{2+}$ were found to be approximately 20 and 3 times faster, respectively, than for [Fe^{IV}(O)(N4Py)]$^{2+}$ (**Table 5.4**). However, the analogous k_2 values reported for [Fe^{IV}(O)(Me$_3$NTB)(NCMe)]$^{2+}$ and [Fe^{IV}(O)(TQA)(NCMe)]$^{2+}$ were measured at -40°C, not room temperature, but were still more than 1 order of magnitude larger than those for [Fe^{IV}(O)(^{tpb3}TPA)(NCMe)]$^{2+}$. Taken together the order of reactivity for these oxoiron(IV) complexes is as follows: [Fe^{IV}(O)(TQA)(NCMe)]$^{2+}$ ≈ [Fe^{IV}(O)(Me$_3$NTB)(NCMe)]$^{2+}$ >> [Fe^{IV}(O)(^{tpb3}TPA)(NCMe)]$^{2+}$ > [Fe^{IV}(O)(N4Py)]$^{2+}$. This reactivity ordering is crudely paralleled by the relative stability of the complexes at room temperature. We cannot rule out the possibility that there is some steric retardation of reaction for the ^{tpb3}TPA-ligated system, but these results imply that the S = 2 excited state is at lower energy than for [Fe^{IV}(O)(N4Py)]$^{2+}$ but at higher energy than for [Fe^{IV}(O)(Me$_3$NTB)(NCMe)]$^{2+}$. The S = 1 ground and S = *2* excited states of the latter are believed to be effectively isoenergetic at room temperature, which endows it with reactivity comparable to the high-spin system [Fe^{IV}(O)(TQA)]$^{2+}$. Indeed, theoretical calculations suggest that for [Fe^{IV}(O)(Me$_3$NTB)(NCMe)]$^{2+}$ there might be a

geometry change from octahedral to trigonal bipyramidal during transition state, which enhances its reactivity.[22] This leads one to consider whether incorporation of bulkier aryl substituents into a $[Fe^{IV}(O)(^{Ar3}TPA)]^{2+}$ complex, might induce a similar geometry change in the transition state for HAA and lead to enhanced reactivity.

5.3 Conclusion

In conclusion, oxidation of $[Fe^{II}(5^{tpb3}TPA)(OH_2)](OTf)_2$ using an organic solvent led to formation of the corresponding oxoiron(IV) complexes. Despite the trigonal bipyramidal geometry of the starting complex, the oxoiron(IV) complexes were found to incorporate a sixth ligand, either MeCN or TfO^- (depending on the solvent used). Unfortunately, this yielded 6-coordinate complexes $[Fe^{IV}(O)(^{tpb3}TPA)(NCMe)]^{2+}$ and $[Fe^{IV}(O)(^{tpb3}TPA)(OTf)]^{+}$, rather than the desired TBP complex $[Fe^{IV}(O)(^{tpb3}TPA)]^{2+}$. Furthermore, Mössbauer studies confirmed this endowed the oxoiron(IV) complexes with intermediate-spin (S = 1) configurations. Substitution of the triflate and MeCN co-ligands with bromide anion yielded the highly unstable complex $[Fe^{IV}(O)(^{tpb3}TPA)(Br)]^{+}$. Reactivity studies were conducted for $[Fe^{IV}(O)(^{tpb3}TPA)(NCMe)]^{2+}$ at room temperature and it was found able to oxidize inert C-H bonds, which was not observed for its parent complex $[Fe^{IV}(O)(TPA)(NCMe)]^{2+}$. Whereas it proved more reactive than $[Fe^{IV}(O)(N4Py)]^{2+}$, it was significantly less reactive than the 6-coordinate S = 2 complex $[Fe^{IV}(O)(TQA)]^{2+}$. At present reactivity studies for coordinating substrates are being conducted to investigate the possibility of exploiting the labile site in $[Fe^{IV}(O)(^{tpb3}TPA)(NCMe)]^{2+}$ to activate C-H bonds (and limit entropic barriers to reaction) by precoordination of substrate. In addition, we are examining the possibility that more bulky aryl substituents can enhance reactivity by lowering the energy required for a geometry change to TBP, which would be S = 2, in the transition state (or before).

5.4 References

(1) Krebs, C.; Galonić Fujimori, D.; Walsh, C. T.; Bollinger, J. M. *Acc. Chem. Res.* **2007**, *40*, 484–492.

(2) Price, J. C.; Barr, E. W.; Hoffart, L. M.; Krebs, C.; Bollinger, J. M. *Biochemistry* **2005**, *44*, 8138–8147.

(3) McDonald, A. R.; Que, L. *Coord. Chem. Rev.* **2013**, *257*, 414–428.

(4) Shaik, S. *Nat. Chem.* **2010**, *2*, 347.

(5) Biswas, A. N.; Puri, M.; Meier, K. K.; Oloo, W. N.; Rohde, G. T.; Bominaar, E. L.; Münck, E.; Que, L. *J. Am. Chem. Soc.* **2015**, *137*, 2428–2431.

(6) Wong, S. D.; Bell III, C. B.; Liu, L. V; Kwak, Y.; England, J.; Alp, E. E.; Zhao, J.; Que Jr., L.; Solomon, E. I. *Angew. Chem. Int. Ed.* **2011**, *50*, 3215–3218.

(7) Puri, M.; Que, L. *Acc. Chem. Res.* **2015**, *48*, 2443–2452.

(8) Lim, M. H.; Rohde, J.-U.; Stubna, A.; Bukowski, M. R.; Costas, M.; Ho, R. Y. N.; Münck, E.; Nam, W.; Que, L. *Proc. Natl. Acad. Sci.* **2003**, *100*, 3665–3670.

(9) Shan, X.; Que, L. *Chem. Commun.* **2008**, No. 19, 2209–2211.

(10) Rohde, J.-U.; Stubna, A.; Bominaar, E. L.; Münck, E.; Nam, W.; Que, L. *Inorg. Chem.* **2006**, *45*, 6435–6445.

(11) Zang, Y.; Kim, J.; Dong, Y.; Wilkinson, E. C.; Appelman, E. H.; Que, L. *J. Am. Chem. Soc.* **1997**, *119*, 4197–4205.

(12) Paine, T. K.; Costas, M.; Kaizer, J.; Que, L. *J. Biol. Inorg. Chem.* **2006**, *11*, 1098–1099.

(13) Lange, S. J.; Miyake, H.; Que, L. *J. Am. Chem. Soc.* **1999**, *121*, 6330–6331.

(14) MacFaul, P. A.; Ingold, K. U.; Wayner, D. D. M.; Que, L. *J. Am. Chem. Soc.* **1997**, *119*, 10594–10598.

(15) Zhou, Y.; Shan, X.; Mas-Ballesté, R.; Bukowski, M. R.; Stubna, A.; Chakrabarti, M.;

Slominski, L.; Halfen, J. A.; Münck, E.; Que, L. *Angew. Chem. Int. Ed.* **2008**, *47*, 1896–1899.

(16) Tsang, W. *J. Phys. Chem.* **1986**, *90*, 1152–1155.

(17) Stein, S. E.; Brown, R. L. *J. Am. Chem. Soc.* **1991**, *113*, 787–793.

(18) England, J.; Martinho, M.; Farquhar, E. R.; Frisch, J. R.; Bominaar, E. L.; Münck, E.; Que, L. *Angew. Chem. Int. Ed.* **2009**, *48*, 3622–3626.

(19) Howell, J. M.; Feng, K.; Clark, J. R.; Trzepkowski, L. J.; White, M. C. *J. Am. Chem. Soc.* **2015**, *137*, 14590–14593.

(20) Nanjo, T.; de Lucca, E. C.; White, M. C. *J. Am. Chem. Soc.* **2017**, *139*, 14586–14591.

(21) Borrell, M.; Costas, M. *J. Am. Chem. Soc.* **2017**, *139*, 12821–12829.

(22) Seo, M. S.; Kim, N. H.; Cho, K.-B.; So, J. E.; Park, S. K.; Clémancey, M.; Garcia-Serres, R.; Latour, J.-M.; Shaik, S.; Nam, W. *Chem. Sci.* **2011**, *2*, 1039–1045.

Chapter 6

Conclusion and Future Work

6.1 Conclusion

The mains aims of this thesis are to obtain a stable mononuclear end-on superoxocopper(II) complex and a high-spin trigonal bipyramidal (TBP) oxoiron(IV) complex supported by bis- and tris(2-pyridylmethyl)amine ligands. To achieve this we sought to incorporate bulky aryl substituents on the pyridine donors of the ligands in such a way that ligand oxidation, weakening of ligand donor strength, and steric inhibition of reaction with substrates are all minimized. The motivation for doing is to allow exploration of the inherent reactivity properties of superoxocopper(II) complexes and TBP oxoiron(IV) complexes in the absence of mitigating factors, such as sterics and the nature of donor atoms. This requires that supporting ligands closely resemble the 2-pyridylmethylamine containing systems that dominate these fields of chemistry, such that direct comparison with published data is possible.

6.1.1 Synthesis and Complexation of the Ligands

In chapter 2, we successfully synthesized the target ^{Ar3}TPA ligands with large aryl substituents and the corresponding complexes with divalent Mn – Cu ions. It was shown by a combination of NMR spectroscopy and X-ray crystallography that the cobalt(II) and copper(II) complexes are always trigonal bipyramidal. In contrast, the iron(II) complexes can (under certain conditions) access this geometry only when accompanied by weak field monodentate co-ligands. Importantly, it was shown that the field of the complexes was not weakened by incorporation of bulky aryl groups onto the 5th position of the pyridyl donors, which implies there is minimal steric repulsion with the metal centre, even though the effective bulk of the donors has been greatly increased relative to TPA. This is crucial for subsequent reactivity studies.

In chapter 3, the tridentate ^{tpb2}RBPA (R = Me,Bn) ligands were synthesized and various monochelate metal(II) complexes prepared. It seems that meridional coordination of the ligands is favoured, which is likely favoured to minimize steric clashes between the bulky tpb

substituents. No evidence was obtained for formation of bischelate metal(II) complexes, which implies the steric bulk incorporated is sufficient to prevent it. Cyclic voltammetry and X-ray crystallographic studies indicate that steric bulk on 5th position of the pyridyl donors did not noticeably weaken ligand field relative to the parent BPA ligands. However, we were unable to obtain good NMR data for the Co and Fe complexes due to high levels of coordinative flux and, perhaps for related reasons, elemental analysis also proved problematic for these systems. As a consequence, only the purity of the copper(II) complexes were satisfactorily confirmed. Efforts to resolve these problems for the other divalent metals are ongoing.

6.1.2 Mononuclear End-on Superoxocopper(II) Complex

Chapter 4 focused on our efforts to stabilize a mononuclear end-on complex against self-decay via dimerization and ligand oxidation. We found that the $[Cu^{II}(\eta^1\text{-}O_2^{\bullet-})(^{Ar3}TPA)]^+$ complexes could be synthesized without trace of peroxo-bridged dicopper(II) complex formation or any other form of self-decay over a wide temperature range. Furthermore, O_2 binding was found to display temperature-dependent reversibility and superoxocopper(II) complex formation was observed at temperatures as high as 0°C. These observations are remarkable as the overwhelming majority of published superoxocopper(II) complexes can only be trapped and studies at very low temperatures (< -80°C). Various reaction kinetics studies, including temperature dependent studies, with phenolic substrates were performed and although the reactivity of $[Cu^{II}(\eta^1\text{-}O_2^{\bullet-})(^{Ar3}TPA)]^+$ complexes was found to be sluggish relative to other TPA-systems, the data obtained suggests that electronic factors (rather than sterics) *may* be responsible for this. To verify such suggestions, computational and/or electrochemical studies will be needed. In addition, we have also obtained the mononuclear end-on superoxocopper(II) complex $[Cu^{II}(\eta^1\text{-}O_2^{\bullet-})(^{Ar2}MeBPA)]^+$, which is a rare example of such a species being supported by a tridentate ligand and it is, also, the first observation of a monometallic O_2 adduct supported by a BPA ligand. Oxygenation of the BPA complexes appears to be very sensitive

to conditions and, clearly, more work is required before we are able to fully exploit these systems.

6.1.3 Oxoiron(IV) Complex

Although ours attempts to synthesize trigonal bipyramidal high-spin (S = 2) oxoiron(IV) complexes supported by the ^{Ar3}TPA ligands were unsuccessful, we were able to prepare a series of 6-coordinate oxoiron(IV) complexes with S=1 spin-state, $[Fe^{IV}(O)(^{tpb3}TPA)(X)]^{n+}$(X = NCMe, n = 1; OTf and Br, n = 2). The spin-states of the complexes were confirmed using a combination of UV-vis and Mössbauer spectroscopic studies. Pleasingly, $[Fe^{IV}(O)(^{tpb3}TPA)(NCMe)]^{2+}$ was stable at room temperature and was able to react with substrates containing strong C-H bonds, such as cyclohexane. Although there was some evidence of steric inhibition of reaction, in most cases it seemed to be minimal. This was exemplified by a linearity of a plot of second order rate constants for substrate oxidation (adjusted according to numbers of oxidizable C-H bonds) versus C-H bond dissociation enthalpy. If reaction was under steric control, it is likely that size and shape of the substrates would have controlled rate of reaction, not BDE.

6.2 Future Work

6.2.1 Superoxocopper(II) Chemistry

The main obstacle to publication of some of our $[Cu^{II}(\eta^1\text{-}O_2^{\bullet-})(^{Ar3}TPA)]^+$ work is the absence of vibrational spectroscopic (more specifically, resonance Raman) data that is routinely required for confirmation of superoxocopper(II) complex formation. Other goals in this work are to obtain crystals suitable for X-ray crystallography, measure KIEs for other phenols, complete reactions studies for the TPA ligands bearing aromatic substituents other than tpb, and to expand the substrate scope to probe the possibilities of C-H and N-H oxidation reactions. Presently, the substrates 1-benzyl-1,4-dihydronicotinamide (BNAH) and 1,3-dimethyl-2,3-dihydrobenzimidazole (BmImH), which possess weak C-H bonds and have previously been successfully investigated as substrates for reaction with superoxocopper(II) complexes by Karlin and co-workers, are being prepared for further investigation.[1] Additionally, the possibility of nucleophilic reactivity with substrates including benzaldehydes and benzoyl chloride is intended to be further studied. Lastly, there are plans to exploit the ligands ability to stabilize reactive intermediates in reaction of the superoxocopper(II) complexes with NO gas. It is hope to be able to stabilize the resulting peroxynitritecopper(II) intermediate, such that its reactivity properties can be studied in more detail than is possible at present.

The oxygenation of $[Cu^{I}(^{Ar2}MeBPA)]^+$ requires optimization. One strategy that can be pursued is to try to employ carbon monoxide complexes in reacting with dioxygen. This strategy is widely used by Karlin and coworkers,[2] and not only inhibits side reaction, including disproportionation, it also eliminates acetonitrile from the reaction mixture. This is beneficial because MeCN binds competitively with dioxygen, which may inhibit superoxocopper(II) complex formation, and it eliminates the possibility of a 5-coordinate superoxocopper(II) complex containing a MeCN co-ligand. Once the solvent range for its synthesis has been

expanded with complete oxygenation, its reactivity with a range of substrates will be further studied.

6.2.2 Oxoiron(IV) Chemistry

Since the ^{Ar3}TPA ligands are able to enforce trigonal bipyramidal geometries under the right conditions, careful selection of co-ligands, counteranions and solvents to exclude any potential co-ligands might allow access to our targeted trigonal bipyramidal oxoiron(IV) complex. One of the possible synthetic avenues is to couple the $[Fe^{II}(^{tpb3}TPA)(OH_2)]^{2+}$ dication, which was crystallographically characterized, with more weakly coordinating anions than triflate, for example, $[B(C_6F_5)_4]^-$. Oxidation of the resulting complex, either with oxo-transfer agents or electrochemically, in non-coordinating solvents would be expected to yield the desired outcome.

Apart from mechanistic studies involving measurement of a greater range of KIEs and Eyring parameters, the exploitation of the labile site in $[Fe^{IV}(O)(^{tpb3}TPA)(NCMe)]^{2+}$ is intended by examining coordinating substrates, such an benzyl alcohol. It is hoped that coordination of the substrates will activate their constituent C-H bonds and reduce entropic barriers to reaction, thereby accelerating reaction. Finally, the reactivity of more sterically encumbered ^{Ar3}TPA ligands with substrates is planned for further examination. Steric inhibition of reaction may become more significant, but it is possible that the greater bulk will reduce kinetic barriers to reaction by favouring formation of trigonal bipyramidal (i.e., high-spin) transition states.

6.3 Reference

(1) Peterson, R. L.; Himes, R. A.; Kotani, H.; Suenobu, T.; Tian, L.; Siegler, M. A.; Solomon, E. I.; Fukuzumi, S.; Karlin, K. D. *J. Am. Chem. Soc.* **2011**, *133*, 1702–1705.

(2) Maiti, D.; Lee, D.-H.; Narducci Sarjeant, A. A.; Pau, M. Y. M.; Solomon, E. I.; Gaoutchenova, K.; Sundermeyer, J.; Karlin, K. D. *J. Am. Chem. Soc.* **2008**, *130*, 6700–6701.

(3) Barbieri, A.; De Gennaro, M.; Di Stefano, S.; Lanzalunga, O.; Lapi, A.; Mazzonna, M.; Olivo, G.; Ticconi, B. *Chem. Commun.* **2015**, *51*, 5032–5035.

(4) Park, J.; Morimoto, Y.; Lee, Y.-M.; You, Y.; Nam, W.; Fukuzumi, S. *Inorg. Chem.* **2011**, *50*, 11612–11622.

(5) Nehru, K.; Seo, M. S.; Kim, J.; Nam, W. *Inorg. Chem.* **2007**, *46*, 293–298.

Chapter 7

Material and Methods

7.1 General Information

Unless otherwise stated, ligand syntheses were conducted under an inert atmosphere using standard Schlenk techniques, and complexations were conducted in an argon filled glovebox. Toluene, tetrahydrofuran and pentane were dried and distilled from sodium and benzophenone. Acetonitrite and dichloromethane were either dried by refluxing over calcium hydride and distilled prior to use or bought as anhydrous solvents from Kanto Chemical Co., Inc. Anhydrous DME was purchased from Sigma Aldrich. Prior to use all dried solvents were degassed using the freeze-thaw-pump method. Thin-layer chromatography (TLC) was performed using silica gel aluminum or silica gel glass plates. Flash column chromatography was undertaken with Merck silica gel. NMR spectra were recorded using JEOL ECA400 or Bruker Advance AV 400, AV 500 and AV300 MHz NMR spectrometers. UV-Vis spectra were recorded using an Ailgent Cary 8454 diode-array spectrometer equipped with a Unisoku cryostat. Elemental analysis was conducted using a Perkin Elmer Series II CHNS/O analyser. Mass spectra were recorded using JEOL-T100LP cold-spray ionization (CSI) mass spectrometer using either standard electrospray ionization (ESI; ion soures desolving chamber temperature = 250℃) or CSI positive ion modes.

1-bromo-2,4,6-triphenylbenzene, 1-iodo-2,6-di(4'-*tert*-butylphenyl)benzene and 5-bromo-2-(chloromethyl)pyridine was synthesized via literature procedure described by Naumov, Power and Feringa respectively.[1–3]

7.2 Procedure for Synthesis and Complexation

7.2.1 Ligand Synthesis

1. Synthesis of 1,3,5-trimethylphenylboronic acid

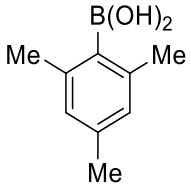

This compound was synthesized via a modified literature procedure,[4] using trimethylborate in place of triethylborate with a yield of 58 %). ^{1}H NMR (400 MHz, $CDCl_3$): δ 2.26 (s, 6H), 2.27 (s, 3H), 6.81 (s, 2H).

2. Synthesis of 2,4,6-triphenylbenzene boronic acid

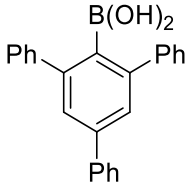

Magnesium turning (1.49 g, 61.51 mmol) was activated by reaction with I_2 (1 crystal) in refluxing THF (40 mL) until the decolourization of I_2. Subsequently, 1-bromo-2,4,6-triphenylbenzene (16 g, 41.526 mmol) was added portionwise and the resulting mixture heating at reflux for 16 h. After this, the reaction was allowed to cool to 0℃. Excess trimethylborate (8.52 g, 82.01 mmol) was then added and the mixture heated to reflux for a further 24 h. Upon cooling to room temperature, MeOH, ethyl acetate and diethyl ether were added sequentially and the reaction mixture filtered through Celite. The residue further was washed repeatedly with diethyl ether and ethyl acetate until the filtrate was no longer yellow. The filtrates were combined and solvent was removed using a rotary evaporator. The solid obtained was redissolved in ether and 2M HCl added, after which it was stirred for 4 h. After separation from the organic layer, the aqueous layer was extracted thrice with diethyl ether. The combined organic layers were then washed with brine, dried over $MgSO_4$, and filtered. The filtrate was

reduced to dryness to give the product as a crude yellow solid (12.92 g, 90 %). ^{1}H NMR obtained was similar to the published data.[5]

3. Synthesis of 1-iodo-2,6-diphenylbenzene

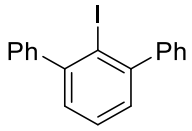

This compound was synthesized via a modification of a published procedure.[6] n-BuLi (124 mL of 2.0 M in cyclohexane) was added dropwiseto a solution of bromobenzene (35.3 g, 224.6 mmol) in diethyl ether (200 mL) at -78℃. The mixture obtained was then allowed to warm to room temperature and sequentially stirred for 3 h. Subsequently, 1,3-dichlorobenzene (8.25 g, 56.4 mmol) was slowly added and the reaction mixture then stirred overnight. After cooling to 0℃, iodine (42.75 g, 168.4 mmol) was slowly added and the resulting mixture stirred for a further 1 h. Next, a saturated aqueous solution of sodium sulfite was added to the reddish brown coloured reaction mixture until it decolourized. After separation of the organic layer from the aqueous layer, the latter was extracted with diethyl ether twice. The combined organic layers were washed once with water and once with brine, dried over $MgSO_4$, filtered, and all volatiles remove from the filtrate in vacuo. The crude brown oil obtained was recrystallized from hot MeOH to give the product as a yellow solid (9.04 g, 45 %). ^{1}H NMR (400 MHz, DMSO-d6) δ 7.27 (d, 2H, J = 7.5 Hz), 7.34 (d, 4H, J = 7.8 Hz), 7.39 – 7.49 (m, 7H).

4. Synthesis of 2,6-diphenylbenzene boronic acid

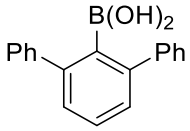

This compound was synthesized via a modified literature procedure.[5] To a solution of iodoterphenylbenzene (1.5 g, 4.21 mmol) in THF (16mL), cooled – 78°C, *n*-BuLi (2 mL of 2.0 M in cyclohexane) was added dropwise. The resulting mixture was warmed to room temperature and stirred for 2 h. After cooling the reaction mixture to – 30°C, $B(OMe)_3$ (0.525 g, 5.05 mmol) was added to it. It was then was allowed to warm to room temperature and stirred overnight. Subsequently, water was added and the reaction mixture stirred for a further 4 h. The organic layer was separated and the aqueous layer was extracted twice with diethyl ether. The combined organic fractions were washed once each with brine and water, before being sequentially dried over $MgSO_4$, filtered, and reduced to dryness using a rotary evporator. The resulting crude yellow solid was washed with hexane to yield the product as a white solid (0.5 g, 43 %). ^{1}H NMR (500 MHz, DMSO-d6) δ 7.26 (t, 2H, J = 6.9 Hz), 7.33 (t, 2H, J = 6.2 Hz), 7.43 – 7.39 (m, 5H), 7.51 (t, 4H, J = 7.2 Hz), 7.88 (d, 2H, J = 6.4 Hz).

5. Synthesis of 2,6-di(4'-*tert*-butylphenyl)benzene boronic acid

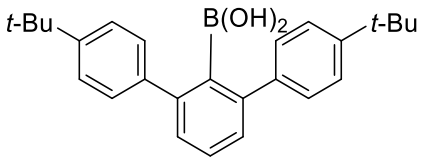

A 250 mL three-necked round bottomed flask was charged with 1-iodo-2,6-di(4'-*tert*-butylphenyl)benzene (6.00 g, 13 mmol) and 100 mL of dry hexane, and cooled to -78 ºC. To the resulting white suspension, 2M *n*-BuLi in cyclohexane (13 mL, 0.026 mol) was added dropwise. The resulting mixture was allowed to slowly warm to room temperature and then heated to reflux for 4 h. Subsequent to the reaction mixture cooling to room temperature all volatiles were removed under vacuum. The resulting residue was dissolved in 100 mL of dry

hexane and cooled to 0 ºC. Trimethyl borate (2.9 mL, 0.026 mol, 2.0 equiv.) was then added dropwise to it and the reaction mixture was refluxed for 16 h. Afterwards, H_2O was added to quench the reaction and it was stirred for a further 4 h. The organic and aqueous phases were separated, and the aqueous layer was extracted twice with diethyl ether. The combined organic layers were washed with brine, dried over MgSO4, filtered, and solvents removed under vacuum to give the product as a viscous yellow-orange oil (3.90 g, 54 %). ^{1}H NMR (400 MHz, $CDCl_3$) δ 1.30 (s, 18H), 3.22 (s, 2H), 7.30 (d, 4H, J = 7.4 Hz), 7.38 (d, 4H, J = 7.2 Hz), 7.87 (m, 3H).

6. General Procedure for the Synthesis of 5-aryl-2-pyridinecarboxaldehyde

An aqueous solution of sodium carbonate (2 M) was added to a two-necked round bottom flask was containing a mixture of 5-bromo-2-pyridinecarboxaldehyde (4.23 g, 22.7 mmol), aryl boronic acid (34.1 mmol, 1.5 eq), $Pd(PPh_3)_4$ (0.613 mmol, 0.03 eq) and anhydrous toluene (80 mL). The resulting mixture was heated to reflux for 10 h. Subsequent to cooling to room temperature, the organic and aqueous layers were separated and the latter was extracted twice with dichloromethane. The combined organic layers washed twice with water and once with brine, dried over sodium sulfate, filtered, and all volatiles were removed using a rotary evaporator. The resulting crude product was purified by column chromatography.

a. 5-(1,3,5-trimethylphenyl)-2-pyridinecarboxyaldehyde

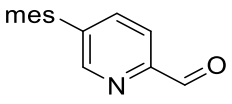

5-mesityl-2-pyridinecarboxyaldehyde was purified using an ethyl acetate/hexane (1:9) mixture to give the product as a yellow oil (3.13 g, 73 %). ^{1}H NMR (400 MHz, $CDCl_3$) δ 2.00 (s, 6H), 2.35 (s, 3H), 6.99 (s, 2H), 7.70 (dd, 1H, J = 1.6, 7.5 Hz), 8.05 (d, 1H, J = 8.2 Hz), 8.60 (d, 1H, J = 0.9 Hz), 10.1 (s, 1H); ^{13}C NMR (400 MHz, $CDCl_3$): δ 20.8, 21.1, 121.6, 128.7, 134.0, 135.8, 138.2, 141.7, 151.0, 151.4.

b. 5-(2,4,6-triphenylphenyl) -2-pyridinecarboxyaldehyde

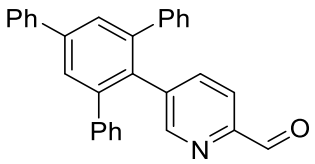

5-(2,4,6-triphenyl)-benzene-2-pyridinecarboxyaldehyde was purified using an ethyl acetate/dichloromethane (1:9) mixture to give the product as a white solid (1.23 g, 71 %). ^{1}H NMR (400 MHz, $CDCl_3$) δ 7.08 – 7.11 (m, 6H), 7.19 – 7.22 (m, 5H), 7.35 (d, 1H, J = 8.1 Hz), 7.41 (d, 1H, J = 7.4 Hz), 7.48 (t, 2H, J = 7.2 Hz), 7.59 – 7.63 (m, 1H), 7.70 – 7.73 (m, 4 H), 8.30 (dd, 1H, J = 2.5, 2 Hz), 9.92 (s, 1H); ^{13}C NMR (400 MHz, $CDCl_3$) δ 120.48, 127.22, 127.33, 128.08, 128.27, 128.65, 129.09, 130.09, 133.30, 139.84, 140.00, 140.53, 140.75, 141.68, 142.93, 150.00, 152.54.

7. General procedure for the synthesis of (5-aryl-pyridin-2-yl) methanol

Sodium borohydride (15.9 mmol 2eq) was added portionwise to a solution of 5-aryl-2-pyridinecarboxaldehyde (7.95 mmol, 1 eq) in methanol (45 mL), at 0 °C. The reaction mixture was then refluxed for three hours. Subsequent to cooling to ambient temperatures and removal of solvent, water was added. The resulting mixture was extracted thrice with dichloromethane, and the combined organic layers were washed once with brine and all volatiles removed in vacuo. The crude product thereby obtained was used for next step without further purification.

a. (5-(1,3,5-trimethylphenyl)-pyridin-2-yl) methanol

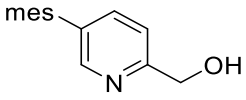

Pale brown oil (1.51 g, 94 %). ^{1}H NMR (400 MHz, $CDCl_3$) δ 2.01 (s, 6H), 2.35 (s, 3H), 4.85 (s, 2H), 6.97 (s, 2H), 7.39 (d, 1H, J = 8.2 Hz), 7.51 (dd, 1H, J = 2.1, 8.0 Hz), 8.36 (s, 1H).

b. (5-(2,4,6-triphenylphenyl) pyridin-2-yl) methanol

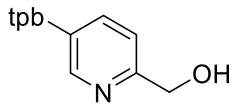

Off-white solid (2.76 g, 84 %). ^{1}H NMR (400 MHz, $CDCl_3$) δ 4.58 (s, 2H), 6.89 (d, 1H, J = 7.8 Hz), 7.10 – 7.23 (m, 11H), 7.36 – 7.48 (m, 3H), 7.69 – 7.71 (m, 4H), 8.04 (s, 1H); ^{13}C NMR (400 MHz, $CDCl_3$) δ 63.93, 119.09, 126.89, 127.31, 127.90, 128.12, 128.59, 129.04, 130.11, 134.05, 134.10, 139.56, 140.21, 141.02, 141.26, 143.03, 150.65, 156.35.

8. General Procedure for the Synthesis of 2-(chloromethyl)-5-aryl-pyridine hydrochloride salt

Thionyl chloride (138 mmol, 63 eq) was added to (5-aryl-pyridin-2-yl) methanol (2.20 mmol) in a two-necked round bottom flask that was cooled using an ice bath. After the initial vigorous reaction subsided, the reaction mixture was refluxed for three h. The resulting solution was, subsequently, cooled to room temperature and all volatiles were removed using a rotary evaporator. The crude product thereby obtained was used without any further purification.

a. 2-(chloromethyl)-5-(1,3,5-trimethylphenyl)-pyridine hydrochloride salt

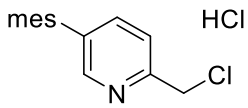

Brown oil (0.615 g, 99 %). ^{1}H NMR (400 MHz, CD_3CN) δ 1.99 (s, 6H), 2.32 (s, 3H), 5.21 (s, 2H), 7.02 (s, 2H), 8.06 (d, 1H, J = 8.2 Hz), 8.24 (dd, 1H, J = 1.8 ,8.2 Hz), 8.47 (d, 1H, J = 1.8 Hz).

b. 2-(chloromethyl)-5-(2,4,6-triphenylphenyl)-pyridine hydrochloride salt

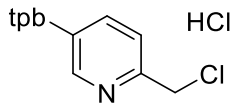

Orange solid (0.761 g, 74 %). ^{1}H NMR (500 MHz, CD_3CN) δ 4.82 (s, 2H), 7.18 (s, 4H), 7.24 – 7.27 (m, 6H), 7.43 – 7.52 (m, 4H), 7.71 – 7.82 (m, 5H), 8.03 (s, 1H).

9. Synthesis of (5-(1,3,5-trimethylphenyl)pyridin-2-yl)methanamine

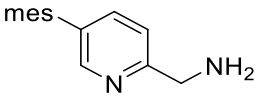

Potassium phthalimide (0.448 g, 2.42 mmol) and sodium carbonate (0.256 g, 2.42 mmol) were added to a solution of 2-(chloromethyl)5-mesitylpyridine (0.612 g, 2.18 mmol) in DMF (10 mL), and the resulting mixture was refluxed for 1 h. Subsequent to cooling, the reaction mixture was filtered. The filtrate was then concentrated in vacuo and water (3 mL) added to it. The reaction mixture was filtered and the residue obtained was dissolved in an ethanol (20 mL) solution of hydrazine monohydrate (0.407 mL, 2.82 mmol), and heated to reflux under a nitrogen atmosphere for 3 h. Next, the solution was cooled and water (10 mL) added to it. 1M hydrochloric acid was used to adjust the pH of the solution to 2 and it was then refluxed for 2 h. After the reaction mixture was cooled and filtered, 1M aqueous sodium hydroxide was added to the filtrate to adjust its pH to 12. The aqueous solution was extracted thrice with dichloromethane, and the combined organic layers were washed twice with water, dried over sodium sulfate and filtered. The brown filtrate was reduced to dryness in vacuo to give the product as a viscous brown oil (0.284 g, 58%). ^{1}H NMR (400 MHz, $CDCl_3$) δ 2.00 (s, 6H), 2.33 (s, 3H), 4.05 (s, 2H), 6.96 (s, 2H), 7.35 (d, 1H, J = 7.8 Hz), 7.46 (dd, 1H, J = 2.3, 7.8 Hz), 8.36 (s, 1H).

10. Synthesis of (5-(2,4,6-triphenylbenzene)-2-pyridyl)methanamine

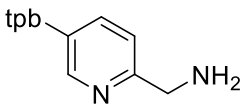

Potassium phthalimide (0.475 g, 2.57 mmol) and sodium carbonate (0.272 g, 2.57 mmol) were added to a solution of 2-(chloromethyl)-5-(2,4,6-triphenylbenzene)-pyridine (1.08 g, 2.31 mmol) in DMF (10 mL), and the resulting mixture was refluxed for 3 h. After cooling, the reaction mixture was filtered and the filtrate concentrated in vacuo. Water (3 mL) and

concentrated hydrochloric acid was added sequentially to the crude material obtained and it was heated to reflux for 2 days. Subsequently, the reaction mixture was filtered and dichloromethane was added to extract thrice with water. The organic extracts were combined, washed twice with aqueous sodium hydroxide solution and once with brine, dried over sodium sulfate, filtered, and reduced to dryness to give the product as a white solid. (0.80 g, 84 %). ^{1}H NMR (400 MHz, $CDCl_3$): δ 3.83 (s, 2H), 6.93 (d, 1H, J = 7.8 Hz), 7.13 (t, 5H, J = 6.8 Hz), 7.20 (d, 5H, J = 5.0 Hz), 7.39 (t, 1H, J = 7.3 Hz), 7.47 (t, 2H, J = 7.3 Hz), 7.71 (d, 5H, J = 5.0 Hz), 8.06 (s, 1H);); ^{13}C NMR (400 MHz, $CDCl_3$) δ 47.39, 119.79, 126.83, 127.30, 127.83, 128.05, 128.55, 128.99, 130.10, 133.50, 134.24, 139.43, 140.25, 140.90, 141.31, 143.01, 151.37, 159.09.

11. Synthesis of tris(5-(1,3,5-trimethylphenyl)-2-pyridylmethyl)amine, ^{mes3}TPA

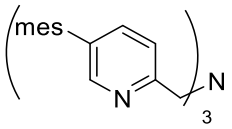

Compound (5-(1,3,5-trimethylphenyl)pyridin-2-yl)methanamine (0.429 g, 1.90 mmol) was added to a flask containing sodium triacetoxyborohydride (0.403 g, 1.90 mmol), 5-(1,3,5-trimethylphenyl)-2-pyridinecarboxyaldehyde (0.215 g, 0.952 mmol) and dichloromethane (18 mL). The resulting mixture was stirred for eighteen hours. Subsequently, concentrated aqueous sodium hydrogen carbonate solution (9.06 mL) was added and it was stirred for a further 30 min. The organic layer was separated and the aqueous layer was extracted twice with dichloromethane. The combined organic layers were washed once with water and brine respectively, and then dried over sodium sulfate. After filtration, all volatiles were removed from the filtrate. The residue was triturated with pentane to give the product as a yellow solid that was dried in vacuum (0.186 g, 30 %). ^{1}H NMR (400 MHz, $CDCl_3$): δ 2.01 (s, 18H), 2.33 (s, 9H), 4.06 (s, 6H), 6.96 (s, 6H), 7.52 (dd, 3H, J = 2.8, 7.8 Hz), 7.73 (d, 3H, J = 8.2 Hz), 8.39

(dd, 3H, J = 0.9, 2.3 Hz); ^{13}C NMR (400 MHz, $CDCl_3$): δ 21.0, 21.1, 60.1, 122.6, 128.4, 128.7, 135.1, 136.4, 137.5, 137.7, 149.7, 157.7.

12. Synthesis of (5-bromopyridin-2-yl)methanol

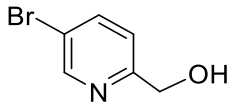

This compound was synthesized via a modified literature procedure.[7] Sodium borohydride (4.07 g, 107.52 mmol) was added portionwise to a solution 5-bromo-2-carboxaldehyde (10.00 g, 53.8 mmol) in methanol (120 mL), at room temperature. The resulting reaction mixture was stirred overnight, after which 2M aqueous hydrochloric acid was added until pH = 1. Stirring was undertaken for a further 30 min. All the solvent was then removed using a rotary evaporator and an aqueous solution of NaOH was added until a pH of 12 was achieved. The resulting aqueous layer was extracted thrice with dichloromethane and the combined organic layers were dried using magnesium sulfate, filtered, and reduced to dryness under vacuum to give the product as a white solid. (9.75 g, 96 %). ^{1}H NMR (500 MHz, $CDCl_3$) δ 3.41 (bs, 1H), 4.72 (s, 2H), 7.19 (d, 1H, J = 8.3 Hz), 7.81 (dd, 1H, J = 1.95 Hz; J = 8.30 Hz), 8.62 (d, 1H, J = 1.95 Hz).

13. Synthesis of Tris(5-bromo-2-pyridylmethyl)amine

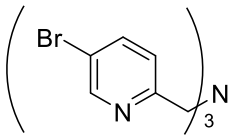

This compound was synthesized via a modified published procedure.[8] Acetonitrite (30 mL) was added into a flask containing acetaldehyde ammonium trimer (1.20 g, 9.28 mmol), 5-bromo-2-(chloromethyl)pyridine (8.62 g, 41.8 mmol), potassium carbonate (5.77 g, 41.8 mmol) and potassium iodide (6.93 g, 41.8 mmol). The reaction mixture was refluxed overnight. After cooling to room temperature, all the solvent was removed using a rotary evaporator. The resulting brown solid was dissolve in chloroform and extracted once with water. The aqueous

layer was extracted thrice with chloroform, and the combined organic layers were extracted once with brine. The brown chloroform solution was then dried over sodium sulfate, filtered, and all volatiles were removed in vacuo. The crude brown product was purified via silica-gel column chromatography (dichloromethane/ethyl acetate 60:40) to yield a light brown solid (4.60 g, 94 %). ^{1}H NMR (400 MHz, $CDCl_3$) δ 3.80 (s, 6H), 7.39 (d, 3H, J = 8.32 Hz), 7.75 (dd, 3H, J = 2.32 Hz; J = 8.32 Hz), 8.57 (d, 3H, J = 2.32 Hz). ^{13}C NMR (400 MHz, $CDCl_3$) δ 59.37, 119.28, 124.55, 139.17, 150.33, 157.52.

14. Synthesis of Tris(5-(aryl-2-pyridylmethyl)amine

a. Tris(5-(2,4,6-triphenylphenyl)-2-pyridylmethyl)amine, ^{tpb3}TPA

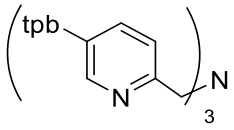

Methanol (38 mL) and aqueous sodium carbonate solution (58 mL of 2M) was added to a solution of tris(5-bromo-2-pyridylmethyl)amine (4.00 g, 7.59 mmol), 2,4,6-triphenylbenzene boronic acid (11.960 g, 34.15 mmol) and $Pd(PPh_3)_4$ (1.0 g, 0.6 mmol) in toluene (100 mL), after which the resulting mixture was heated at 100 °C, with vigorous stirring, for 48 h. Subsequently, additional boronic acid (0.598 g, 1.70 mmol) and $Pd(PPh_3)_4$ (0.148 g, 0.098 mmol) was added and heating was continued for a further 48 h. The brown suspension obtained was cooled to room temperature and the organic layer was separated from the aqueous layer and the latter was extracted thrice with dichloromethane. The combined organic layers were washed twice with an aqueous solution of sodium carbonate (2 M) and once with brine once, before being dried over sodium sulfate. After filtration, all solvent was removed from the filtrate using a rotary evaporator. Ethyl acetate was added to the residue and the suspension obtained after stirring for 30 min was filtered. The solid isolated was dried under vacuum to give the product as a white solid. (6.84 g, 75 %). ^{1}H NMR (400 MHz, $CDCl_3$) δ 3.31 (s, 6H), 6.77 (d, 3H, J = 8 Hz), 6.96 (t, 6H, J = 7.2 Hz) 7.02–7.11 (m, 27H), 7.38 (t, 3H J = 7.2 Hz),

7.47 (t, 6H, *J* = 7.2 Hz), 7.70–7.71 (m, 12H), 8.00 (d, 3H, *J* = 1.6 Hz). ^{13}C NMR (400 MHz, $CDCl_3$) δ 58.92, 122.40, 126.85, 127.30, 127.93, 128.33, 129.01, 130.06, 133.83, 134.53, 139.08, 140.28, 140.98, 141.25, 142.92, 150.78, 157.06.

b. Tris(5-(2,6-diphenylphenyl)-2-pyridylmethyl)amine, ^{tpy3}TPA

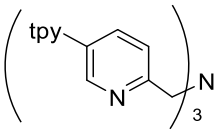

The synthesis of tris(5-(2,6-diphenylphenyl)-2-pyridylmethyl)amine was conducted using an anlogous procedure to tris(5-(2,4,6-triphenylphenyl)-2-pyridylmethyl)amine and yielded the product as a white solid (1.18 g, 64 %). ^{1}H NMR (400 MHz, CD_2Cl_2) δ 3.24 (s, 6H), 6.71 (d, 2H, *J* = 6.4 Hz), 6.97 – 6.99 (m, 6H), 7.02 – 7.07 (m, 27H), 7.45 (d, 6H, *J* = 6.1 Hz), 7.52 (t, 3H, *J* = 6.3 Hz), 7.91 (d, 3H, *J* = 1.6 Hz). ^{13}C NMR (400 MHz, $CDCl_3$) δ 58.89, 122.47, 126.71, 127.83, 128.10, 129.61, 130.04, 134.02, 135.56, 139.03, 141.26, 142.40, 150.72, 157.00.

c. Tris(5-(2,6-di(4'-*tert*-butylphenyl)phenyl)-2-pyridylmethyl)amine, ^{dtbt3}TPA

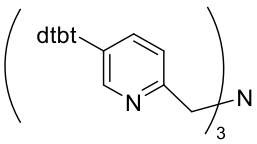

The synthesis of tris(5-(2,6-di(4'-*tert*-butylphenyl)phenyl)-2-pyridylmethyl)amine was conducted using an analogous procedure to tris(5-(2,4,6-triphenylphenyl)-2-pyridylmethyl)amine. However, it was necessary to wash the crude product through a silica gel plug to remove all the unreacted boronic acid. Hexane (100 %) was used to elute the latter and the product was flushed out with an ethyl acetate/hexane (1:4) mixture. The product was further purified by recrystallization from acetonitrile and gave a pale pink solid (0.73 g, 32 %). ^{1}H NMR (400 MHz, $CDCl_3$) δ 1.14 (s, 54H), 3.37 (s, 6H), 6.97 – 6.99 (m, 15H), 7.05 – 7.09 (m, 15H), 7.40 – 7.42 (m, 6H), 7.45 – 7.49(m, 3H), 8.01 (s, 3H). ^{13}C NMR (400 MHz, $CDCl_3$) δ

31.36, 34.38, 58.16, 122.01, 124.72, 127.95, 129.71, 134.18, 135.36, 138.33, 139.19, 142.28, 149.38, 151.14, 156.10.

15. Synthesis of (5-bromopyridin-2-yl)-N-methylmethanamine

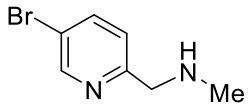

An aqueous solution of $MeNH_2$ (4.6 mL, 134 mmol, 5 equiv) was added dropwise to a solution of 5-bromo-2-pyridinecarboxaldehyde (5.00 g, 26.8 mmol) in methanol (10 mL) that has been cooled to 0 °C. The resulting mixture was allowed to warm to room temperature, with continuous stirring for 3 h. It was then cooled to 0°C again and $NaBH_4$ (2.03 g, 53.7 mmol, 2 equiv) was added portionwise to it, after which it was stirred overnight at room temperature. Subsequently, the solvent was removed at reduced pressure and diethyl ether and saturated aqueous Na_2SO_3 solution was added to the residue. The basic aqueous layer, with pH ≥12, was extracted twice with diethyl ether. The combined organic layers were washed once each with saturated aqueous Na_2SO_3 and brine. Removal of all solvents under vacuum yielded the crude product as a clear yellow oil (5.10 g, 94%). The product was used in the subsequent reaction without further purification. ^{1}H NMR (400 MHz; $CDCl_3$) δ 2.46 (s, 3H), 3.82 (s, 3H), 7.23 (d, 1H, J = 8.2 Hz), 7.77 (dd, 1H, J = 2.5, 8.5), 8.60 (s, 1H). ^{13}C NMR (400 MHz, $CDCl_3$) δ 35.95, 56.29, 118.75, 123.57, 138.95, 150.20, 158.19.

16. Synthesis of *N*,*N*-bis(5-bromo-2-pyridylmethyl)-*N*-methylamine

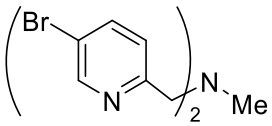

5-bromo-2-pyridinecarboxaldehyde (3,15 g, 16.9 mmol) and $NaBH(OAc)_3$ (4.89 g, 22.9mmol) were added to a solution of (5-bromopyridin-2-yl)-N-methylmethanamine (3.15 g, 15.7 mmol) in dichloromethane (20 mL), at room temperature. The resulting mixture was stirred overnight and, subsequently, quenched by addition of an aqueous solution of NaOH (20 mL, 2M). After

stirring for a further 1 hour, the mixture was extracted with dichloromethane. The organic layer was dried over Na_2SO_4, filtered, and all solvent removed from the filtrate to give a dark brown oil. This crude product was dissolved in tetrahydrofuran (20 mL) and excess KH was added to it. The mixture obtained was stirred for 1.5 h and all volatiles were removed under reduced pressure. The resulting reddish brown solid was extracted with several portions of warm pentane. The combined extracts were concentrated to dryness in vacuo to yield the product as a pale solid solid (3.95 g, 68%). ^{1}H NMR (400 MHz; $CDCl_3$) δ 2.30 (s, 3H), 3.70 (s, 4H), 7.39 (d, 2H, J = 8.2 Hz), 7.78 (dd, 2H, J = 2.3, 8.2 Hz), 8.60 (d, 2H, J = 2.3 Hz); ^{13}C NMR (400 MHz; $CDCl_3$): δ 42.77, 62.80, 119.04, 124.34, 139.06, 150.19,157.73.

17. Synthesis of *N,N*-bis(5-aryl-2-pyridylmethyl)-*N*-methylamine

a. *N,N*-bis(5-(2,4,6-triphenylphenyl)-2-pyridylmethyl)-*N*-methylamine, ^{tpb3}MeBPA

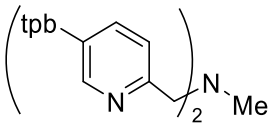

Methanol (38 mL) and aqueous sodium carbonate (58 mL of 2M) were added to a solution of *N,N*-bis(5-bromo-2-pyridylmethyl)-*N*-methylamine (2.82 g, 7.59 mmol), 2,4,6-triphenylbenzene boronic acid (7.97 g, 22.8 mmol) and $Pd(PPh_3)_4$ (0.918 g, 0.607 mmol) in toluene (100 mL), after which the resulting mixture was heated at 100 °C, with vigorous stirring, for 48 h. Subsequently, additional boronic acid (2.93 g, 8.37 mmol) and $Pd(PPh_3)_4$ (0.148 g, 0.027 mmol) were added and heated was continued for another 48 h. The brown suspension obtained was cooled to room temperature and the organic layer was separated from the aqueous layer. Next, the aqueous layer was extracted thrice with dichloromethane and the combined organic layers were washed twice with a concentrated aqueous solution of Na_2CO_3 (2 M) and once with brine, before being dried over sodium sulfate. The organic solution obtained after filtration was reduced to dryness in vacuo to give crude product as a brown material. Purification was undertaken by column chromatography using hexane/ethyl acetate (4:1) as the

eluant, followed by washing with methanol to yield the product as a white solid (3.37 g, 54 %). ^{1}H NMR (400 MHz; $CDCl_3$) δ 2.05 (s, 3H), 3.43 (s, 4H), 6.97 (d, 2H, J = 7.8 Hz), 7.11 (m, 22H), 7.38 (t, 2H, J = 7.3 Hz), 7.47 (t, 4H, J = 7.3 Hz), 7.70 (t, 8H, J = 7.8 Hz), 8.04 (d, 2H, J = 1.8 Hz); ^{13}C NMR (400 MHz; $CDCl_3$): δ 42.47, 62.91, 122.32, 126.88, 127.34, 127.87, 128.00, 128.44, 129.05, 130.16, 133.88, 134.50, 139.25, 140.32, 140.98, 141.33, 143.01, 151.18, 156.43; m/z 822 (100% $M+H^+$).

b. *N,N*-bis(5-(2,6-diphenylphenyl)-2-pyridylmethyl)-*N*-methylamine, ^{tpy3}MeBPA

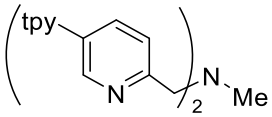

The synthesis of *N,N*-bis(5-(2,6-diphenylphenyl)-2-pyridylmethyl)-*N*-methylamine followed an analogous procedure to *N,N*-bis(5-(2,4,6-triphenylphenyl)-2-pyridylmethyl)-*N*-methylamine (1.42 g, 54 %). ^{1}H NMR (400 MHz; $CDCl_3$) δ 2.05 (s, 3H), 3.37 (s, 4H), 6.95 (d, 2H, J = 7.8 Hz,), 7.07 (m, 22H) , 7.45 (m, 8H), 7.96 (s, 2H); ^{13}C NMR (400 MHz; $CDCl_3$): δ 42.44, 62.88, 122.26, 126.72, 127.90, 128.11, 129.73, 130.11, 134.05, 135.50, 139.19, 141.31, 142.44, 151.12, 156.34.

18. Synthesis of *N,N*-bis(5-bromo-2-pyridylmethyl)-N-benzylamine

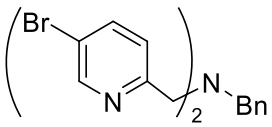

A mixture of acetonitrite (190 mL), freshly distilled benzylamine (0.614 g, 5.74 mmol), 5-bromo-2-(chloromethyl)pyridine (2.50 g, 12.11 mmol), sodium carbonate (21.29 g, 200.87 mmol), and water (19 mL) were heated at reflux for 168 h. Subsequently, the reaction mixture was cooled to room temperature and then filtered to remove undissolved material. The solvent in the filtrate was removed using a rotary evaporator and replaced with water, after which extraction with dichloromethane was performed thrice. The combined organic extracts were dried over sodium sulfate, filtered, and all solvent removed in vacuo to give a brown solid. This

crude product was purified via silica gel column chromatography (12 % ethyl acetate/Hexane) and afforded a yellow solid (2.37 g, 92 %). ^{1}H NMR (400 MHz; $CDCl_3$): δ 3.66 (s, 2H), 3.75 (s, 4H), 7.22 (m, 1H), 7.30 (m, 2H), 7.37 (m, 2H), 7.42 (d, 2H, J = 8.68 Hz), 7.73(dd, 2H, J = 2.28 Hz; 8.24 Hz), 8.56 (d, 2H, J = 1.8 Hz); ^{13}C NMR (400 MHz; $CDCl_3$): δ 58.59, 59.23, 119.09, 124.27, 127.35, 128.49, 128.92, 138.49, 139.08, 150.09, 158.21.

19. Synthesis of *N*,*N*-bis(5-(2,4,6-triphenylphenyl)-2-pyridylmethyl)-N-benzylamine, ^{tpb2}BnBPA

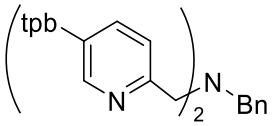

Methanol (17 mL) and aqueous sodium carbonate solution (26 mL of 2M) were added to a solution of *N*,*N*-bis(5-bromo-2-pyridylmethyl)-N-benzylamine (1.50 g, 3.35 mmol) and 2,4,6-triphenylbenzene boronic acid (3.52 g, 13.4 mmol) in toluene (100 mL). After degassing using 3 freeze-pump-thaw cycles, $Pd(PPh_3)_4$ (0.405 g, 0.268 mmol) was added and the mixture obtained was heated at 100°C, with vigorous stirring, for 48 h. Subsequently, additional boronic acid (2.28 g, 6.50 mmol) and $Pd(PPh_3)_4$ (0.101 g, 0.067 mmol) were added and heating was continued for a further 48 h. The brown suspension obtained was cooled to room temperature and the organic layer was separated from the aqueous layer. The latter was extracted thrice with dichloromethane, and the combined organic layers were then washed twice with an aqueous solution of sodium carbonate (2 M) and once with brine. After being dried over sodium sulfate and filtered, the organic solution was reduced to dryness in vacuo. The crude brown material obtained was purified by column chromatography, using hexane/ethyl acetate (9:1) as an eluant, followed by washing with methanol and yielded the product as a white solid (1.20 g, 40 %). ^{1}H NMR (500 MHz; $CDCl_3$): δ 3.35 (s, 2H), 3.43 (s, 4H), 6.98 – 7.13 (m, 26 Hz), 7.18 (d, 2H, J = 7.0 Hz), 7.39 (t, 2H, J = 7.3 Hz), 7.47 (t, 4H, J =

7.1 Hz), 7.70 (t, 9H, *J* = 3.75 Hz), 8.00 (d, 2H, *J* = 1.75 Hz); ^{13}C NMR (400 MHz; $CDCl_3$): δ ppm 57.83, 59.14, 122.35, 126.86, 127.08, 127.32, 127.85, 127.96, 128.25, 128.37, 129.02, 129.23, 129.90, 130.10, 133.81, 134.54, 139.21, 140.31, 140.98, 141.27, 142.97, 150.83, 157.21.

7.2.2 Synthesis of Complexes

1. Procedure for Formation of M(^{Ar3}TPA)(X)$_2$ (X = OTf, ClO_4) and M(^{Ar2}MeBPA)(OTf)$_2$ Complexes.

A solution of $M(X)_2(NCMe)_2$ (0.415 mmol) in acetonitrile (10 mL) was added to a vial containing ^{Ar3}TPA or ^{Ar2}MeBPA (0.415 mmol) and the resulting mixture was stirred at room temperature overnight. The solution obtained was filtered and the solvent in the filtrate was reduced in volume until precipitate began to form, at which point copious diethyl ether was added. After stirring for 30 min, the resulting suspension was filtered and the solid product dried under vacuum**.**

a. [Mn^{II}(^{tpb3}TPA)(OTf)$_2$]

White solid (0.44 g, 69 %). MS (+ESI): *m/z* 1407.42 $[(M\text{-}OTf)]^+$, 628.83 $[(M\text{-}MeCN)]^{2+}$, 649.39$[(M\text{-}(MeCN)_2)]^{2+}$. Single X-ray crystal was obtained via vapour diffusion of diethyl ether into the acetonitrile solution containing the complex.

b. [Fe^{II}(^{mes3}TPA)(NCMe)$_2$](ClO$_4$)$_2$

Yellow Solid (0.125 g, 60 %). Single X-ray crystal was obtained via vapour diffusion of diethyl ether into the acetonitrile solution containing the complex.

c. [Fe^{II}(^{tpb3}TPA)(OH$_2$)](OTf)$_2$

Yellow solid (0.49 g, 76 %). ^{1}H NMR (400 MHz, CD_2Cl_2, broad signals) δ - 13.83 (3H), 6.04 (30H), 7.54 (21H), 48.59 (3H), 139.01 (3H). ^{1}H NMR (400 MHz, CD_3CN, broad signals) δ 6.52 (bs, 6H), 6.70 (d, 3H, *J* = 7.2 Hz), 6.92 (d, 12H, *J* = 3.6 Hz), 7.14 (d,18H), 7.40 (t, 3H, *J* = 7.2 Hz), 7.47 (t, 6H, *J* = 7.0 Hz), 7.74 (d, 12H), 8.43 (bs, 3H), 10.57 (bs, 3H). ^{19}F NMR (400

MHz, CD_2Cl_2, broad signals) δ -74.03, 17.20. ^{19}F NMR (400 MHz, CD_3CN, broad signals) δ -77.20. μ_{eff} (Evans' NMR Method): 5.2 μ_B in CD_2Cl_2. MS (+ESI): *m/z* 1408.55 $[(M\text{-}OTf)]^+$, 629.80 $[(M\text{-}MeCN)]^{2+}$, 650.31$[(M\text{-}(MeCN)_2)]^{2+}$. Anal. Calcd. for $C_{96}H_{79}F_6FeN_4O_{8.50}S_2$: C, 69.03; H, 4.93; N, 3.43; S, 4.34. Found: C, 69.52; H, 3.38; N, 4.80; S, 3.87.

d. $[Fe^{II}(^{tpy3}TPA)(OTf)_2]$

Yellow solid. (0.39 g, 70 %). ^1H NMR (400 MHz, CD_2Cl_2, broad signals) δ -13.85 (3H), 4.85 (6H), 5.99 (24H), 6.92 (3H), 7.34 (6H); ^1H NMR (400 MHz, CD_3CN, broad signals) δ 6.55 (3H), 6.81 (12H), 7.10 (24H), 7.46 (6H), 7.57 (3H), 8.67 (3H), 11.04 (3H); ^{19}F NMR (400 MHz, CD_2Cl_2, broad signals) δ -74.45, 17.66. ^{19}F NMR (400 MHz, CD_3CN, broad signals) δ -77.20; μ_{eff} (Evans' NMR Method): 4.9 μB in CD_2Cl_2. MS (+ESI): *m/z* 1179.39 $[(M\text{-}OTf)]^+$, 535.73 $[(M\text{-}MeCN)]^{2+}$, 649.39$[(M\text{-}(MeCN)_2)]^{2+}$. Efforts in obtaining data for elemental analysis is currently on-going.

e. $[Fe^{II}(^{dtbt3}TPA)(OTf)](OTf).MeCN.2H_2O$

Yellow solid. (0.52 g, 76 %).^1H NMR (400 MHz, CD_3CN, broad signals) δ - 13.85 (3H), 4.80 (6H), 5.95 (bd, 24H, *J* = 32.5 Hz), 6.88 (s, 3H), 7.30 (d, 6H, *J* = 7.5 Hz), 53.35 (s, 6H), 113.59 (s, 3H); ^1H NMR (400 MHz, CD_2Cl_2, broad signals) δ - 13.32 (3H), 5.36 (9H), 6.54 (12H), 7.36 (12H), 50.64 (3H), 133.70 (3H); ^{19}F NMR (400 MHz, CD_2Cl_2, broad signals) δ -73.17, 11.12. ^{19}F NMR (400 MHz, CD_3CN, broad signals) δ ppm: -73.07; μ_{eff} (Evans' NMR Method): 4.7 μ_B (CD_3CN) 5.3 (CD_2Cl_2). MS (+ESI): *m/z* 1516.82 $[(M\text{-}OTf)]^+$, 703.94 $[(M\text{-}MeCN)]^{2+}$. Anal. Calcd. for $C_{100}H_{109}F_6FeN_5O_8S_2$: C, 68.91; H, 6.30; N, 4.02; S, 3.68. Found: C, 68.50; H, 6.13; N, 3.70; S, 3.23.

f. $[Co^{II}(^{tpb3}TPA)(OTf)](OTf)$

Green solid (0.423 g, 66 %). ^1H NMR (400 MHz, CD_3CN, broad signals) δ - 2.20 (s, 3H), 6.84 (s, 6H), 7.34 (t, 12H, *J* = 7.72 Hz), 7.52 (t, 9H, *J* = 7.60 Hz), 7.82 (d, 6H, *J* = 7.76 Hz), 8.36 (s, 12H), 8.63 (s, 6H), 50.42 (s, 3H), 87.77 (s, 6H), 162.72 (s, 3H) ; ^1H NMR (400 MHz, CD_2Cl_2,

broad signals) δ - 4.94 (3H), 6.11 (27H), 7.31 – 7.47 (6H), 7.51 (15H), 7.85 (3H), 39.43 (1H), 159.04 (3H); ^{19}F NMR (400 MHz, CD_2Cl_2, board signals) δ -75.06, 2.62. ^{19}F NMR (400 MHz, CD_3CN, board signals) δ -78. μ_{eff} (Evans' NMR Method): 4.32 μ_B in CD_2Cl_2. MS (+ESI): *m/z* 1411.63 $[(M\text{-}OTf)]^+$, 630.81 $[(M\text{-}MeCN)]^{2+}$, 651.88$[(M\text{-}(MeCN)_2)]^{2+}$. Efforts in data for obtaining elemental analysis is currently on-going.

g. $[Co^{II}(^{tpy3}TPA)(OTf)](OTf)$

Green solid (0.387 g, 70 %). ^{1}H NMR (400 MHz, CD_2Cl_2, broad signals) δ - 4.94 (s, 3H), 6.05 (s, 24H), 6.79 (s, 6H), 7.63 (s, 9H), 39.24 (s, 3H), 157.82 (s, 3H); ^{1}H NMR (400 MHz, CD_3CN, broad signals) δ - 3.04 (s, 3H), 6.84 (s, 6H), 7.41 (s, 15H), 8.19 (s, 12H), 8.47 (s, 6H), 50.03 (s, 3H),), 91.23 (s, 6H), 165.61 (s, 3H); ^{19}F NMR (400 MHz, CD_2Cl_2, broad signals) δ -75.32, 2.16. ^{19}F NMR (400 MHz, CD_3CN, broad signals) δ -78. MS (+ESI): *m/z* 1182.41 $[(M\text{-}OTf)]^+$, 537.24 $[(M\text{-}MeCN)]^{2+}$. μ_{eff} (Evans' NMR Method): 3.4 μ_B in CD_2Cl_2.**$[Ni^{II}(^{tpb3}TPA)(OTf)_2]$**

White solid (0.492 g, 76 %). ^{1}H NMR signals were too broad for analysis in both CD_3CN and CD_2Cl_2 solution. ^{19}F NMR (400 MHz, CD_2Cl_2, broad signals) δ ppm: -75.94, -34.86. ^{19}F NMR (400 MHz, CD_3CN, board signal) δ ppm: -78. μ_{eff} (Evans' NMR Method): 2.7 μ_B in CD_2Cl_2. MS (+ESI): *m/z* 1410.64 $[(M\text{-}OTf)]^+$, 651.24 $[(M\text{-}MeCN)]^{2+}$, 630.23 $[(M\text{-}(MeCN)_2)]^{2+}$. Efforts in obtaining data for elemental analysis is currently on-going.

h. $[Ni^{II}(^{tpy3}TPA)(OTf)_2]$

White solid (0.381 g, 69 %). ^{1}H NMR signals were too broad for analysis in both CD_3CN and CD_2Cl_2 solution. ^{19}F NMR (400 MHz, CD_2Cl_2, broad signals) δ ppm: -75.94, -34.86. ^{19}F NMR (400 MHz, CD_3CN, broad signals) δ ppm: -78. μ_{eff} (Evans' NMR Method): 3.30 μ_B in CD_2Cl_2. MS (+ESI): *m/z* 1181.41 $[(M\text{-}OTf)]^+$, 536.74 $[(M\text{-}MeCN)]^{2+}$. Efforts in obtaining data for elemental analysis is currently on-going.

i. $[Cu^{II}(^{tpb3}TPA)(NCMe)](ClO_4)_2.H_2O$

Green solid (0.487 g, 80 %). MS (+ESI): *m/z* 1366.41 $[(M\text{-}ClO_4)]^+$, 653.74 $[(M\text{-}MeCN)]^{2+}$

Anal. Calcd. for $C_{90}H_{68}Cl_2CuN_4O_9$: C, 72.84; H, 4.62; N, 3.78. Found: C, 72.40; H, 3.78; N, 4.08.

j. $[Cu^{II}(^{tpy3}TPA)(NCMe)](ClO_4)_2$

Green solid (0.411 g, 80 %). MS (+ESI): *m/z* 1138.46 $[(M\text{-}ClO_4)]^+$, 539.30 $[(M\text{-}MeCN)]^{2+}$. Efforts in obtaining data for elemental analysis is currently on-going.

k. $[Fe^{II}(^{tpb2}MeBPA)(OTf)_2(NCMe)]$

Yellow Solid (0.318 g, 65 %). ^1H NMR signals were too broad for analysis in both CD_3CN and CD_2Cl_2 solution. μ_{eff} (Evans' NMR Method): 4.47 μ_B in CD_2Cl_2. MS (+ESI): *m/z* 1029.32 $[(M\text{-}OTf)]^+$, 460.70 $[(M\text{-}MeCN)]^{2+}$, 481.16 $[(M\text{-}(MeCN)_2)]^{2+}$. Anal Calcd for $C_{63}H_{47}FeF_6N_3O_6S_2$: C, 64.15; H, 4.14; N, 5.60. Found: C, 64.70; H, 4.29; N, 4.65.

l. $[Co^{II}(^{tpb2}MeBPA)(OTf)_2(NCMe)].2H_2O$

Pink Solid (0.352 g, 72 %). ^1H NMR signals were too broad for analysis in both CD_3CN and CD_2Cl_2 solution. μ_{eff} (Evans' NMR Method): 4.23 μ_B in CD_2Cl_2. MS (+ESI): *m/z* 1029.32 $[(M\text{-}OTf)]^+$, 460.70 $[(M\text{-}MeCN)]^{2+}$, 481.16 $[(M\text{-}(MeCN)_2)]^2$ Efforts in obtaining data for elemental analysis is currently on-going.

m. $[Ni^{II}(^{tpb2}MeBPA)(OTf)_2(NCMe)]$

White Solid (0.368 g, 75 %). ^1H NMR signal was too board for analysis in both CD_3CN and CD_2Cl_2. μ_{eff} (Evans' NMR Method): 2.52 μ_B in CD_2Cl_2. MS (+ESI): *m/z* 1028.32 $[(M\text{-}OTf)]^+$, 460.20 $[(M\text{-}MeCN)]^{2+}$.Anal Calcd. for $C_{63}H_{47}NiF_6N_3O_6S_2$: C, 64.19; H, 4.02; N, 3.56; S, 5.44. Found: C, 64.40; H, 4.16; N, 3.83

n. $[Cu^{II}(^{tpb2}BnBPA)(NCMe)(OTf)_2].H_2O$

Blue Solid (0.400 g, 77 %). μ_{eff} (Evans' NMR Method): 1.71 μ_B in CD_2Cl_2. Anal Calcd. for $C_{69}H_{53}CuF_6N_3O_7S_2$: C, 64.86; H, 4.18; N, 3.29. Found: C, 65.06; H, 3.61; N, 3.31.

o. [Cu^{II}(^{tpb2}MeBPA)(NCMe)] $(OTf)_2$

Blue solid (0.370 g,75 %). μ_{eff} (Evans' NMR Method): 1.61 μ_B in CD_2Cl_2. Anal. Calcd. for $C_{65}H_{50}CuF_6N_4O_6S_2$: C, 60.13; H, 3.80; N, 3.69; S, 5.63. Found: C, 60.34; H, 4.20; N, 4.04; S, 4.44.

p. [Cu^{II}(^{tpb2}MeBPA)Cl_2]

Blue Solid (85 %). Single X-ray crystal was obtained via vapour diffusion of pentane into the dichloromethane solution containing the complex. Efforts in obtaining data for elemental analysis is currently on-going.

2. General Procedure for Formation of M(^{Ar3}TPA)$(Br)_2$ Complexes, followed by Subsequent Anion Metathesis

THF (5 mL) was added into a vial containing ^{tpb3}TPA (0.200 g, 0.166 mmol) and MBr_2 (0.166 mmol), and this mixture was stirred at room temperature overnight. The resulting suspension was isolated by filtration, washed with THF and dried in vacuo. The yellow solid obtained was dissolved in MeCN (5 mL) and $AgSbF_6$ or $AgClO_4$ (1 eq) was added to it. After being stirred overnight, the reaction mixture was filtered to remove solid, AgBr and the filtrate reduced to dryness. This yielded the crude product, which was purified by recrystallization from vapour diffusion of diethyl ether into acetonitrile solution containing the complex. An analogus method was used to synthesize [Fe(5^{tbu3}TPa)Br][$B(C_6F_5)_4$], but involved reaction of [Fe(^{dtbt3}TPa)Br][Br] with Na[$B(C_6F_5)_4$] in THF and yielded NaBr as a by-product. Single X-ray crystal was obtained via vapour diffusion of pentane into the dichloromethane solution containing the complex.

Limited characterization was performed, as only the structural properties were of interest.

3. General procedure for formation of the complexes $[Cu^{I}(L)(NCMe)]Y$, Y= $[B(C_6F_5)_4]$ and SbF_6

A solution of $[Cu^{I}(NCMe)_4][B(C_6F_5)_4]$ (0.166 mmol) in THF (5 mL) was added into a vial containing ^{Ar3}TPA (0.166 mmol) or ^{Ar2}MeBPA (0.166 mmol) or ^{tpb2}BnBPA (0.166 mmol) and the resulting mixture was stirred overnight, at room temperature. The solution obtained was filtered and the volume of solvent was reduced until yellow precipitate was observed. No further purification is needed.

A similar procedure was used to synthesize complexes with SbF_6 ions, but MeCN was used as a solvent and purification was effected by recrystillization via vapour diffusion of diethyl ether into concetrated acetonitrile solutions of complex. ^{1}H NMR data obtained was the same as the correponding complexes with $[B(C_6F_5)_4]$ anions.Efforts in obtaining good elemental analysis was currently undergoing.

a. $[Cu^{I}(^{tpb3}TPA)(NCMe)][B(C_6F_5)_4]$

Yellow solid (0.28 g, 85 %). ^{1}H NMR (400 MHz, CD_3CN) δ 3.34 (s, 6H), 6.84 (t, 6H, J = 7.4 Hz), 6.91 (d, 3H, J = 8.0 Hz), 7.04 (t, 12H, J = 7.6 Hz), 7.12 (d, 12H, J = 7.2 Hz, 7.29 (d, 4H, J = 2 Hz), 7.42 – 7.52 (m, 12 H), 7.76 (s, 6H), 7.80 – 7.82 (m, 6H). MS (+ESI): *m/z* 1265.50 $[(M)]^+$

b. $[Cu^{I}(5^{tpy3}TPA)(NCMe)][B(C_6F_5)_4]$

Yellow solid (0.23 g, 80 %). ^{1}H NMR (400 MHz, CD_3CN) δ 3.31 (s, 6H), 6.82 (t, 6H, J = 7.0 Hz), 6.87 (d, 3H, J = 7.9 Hz), 6.99 – 7.05 (m 18 H). 7.26 (dd, 3H, J = 7.9 Hz, 2.2 Hz), 7.48 – 7.50 (m, 6H), 7.57 – 7.67 (m , 6H), 7.42 – 7.52 (m, 12 H), 7.77 (d, 3H, J = 1.8 Hz). MS (+ESI): *m/z* 1037.37 $[(M)]^+$.

c. [Cu^{I}(^{dtbt3}TPA)(NCMe)] [$B(C_6F_5)_4$]

Yellow solid (0.260 g, 75 %). ^{1}H NMR (400 MHz, CD_3CN) δ 1.08 (s, 54 H), 3.43 (s, 6H), 6.86 – 6.90 (m, 18H), 7.07 (d, 12H, J = 8.4 Hz), 7.20 (dd, 3H, J = 2.2 Hz, 7.9 Hz), 7.43 (d, 6H, J = 7.6 Hz), 7.53 – 7.57 (m, 3H), 7.77 (s, 3H).

d. [Cu^{I}(^{tpb2}MeBPA)(NCMe)][$B(C_6F_5)_4$].H_2O

Yellow solid (0.207 g, 78 %) . ^{1}H NMR (400 MHz, CD_3CN) δ 2.32 (s, 3H), 3.42 (s, 4H), 7.01 – 7.08 (m, 6H), 7.15 – 7.16 (m, 14H), 7.37 (dd, 2H, J = 2.0 Hz, 7.9 Hz), 7.41 – 7.61 (m, 8H), 7.76 (s, 4H), 7.81 (d, 4H, J = 7.5 Hz), 7.92 (s, 2H). MS (+ESI): *m/z* 884.36 $[(M)]^+$ $[(M)]^+$**.** Anal. Calcd. for $C_{87}H_{52}BCuN_4OF_{20}$: C, 64.36; H, 3.23; N, 3.45. Found: C, 64.53; H, 3.31; N, 3.13.

e. [Cu^{I}(^{tpy2}MeBPA)(NCMe)][$B(C_6F_5)_4$]

Yellow solid (0.221 g, 83 %). ^{1}H NMR (400 MHz, CD_3CN) δ 2.29 (s, 3H), 3.38 (s, 4H), 6.96 – 7.05 (m, 14H), 7.08 – 7.12 (m, 8H), 7.30 (dd, 2H, J = 2.1 Hz, 8.0 Hz), 7.45 – 7.47 (m, 4H), 7.54 – 7.58 (m, 2H), 7.84 (s, 2H).

f. [Cu^{I}(^{tpb2}BnBPA)(NCMe)][$B(C_6F_5)_4$].H_2O

Yellow solid (0.214, 77 %). ^{1}H NMR (400 MHz, CD_3CN) δ 3.41 – 3.45 (m, 6H), 7.04 – 7.07 (m, 5H), 7.17 (d, 18H, J = 4.4 Hz), 7.31 – 7.52 (m, 12H), 7.77 (s, 4H), 7.81 (d, 4H, J = 7.6 Hz), 7.91 (s, 2H). MS (+ESI): *m/z* 960.34 $[(M)]^+$. Anal. Calcd for $C_{93}H_{56}BCuN_4OF_{20}$: C, 65.71; H, 3.32; N, 3.30. Found: C, 65.61; H, 3.26; N, 3.48.

7.3 Physical Methods

7.3.1 Cyclic Voltammetry

Cyclic voltammograms were recorded using a glassy carbon working electrode, a silver referene elecrode and platinum wire counter electrode. All measurements were performed under an inert atmosphere (either in an argon filled glovebox or under a blanketing nitrogen atmosphere), at room temperature, in acetonitrile solution containing 0.1 M tetrabutylammonium hexafluorophosphate electrolyte. The ferrocenenium/ferrocene redox couple was used as an internal reference in every experiment.

7.3.2 Solution State Evans' NMR Measurements

The solution state magnetic susceptibility (χ_m) of the metal complexes was measured using Evans' NMR method.[9–12] Coxial NMR tubes were used and toluene was added as an internal standard to all of the NMR solvents used (CD_3CN or CD_2Cl_2). Solutions of the paramagnetic metal complexes (10 mM) were placed in the coaxial insert, with the standard (5 mm diameter) outer NMR tube containing only deuterated solvent and toluene. The molar magnetic susceptibility (χ_m) and magnetic moments (μ_{eff}) were calculated using the the difference in chemical shift of the toluene methyl signal between the two coaxial tubes and following equation:

$$\chi_m = \frac{3\Delta f}{1000 f c}$$

$$\mu_{eff} = 798\sqrt{T X_m}$$

χ_m = molar magnetic susceptibility of the sample in m^3 mol^{-1}; Δf = difference in the chemical shift Hz of the internal reference between the inner and outer tubes; f = operating frequency of the NMR spectrometer in Hz; c = concentration of the sample in M ; T = temperature of the measurement in K

7.4 UV-vis Spectroscopic Experiments

7.4.1 Reaction of Copper(I) Complexes with O_2

Rubber septum stoppered UV-vis cuvettes (1 cm pathlength) containing 0.5 mM solutions of complex, $[Cu^{I}(^{Ar3}TPA)(NCMe)]^{+}$ or $[Cu^{I}(^{Ar2}MeBPA)(NCMe)]^{+}$ in THF (2 mL) were prepared in an Ar filled glovebox. After being pre-cooled to the required temperature using the cryostat of the UV-vis spectrometer (outside of the glovebox), dioxygen was bubbled into the solution using a long needle connected to an O_2-filled balloon. The course of reaction was monitored using UV-vis spectroscopy.

7.4.2 Kinetics Studies for Reaction With Substrates

Kinetic studies were conducted, at the requisite temperatures, by injecting THF solutions of substrate into the preformed 0.5 mM THF solutions of $[Cu^{II}(\eta_1\text{-}O_2^{\bullet-})(^{Ar3}TPA)]^{+}$. The course of reaction was monitored by measuring decay of the UV-vis spectral bands centred around 420 nm (the rest of the phenol) and/or 760 nm(for 2,6-di-*tert*butyl-*para*-methoxy-phenol) . In all cases, reaction proceeded via pseudo-first-order decay. The observed rate constants, k_{obs}, were found to be linearly dependent upon substrate concentration and fitting of the data obtained yielded second order rate constants, k_2. The purging of Ar to remove excess dioxygen would not affect k_{obs}.

Identification of organic reaction products was undertaken by, first, filtering the reaction mixture through a small pad of silica gel, to remove copper containing compounds, after which the filtrate was injected directly into a GC-MS instrument.

7.4.3 Generation of $[Cu^{II}(OOH)(^{tpb3}TPA)]^{+}$

A 0.5 mM solution of $[Cu^{II}(^{tpb3}TPA)(NCMe)](ClO_4)_2$ in $^{n}BuCN$ (2 mL), prepared under an inert atmosphere in a 1 cm pathlength cuvette and sealed using a rubber septum, was pre-cooled to -80°C using the UV-vis cryostat. Subsequently, excess H_2O_2 (2 eq) and NEt_3 (5 eq),

dissolved in 1 mL of ^{n}BuCN, was added and the course of reaction monitored via UV-Vis spectroscopy.

Alternatively, it could be generated by adding TEMPO-H (10 eq) into pregenerated solutions of $[Cu^{II}(\eta_1\text{-}O_2^{\bullet-})(^{Ar3}TPA)]^+$. in THF (0.5 mM, 2 mL) at -80°C. Once again, course of reaction was monitored by UV-vis spectroscopy.

7.4.4 Synthesis of $[Fe^{IV}(O)(^{Ar3}TPA)(X)]^{n+}$, X = MeCN (n = 2) or OTf (n = 1)

Inside an Ar filled glovebox, a 2 mM solution of $[Fe^{II}(^{Ar3}TPA)(OTf)](OTf)$ in dichloromethane (2 mL) was added to a 1 cm pathlength UV-vis cuvette, which was then sealed with a rubber septum. The cuvette was pre-cooled to -80°C using a UV-vis cryostat (outside of the glovebox) and 1.5 eq of the oxidant 4-t$BuSO_2$-2-tBu-C_6H_3IO was added to it. The resulting reaction, which resulted in growth of an absorbance centred at *ca.* 780 nm, was monitored using UV-vis spectroscopy. This was assigned to the species $[Fe^{IV}(O)(^{Ar3}TPA)(OTf)]^+$.

Similarly, the reaction could also be conducted in MeCN solution at temperatures ≥ -40 °C but yielded a different species, which was characterized by an absorbance centred at *ca.* 740 nm. This is associated with formation of the complex $[Fe^{IV}(O)(^{Ar3}TPA)(NCMe)]^{2+}$. Support for this notion was provided by observation of the same spectral feature upon addition of MeCN (1-2 eq) to a preformed dichloromethane solution of $[Fe^{IV}(O)(^{Ar3}TPA)(OTf)]^+$, at -80 °C.

7.4.5 Generation of $[Fe^{IV}(O)(^{tpb3}TPA)(Br)]^+$

Substitution of the TfO ligand in $[Fe^{IV}(O)(^{Ar3}TPA)(OTf)]^+$ (at -80 °C) and NCMe in $[Fe^{IV}(O)(5^{Ar3}TPA)(NCMe)]^{2+}$ was performed by addition of 1 – 2 eq of tetrabutylammonium salts, NBu_4Br, at temperatures of -80 and -40°C, respectively. These anion substituted complexes proved to be much more unstable than the NCMe coordinated complex.

7.4.6 Kinetic Studies for Reaction of Oxoiron(IV) Complexes With Substrates

7.4.6.1 PPh_3 and Substrates with Weak C-H bonds

Kinetic studies were conducted at -60 (PPh_3) or -40°C (CHD and DHA), under an Ar atmosphere, by injecting dichloromethane solutions of substrate into 2 mM dichloromethane/acetonitrile(9:1 mixture) solutions of oxoiron(IV) complex, formed as described above. The course of reaction was monitored using UV-vis spectroscopy via decay of the near-IR features that are characteristically observed for nonheme oxoiron(IV) complexes. In all cases, reaction proceeded in a pseudo-first-order fashion. Furthermore, the observed rate constants, k_{obs}, obtained were found to be linearly dependent on substrate concentration. Thus, second order rate constant, k_2, were obtained by fitting the data. Analysis of organic products was conducted using ^{31}P NMR in the case of triphenylphosphine and ^{1}H NMR for cyclohexadiene and 9,10-dihydroanthrance.

7.4.6.2 Substrates with strong C-H bonds

Kinetic studies for substrates with strong C-H bonds were conducted at room temperature under an Ar atmosphere, by injecting dichloromethane solutions of substrate into preformed 2 mM solutions of $[Fe^{IV}(O)(^{tpb3}TPA)(MeCN)](OTf)_2$ in MeCN. The progress of reaction was monitored using UV-vis spectroscopy via of its characteristic NIR feature (at 740 nm). Once again, pseudo-first-order decay was observed and the resulting rate constants, k_{obs}, showed a linearly dependence on the substrate concentration. Fitting of the data yielded second-order rate constants, k_2. Analysis of the organic products of reaction was undertaken by, first, filtering the reaction mixture through a plug of silica gel, which was then washed with additional dichloromethane (2 mL), and then injecting the filtrate into a GC-MS instrument. Quatification was performed using napthalene as internal reference.

7.5 X-Ray Dffraction Spectroscopy

Single crystal X-ray crystallographic data for the complexes were collected using a Bruker APEX II diffractometer. The structures were solved using SHELXT 2014 by direct methods, and refined using the SHELXT 2016 via full-matrix least squares/difference on F^2. All the non-hydrogen atomes were refined anisotropically. The crystals struncture in all the chapter were drawn using ORTEP-3[13]

Table 7.1: X-ray crystallographic data for $[Fe(^{Ar3}TPA)]^{2+}$.

Compounds	$Fe^{II}(^{mes3}TPA)(NCMe)_2](ClO_4)_2$	$[Fe(^{tpb3}TPA)(H_2O)](OTf)_2$	$[Fe(^{tpy3}TPA)(OTf)_2]$	$[Fe(^{5dtbu3}TPA)(MeCN)(ClO_4)](ClO_4)$
Appearance	red plate	pale yellow plate	yellow block	Colourless block
Formula	$C_{60.50}H_{75.50}Cl_2FeN_{9.50}O_9$	$C_{96}H_{79}F_6FeN_4O_{8.50}S_2$	$C_{76}H_{58.50}Cl_2F_6FeN_4O_{6.25}S_2$	$C_{99}H_{106.50}Cl_2FeN_{5.50}O_8$
FW/ g mol^{-1}	1206.55	1658.60	1432.63	1628.14
Cryst. Syst.	triclinic	monoclinic	triclinic	monoclinic
Space Group	P -1	C 1 2/c 1	P -1	C 1 2/c 1
Size/ mm^3	0.040 x 0.240 x 0.320	0.020 x 0.200 x 0.240	0.160 x 0.220 x 0.240	0.200 x 0.220 x 0.240
T/ K	103(2)	100(2)	100(2)	100(2)
Wavelength/ Å	0.71073	0.71073	0.71073	0.71073
a/ Å	13.1854(4)	62.182(3)	14.8484(8)	40.6299(9)
b/ Å	16.2656(5)	10.4930(6)	15.5278(8)	17.4860(3)
c/ Å	17.0914(6)	24.9569(15)	31.3262(16)	31.5181(11)
α / °	83.743(2)	90	100.2336(18)	90
β / °	69.5311(18)	91.3482(15)	100.8217(16)	126.9392(6)
γ / °	66.3279(17)	90	90.0642(16)	90
V/ Å^3	3143.07(18)	16279.3(16)	6976.9(6)	17897.5(8)
Z	2	8	*4*	8
d_{calc} / g cm^{-3}	1.275	1.353	1.364	1.208
μ / mm^{-1}	0.386	0.313	0.425	0.287
Refl. collected	82348	66535	33515	99002
Goodness of Fit	1.013	1.018	1.053	1.018
Δ, σ_{max}	0.001	0.002	0.025	0.004
R; I>2σ(I)	0.0567	0.0772	0.0824	0.0585
Largest diff. peak and hole, eÅ^{-3}	1.201/ -0.578	1.072/ -0.726	1.505 / -1.103	1.106 / -0.988
R.M.S. deviation from mean/ eÅ^{-3}	0.080	0.079	0.108	0.064

Table 7.2: X-ray crystallographic data for the $[M(^{Ar3}TPA)]^{2+}$.

Compounds	$[Co(^{tpb3}TPA)(MeCN)](SbF_6)_2$	$[Cu(^{tpb3}TPA)(MeCN)](ClO_4)_2$	$[Cu(^{tpy3}TPA)(MeCN)](ClO_4)_2$	$[Mn(^{tpb3}TPA)(OTf)_2]$
Appearance	light green needle	yellow-green plate	green plate	colorless needle
Formula	$C_{104}H_{79.50}CoF_{12}N_{11}Sb_2$	$C_{96}H_{75}Cl_2CuN_7O_8$	$C_{84}H_{76}Cl_2CuN_8O_9$	$C_{92}H_{66}F_6MnN_4O_6S_2$
FW/ g mol^{-1}	2013.71	1589.07	1475.96	1556.54
Cryst. Syst.	hexagonal	monoclinic	triclinic	tetragonal
Space Group	P 63	P 1 21/c 1	P -1	I 41/a
Size/ mm^3	0.020 x 0.040 x 0.120	0.040 x 0.100 x 0.140	0.060 x 0.200 x 0.240	0.040 x 0.080 x 0.180
T/ K	100(2)	100(2)	100(2)	100(2)
Wavelength/ Å	0.71073	0.71073	0.71073	0.71073
a/ Å	21.9865(10)	19.1320(7)	13.006(2)	33.5308(5)
b/ Å	21.9865(10)	21.4930(8)	18.101(3)	33.5308(5)
c/ Å	21.8453(10)	20.3676(6)	18.182(3)	34.0909(6)
α / °	90	90	111.143(4)	90
β / °	90	90.9959(13)	100.873(4)	90
γ / °	120	90	101.074(4)	90
V/ Å^3	9145.4(9)	8374.0(5)	3759.2(11)	38328.9(13)
Z	4	4	2	16
d_{calc} / g cm^{-3}	1.463	1.260	1.304	1.079
μ / mm^{-1}	0.845	0.386	0.426	0.241
Refl. collected	58335	73826	48573	121188
Goodness of Fit	0.992	1.142	1.038	1.025
Δ, σ_{max}	0.001	0.003	0.003	0.001
R; I>2σ(I)	0.0645	0.0806	0.0833	0.0741
Largest diff. peak and hole, eÅ^{-3}	0.881 / -0.808	1.909 / -0.596	0.616 / -1.895	0.904 / -0.828
R.M.S. deviation from mean/ eÅ^{-3}	0.116	0.089	0.102	0.065

Table 7.3: X-ray crystallographic data for the [M(^{Ar2}MeBPA)(OTf)$_2$(MeCN)]

Compounds	[Fe(^{tpb2}MeBPA)(OTf)$_2$ (MeCN)]	[Co(^{tpb2}MeBPA)(OTf)$_2$ (MeCN)]	[Ni(^{tpb2}MeBPA)(OTf)$_2$ (MeCN)]
Appearance	Colourless Plate	Pink Prism	blue block
Formula	$C_{65}H_{50}F_6FeN_4O_6S_2$	$C_{65}H_{50}CoF_6N_4O_6S_2$	$C_{65}H_{50}F_6N_4NiO_6S_2$
FW/ g mol^{-1}	1217.06	1220.14	1219.92
Cryst. Syst.	monoclinic	monoclinic	monoclinic
Space Group	P 1 21/n 1	P 1 21/n 1	P 1 21/n 1
Size/ mm^3	0.040 x 0.200 x 0.220	0.100 x 0.120 x 0.240	0.140 x 0.200 x 0.240
T/ K	100(2)	100(2)	173(2)
Wavelength/ Å	0.71073	0.71073	0.71073
a/ Å	10.7902(2)	19.4877(9)	19.4445(4)
b/ Å	31.0039(6)	10.3189(4)	10.3637(2)
c/ Å	17.1517(3)	28.5817(14)	28.4641(7)
α / °	90	90	90
β / °	91.4430(10)	91.8983(18)	92.1640(10)
γ / °	90	90	90
V/ Å^3	5736.08(18)	5744.4(4)	5731.9(2)
Z	4	4	4
d_{calc} / g cm^{-3}	1.409	1.411	1.414
μ / mm^{-1}	0.412	0.448	0.488
Refl. Collected	96609	12805	76386
Goodness of Fit	1.152	1.117	1.028
Δ, σ_{max}	0.003	0.001	0.002
R; I>2σ(I)	0.1249	0.0868	0.0576
Largest diff. peak and hole, eÅ^{-3}	1.465 / -0.894	0.577 / -0.698	0.517/ -0.656
R.M.S. deviation from mean/ eÅ^{-3}	0.120	0.130	0.070

Table 7.4: X-ray crystallographic data for the [Cu(^{tpb2}BnBPA)$(OTf)_2$(MeCN)] and [Cu(^{tpb2}MeBPA)Cl_2].H_2O

Compounds	[Cu(5^{tpb2}BnBPA)$(OTf)_2$(MeCN)]	[Cu(^{tpb2}MeBPA)Cl_2].H_2O
Appearance	Blue Plate	black plate
Formula	$C_{75}H_{64}CuF_6N_4O_7S_2$	$C_{61}H_{49}Cl_2CuN_3O$
FW/ g mol^{-1}	1374.96	974.47
Cryst. Syst.	triclinic	orthorhombic
Space Group	P -1	P b c a
Size/ mm^3	0.060 x 0.160 x 0.260	0.010 x 0.040 x 0.060
T/ K	233(2)	100(2)
Wavelength/ Å	0.71073	0.71073
a/ Å	9.4326(14)	14.0852(3)
b/ Å	18.187(3)	18.8505(6)
c/ Å	20.774(3)	37.5342(11)
α / °	101.913(4)	90
β / °	97.463(4)	90
γ / °	90.240(4)	90
V/ Å^3	5620.9(4)	9965.8(5)
Z	2	8
d_{calc} / g cm^{-3}	1.321	1.299
μ / mm^{-1}	0.449	0.591
Refl. Collected	57788	71023
Goodness of Fit	1.019	1.015
Δ, σ_{max}	-	0.003
R; I>2σ(I)	0.0834	0.0734
Largest diff. peak and hole, eÅ^{-3}	0.982 / -0.476	0.478 / -0.555
R.M.S. deviation from mean/ eÅ^{-3}	0.082	0.084

Table 7.5: X-ray crystallographic data for the [Cu(^{tpb2}BnBPA)MeCN][OTf] and [Cu(^{tpy2}MeBPA)MeCN][SbF_6]

Compounds	[Cu(^{tpb2}BnBPA)MeCN][OTf]	[Cu(^{tpy2}MeBPA)MeCN][SbF_6]
Appearance	Yellow Plate	Colourless Block
Formula	$C_{70}H_{54}CuF_3N_4O_3S$	$C_{51}H_{42}CuF_6N_4Sb$
FW/ g mol^{-1}	1151.77	1010.17
Cryst. Syst.	monoclinic	triclinic
Space Group	P 1 21/n 1	P -1
Size/ mm^3	0.040 x 0.080 x 0.160	0.130 x 0.200 x 0.200
T/ K	100(2)	100(2)
Wavelength/ Å	0.71073	0.71073
a/ Å	11.2750(5)	12.5313(6)
b/ Å	19.6768(7)	13.6363(7)
c/ Å	25.3370(9)	13.6821(7)
α / °	90	95.6584(18)
β / °	90.5137(15)	99.447(2)
γ / °	90	101.2000(17)
V/ Å^3	5620.9(4)	2241.7(2)
Z	4	2
d_{calc} / g cm $^{-3}$	1.361	1.497
μ / mm^{-1}	0.490	1.142
Refl. Collected	74237	54487
Goodness of Fit	1.014	1.024
Δ, σ_{max}	0.001	0.001
R; I>2σ(I)	0.0518	0.0524
Largest diff. peak and hole, eÅ^{-3}	0.416 / -0.611	1.562 / -1.428
R.M.S. deviation from mean/ eÅ^{-3}	0.076	0.127

7.6 Reference

(1) Hintermann, L.; Dang, T. T.; Labonne, A.; Kribber, T.; Xiao, L.; Naumov, P. *Chem. A. Eur. J.* **2009**, *15*, 7167–7179.

(2) Hardman, N. J.; Twamley, B.; Stender, M.; Baldwin, R.; Hino, S.; Schiemenz, B.; Kauzlarich, S. M.; Power, P. P. *J. Organomet. Chem.* **2002**, *643–644*, 461–467.

(3) van den Heuvel, M.; van den Berg, T. A.; Kellogg, R. M.; Choma, C. T.; Feringa, B. L. *J. Org. Chem.* **2004**, *69*, 250–262.

(4) Wipf, P.; Jung, J.-K. *J. Org. Chem.* **2000**, *65*, 6319–6337.

(5) Dickie, D. A.; MacIntosh, I. S.; Ino, D. D.; He, Q.; Labeodan, O. A.; Jennings, M. C.; Schatte, G.; Walsby, C. J.; Clyburne, J. A. C. *Can. J. Chem.* **2008**, *86*, 20–31.

(6) Saednya, A.; Hart, H. *Synthesis* . **1996**, 1455–1458.

(7) Neto, C.; Oliveira, M. C.; Gano, L.; Marques, F.; Thiemann, T.; Santos, I. *J. Inorg. Biochem.* **2012**, *111*, 1–9.

(8) Mikata, Y.; Nodomi, Y.; Ohnishi, R.; Kizu, A.; Konno, H. *Dalt. Trans.* **2015**, *44*, 8021–8030.

(9) Evans, D. F. *J. Chem. Soc.* **1959**, 2003–2005.

(10) Grant, D. H. *J. Chem. Educ.* **1995**, *72*, 39.

(11) Crawford, T. H.; Swanson, J. *J. Chem. Educ.* **1971**, *48*, 382.

(12) Evans, D. F.; Fazakerley, G. V; Phillips, R. F. *J. Chem. Soc. A Inorg., Phys. Theor.* **1971**, 0, 1931–1934.

(13) Farrugia, L. J. *J. Appl. Crystallogr.* **2012**, *45*, 849–854.

Appendix

A1: ^{1}H NMR Spectrum of [Fe^{II}(^{tpy3}TPA)(OTf)](OTf)

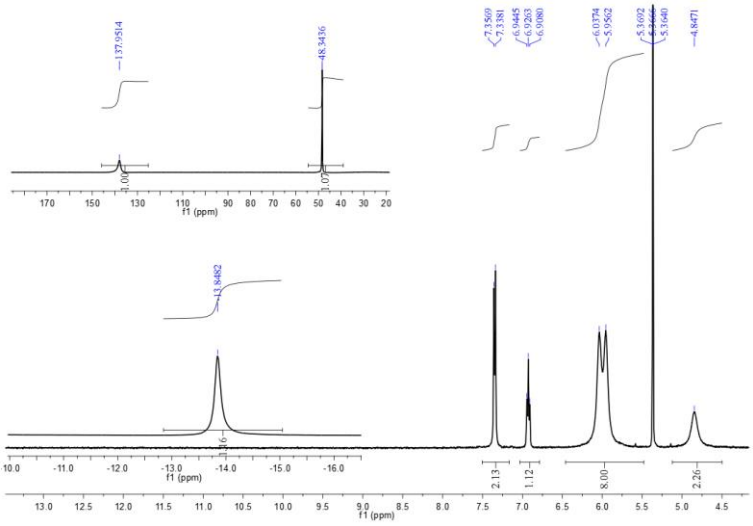

Figure S1: ^{1}H NMR Spectrum of [Fe^{II}(^{tpy3}TPA)(OTf)](OTf) in CD_2Cl_2

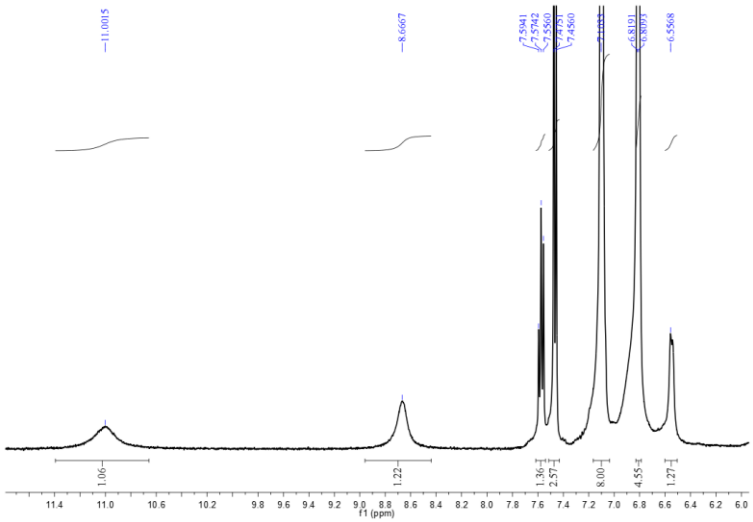

Figure S2: ^{1}H NMR Spectrum of [Fe^{II}(^{tpy3}TPA)(OTf)](OTf) in CD_3CN

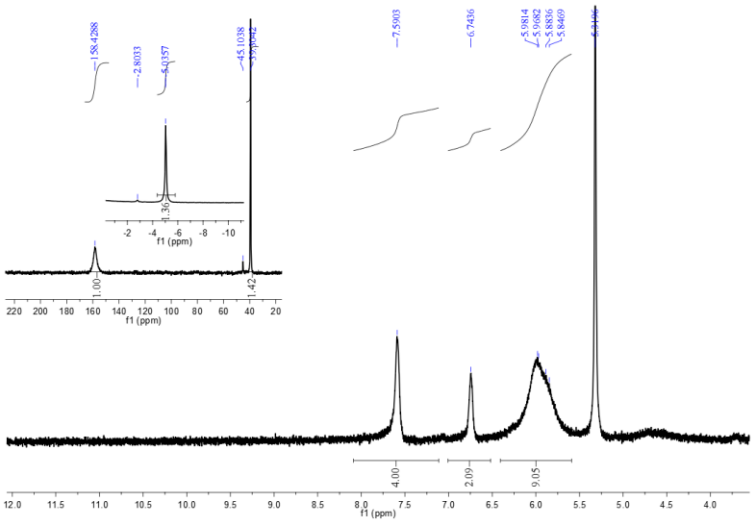

Figure S3: ^{1}H NMR spectrum for [Co^{II}(^{tpy3}TPA)(OTf)](OTf) in CD_2Cl_2

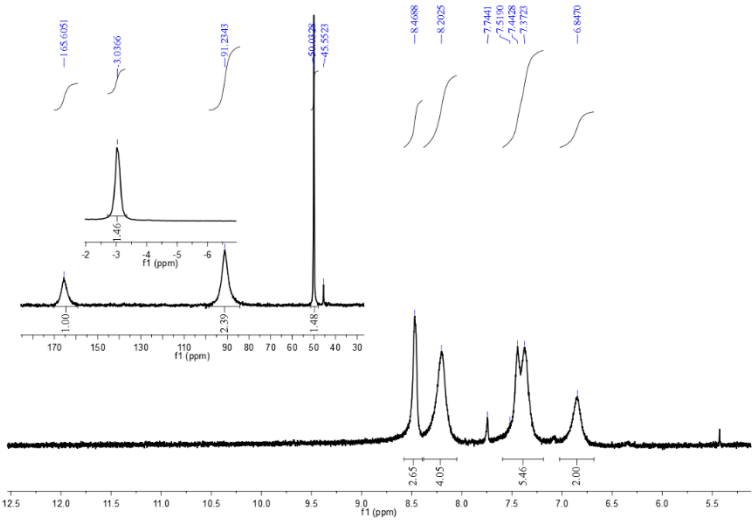

Figure S4: ^{1}H NMR spectrum for [Co^{II}(^{tpy3}TPA)(OTf)](OTf) in CD_3CN

A2. Reaction of $[Cu^{II}(\eta^1\text{-}O_2^{\bullet-})(^{tpy3}TPA)]^+$ with TEMPO-H

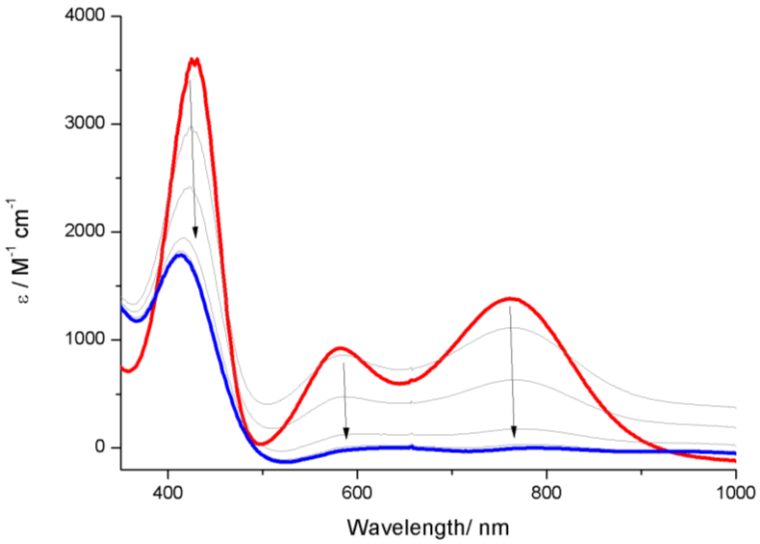

Figure S5: UV-vis spectrum for the formation of $[Cu^{II}(OOH)(^{tpy3}TPA)]^+$ (blue) by reacting $[Cu^{II}(\eta^1\text{-}O_2^{\bullet-})(^{tpy3}TPA)]^+$ (red) with TEMPO-H (10 eq) at –80°C.

A3: Kinetic Plot for the Hydrogen Atom Abstraction of Phenol by $[Cu^{II}(\eta^1\text{-}O_2^{\bullet-})(^{Ar3}TPA)]^+$

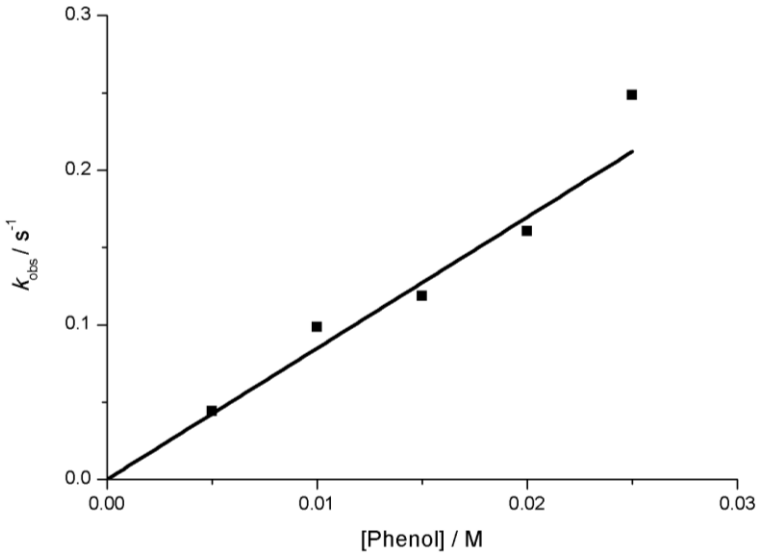

Figure S6: Plot of pseudo first order rate of reaction against concentration of 2,6-ditertbutyl-*para*-methoxyphenol by $[Cu^{II}(\eta^1\text{-}O_2^{\bullet-})(^{tpb3}TPA)]^+$ (0.5 mM) to find the second order reaction rate in THF at – 40 °C.

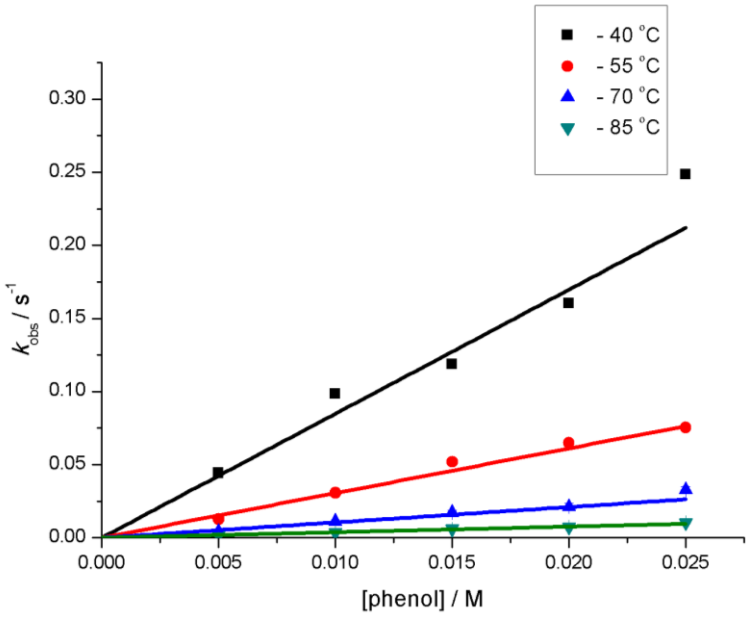

Figure S7: Plot of pseudo first order rate of reaction against concentration of 2,6-ditertbutyl-*para*-methoxyphenol by $[Cu^{II}(\eta^1\text{-}O_2^{\bullet-})(^{tpb3}TPA)]^+$ (0.5 mM) to find the second order reaction rate in THF at various temperature (-40°C (black); -55°C (red); -70°C (blue); -85°C (green)).

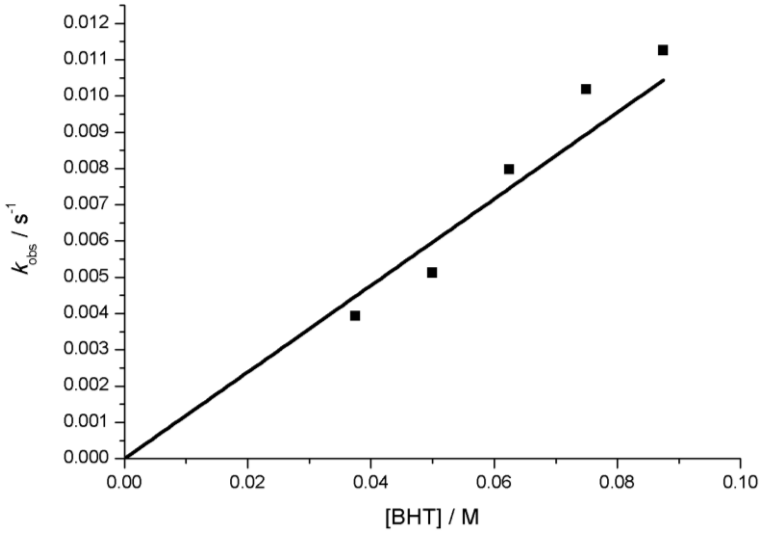

Figure S8: Plot of pseudo first order rate of reaction against concentration of 2,6-ditertbutyl-*para*-methylphenol by $[Cu^{II}(\eta^1\text{-}O_2^{\bullet-})(^{tpb3}TPA)]^+$ (0.5 mM) to find the second order reaction rate in THF at – 40 °C

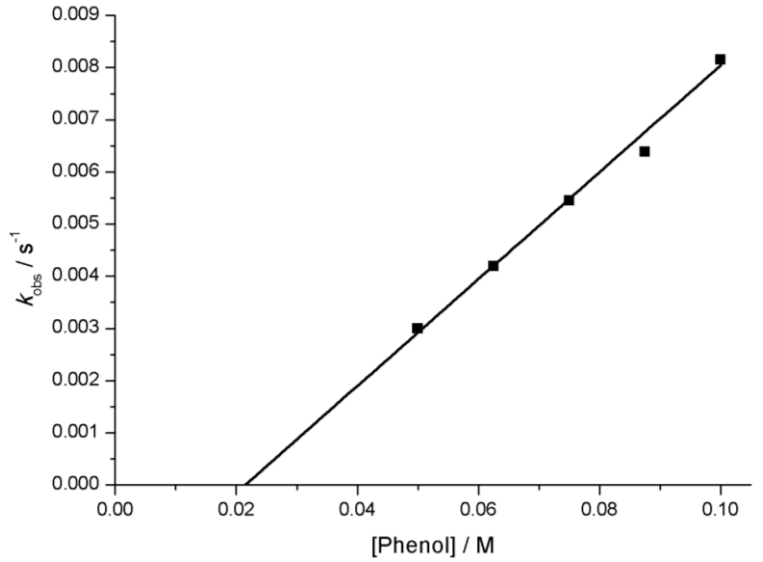

Figure S9: Plot of pseudo first order rate of reaction against concentration of 2,6-ditertbutyl-*para*-ethyphenol by $[Cu^{II}(\eta^1\text{-}O_2^{\bullet-})(^{tpb3}TPA)]^+$ (0.5 mM) to find the second order reaction rate in THF at – 40 °C.

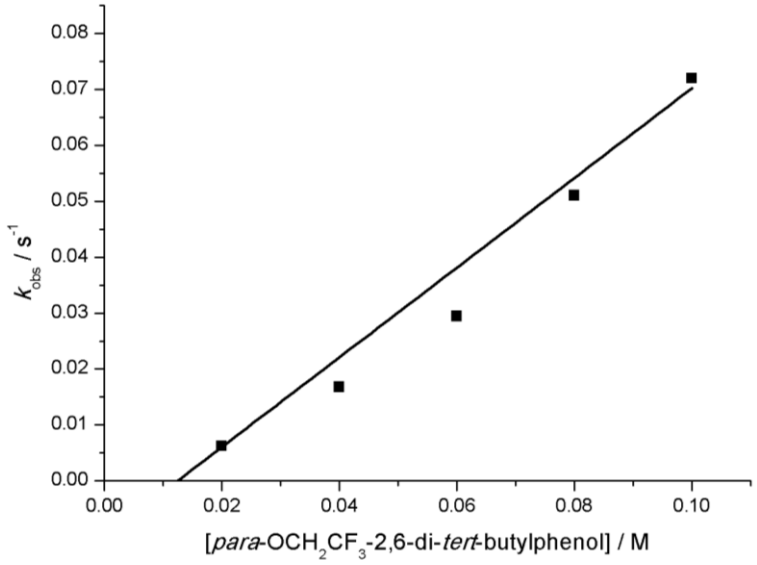

Figure S10: Plot of pseudo first order rate of reaction against concentration of *para*-OCH_2CF_3-2,6-ditertbutylphenol by $[Cu^{II}(\eta^1\text{-}O_2^{\bullet-})(^{tpb3}TPA)]^+$ (0.5 mM) to find the second order reaction rate in THF at – 40 °C.

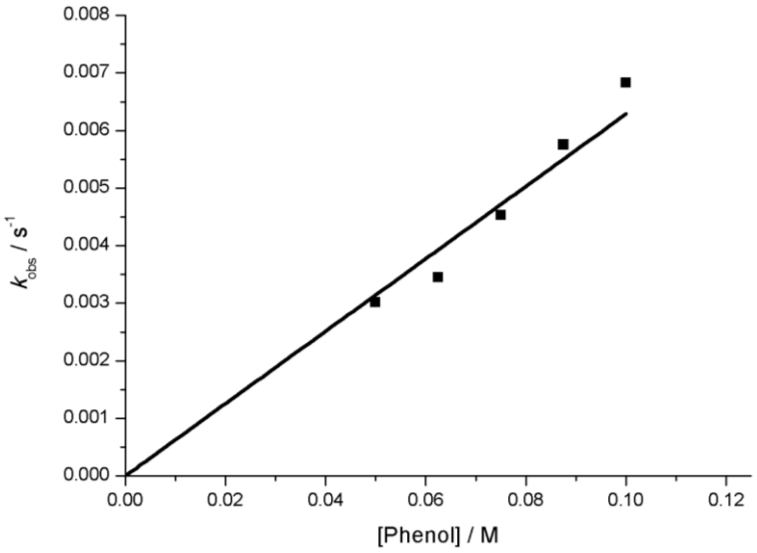

Figure S11: Plot of pseudo first order rate of reaction against concentration of tri-*tert*-butylphenol by $[Cu^{II}(\eta^1\text{-}O_2^{\bullet-})(^{tpb3}TPA)]^+$ (0.5 mM) to find the second order reaction rate in THF at – 40 °C.

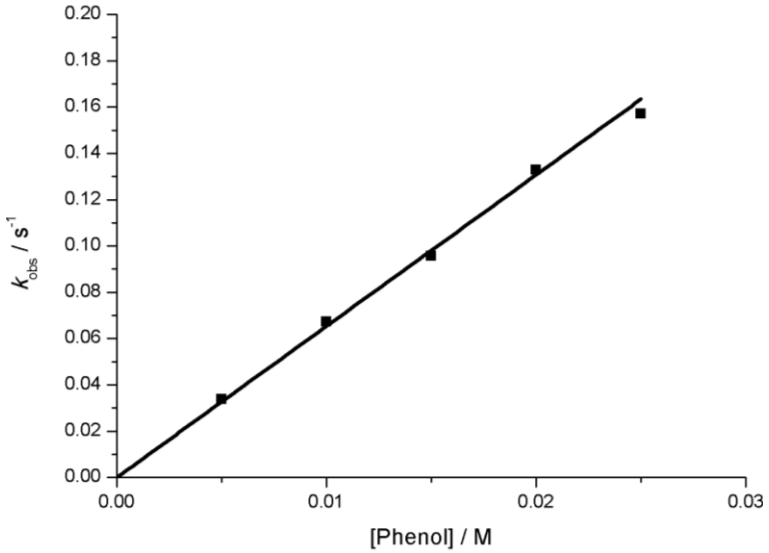

Figure S12: Plot of pseudo first order rate of reaction against concentration of 2,6-ditertbutyl-*para*-methoxyphenol by $[Cu^{II}(\eta^1\text{-}O_2^{\bullet-})(^{tpy3}TPA)]^+$ (0.5 mM) to find the second order reaction rate in THF at – 40 ℃.

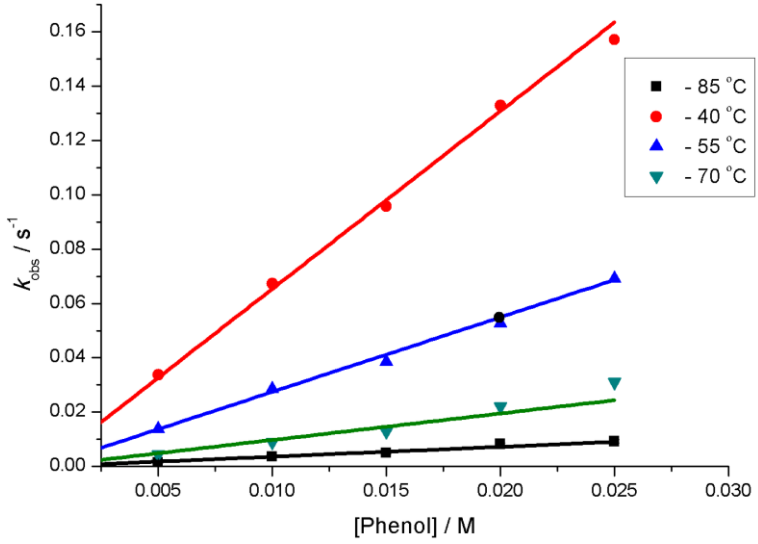

Figure S13: Plot of pseudo first order rate of reaction against concentration of 2,6-di-*tert*-butyl-*para*-methoxyphenol by $[Cu^{II}(\eta^1\text{-}O_2^{\bullet-})(^{tpy3}TPA)]^+$ (0.5 mM) to find the second order reaction rate in THF at various temperature (-40℃ (black); -55℃ (red); -70℃ (blue); -85℃ (green)).

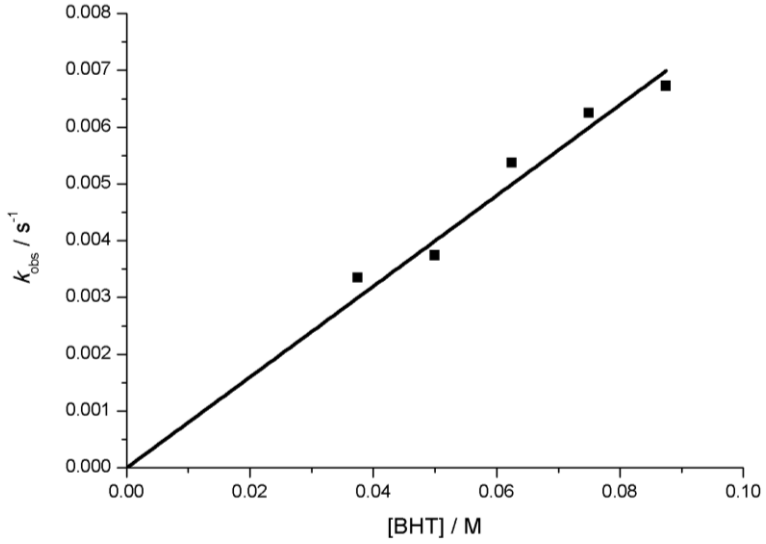

Figure S14: Plot of pseudo first order rate of reaction against concentration of 2,6-ditertbutyl-*para*-methylphenol by $[Cu^{II}(\eta^1\text{-}O_2^{\bullet-})(^{tpy3}TPA)]^+$ (0.5 mM) to find the second order reaction rate in THF at – 40 °C.

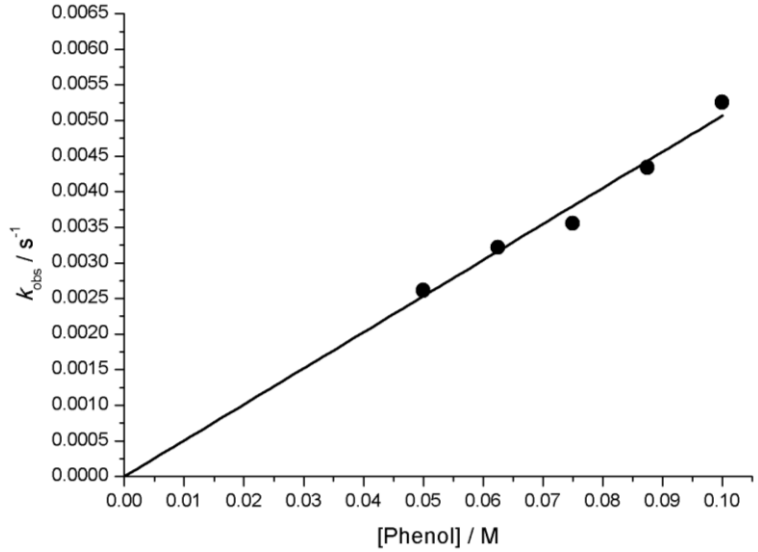

Figure S15: Plot of pseudo first order rate of reaction against concentration of tri-*tert*butylphenol by $[Cu^{II}(\eta^1\text{-}O_2^{\bullet-})(^{tpy3}TPA)]^+$ (0.5 mM) to find the second order reaction rate in THF at – 40 °C.

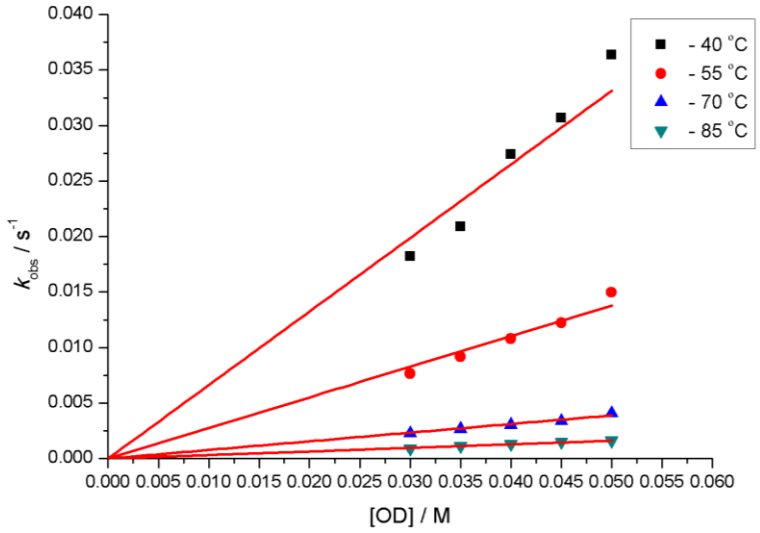

Figure S16: Plot of pseudo first order rate of reaction against concentration of 2,6-di-*tert*-butyl-*para*-methoxyphenol-deuterated by $[[Cu^{II}(\eta^1\text{-}O_2^{\bullet-})(^{tpy3}TPA)]^+$ (0.5 mM) to find the second order reaction rate in THF at various temperature (-40℃ (black); -55℃ (red); -70℃ (blue); -85℃ (green)).

A4: Mössbauer Spectrum for $[^{57}Fe^{IV}(O)(^{tpb3}TPA)(OTf)]^{2+}$ in Acetone

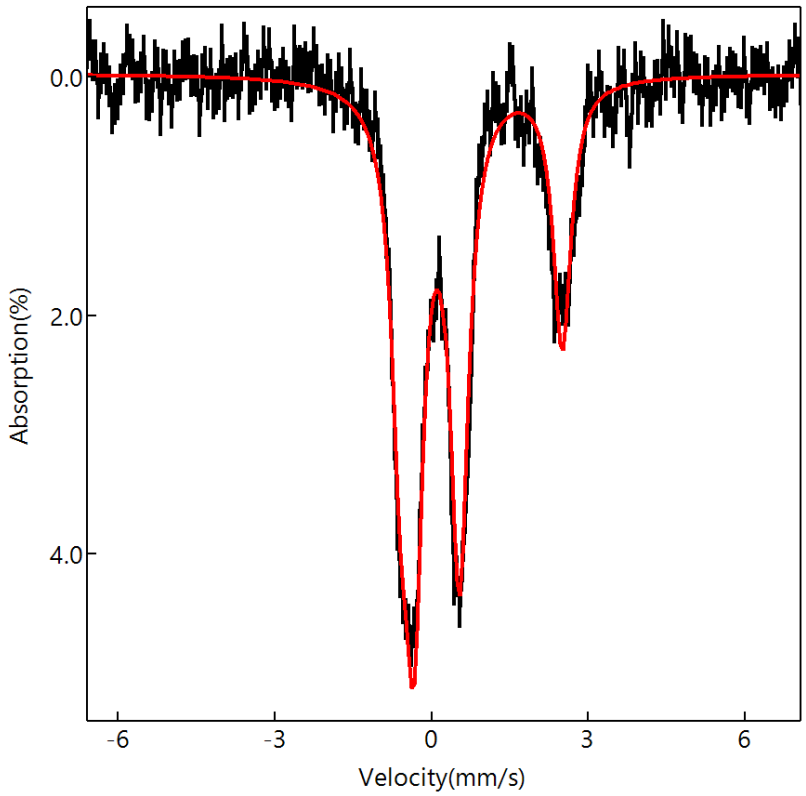

Figure S17: Zero-field Mössbauer spectrum (black) of $[^{57}Fe^{IV}(O)(^{tpb3}TPA)(OTf)]^{+}$ recorded in acetone solution at 4.2 K with simulated data (red). The applied magnetic field condition was not performed, however, based on the isomer shift and quadrupole splitting, it can be concluded that $[^{57}Fe^{IV}(O)(^{tpb3}TPA)(OTf)]^{+}$ possessed *S*=1 spin-state

A5: Kinetics Plot for $[Fe^{IV}(O)(^{tpb3}TPA)]^{2+}$

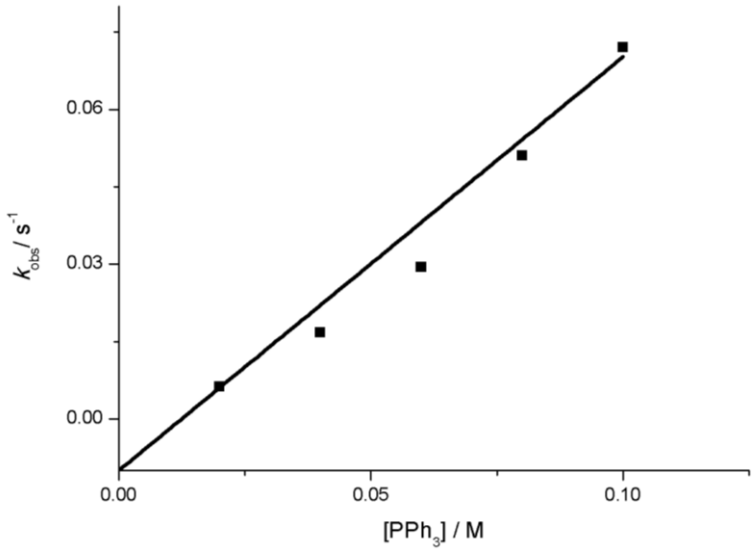

Figure S18: Plot of pseudo first order rate of reaction against concentration of PPh_3 to find the second order reaction rate in DCM/MeCN(9:1) at – 60℃.

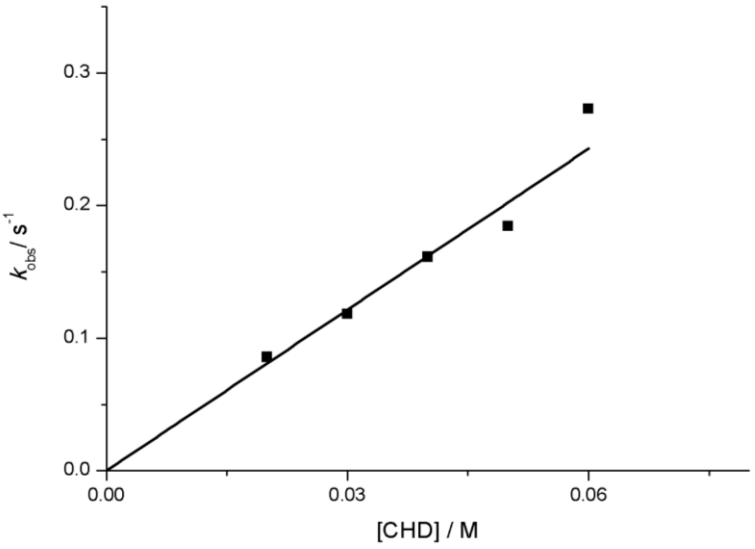

Figure S19: Plot of pseudo first order rate of reaction against concentration of 1,4-cyclohexadiene to find the second order reaction rate in DCM/MeCN(9:1) at – 40℃.

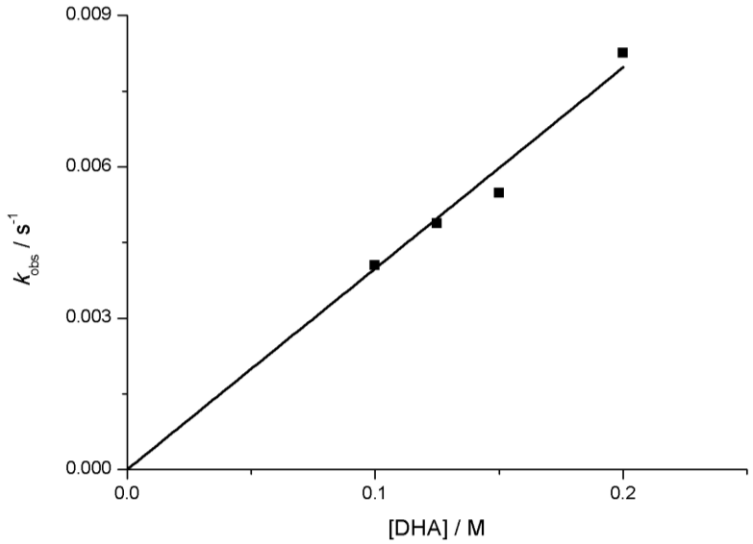

Figure S20: Plot of pseudo first order rate of reaction against concentration of 9,10-dihydroanthrance to find the second order reaction rate in DCM/MeCN(9:1) at – 40 ℃.

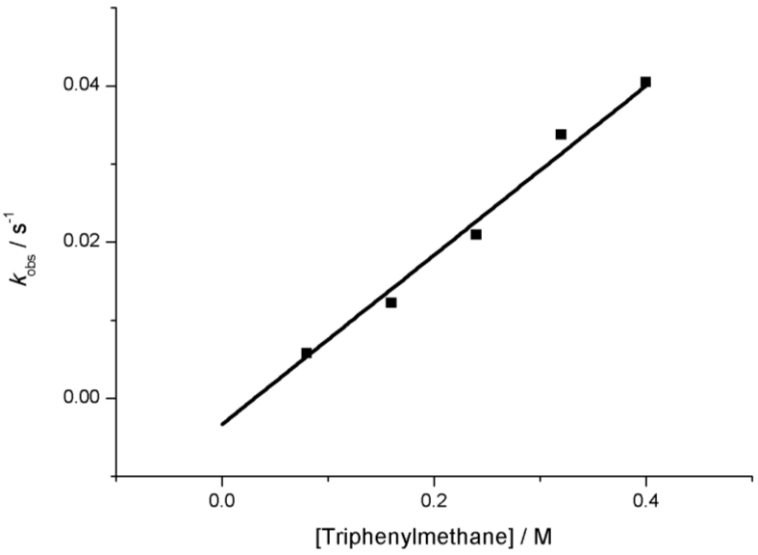

Figure S21: Plot of pseudo first order rate of reaction against concentration of triphenylmethane to find the second order reaction rate in MeCN at room temperature.

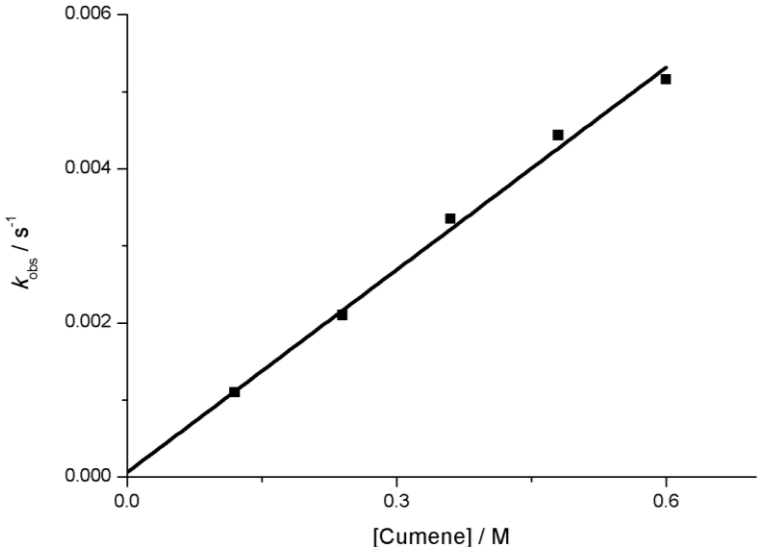

Figure S22: Plot of pseudo first order rate of reaction against concentration of cumene to find the second order reaction rate in MeCN at room temperature.

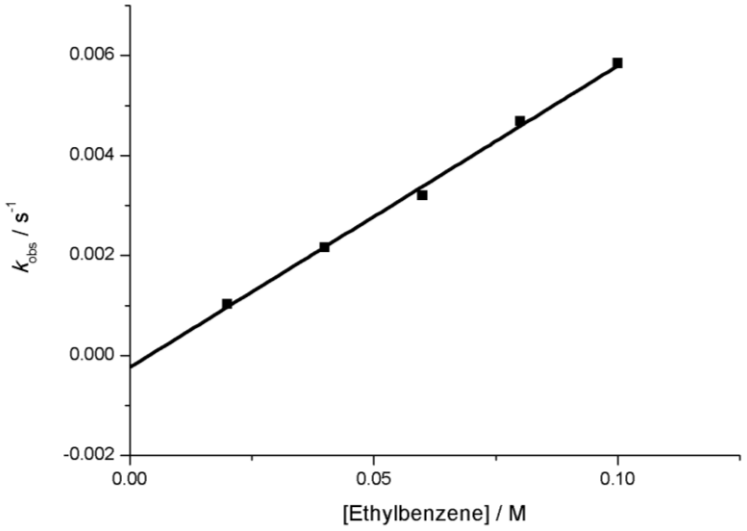

Figure S23: Plot of pseudo first order rate of reaction against concentration of ethylbenzene to find the second order reaction rate in MeCN at room temperature.

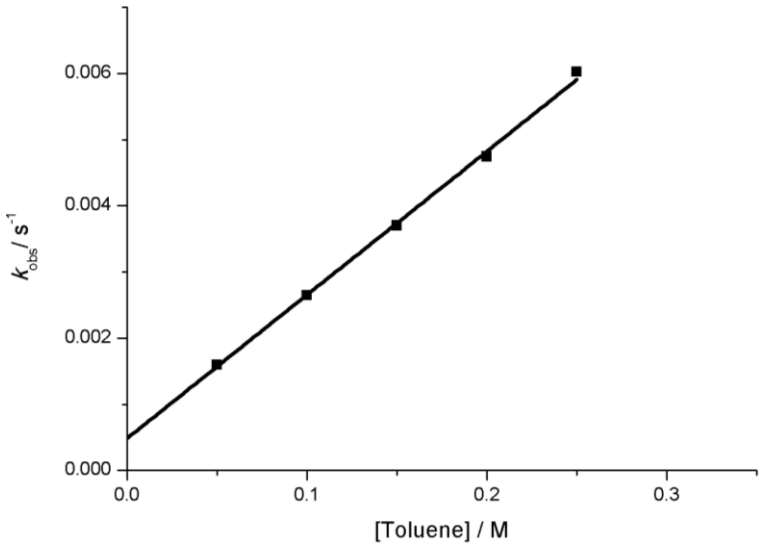

Figure S24: Plot of pseudo first order rate of reaction against concentration of toluene to find the second order reaction rate in MeCN at room temperature.

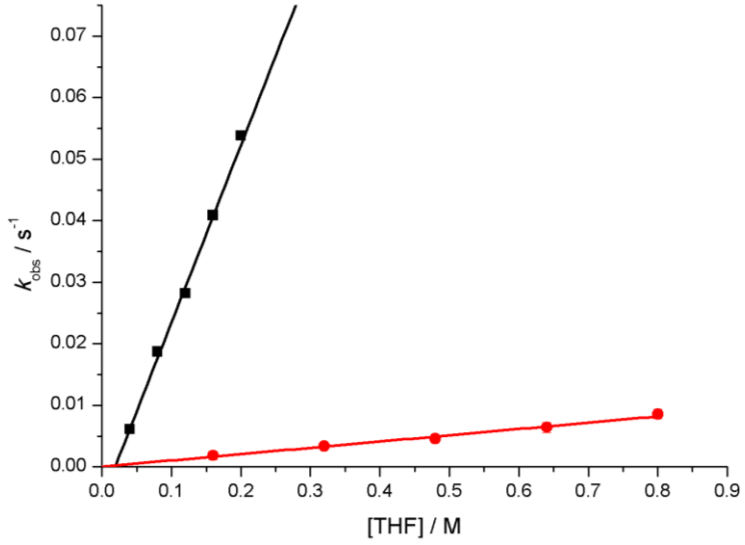

Figure S25: Plot of pseudo first order rate of reaction against concentration of THF (Black) or THF-d8 (red) to find the second order reaction rate in MeCN at room temperature.

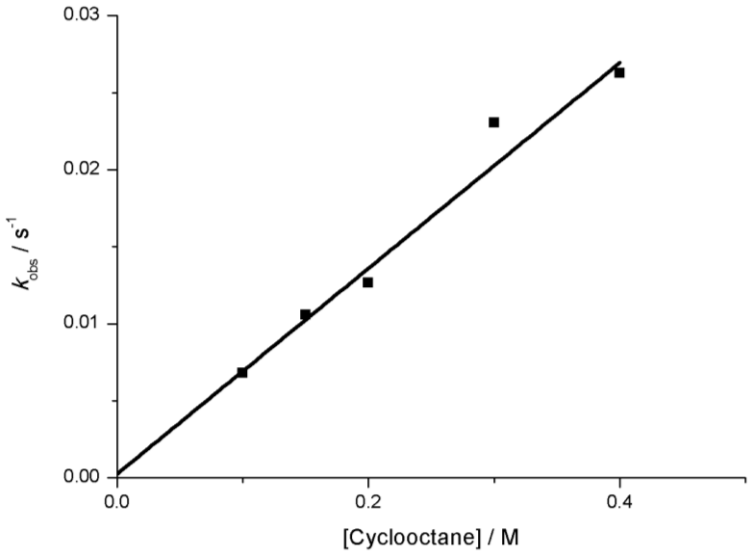

Figure S26: Plot of pseudo first order rate of reaction against concentration of cyclooctane to find the second order reaction rate in MeCN at room temperature.

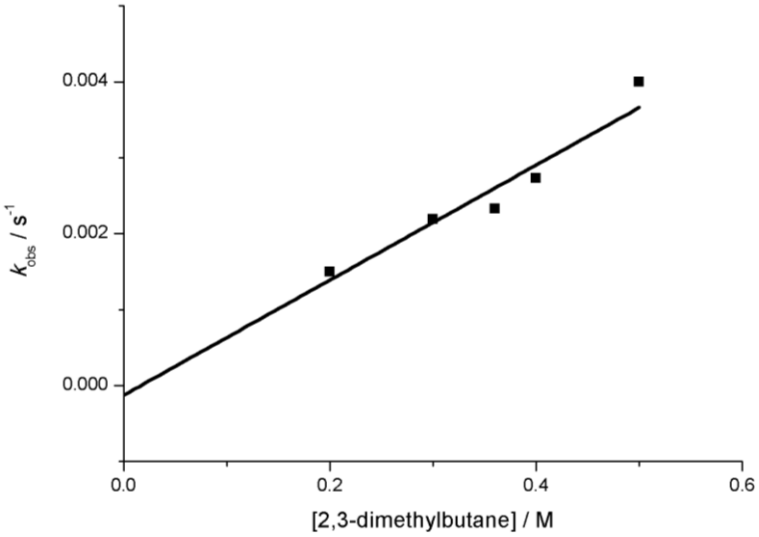

Figure S27: Plot of pseudo first order rate of reaction against concentration of 2,3-dimethylbutane to find the second order reaction rate in MeCN at room temperature.

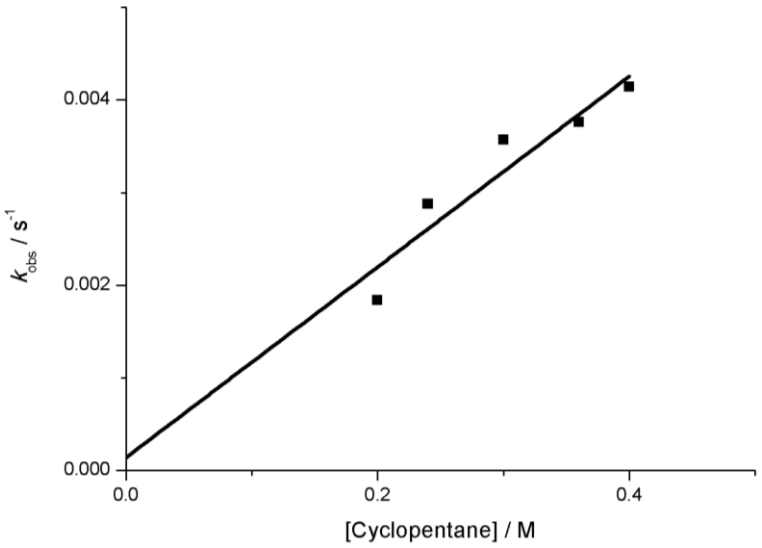

Figure S28: Plot of pseudo first order rate of reaction against concentration of cyclopentane to find the second order reaction rate in MeCN at room temperature.

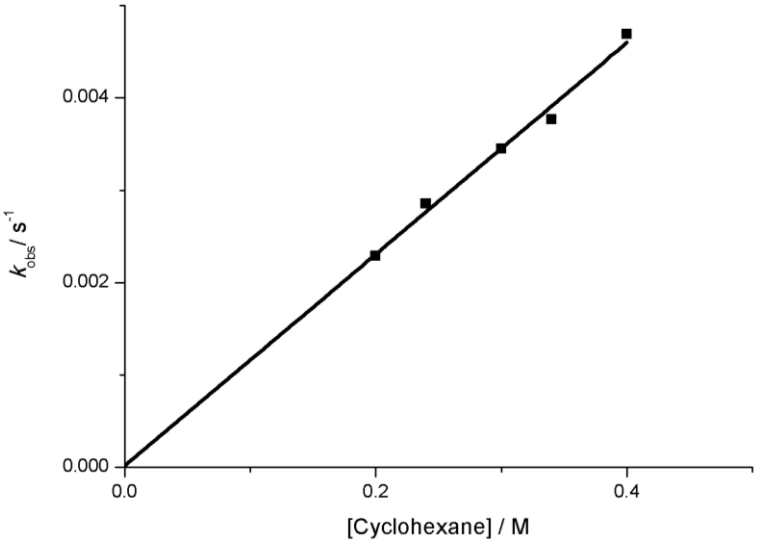

Figure S29: Plot of pseudo first order rate of reaction against concentration of cyclohexane to find the second order reaction rate in MeCN at room temperature.